Content

Core of the report. 2
2 Project objectives, work progress and achievements, project management 2
2.1 Project objectives for the period. 2
Recommendations from our Scientific Advisory Board 5
2.2 Work progress and achievements for the period. 7
WP1 7
WP2 23
WP3 30
WP4 38
WP5 47
WP6 61
WP7 113
WP8 122
WP9 128
WP10 137
2.3 Project management during the period. 141
WP11 141
Consortium management tasks and achievements per scientific component: 141
Networking and Dissemination of the Results 142
Overall Management of the Project 143
Financial management 146

Core of the report.

2 Project objectives, work progress and achievements, project management

2.1 Project objectives for the period.

WP1 - Mapping the ciliome

O1.2 To identify supramolecular ciliary complexes using a combination of biochemical fractionation, immunoisolation, and proteomic analysis by quantitative mass spectrometry (MS)

O1.5 Development of reagents and methods (antibodies, isolation protocols, ligands) for the study of specific complexes that emerged as candidates for disease markers

O1.6 Identify protein interactions perturbed in specific ciliary diseases

O1.7 Determine the distinct cellular/ciliary distribution of ciliome components

WP2 - Central resource for data integration

O2.1 To provide a robust, accessible and seamless system for storing, querying and updating data generated in the project

O2.2 To provide systems biology read data to produce a model of the ciliary system and its relation to human pathology and disease

O2.4 To integrate literature data with new finding that arise from experiments performed in the project

O2.5 To analyse interactome data using socioaffinity and related concepts in order to derive accurate complex and interaction sets for feeding into WP3 and WP4

O2.6 To provide a forum for dissemination of data within the consortium and to the external scientific community

WP3 - Construction, comparison and application of ciliary interactomes

O3.1 Generate large scale systems biology ready interaction and reaction information

O3.2 Assemble ciliary interactomes, functional networks, and pathways

O3.3 Apply comparative evolutionary analysis to ciliary function and disease

O3.4 Make molecular models and predictions for experimental testing

WP4 - Integrative modelling and predictions of ciliary system behavior

O4.1 To integrate outcome from all WPs into a network view of core ciliary processes

O4.2 To partition this network into functional modules

O4.3 To model and simulate modular ciliary processes with explanatory or predictive purposes

WP5 - Assay systems to study functional ciliary modules

O5.1 Quantifying ciliary transport

O5.2 Assaying ciliary polarization

O5.3 Measuring ciliary signaling

WP6 - Assays to distort Ciliopathy-Associated Modules (CAMs)

O6.1 Employ a semi high-throughput approach in mammalian cell culture and *C. elegans* to validate and further interrogate the roles of candidate CAM components (informed from WP1-4, 7 and 8) in cilium formation, maintenance, function, signaling and trafficking.

O6.2 Establish and functionally assess animal models (zebrafish, Xenopus, mice) of individual candidate and known CAM components, employing systematic integrated and strategic methodologies (e.g. ciliary transport, polarity, signaling) developed in WP5 and elsewhere

O6.3 Employ animal models (*C. elegans*, zebrafish, mice) to determine the genetic interrelationships between known/candidate components of individual and different CAMs

WP7 - Systematic RNAi screens to distort and identify ciliopathy-associated modules

O7.1 to distort the expression of known CAM genes in small- and medium-scale ciliome-wide screens

O7.2 to confirm known and to identify novel CAM genes using large-scale genome-wide screens

O7.3 integrate a high confidence list of validated known and novel CAM genes with other WPs to prioritize targets of interest

O7.4 integrate RNAi screening data with outputs from other WPs and the central SYSCILIA resource to create a public database of validated CAM genes

WP8 - Assessment of the involvement of the predicted ciliary molecular machines in the pathogenesis of ciliopathies

O8.4 To integrate data on functional sequence variants and clinical information with information on CAMs to come to a system model for explaining and predicting phenotypes and their variability

WP9 - Translational systems biology: ciliotherapeutics

O9.3 Lead compound characterization

WP10 - Dissemination and translation of knowledge

O10.1 Coordinate training activities – workshops, webinars, etc. - inside the project to ensure more efficient collaborations.

O10.2 Manage outreach in the form of external conferences, to ensure efficient dissemination of knowledge, impact and intellectual property to the external scientific community and relevant industries in Europe

O10.3 Dissemination and outreach to the scientific community of SYSCILIA results, methods, standards and models

O10.4 Translation of results and knowledge to industrial application

O10.5 Monitor intellectual property rights (IPR) issues as they arise

O10.6 Stipulate and update internal confidentiality agreements and external know-how agreements

O10.8 Determine the appropriate time point for the dissemination of result from the consortium to the public

O10.9 Assist in identifying of and liasing with industrial partners for the further exploitation of results

WP11 - Overall Management of the Project

O11.1 Proper conductance of the RTD specifically steering the conductance of the detailed implementation plan

O11.2 Financial management

O11.3 Managing seamless integration of all WP activities

O11.4 Communication and progress monitoring,

O11.5 Organisation of training activities, committee meetings, retreats

O11.6 Management and delivery of progress reports to the commission

O11.7 Management of Conflict resolution

O11.8 Quality assurance and control

O11.9 Risk Management

O11.10 Dissemination and translation of results

Recommendations from our Scientific Advisory Board

April 23, 2015, Pozzuoli, Italy
Scientific Advisory Board (SAB) on the 2015 meeting of the SYSCILIA consortium

SAB members present: Alfred Wittinghofer, Martijn H. Breuning and Erich E. Wanker

The fifth annual meeting of the SYSCILIA consortium was held from 22-24 April at the TIGEM in Pozzuoli, Italy. It was the fourth meeting at which SAB members were present.

Once again we were impressed with the constructive atmosphere, the enormous enthusiasm of all participants, the readiness to share ideas, data and tools, and the willingness to collaborate closely in order to realise project goals. After having experienced several EU-funded projects, the SAB members find SYSCILIA exceptional. The consortium is highly integrated and clearly follows a common research goal.

In previous meetings, research plans and future experiments were presented. Now, in this final meeting many researchers reported very interesting results at a very mature stage. This includes the mapping of the ciliome, the sequencing of patient DNAs, and the knockdown of genes in *Zebrafish Danio rerio, C. elegans, Xenopus*, retina explants form mice, and cell lines. The exome sequencing results strongly supported the notion that more than one gene is modified in ciliopathies and that the spectrum of mutations may eventually explain the variety of phenotypes of the disease. In a collaborative manner, both genome wide and focussed RNAi screens have been successfully completed. Furthermore, a large number of new genes that potentially play an important functional role in cilia formation were functionally validated in cell and *in vivo* model systems.

The consortium has continued the effort started earlier to generate a comprehensive set of protein-protein interactions in ciliogenesis using affinity chromatography-based MS methods and systematic yeast-two-hybrid screens. In total, ~58,000 interactions connecting 4,500 human proteins were collected. A significant fraction of interactions was validated in independent assays and functional studies. Using the available data, various approaches to predict functionally relevant protein clusters were presented. Furthermore, the effects of disease-causing mutations on protein-protein interactions were successfully examined. Quantitative measurements of gene expression were performed at protein as well as RNA level and data were integrated with the protein-protein interaction data sets generated. To avoid working with false positive interactions that are inevitable in systematic operations, the computational biologists developed various strategies to define high-confidence interactions for meaningful further experimental validation. Similarly, computational strategies to predict potentially disease-relevant ciliary genes as well as new functional protein complexes were successfully developed and applied.

In the work package on ciliotherapeutics, high-throughput testing of known drugs for their effects on cilia formation identified several promising compounds. These molecules were subsequently tested in various cell model systems. In addition, good progress was reported on the use of drugs that can initiate the read-through of early stop mutations causing the Usher Syndrome. This approach is innovative and in the medium term may open up novel therapeutic avenues.

The bioinformatics groups have been very active in collecting, storing and organizing the huge datasets, implementing good practice data integration. Furthermore, SYSCILIA researchers have been highly active in exchanging materials and data, as well as organising meetings and webinars. In recent years, a large number of peer-reviewed

papers has appeared in the highest-ranking journals. Furthermore, the collaborating groups are in the process of publishing additional “landmark papers” in order to make their data available to the public and to demonstrate the success of their systems biology approach. It is expected that the release of the available data sets will stimulate additional basic and applied research in the Cilia community.

Overall, it is important to note that this collaborative project has been highly productive. The SAB appreciated the disclosure of part of the exome sequencing results from patients, but urges the quick release of the full data set which will be a great value both to diagnostic as well as to research laboratories. The same holds true for all the other data that the cilia community is eagerly awaiting to be released into the public domain. Evidently the functional role of most proteins, and protein-protein interactions have as yet not been completely elucidated, indicating focal areas of future research.

The large majority of the deliverables and milestones stated in the initial application have been reached; in several aspects the consortium over-fulfilled the original plan. It will be interesting to see how the gained knowledge will be used in future studies to answer mechanistic questions about ciliary development, maintenance and transport. In our view, it seems very likely that the generated knowledge will lead to the development of novel disease-modifying therapies that in the long run will create benefit for patients, their families and health systems.

A systems biology approach was very successfully applied in this collaborative project. The generated data will clearly promote basic and translational research in the field, which is in line with the mission of the Horizon 2020 program.

Alfred Wittinghofer
Martijn Breuning
Erich Wanker

2.2 Work progress and achievements for the period.

Work package number	**WP1**	Start date or starting event:		month 1
Work package title	**Mapping the ciliome**			
Activity Type	RTD			
Participant number	**17 (L)**	1a	1b	6	16
Participant short name	UTUB	RUNMC *Roepman*	RUNMC *Kremer*	JoGuMz	WWU
Person-months per participant:	112^{+50}	50^{+27}	22^{+7}	25^{+7}	27^{+14}
Actual person months per participant* month 48 - 60	22^{+8}	6.5	0.95	17.4^{+11}	3.46

* This is considered as use of resources.
Deviations are explained in the end of the report for this Work package.

A summary of progress towards objectives of WP1:

Objective 1.1. *To identify the ciliary inventory of proteins of various cilia types*

All deliverables under this Objective were delivered.

Objective 1.2. *To identify supramolecular ciliary complexes using a combination of biochemical fractionation, immunoisolation, and proteomic analysis by quantitative mass spectrometry (MS).*

The ciliary protein network was analysed by SF-TAP. The complete and final dataset with SF-TAP complexes for 217 different bait proteins was submitted to WP2 where bio-informatic analysis using socio-affinity and hierarchical clique determination was accomplished. This resulted in novel interactions and complexes of which selected ones were validated by targeted approaches (SRM/PRM).

Objective 1.3. *To identify binary ciliary interactions using yeast two-hybrid screens*

All deliverables under this Objective were delivered. Data related to this objective are documented in Task 1.3.

Objective 1.4. *Search for protein interactions and protein complex compositions that are altered in disease using mouse and zebrafish disease models and human biopsy samples using quantitative proteomic methods*

All deliverables under this Objective were delivered. PalMyr colocalisation experiments substantiated the interaction between PDZD7 and IFT27, 46 and 57.

Objective 1.5. *Development of reagents and methods (antibodies, isolation protocols, ligands) for the study of specific complexes that emerged as candidates for disease markers*

As described in D1.13, a new method was developed that is able to dissolve protein complexes in a stepwise manner. The method is called EPASIS. In the method, complexes are exposed to increasing concentrations of detergent that break off weak interactions first and strong interactions afterwards. Applying EPASIS to the IFT-B complex showed different members of the complex as being anchored with different binding forces within the complex. Furthermore, this method allows the determination of relative binding affinities within a complex. It was applied to a total of 18 complexes.

Objective 1.6. *Identify protein interactions perturbed in specific ciliary diseases*

As described in D1.10, the quantitative proteomic analysis of three mutations of IFT-B complex components that were predicted to impact on the structure of the proteins showed the following: The protein complexes were siginificantly changed. Three heterozygous mutations in MKS could be analyzed in terms of their underlying perturbations of protein interactions. The R607H mutation of IFT88 leads to a specific loss of interaction of IFT-B1 with IFT-B2. The T41I mutation in HSPB11 appears to only disrupt IFT-B2. The E1153G mutation of IFT172 appears to only disrupt IFT-B1.

Objective 1.7. *Determine the distinct cellular/ciliary distribution of ciliome components*

We determined the distinct cellular localisation of POCB1, CEP250 and CCDC113. POCB1 is localized to the centriole and basal body of the connecting cilium, CEP250 is localized globally to cones, CCDC113 is localized to the base of the connecting cilium.

A summary of progress towards each task in WP1:

- ***Task 1.1. Defining the ciliary inventory of proteins***

Deliverables under this Task: D1.1 (month 6) and D1.3 (month 18) both delivered.

A: Isolation of cilia and their associated molecular components via biochemical enrichment

B: Defining the composition of cilia through proteomic methods

We have delivered both deliverables under this task. According to schedule, we are employing the results to dissect and specify ciliary functions and evaluate ciliopathy-associated variants.

- ***Task 1.2. Defining ciliary protein interactions via proteomic methods***

Deliverables under this Task: D1.4 (month 24), D1.6 (month 30), D1.7 (month 30), D1.8 (month 30) and D1.11 (month 42) all delivered.

A: Targeted isolation of ciliary proteins and their associated molecular components via affinity purification in combination with mass-spectrometry

Partner 1a and 17:
Great effort and care was taken to produce a final dataset of SF-TAP purified, ciliary protein complexes. To achieve this, we performed additional SF-TAP experiments to a robust dataset which was then manually inspected to remove false positive identifications due to carry over of peptides during mass spectrometric analysis. Furthermore, experiments of low quality were removed. This resulted in a dataset, consisting of SF-TAP complexes for 217 different bait proteins, resulting in a network of 4701 proteins with over 41,352 unique protein interactions. This dataset was submitted to WP2 partners where network analysis by socio-affinity and hierarchical clique determination was performed.

Partner 6:
In previous studies (see 4th annual report and Bauss et al. 2014), we affirmed interactions between the USH proteins SANS and Vlgr1a, respectively, with Magi2, a protein involved in endocytic processes at the base of primary cilia. We (in collaboration with partner 17) thus performed tandem affinity purification (SF-TAP), and mass spectrometry with Magi2. Mass spectrometry resulted in 41 protein hits that were not found in the negative control, among which proteins involved in the regulation of the actin cytoskeleton, e.g. beta-actin itself, WASL (Wiskott-Aldrich syndrome-like), BAIAP2 (BAI1-associated protein 2), and WIPF2 (WAS/WASL interacting protein family, member 2). We also performed SF-TAP analysis with SF-CIB2, a rather recently discovered USH protein (Riazuddin et al. 2012), which resulted in 120 distinct hits. Interestingly, 54 of those hits overlap with hits obtained from TAP-analysis of full-length Vlgr1a isoform.

We have previously reported that we gathered evidence that the USH1G protein SANS interacts with several IFT proteins by 1:1 yeast-two-hybrid assays in collaboration with partner 1a. IFT20, IFT52, IFT57 and IFT74 have been confirmed in reciprocal co-immunoprecipitation. We now verified IFT52 and IFT74 as SANS binding proteins in cellular system using our recently established membrane targeting assay (Bauss et al. 2014). In addition, we showed the partial co-localization of SANS and IFT20, IFT52 and IFT57 at ciliary compartments of retinal photoreceptor cells, namely the basal body of the connecting cilium and its adjacent centriole applying indirect immunofluorescence staining **(figure 1.1)**. We have previously demonstrated that SANS directly binds to the USH modifier PDZD7, a protein, which has recently been found to interact with a subset of IFT complex B proteins by partner 1b. We will follow up the SANS-PDZD7-IFT complex B in cooperation with partner 1b.

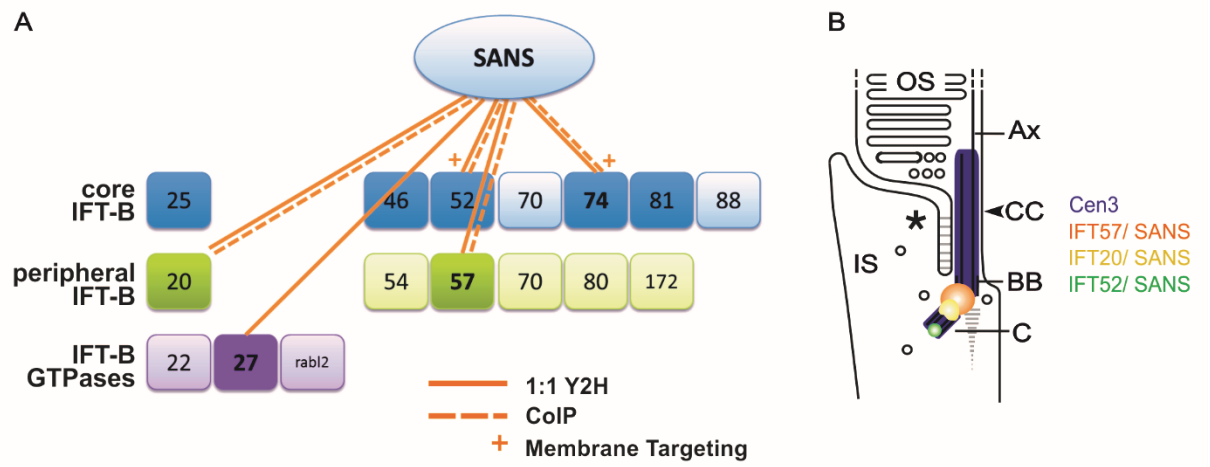

***Figure 1.1*: (A)** Interaction of SANS with IFT complex B proteins revealed by complementary methods. **(B)** Scheme of co-localization of SANS, IFT20, IFT52 and IFT57 in the photoreceptor cell depicted by immunofluorescence analysis in cryosections through the murine retina.

B: Ciliary complex comparison between different cellular states or disease causing mutant and wild type protein

Partner 17:

Following the interactome analysis of ciliary protein complexes we started to dissect the function of single complex components. We wanted to understand changes of the interactome related to different states of the cell, e.g. proliferating versus resting conditions, or isoform-specific complexes. We started with analysis of the Clusterin-associated protein 1 (Cluap1), which is a well-known IFT-B component but, interestingly enough, also described to be up-regulated in cancer cell lines (Ishikura et al., 2007; Takahashi et al., 2004). 12 splice variants are predicted with seven of them supposed to be protein coding sequences (ENSG00000103351.10). SF-tagged constructs resembling isoform 1, 2, 3 and 4 were tagged with SF for affinity. First, we overexpressed Cluap1v4 in SILAC-labelled HEK293T cells and either starved the cells for 24hrs or kept them in growing medium. The comparison of the results revealed a distinct interactome pattern (**figure 1.2A**). As expected, we could identify IFT20, an IFT-B protein, as well as BBS2 and BBS7 as complex components under starving conditions. Further, CEP170, a potentially IFT-B associated protein affecting ciliogenesis, could be identified. To better understand which Cluap1 isoform is involved in IFT-B complex association we overexpressed two different Cluap1 isoforms and compared the interactome data (**figure 1.2B)**. Isoform 1 bound more specifically to IFT components whereas isoform 4 interacted with BBS proteins. Because MAPK1/ ERK2 was one very prominent interactor we started to analyze the localization of the latter in ciliated IMCD3 cells. ERK2 was localized to cilia and co-localized with Cluap1 in the cytoplasm (**figure 1.2C, D)**. To confirm the mass spectrometry data SF-tagged Cluap1v4, Cluap1v1, IFT20, -80 and BBS2 was expressed in HEK293T cells and the STREP-tag purified eluates were analyzed by Western blot. IFT and BBS2 eluates were blotted with an antibody specific for two peptides of the C-terminal region which is the same for isoform 1, 2 and 4. In Hek293T lysates two isoforms could be detected with the short variant proven to be higher expressed. Interestingly, in eluates of the IFT-B constructs only the long isoform was found to be enriched, whereas in BBS2 eluates the short isoform was detected (**figure 1.2E**).

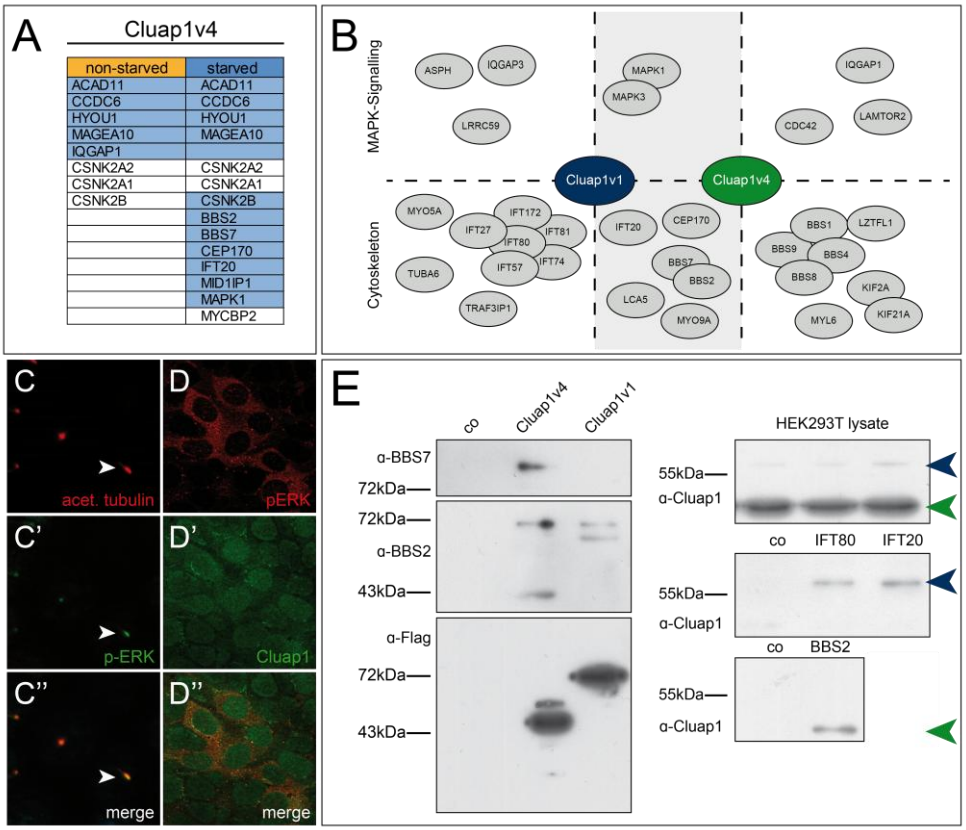

Figure 1.2: Analysis of HEKT293 eluates with Cluap1v1 and/ or Cluap1v4 used as bait. **A**) Cluap1v4 interactors with a significance A ≤ 0.05 and a p-value ≤ 0.05 (one sample ttest). **B**) Interactors specifically enriched in Cluap1v1 eluates (left) versus Cluap1v4 (right) and proteins found to be bound by both isoforms (middle). **C,D**) pERK was localized to cilia (C-C'') and pERK co-localized with Cluap1 in the cytoplasm (D-D'') **E**) Western blot of STREP-tag purified Cluap1 samples blotted for BBSome proteins and STREP-tag purified IFT samples blotted for Cluap1 confirmed the mass spectrometry data.

C: Identify proteins that interact with the target proteins in their native setting in a specific organ.

Partner 1b:

We have generated transgenic zebrafish lines that express SF-TAP tagged USH scaffold proteins (Sansa, Sansb, Cip98a and Cip98b) under the control of a photoreceptor specific promotor. The affinity purification technique from zebrafish larvae of 4dpf needs optimization. So far, we did not succeed to obtain SF-TAP tagged proteins from a protein lysate of ~200 larvae after a single round of affinity-purification. To overcome this problem, we apply two different strategies in parallel: A) Additional breeding of transgenic fish in order to increase the numbers of larvae per experiment. B) Analyse samples of a one-step affinity-purification via mass spectrometry.

In collaboration with partner 6, mice have been injected with rAAV-viruses for expression of murine SF-TAP-tagged Ush2a_icd and SF-TAP-tagged Dfnb31 (= Whirlin/Ush2d). Results of the performed TAP experiments are being reported by partner 6.

Partner 1b has initiated GST-pulldown experiments from bovine retina's for a refinement of the NINL/DZANK1 and NINL/CC2D2A/MICAL3 modules. Mass-spec analysis of the proteins pulled from the lysates will be performed in collaboration with partner 17.

Partner 6:

As reported in the 4th annual SYSCILIA report, partner 1b and we have generated rAAV for the transfer of SF-TAP-transgenes by subretinal injections into mouse eyes. In this reporting period, we have injected N-SF-TAP-whirlin and N-SF-TAP-USH2A-cytoplasmic domain (cloned by partner 1b) into both eyes of 15 and 19 mice, respectively. After two months, the retinas were subjected to single affinity purification with anti-FLAG beads. Subsequent mass spectroscopy analyses by partner 17 resulted in 112 hits that differed from uninjected control retinas for SF-USH2a-cytoplasmic domain and 288 distinct hits for SF-whirlin. 31 of those hits overlap between SF-USH2a and SF-whirlin transfected retinas. Among these putative complex partners were proteins known to be associated with cytoskeletal elements and intracellular transport such as filamin-A, unconventional myosin-Ib, annexin A2, microtubule-associated protein RP/EB family member 3, Calponin-3, LIM domain and actin-binding protein 1, and MAGUK p55 subfamily member 2. Further, many hits were ribosomal proteins. However, the two tagged proteins themselves could not be detected in the silver gel nor by mass spectroscopy. The experiments will be repeated. We have also injected rAAV for SF-tagged SANS subretinally in 13 mice deficient for wt-sans (Jackson shaker, js/js mice). The mice will be dissected in the beginning of July, and the retinas will be subjected to mass spectrometric analysis.

Partner 16:

Partner 16 has provided 5 new cDNA constructs for yeast two hybrid screening of novel candidate PCD-causing genes (WDR16) and known PCD-causing genes (DNAH11, aa2479-3466 and CCDC39).
In collaboration with Partner 1a, binary interactions were tested among CCDC114, whose mutations cause outer dynein arm defects in PCD, and PCD-candidate gene CCDC151. Partner 16 demonstrated that CCDC114 and CCDC151 co-immunoprecipitate in HEK cells. These studies have been recently published describing CCDC151 as a novel PCD-causing gene that causes outer dynein arm defects in motile cilia (Hjeij et al, Am J Hum Genet. 2014).

Partner 16 has performed new NTAP experiments for potential ciilary genes (RFX1) and known PCD-causing genes (C21orf59) as well as multiciliation / ciliogenesis factors (CCNO, MCIDAS). Partner 16 has recently published papers describing mutations in CCNO (Wallmeier et al, Nat Genet. 2014) and MCIDAS (Boon et al, Nat Commun. 2014), which cause a severe form of respiratory disease resulting from reduced generation of multiple motile cilia (RGMC).
In collaboration with Partner 17, NTAP-CCNO and NTAP-MCIDAS were screened for interaction partners. NTAP-MCIDAS identified several interaction candidates, which may serve as a valuable resource for defining the ciliary interactome, as this dataset likely represents basal-body associated and transcription factors critical for the generation of multiple motile cilia.

➢ ***Task 1.3. Defining ciliary interactions by genetic methods via yeast two hybrid screening***

Deliverables under this Task: D1.2 (month 12) and D1.5 (month 24) both delivered.

Partner 1b:

In the previous period, we reported in this section on the interactions between the Usher Syndrome (USH)-associated scaffold protein PDZD7 and members of the IFT-B complex. Tandem affinity purification experiments of SF-TAP-tagged PDZD7 revealed the IFT-B complex proteins IFT25, IFT27, IFT46, IFT74 and IFT81 as potential members of the PDZD7 protein complex. TAP analyses of all other USH proteins were negative for intraflagellar transport proteins.

We have confirmed the putative interactions between PDZD7 and IFT25 (HSPB11) and IFT27 via co-immunoprecipitation assays (**figure 1.3A**). Expression of IFT57 was unsuccessful in this attempt and IFT74 did not co-precipitate with PDZD7 in a separate experiment. We are currently extending our co-immunoprecipitation experiments to IFT46, 57 and 81. These first results imply PDZD7 as a functional connector between USH proteins and the intraflagellar transport machinery (**figure 1.3B)**.

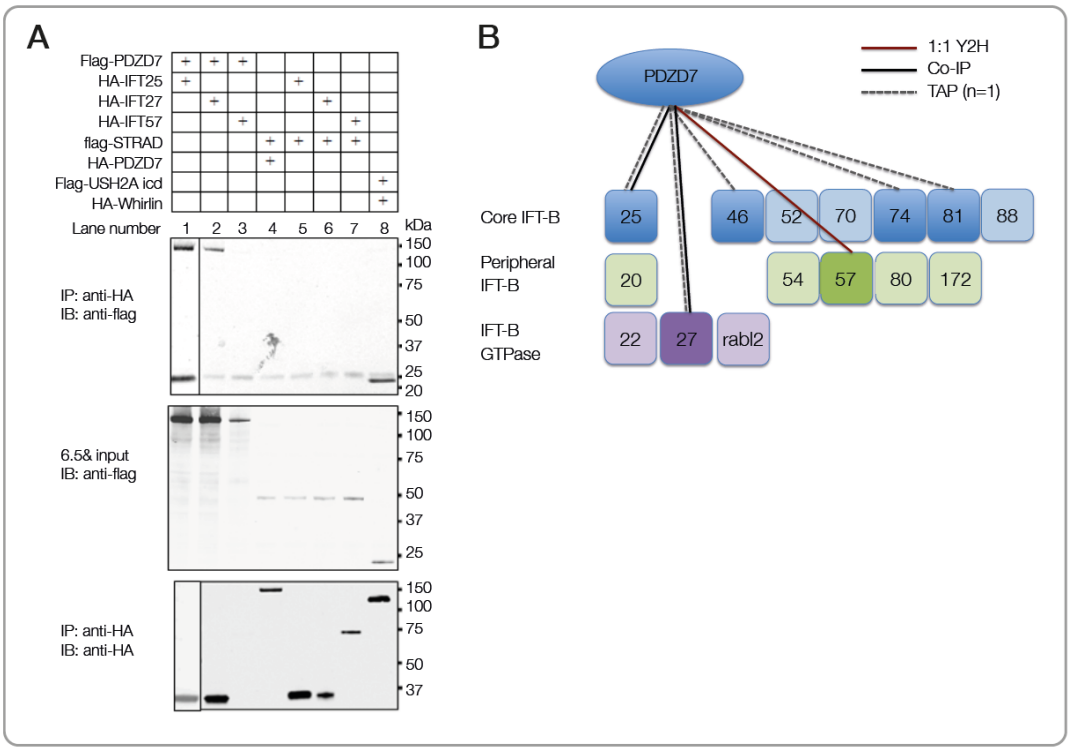

Figure 1.3. PDZD7 interacts with several IFT-B complex members. **A**) Co-immunoprecipitation with anti-HA affniity purification of 3xHA-tagged IFTs and 3xFLAG-tagged PDZD7, expressed in HEK293T cells. The top panel revealed that flag-PDZD7 (protein input shown in the middle panel) co-immunoprecipitated with HA-IFT25 (lane 1) and HA-IFT27 (lane 2), but not with HA-IFT57 (lane 3). The anti-HA immunoprecipitates are shown in the bottom panel, in which the expression of HA-IFT57 in lane 3 is absent. **B**) overview of the identified interactions between PDZD7 and the IFT-B complex. PDZD7 associates with members of the core IFT-B module, peripheral IFT-B module and IFT-B GTPases.

Recently, interactions between SANS, another USH scaffold protein, and IFT-B proteins were identified by partner 6 (this report and report of month 48). GST-pull-down experiments suggesting an interaction between SANS and PDZD7 were published in 2009 by Schneider et al (PMID 19028668).

Via a dedicated 1-on-1 interaction assay in yeast, we have provided additional evidence of an interaction between SANS and PDZD7. Since we only found a positive interaction between full length SANS and full length PDZD7 or the N-terminal region of PDZD7, we were not able to completely pinpoint the region of the proteins that mediate the interaction.
In addition, we further investigated the interaction between PDZD7 and IFT-B complex members. As it turns out, PDZD7 is rather sticky in co-immunoprecipitation experiments. Althoughwe did observe interactions between PDZD7 and IFT25, 27, 46 and 57, we are not sure how specific they are. PalMyr colocalisation experiments substantiated the interaction between PDZD7 and IFT27, 46 and 57. Single transfection of mRFP-tagged PDZD7, -IFT46 and -IFT57 did not show the typical membrane localization that we observe when co-transfected with (membrane-targeted) PalMyr-eCFP fusion proteins (**figure 1.4**).

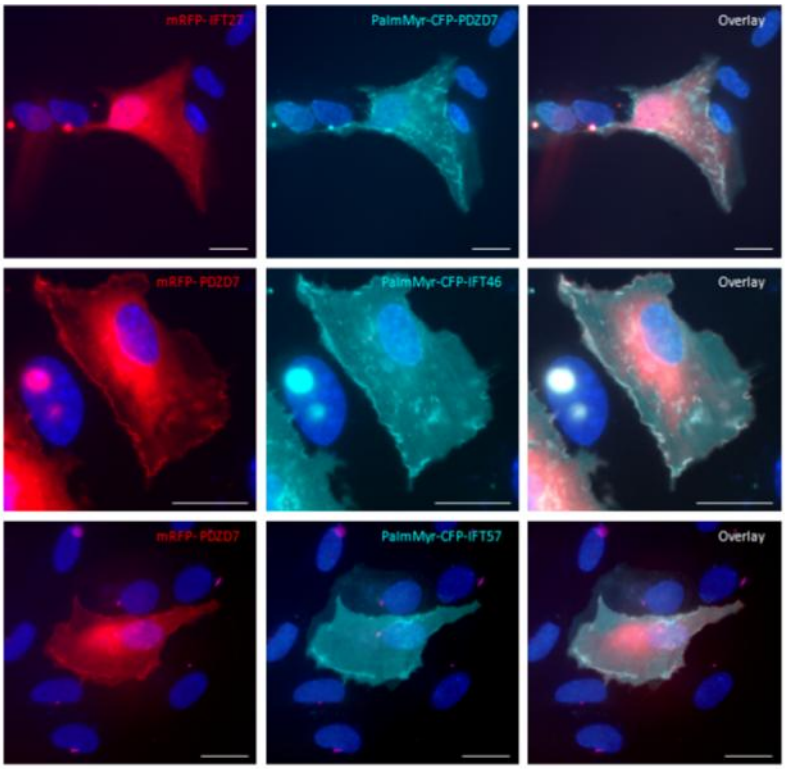

Figure 1.4. **PalMyr colocalisation assay of PDZD7 and several IFT complex B members.** PalMyr eCFP fusion protein localise (artificially) to the cell membrane. The interaction proteins (tagged with mRFP) are recruited to the membrane.

- ***Task 1.4. Defining ciliary interactions via quantitative proteomic methods***

Deliverables under this Task: D1.7 (month 30), D1.9 (month 36), D1.12 (month 42), D1.10 (month 36) and D1.15 (month 60) all delivered.

A: Quantitative and comparative MS analysis.

Partner 17:
Variants identified in the medical sequencing as well pathogenicity testing in zebrafish (partner 4, WP8) were used for prediction of potential impact on protein-protein-interactions and the structure of the protein affected (partner 15, WP3). To validate the predictions, 7 IFT complex B

variants were used to quantitatively compare the complexes to the WT protein complex. In initial experiments, we could identify alterations. These variants affected the two sub-modules of IFT-B selectively (**figure 1.5**). This validates several predictions and strengthens the hypothesis that the IFT complex B is actually composed of two distinct sub-modules and not a core with associated components.

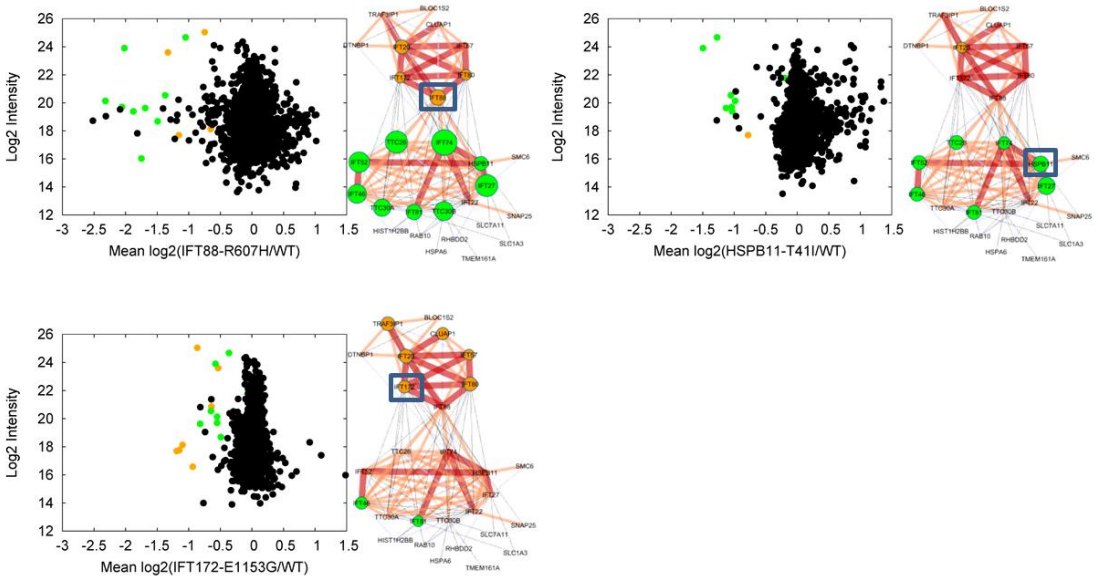

***Figure 1.5*:** Scatter plots and networks, showing the alterations within the IFT-complex B, induced by variants that were predicted to alter interactions domains or the structure of the affected protein.

To further validate the existence of two sub-complexes within IFT complex B, we applied two separate approaches. 1st we separated the IFT88 associated complexes, purified from HEK293 cells, stably expressing IFT88-SF by a sucrose density gradient. This resulted in a separation that almost perfectly resembled the predicted sub-complexes. The only protein that showed a behavior that was different from predictions was IFT172. This seems to have the potential to be present in both sub-complexes (**figure 1.6 a**). 2nd, we applied the EPASIS approach to define sub-complexes. Both, IFT88 and IFT27 were stably expressed in HEK293 cells and the complexes purified. In both cases, we could show an almost perfect separation of the complexes. IFT27 in IFT88 EPASIS eluted with complex B1 instead of B2. The same was true for TTC30B which also co-eluted with complex B1 instead of B2 as expected. Taken together, despite these discrepancies, we could show that there are two core complexes formed, not one core and some associated subunits, as described in literature (**figure 1.6 b, c**). This is also reported in deliverable report D1.13.

The EPASIS approach was further applied to determine binding profiles to generate kinetic data for the following complexes: 14-3-3 epsilon, the GID complex, NINL, LCA5, DNYLT1, RAC1, RALB, SHC1, BRAF, IFT88, IFT20, IFT27, IFT52, IFT57 and IFT88. For all these proteins and their associated complexes, a full and robust dataset is available for the relative determination of affinity and for the determination of sub-modules within complex mixture (see also deliverable report D1.15).

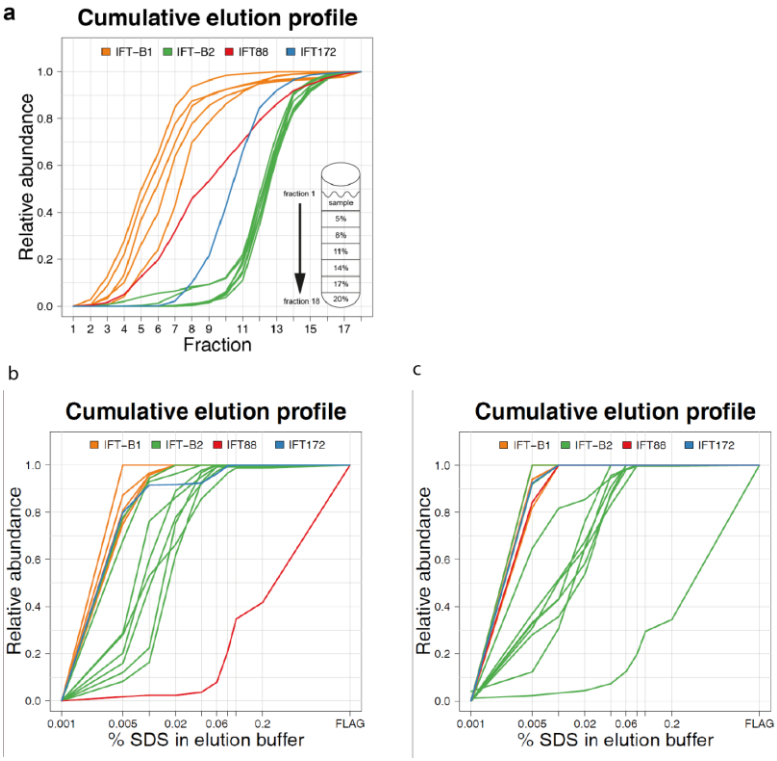

***Figure 1.6*: a**) sucrose density gradient centrifugation to separate IFT-B sub-complexes. Plotted is the cumulative relative amount for each protein, present in ascending fractions. **b**) and **c**) cumulative plot of relative protein amounts for each protein present in fractions with increasing SDS concentrations.

As described under Task 1.2 B, we have dissected the complexes of CLUAP1 and quantitatively compared the complexes of two different isoforms to identify potential differential roles within the cells. Further, we used SILAC labelling and quantitative mass spectrometry to identify 1st, the specific complex components of both isoforms and 2nd, directly compared the complexes, formed by those in normal growth and under starvation (**figure 1.7**).

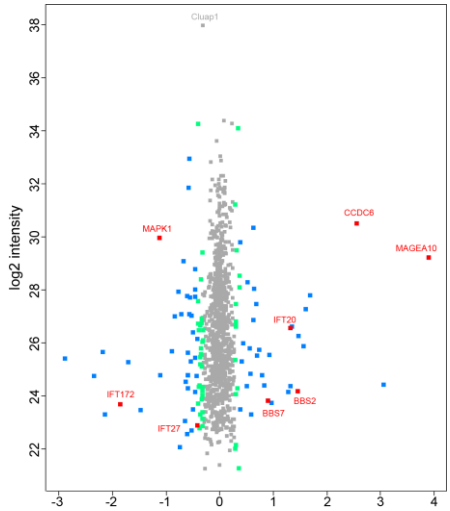

***Figure 1.7*:** Scatter plot for the direct comparison of the complexes of CLUAP1 isoforms, showing the differential interaction of both, IFT and BBS proteins as well as proteins, involved in MAPK signaling.

Additionally, quantitative mass spectrometry was used for the identification of alterations within the IFT complex B. For this comparison, mutations were used that were identified in ciliopathy patients and predicted to affect the binding surfaces or structures of protein domains.

B: Single reaction monitoring (SRM) to achieve absolute quantitative data and to determine stoichiometries of selected complexes.

Partner 17:
Stoichiometry determination of IFT-A has been reported under D1.12. In addition to the interaction of IFT-A with Lebercilin as well as with Tubby related protein 3 by SRM, several interactions that were predicted from the network analysis within WP2 were validated using PRM, an alternative targeted MS approach. By using this approach, we could validate the interaction of IFT-B with a membrane targeting complex, the biogenesis of lysosome-related organelles complex (BLOC). Furthermore, we could successfully validate interactions within a complex formed by Lebercilin, RUFY3 and SSNA1.

The complex formed by WDR83, GRB2, RP2, GLO1, CEP131 could only partially be validated. Although, we could clearly detect GRB2, WDR83 and GLO1 within the RP2 complex, none of these were detectable within the GRB2 complex. Additionally, GLO1 was also present in control samples and therefore more validation would be necessary. Taken together, we applied SRM and PRM to attempt the validation of 34 interactions, 25 of which could be successfully validated. For details also see report on D1.10.

C: Monitoring performance

Performance was constantly monitored as described before and according to the quality assurance plan (see Deliverable report D11.3).

- ***Task 1.5. Defining spatial distribution and in situ visualization of ciliary protein complexes***

Deliverables under this Task: D1.14 (month 48) and D1.13 (month 48) both delivered.

Partner 6:
In the reporting period, we analyzed the distribution of POC1B, a protein essential for ciliogenesis, basal body, and centrosome integrity, in murine and human retina by the means of immunofluorescence. POC1B was predominantly detected in the ciliary region of photoreceptor cells and synapses of the outer plexiform layer (**figure 1.8**). Higher magnifications and co-labeling with ciliary markers revealed that POC1B localized to the periciliary region, the basal body and centriole adjacent to the connecting cilium of photoreceptors. The results have been recently published in *Human Mutation* (Beck et al., 2014).

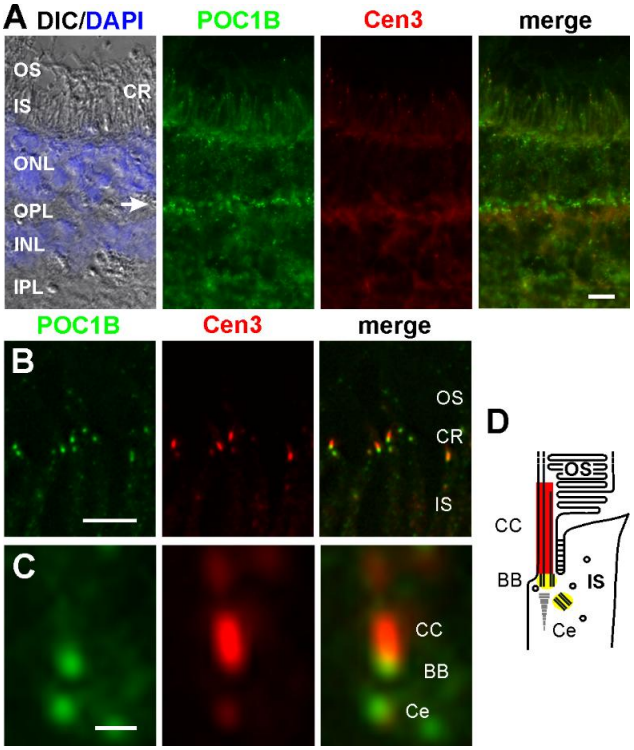

Figure 1.8. Localization of POC1B in the human retina. **A:** Longitudinal cryosections through a human retina stained for POC1B (green) and counterstained for the ciliary marker centrin-3 (Cen3, red) reveals POC1B localization in the ciliary region (CR) of the photoreceptor layer and the synapses of the outer plexiform layer (OPL) (arrow). Overlay of DIC image with DAPI (blue) nuclear stain in the outer (ONL) and inner nuclear layer (INL) shows retina layers. OS, outer segment; IS, inner segment. **B:** Increased magnification of the photoreceptor cells demonstrates colocalization of POC1B and Cen3 in the photoreceptor ciliary region (CR). **C:** High magnification of the photoreceptor cilium reveals substantial localization of POC1B at the centriole (Ce) and the basal body (BB) of the connecting cilium (CC), but not in the CC itself, as schematically demonstrated in **D**. Scale bars: A, 10 μm; B, 5 μm; C, 0.5 μm.

In 2014, a homozygous Cep250 nonsense mutation, in combination with a heterozygous C2orf71 nonsense mutation, was identified to cause an atypical form of USH (Khateb et al., 2014). In order to analyze the subcellular localization of CEP250, we performed immunofluorescence analysis in murine retina. We observed CEP250 staining as dotted stripes projecting in the photoreceptor cell layer (**figure 1.9**). Co-staining for with the ciliary marker centrin 3 revealed that CEP250 is expressed in the area of both segments (**figure 1.9 C-E**). Co-labeling with peanut agglutinin (PNA), a well-established marker for cone photoreceptor cells (**figure 1.9 F-H**), showed CEP250 expression in cones. We currently analyze immunoelectron microscopy data of pre-embedding immunolabeling of murine and porcine retinas. Preliminary data support immunofluorescence data and indicate CEP250 expression in the outer segments of cones.

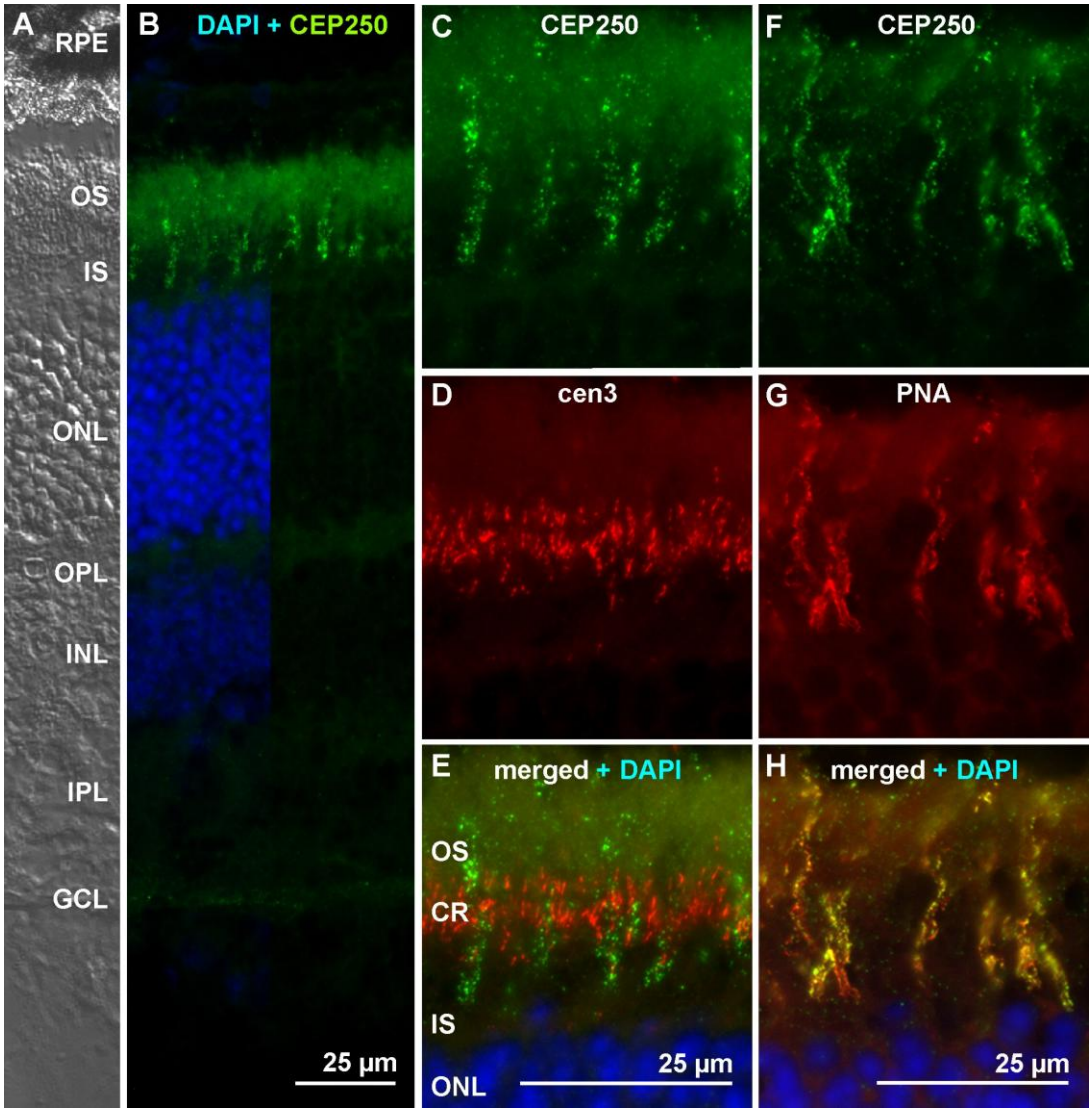

Figure 1.9. **CEP250 localication in the murine retina.**
(**A**) Differential interference contrast (DIC) image of longitudinal cryosection through a mouse retina, nuclei (N) of the outer and inner nuclear layer (ONL/INL); (**B**) indirect immunofluorescence of CEP250 counterstained by DAPI for nuclar DNA.. (**C-E**) Immuno-fluorescence triple labelling of cenrin3 (cen3, ciliary marker, red), nuclei (N) and CEP250 (green) shows that CEP250 is present in outer segment (OS) and inner segment (IS) region. (**F-H**) Immunofluorescence triple labelling of PNA (peanut agglutinin) staining of cones (red), Cep250 (green), nuclei (N) stained by DAPI. Co-localisation of CEP250 and PNA (yellow) indicate that CEP250 is predominantly localized to cones. Ax: axoneme; CC: connecting cilium: S, synapse.

Work on the Bayesian integration of all SYSCILIA data in WP4 by partner 1c has resulted in a set of predicted novel ciliary genes. In this report period we have participated in the validation of the top hits. For this we performed localization studies in the mouse retina. We decided to analyze the localization of six of the putative ciliary proteins. We affirmed previously published data on the ciliary proteins EF-hand domain (C-terminal) containing 1 (EFHC1), WD repeat domain 69 (WDR69/Oda16), and RIB43A domain with coiled-coils 2 (RIBC2) by localizing them to the ciliary apparatus of photoreceptor cells applying indirect immunofluorescence of the proteins co-stained with ciliary markers.

In addition, we analyzed the coiled-coil domain containing 113 (CCDC113), armadillo repeat containing 3 (ARMC3), chromosome 6 open reading frame 165 (C6orf165), and organic solute

carrier partner 1OSCP1, which have not been previously detected in cilia. Immunofluorescence labeling of these proteins and co-staining with ciliary markers revealed the association of the predicted ciliary proteins with the photoreceptor cilium. Immunofluorescence analysis of murine retina sections demonstrated strong CCDC113 labeling between the basal body of the connecting cilium and the adjacent centriole, extending into the inner retina, most likely staining the ciliary rootlet (**figure 1.10**). ARMC3 was mainly localized in the plexiform layers and the outer limiting membrane of the retina and was not detected in the connecting cilium itself but rather in punctuate pattern in the periciliary region. C6orf165 only weakly labeled the bases of a subset of connecting cilia. OSCP1 appears distributed in the photoreceptor inner segments and and the base of the connecting cilium and its adjacent centriole.

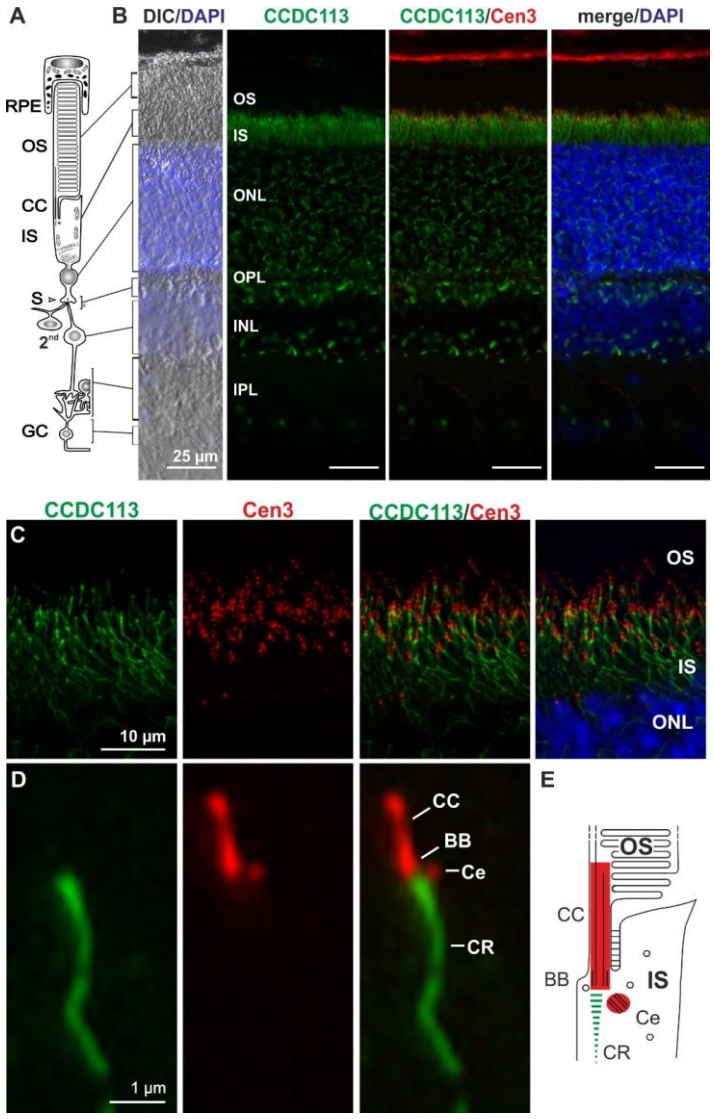

***Figure 1.10*. Ciliary localization of CCDC113. A:** Schematic representation of a rod photoreceptor cell composed of outer segment (OS), connecting cilium (CC), and inner segment (IS), linked to the secondary neurons (2nd) and a ganglion cell (GC) by synapses (S). **B:** Indirect immunofluorescence of CCDC113 (green) in longitudinal sections through an adult murine retina. CCDC113 (green) is localized at basal regions of the CC and adjacent centriole (Ce) (labelled with the ciliary marker Cen3, red) and extending further in strings throughout the whole retina. Nuclei are counterstained with DAPI (blue). **C, D**: Higher magnifications of double immunofluorescence of CCDC113 (green) and centrin-3 (Cen3, red), a molecular marker for the CC, the basal body (BB) and the adjacent centriole (Ce), show localization of CCDC113 at the base of the CC, extending into the ciliary rootlet (CR).

Immmunoelectron microscopy confirmed the localization of CCDC113 to the ciliary rootlet (**figure 1.11)** In addtion, it was found in the basal body, the adjacent centriole and the periciliary region. The high resolution of immuoelectron microscopy showed that ARMC3 was present along the whole connecting cilium, from the ciliary rootlet via the basal body up to the axoneme and also in the periciliary region. Furthermore, anti- ARMC3 strongly labeled the outer limiting membrane and photoreceptor synapses. Furthermore, it was found in many cellular structures throughout the retina down to funnel shaped endfeet at the inner limiting membrane, thus presumably resembling Müller cell localization. Accumulations of C6orf165 were distributed in photoreceptor inner segments including the periciliary region. The basal body and the connecting cilium were also labeled. Furthermore, a subset of photoreceptor outer segments was strongly stained by anti- C6orf165 and the accumulations in the inner segments were much denser in those cells, as well, possibly resembling cones. OSCP1 was found in photoreceptor connecting cilia.

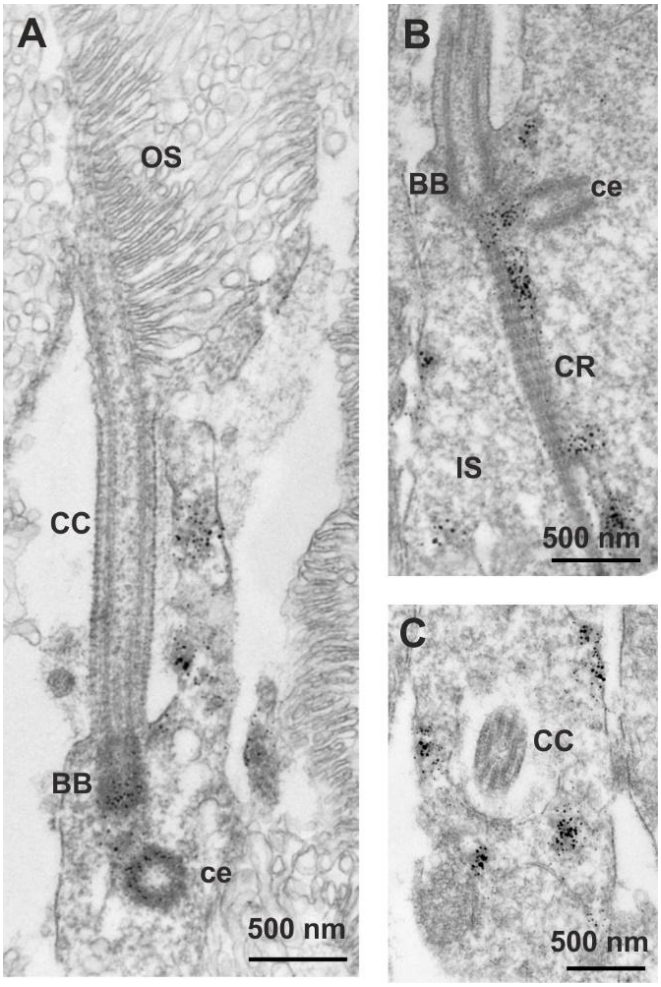

***Figure 1.11*. Ciliary localization of CCDC113 by immunoelectron microscopy. A:** Immunoelectron microscopy of murine photoreceptor cells shows localization of CCDC113 at the basal body (BB) of the connecting cilium (CC), which connects the inner segment (IS) with the outer segment (OS), and the adjacent centriole (ce). **B:** Anti-CCDC113 labels the ciliary rootlet (CR). C: Cross section through at the level of the connecting cilium illustrates CCDC113 accumulations in the periciliary region o inner segment.

Deviations for the technical work planned in Annex I:

For WP1 there are minor deviations for the technical work planned in Annex I. The validation by SRM (D1.10 and D1.13) relies on the analysis of the protein interaction network. Due to technical issues and the necessity of tool development, tailored to the SYSCILIA network, this analysis was delayed. This did not affect the overall progress of WP1 and the project.

Deviations between actual and planned person-months effort. (see also WP11)

Partner 1b:

Partner 1b shifted effort to WP1 and WP6, as for work package 8 it turns out that the work achieving the project tasks and deliverables is mainly done by partner 4, so other partners devote their person months to other workpackages to achieve these tasks..

Partner 6:

Because we have agreed to validate putative ciliary proteins for the Ciliocarta-project (workpackage 4) by localization studies in workpackage 1, and because our first approach to generate transgenic SF-TAP mice failed, so that we had to put a lot of work into solving the problem, we shifted most of our personmonths from other workpackages to workpackage 1. Additional personmonths than indicated in Annex I were necessary to reach those aims. If there is no remaining project budget to cover the additional costs concerning workload and consumables, the expenses will be covered by Johannes Gutenberg University Mainz as part of their commitment towards the success of the project.

Work package number	WP2	Start date or starting event:					Month 1
Work package title	**Central resource for data integration**						
Activity Type	RTD						
Participant number	**15 (L)**	1a	3	4	13	14	17	18
Participant short name	UHEI	RUNMC *Roepman*	EMBL	Duke	CNRS	CCNet	UTUB	UEVE
Person-months per participant:	22^{+3}	8	5	11^{+5}	3^{+2}	23	10^{+5}	2^{+3}
Actual person months per participant* Month 48 - 60	12^{+3}	0^{+2}	0^{+2}	2.39	-	18	2^{+2}	1^{+1}

* This is considered as use of resources.
Deviations are explained in the end of the report for this Work package.

A summary of progress towards objectives of WP2:

Objective 2.1. *To provide a robust, accessible and seamless system for storing, querying and updating data generated in the project*

The data storing and exchange system includes Wiki-pages for internal documents, a consortium website for publications, a GIT-Server for data exchanges, and the BDT/Quest website for data release. These systems are running robustly and kept up-to-date.
The GIT-Server safeguards the experimental and analysis data. Data updates and queries are conducted by the SYSCILIA-IT group upon the agreement on the data protection policy. All versions of the scientific data are stored and managed in a way that it can be easily retrieved, queried and referenced.
SYSCILIA-IT group improved the design and functionalities of the webpage for data query system (QUEST). The improved system creates more comprehensive queries and views, provides a more stable system, and friendlier user experience. This serves also the final data release.

Objective 2.2. *To provide systems biology ready data to produce a model of the ciliary system and its relation to human pathology and disease*

The protein complexes deduced from the experimental data (WP1) are annotated with GeneOntology, OMIM and compared with other experimental sources of the consortium (siRNA, validations). The network model of the interactions between protein complexes is refined.
To analyze mutations and their relations to human pathology, variants and samples from targeted re-sequencing experiment and UK10K are mapped and incorporated to our data set. Additionally, variants and samples from 1000 Genome project (phase III) are also mapped, which provide the background for comparative analysis. A machine-learning model (SVM) is being created and tested, which attempts to classify the diseases and samples based on the ciliopathy data (targeted re-sequencing and UK10K) and the background (1000 Genomes project). Considerable effort has

also been undertaken to define ciliary Gene-Ontologies (GO) as these are poorly described in the existing GO datasets.

Objective 2.3. *To gather and store information about ciliary function from the literature.*

This Objective is achieved.
The previously collected data are being used. Partner 14 keeps an updated collection available upon request. This last period saw intensive investigations regarding the proteomics-derived ciliary landscape to identify potentially novel components and complexes in collaboration with partner 1a, 15 and 17.

Objective 2.4. *To integrate literature data with new finding that arise from experiments performed in the project.*

The literature and public data collected by all partners continue to be incorporated into the system. When combined with the experimental data, incremental updates are performed. The result can be queried via either SYSCILIA-IT group for analysis or partner 14 for literature data sets.

Objective 2.5. *To analyze interactome data using socioaffinity and related concepts in order to derive accurate complex and interaction sets for feeding into WP3 and WP4.*

As described in the last period, partner 15 revised the socioaffinity algorithm. Based on this score, a graphical network is created and results from other experiments (i.e. siRNA screening and targeted re-sequencing) are incorporated. The mappings of involved genes to GeneOntology, 1000 Genomes Project, UK10K, and HPO (by partners 14 and 15 principally) also helps to validate the novel complexes. When experimental updates come in, new set of score and its peripheral data are calculated via the pipeline. This data input helps WP3 and WP4 by finding complexes and validation.

Objective 2.6. *To provide a forum for dissemination of data within the consortium and to the external scientific community.*

The system keeps availing partners of communication and data dissemination. Internal wiki pages are maintained and updated. Webinars organized by partner 14 serve as project shops and teleconferences for regular discussions. Scientific data are maintained and released to external scientific community upon approval of the data producer.

A summary of progress towards each task in WP2:

- ***Task 2.1 The SYSCILIA central resource***

Deliverable under this Task: D2.1 (month 6) delivered.

The central database and wiki web pages for all SYSCILIA partners are maintained. Routine maintenance is processed. Actual information is up-to-date. The ownership of the domain name, http://syscilia.org, has been extended for 5 years and the website for SYSCILIA will be kept up to date via regular correspondence between the SYSCILIA management and partner 15.

- ***Task 2.2. SYSCILIA relational database and comprehensive annotation of the ciliome***

Deliverables under this Task: D2.2 (month 12), D2.3 (month 12), D2.4 (month 12), D2.5 (month 18), D2.7 (month 24), D2.8 (month 24), D2.9 (month 24), D2.10 (month 36), and D2.11 (month 60) all delivered.

The SYSCILIA-IT group (partners 1a, 1c, 3, 15, 18) has worked on the design of the webpage that will host the relational database. The webpage has been designed to facilitate the navigation through the data and the easier extraction of user defined datasets. Updates of experimental results from partners, bioinformatics analyses and data from public databases keep flowing through the system. The BDT/Quest system (described in the report of last period) and GIT version control system govern this process. Due to the concerns that data releases prior to publication, queries from partners are currently processed via SYSCILIA-IT group.
Along with the updates of old datasets, new data are added into the system:

- Receptor annotations from IUPAR
- Comparative genomic hybridization data for cell lines used in SYSCILIA
- Co-occurrence of ciliary genes in different model system (co-evolutionary data)
- Targeted re-sequencing of genes from ciliopathy patients*
- Phenotype screening (siRNA)
- Bayesian integration of co-expression and co-evolution
- Mapping to 1000 Genomes Project
- Mapping to UK10K

The BDT/Quest system is ready to publish the SYSCILIA data when the access is set free.

Partner 4 has collaborated with partner 15 to integrate the ciliopathy patient phenotype data and ciliary resequencing data (from WP8) are integrated into the SYSCILIA relational database and the draft “Cilia Landscape” manuscript. This includes all variants identified in the targeted resequencing project of 785 genes in 457 ciliopathy patients; and 20 IFT genes sequenced in 433 ciliopathy patients (with some overlap between these two sequencing projects). Partner 4 provided support regarding data formats, and possible genetic models that should be taken into consideration. As an example, the contributors of WP2 (including partners 15 and 17) have probed the set of disease mutations for those that might affect protein-protein interactions using structural and interaction information. Using known interaction structures and known binding sites for WD- and TPR-proteins allowed the prediction of mutations affecting protein-interactions leading to 17 mutants, of which partner 17 selected 5 for additional tests. Quantitative comparison of the binding profiles between mutant and wild type showed that three mutations

affected specific IFT-B sub-complexes. A mutation in the predicted interface IFT-B1 subunit IFT88 (R607H, a heterozygous mutation in MKS that scored as a functional null in a zebrafish *in vivo* complementation assay in WP8) leads to a specific loss of IFT-B2, supporting the notion that IFT88 mediates interactions with IFT-B2. In contrast, a mutation in HSPB11 (T41I, heterozygous/MKS), which is central to IFT-B2, appears only to disrupt IFT-B2. Similarily, the B1 subunit IFT172 mutation (E1153G, heterozygous in MKS and ciliopathy and also scoring as a functional null in the zebrafish assay) appears largely to affect only IFT-B1 subunits.

A bioinformatics tool was developed by partners 1a, 1c, 3, 18 and 15 for the construction, maintenance and querying of a relational database using properly annotated tab delimited data files. The tool was developed using SQLalchemy, a set of Python tools for working with databases. Database construction was facilitated by a tool developed by partner 18 that creates the tables of the database and their relationships from a set of tab delimited files. Such a software makes the integration of new data easier when they become available, as the correct formatting of the data files is sufficient for their aggregation to the database. The use of Python and SQLalchemy also facilitated the development of a web application, to make the database accessible for all partners. Flask, a tool for web application development using Python, was used for this purpose. To enable graphical representations of network information the cytoscape.js graph library was integrated. The data integration system, BDT (Big Data Table), and the graphical query/analysis interface, Quest, together form an application entity facilitating the data update integration analysis query workflow. Apart from SYSCILIA the developed tool can be used to facilitate the creation of relational databases in other projects that require the existence of a central data resource. For instance, partner 18 is currently using the tool for the project AdaLab, a project funded by CHIST-ERA, European Coordinated Research on Long-term Challenges in Information and Communication Sciences & Technologies ERA-Net.

One bioinformatician, one software developer and 2 staff scientists from partner 14 worked on the last integration efforts for the database which is to be released to public. The parts of the knowledge base needed to be integrated with the protein-protein interactions as well as parts of the visualisation tools that are relevant for viewing data. Considerable effort (in collaboration with partners 1c, 3 and 15) went into defining and normalising the gene-ontology terms for those data sets in order to make the public view compatible with other main public databases. This work also involved intensive interrogation of the literature regarding the interactions uncovered to describe what is known and whether new putative interactions were plausible or possibly artefacts.

- ***Task 2.3. The ciliary proteomics complexes dataset: socioaffinity scored interactions***

Deliverable under this Task: D2.6 (month 24) delivered.

Given the final datasets from WP1 and discussions with partners 1a, 3, 14, 15, 17 & 18 we refined and improved the socioaffinity metric further to account for missing data, giving vastly improved values and much better networks (see below). These socioaffinity values are then used to cluster proteins into candidate complexes & modules using different algorithms, including that developed

previously by partner 15 for use in Yeast. After comparison and discussion, we (partners 1a, 3, 15, 17, 18) agreed to apply the novel graph-clustering algorithm invented by partner 18. **Figure 2.1** illustrates the procedure in 3 steps.

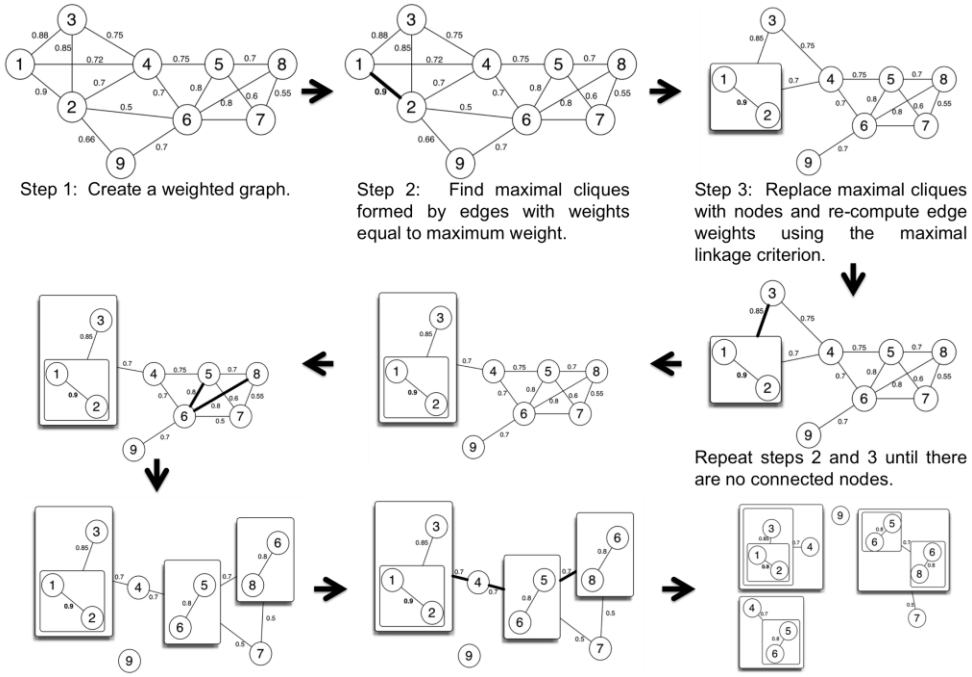

Figure 2.1 **Procedure of the graph-clustering algorithm** (provided by partner 18)

Based on the socio-affinity (SA) scores this algorithm clusters the single genes/proteins into 119 clusters/complexes. The SA is originally designed for genome-wide studies, so that each gene is tagged and reverse tagged to increase the accuracy. For intermediate scale studies, as the case of SYSCILIA TAP experiments, focusing on particular systems, we need to deal with incomplete data that misses reverse tags and baits. To avoid noise, clusters based on unspecific affinity interactions need to be filtered out. We defined 4 measures to assess the quality of these clusters: 1) number of intra-cluster connections with single spoke (no reverse tagging), 2) number of intra-cluster connections with double spoke (reverse tagged), 3) number of not connected members, and 4) the contribution of matrix model in fraction. The principle components analysis (PCA) combines these four measures into one score. It calculates a score for each cluster resulting from the clustering algorithm, and discards clusters with p-value greater than 0.01. From the total 119 clusters, 71 clusters are significant to pass the filter. Along with the guarantee of well-known complexes, the cluster set contains several new complexes. These clusters connect to each other by the sum of SA scores to form the network. Data from other experiments (i.e. siRNA screening from partner 10, targeted resequencing from partner 4, co-evolution score from partner 1c, etc.) embellish the network (see WP3 report for more details).

Novel findings exist in this interactome. For instance, the IFT-B complex is divided into two sub-complexes in the cluster network (**figure 2.2**). It is supported by additional TAP-MS data, which test the mutations selected in 2013 (D3.5). For more details of the mutations in models and experimental results and the analysis please see the reports of WP3 and WP1. **Figure 2.2** shows the cluster interaction network with the threshold of SA score >= 5.6 (high confidence level), and zooms in on the IFT-A, IFT-B1 and IFT-B2 complexes. With help of the automatic annotation, partner 1a, 3, 15, 17, 18 put effort to annotate the significant clusters manually to discover new functional modules and new member of known complexes.

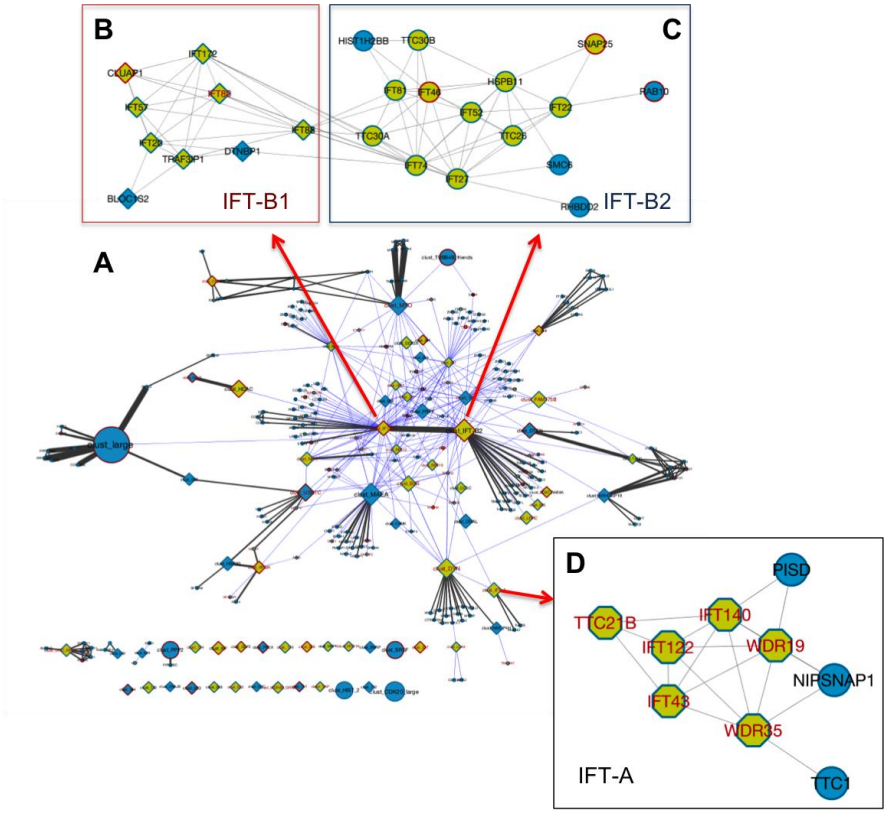

Figure 2.2 **Cluster interaction network with IFT-A and B zoomed in**
This figure shows the cluster interaction network with a SA score threshold of 5.6 (the high confidence interaction dataset) (**A**), and the detail of IFT-A (**D**), IFT-B1(**B**), IFT-B2(**C**) complexes. The IFT complexes contain all of the known member proteins (Pedersen, 2008) and novel members. IFT-B complex is divided into two sub-complexes, which are connected by IFT88. Additional TAP-MS data supports this new finding. Grey lines: SA links; blue lines: Y2H links; node sizes are proportional to the cluster sizes; line widths are proportional to the sum of SA scores between the clusters; Diamonds: ciliary gold-standard genes; hexagons: TAP baits; nodes with red borders: siRNA phenotypic genes; nodes with red labels: classical ciliopathy genes (OMIM and manual annotations); Positions of zoomed clusters are indicated by red arrows.

The finalized socioaffinity was devised by considering different levels of evidence within the dataset, with confidence intervals depending on whether two, one or neither protein was tagged at some point in the study. This led to a vastly improved performance (**figure 2.3**) and consequently an improved set of complexes for the final landscape dataset.

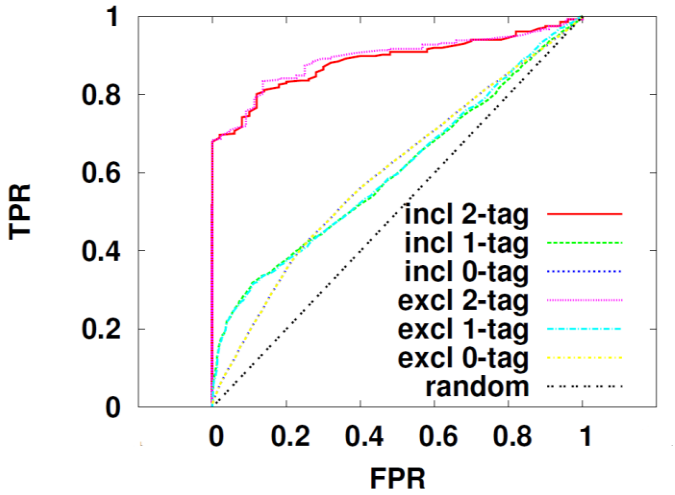

***Figure 2.3* Performance of socioaffinity on final dataset**. ROC curve, True-positive-rate (TPR) versus False-positive-rate (FPR), showing performance of different socioaffinity values. For this analysis Positive interactions were defined as either interactions or complex-co-membership from public databases and negatives taken from our publication (partner 15) in 2012 on defining negatives. "incl" denotes values computed without excluding any baits that might be falsely present owing to overlapping experiments; "excl" are those where these were excluded; the -tag labels refer to whether interactions involved two (i.e. reverse-tagged), one (i.e. only one protein tagged) or zero (i.e. neither protein tagged) in the dataset. Thresholds for clustering were based on FPR and False-discovery-rate (FDR) being above a selected threshold (0.05 for high-confidence; 0.1 for lower-confidence).

Deviations for the technical work planned in Annex I:

The reports for D2.9 and D2.11 were merged, because the BDT/Quest, as an integrative system, serves the release of both the proteomic data and the publication of resources. The tools and the website are readily available. We postpone the publication of these data until the related studies are published, which is preliminarily estimated to be middle August 2015.

Deviations between actual and planned person-months effort. (see also WP11)

Partner 14 and 15 devoted more person months effort to this Work package than indicated in Annex I, to be able to complete the work needed in the final stages of data analysis and integration, but do not request more EU contribution. Partner 14 reallocates their budget under RTD/INNOVATION from Other direct costs to Personnel costs.

Work package number	WP3			Start date or starting event:				month 1
Work package title	Construction, comparison and application of ciliary interactomes							
Activity Type	RTD							
Participant number	3 (L)	1a	1c	13	14	15	16	17	18
Participant short name	EMBL	RUNMC *Roepman*	RUNMC *Huynen*	CNRS	CCNet	UHEI	WWU	UTUB	UEVE
Person-months per participant:	36	13	43^{+8}	3^{+1}	21^{+3}	14^{+2}	3	2^{+2}	6^{+1}
Actual person months per participant* Month 48 - 60	11	0^{+2}	9	-	0	0^{+2}	0	0	5^{+3}

* This is considered as use of resources.
Deviations are explained in the end of the report for this Work package.

A summary of progress towards objectives of WP3:

Objective 3.1. *Generate large scale systems biology ready interaction and reaction information*

The SYSCILIA IT group (partners 1a, 1c, 3, 13, 15, 18) has continued their work on integrating SYSCILIA data into the unified SYSCILIA dataset and is preparing the release of a SYSCILIA database for the scientific community to coincide with publication of the "Ciliary Landscape" paper. The integration of the data was a key element to enable large scale, systematic bioinformatic evaluations and contributed significantly to the preparation of major SYSCILIA manuscripts which are currently in various stages of the publication process as part of objectives O3.2, O3.3 and O3.4.

Objective 3.2. *Assemble ciliary interactomes, functional networks, and pathways*

After completing the interactome assembly for single genes/proteins of the consortium data, we moved forwards to *en détail* characterize the newly identified functional clusters and modules. Partner 18 developed a new clustering algorithm that subsequently was successfully combined with a PCA analysis based filtering approach by partner 15 which led to the identification of sets of clusters with previously unmatched accuracy. Along with well-known functional associated clusters (as confirmed by extensive literature search), several novel ciliary clusters have been identified and were selected for further validations. A manuscript highlighting the major results is in preparation.

Objective 3.3. *Apply comparative evolutionary analysis to ciliary function and disease*

The highly successful and informative evolutionary analyses were completed and published as detailed in earlier reports. During the final period, we continued the Gene Ontology work. The cilia gene ontology terms developed by SYSCILIA have been applied to human and mouse ciliary proteins by the GO consortium. A manuscript is in preparation.

Objective 3.4. *Make molecular models and predictions for experimental testing.*

The subcomplex composition of the dynactin/ dynein motor complex I and its protein interaction with the centrosomal ninein-like protein (NINL) have been modelled and combined with morpholino-induced knockdown experiments in zebrafish. New candidate proteins of the dynactin and dynein motor complex I have been identified and are subject to further investigations. A manuscript on the NINL network has been submitted.

A summary of progress towards each task in WP3:

- ***Task 3.1. Modelling Ciliome complexes in 3D***

Deliverables under this Task: D3.1 (month 18) and D3.5 (month 36) both delivered.

This task and it's deliverables have been completed by month 36.

- ***Task 3.2. Assembling ciliary interactomes and networks***

Deliverables under this Task: D3.3 (month 24), D3.8 (month 48) both delivered.

Much of the final year work in WP3 has been under task 3.2, driven by the data being generated in the experimental WPs.

Even in this late stage of the SYSCILIA project, experimental results for protein interaction data (TAP-MS, Y2H from WP1), large scale genetic screening experiments (siRNA, targeted re-sequencing from partner 10 and partner 4, respectively), and bioinformatic analyses results have kept flowing in. The accumulated data had to be additionally integrated into the single gene/protein level (finished in the last period) datasets, and on cluster/protein complex level. A further improved socio-affinity (SA) algorithm was developed by partner 15 to evaluate the affinity score of each binary interaction. The revised algorithm takes advantage of the availability of sequence coverage data of MS, reverse tagging data of TAP and the addition of replicate experiments, leading to improved accuracy. To obtain a final version of the previously reported ciliary protein clusters, we agreed on using the novel graph-clustering algorithm developed by partner 18 (see WP2, **figure 2.1** for a schematic overview of the clustering algorithm).

Additionally, a principle components analysis (PCA) based filtering procedure was implemented by partner 15 and used to detect and remove unspecific protein associations ('noise') from the experimental data (see WP2 report for details). The two approaches were combined and led to a

prefiltered, high quality ciliary protein cluster network. This network was enriched with further experimental results from the consortium (**Figure 3.1**) and exchanged with experimental partners.

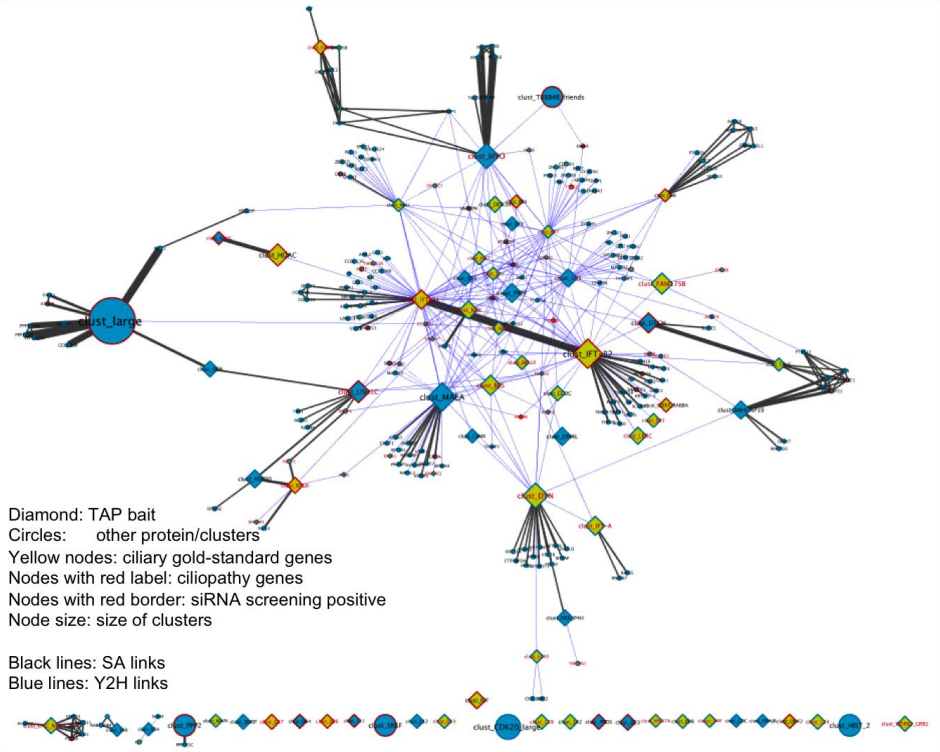

Figure 3.1 **Cluster interaction network**

The full integration into the SYSCILIA database and the SYSCILIA interactome networks including additional data filtering and curation steps, was implemented in automated workflows (see WP2 for details). Work on the EPASIS subcomplex experiments for the the centrosomal ninein-like protein (NINL; see month 48 report) has been completed and a joint manuscript from partners (1a, 1b, 3, 17) is currently in the process of being submitted. As demonstrated by partner 1b a loss of function of NINL, DZANK1, or a genetic interaction leads to dysmorphic photoreceptor outer segments, accumulation of trans-Golgi-derived vesicles and mislocalizations of rhodopsin and usherin in the zebrafish model. The EPASIS subcomplex analysis of NINL provided a detailed understanding of the NINL interactions with dynactin and the dynein motor complex I and led to the identification of previously unknown dynactin and dynein subcomplex members (**Figure 3.2**). The candidate proteins have been communicated with partners and will be subject to further investigations.

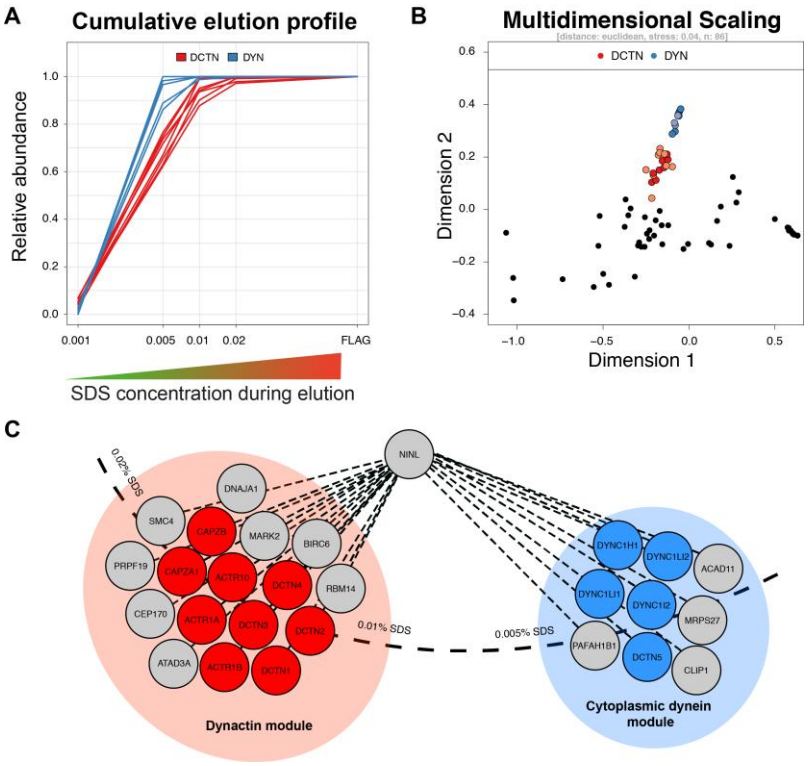

***Figure 3.2* EPASIS subcomplex decomposition.** NINL is a component of the centrosome and a key factor for microtubule formation. It was used as bait in an EPASIS experiment to investigate the structural relationship between NINL and the dynein-dynactin complexes. New candidate proteins could be assigned to the dynactin subcomplex and the dynein motor complex I.

Using the statistical method presented in deliverable report D3.7, partner 18 constructed ciliary sub-networks associated with all ciliary phenotypes. Specifically, for each phenotype in Human Phenotype Ontology the statistical method was used to predict genes associated with the phenotype and the corresponding network was constructed based on the protein-protein interactions from the SYSCILIA TAP data. Only interactions with a high Socio-Affinity score were included. In most cases the predicted disease genes lie in between known disease genes, improving this way the connectivity of the candidate disease network (**Figure 3.3**, **Figure 3.4** and **Figure 3.5**). The result of this analysis is a list of novel potential ciliopathy-associated genes that have to be further investigated in future studies.

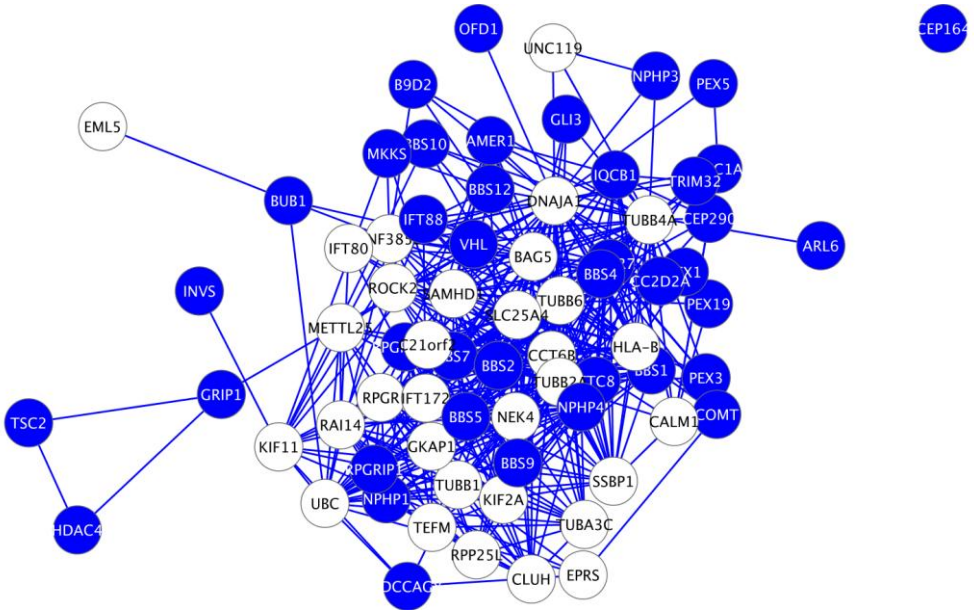

Figure 3.3: **Disease network of Multicystic Kidney dysplasia (MKD).** Nodes in blue correspond to genes that are known to be associated with MKD, while white nodes correspond to predicted MKD genes.

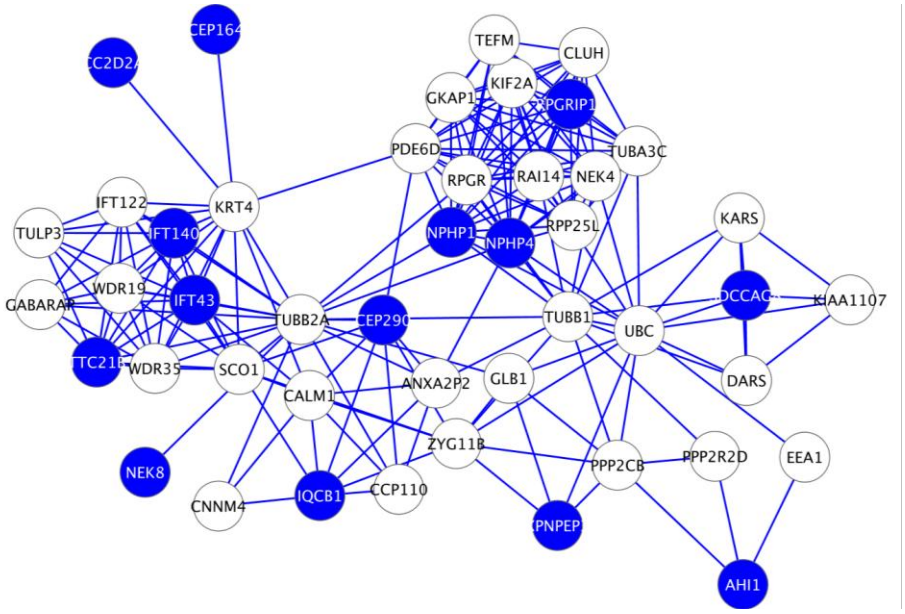

Figure 3.4**: Disease network of Nephronophthisis (NPH).** Nodes in blue correspond to genes that are known to be associated with NPH, while white nodes correspond to predicted NPH genes.

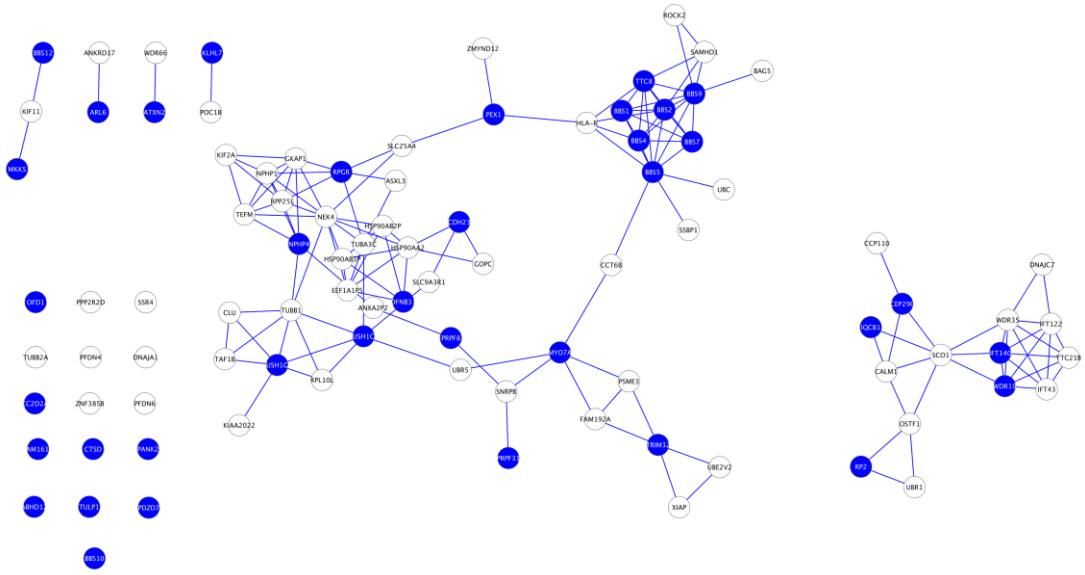

Figure 3.5: **Disease network of Retinitis Pigmentosa (RP).** Nodes in blue correspond to genes that are known to be associated with RP, while white nodes correspond to predicted RP genes.

Partners (1a, 3, 10) have completed the mRNA sequencing of ciliated and unciliated model cell lines as well as mouse embryonic fibroblasts grown with WNT3a conditioned medium. The data is actively used on a manually curated ('case by case') basis to confirm gene expression levels and isoform version information for selected ciliary candidate genes of consortium partners. It is already clear that these datasets will provide rich datamining opportunities. **Figure 3.6** shows an example of the gene expression changes for a centriolar protein under conditions of growth and stasis. We are optimistic that this work will be valuable to the cilia field but also, as these are whole cell datasets, more generally for cell cycle research.

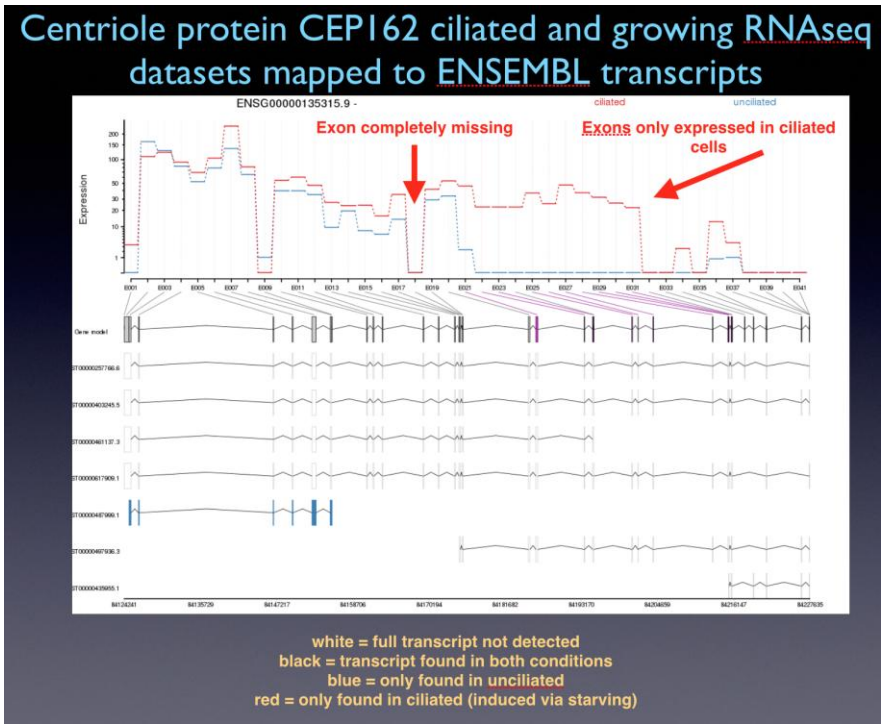

Figure 3.6. **The centriolar protein CEP162 mRNA is found in radically different isoforms in growing and starved (ciliated) cells.**

The SYSCILIA ciliary interaction dataset can now be used to study regulatory aspects of the protein network. Patner 3 has analyzed the interactions with focus on the Ca2+/Calmodulin dependent kinases (CaMKs). Eight CaMKs are present in the SYSCILIA dataset (CHK1, DAPK1, MELK, SIK3, CaMK2A and MARK1-3). Interestingly, MARK2 was found to interact with the CBY1 protein, a homolog of Chibby protein from Drosphila that is involved in Wnt signaling. In humans, CBY1 regulates intracellular trafficking of Polycystin-2 (PC2) and it is also known that mutations in this gene lead to polycystic kidney disease. To elucidate the MARK2 – CYB1 protein interaction plausibility and to identify the potential CYB1 phosphosite sequence which can be phosphorylated by MARK2, the sequence of CBY1 protein was analyzed in more detail. Our results indicate that MARK2 can phosphorylate Serine residues which are present at a +2, +4 or +6 position from Arginine. The protein sequence of CBY1 contains such phosphosites [RKSASLSNLHSLDR], located in the N-terminal natively disordered region of this protein. The comparison of CBY1 sequences between different organisms (human/rat/mouse/cow/xenopus/zebrafish) shows that this N-terminal part is highly conserved. The presence of disorder and conservation in this segment along with a potential phosphosite suggests that CBY1 can be a substrate for MARK2 in cilia. Partner 3 (bioinformatics only) will seek to have this result experimentally tested. This case study has proven to be a valuable exercise and will be the basis to identify the ciliary kinome, by extending it to all ciliary kinases in the dataset.

- ***Task 3.3. Applying an evolutionary perspective to the ciliome***

Deliverables under this Task: D3.4 (month 24), D3.6 (month 36), D3.7 (month 48) and D3.9 (month 60) all delivered.

Work on an evolutionary model of the cilium has finished. For details see the deliverable report D3.9.

The original work on the transition zone by parter 1c has finished now since the manuscript is in revision at Nature Cell Biology. A follow up project has been started with partners 11 (NUID UCD, Blacque) and 10 (LIMM, Johnson) to do a full screen of the top 500 candidate list to find additional transition zone genes based on displacement of known TZ components by siRNA. This work falls outside of the SYSCILIA project, but is a testiment to the productiveness of SYSCILIA collaborations that were experienced during the project.

Partner 1c has been contacted by the Stearns' lab (Stanford university) to collaborate on an evolutionary model of tubulin evolution regarding the centriole/basal body and to find additional interacting proteins based on co-evolution. Partner 1c was able to prove that the model that has been worked with so far was incorrect. Although there might be a possibility that this work may result in a future collaboration, the negative outcome of the results caused the current project to be discontinued, but has been a considerable help to the Stearns' lab. The request for collaboration is indicative of the visibility of SYSCILIA and its partners to the research community.

Partner 3, 1c and 14 are collaborating with the Gene Ontology Consortium (EMBL/EBI) in order to improve the Gene Ontology (GO) coverage of the cilium. Karen R. Christie (MGI, The Jackson Laboratory, Bar Harbor, ME, USA) is annotating ciliary mouse proteins where knockout

phenotypes are available. Partner 3 engaged a masters student Lora Nacheva (3 months EMBL support) to apply GO terms to human proteins. With training from GOC members Prudence Mutowo, Paola Roncaglia (EBI, Hinxton, UK), she used the Protein2GO tool, as well as QuickGO and UniProtKB databases, for annotating human ciliary proteins. We focused on cilia motility genes, mutations in which are known to cause one of the often reported and highly heterogeneous autosomal recessive human ciliopathies – Primary ciliary dyskinesia (PCD). We annotated human gene products, including ciliary dyneins (inner and outer dynein arms) involved in ciliogenesis, cilium movement, microtubule motor activity, sperm motility and left/ right body symmetry determination. For those human ciliary proteins we uploaded 110 annotations in total, 36 of which for cellular component, 56 for biological process and 18 for molecular function. A manuscript is being assembled, jointly authored by these SYSCILIA partners plus the GO team members. We foresee submission to the Cilia journal. In future work, we anticipate developing GO for the many biological processes that involve ciliary function.

- ***Task 3.4 Classification of ciliary membrane proteins***

Deliverable under this Task: D3.2 (month 18) delivered

Task completed by month 18.

Deviations for the technical work planned in Annex I:

There were no major deviations in this WP. Nevertheless, the full impact of this WP is not yet available to the research community. For, as is commonly the case, a significant amount of the work done in WP3 will be published after the end of the project. Some of the planned future papers with WP3 involvement are: The RNAseq cell state paper revaling the alternatively spliced ciliary genes (lead by Partner 3); The ciliary landscape paper with the network and mutations (Lead by Partners 1a & 15); The Ciliacarta Bayesian association paper (Lead by Partner 1c); The Ciliary Gene Ontology paper (Jointly prepared by Partners 1c,3,14).

Deviations between actual and planned person-months effort. (see also WP11)

Partners 1c and 3 devoted slightly more person months to this work package than indicated in Annex I but do not request more EU contribution.

Work package number	WP4	Start date or starting event:				Month 1
Work package title	**Integrative modelling and predictions of ciliary system behaviour**					
Activity Type	RTD					
Participant number	**18 (L)**	1c	3	14	15	17	13
Participant short name	UEVE	RUNMC *Huynen*	EMBL	CCNet	UHEI	UTUB	CNRS
Person-months per participant:	10^{+7}	11^{+3}	11	9	10^{+1}	2^{+2}	22^{+11}
Actual person months per participant* Month 48 - 60	8^{+6}	3^{+3}	$0^{+0.5}$	2	2	0	-

* This is considered as use of resources.
Deviations are explained in the end of the report for this Work package.

A summary of progress towards objectives of WP4:

Objective 4.1: *To integrate outcome from all WPs into a network view of core ciliary processes.*

For the efficient integration of exome-sequencing data (partner 4) with protein-protein interaction data, sequencing data for 1092 controls were downloaded from the "1000 Genomes" project (partner 18). The inclusion of controls not only enables the identification of common variants that most likely do not cause ciliopathies, but also the extraction of features that may allow us to discriminate patients with different ciliopathies and patients from controls. Preliminary results indicate that the independent consideration of the mutational load of ciliary mechanisms cannot be used to classify ciliopathies and most probably combinatorial effects should be taken into account.

Objective 4.2: *To partition this network into functional modules.*

Partner 18 analysed the latest PPI data using the graph-clustering algorithm that had been previously developed (HCI). Moreover, a comparative analysis was conducted to evaluate the performance of the algorithm in comparison to existing methods using data from Saccharomyces Cerevisiae and Drosophila Melanogaster.

Objective 4.3: *To model and simulate modular ciliary processes with explanatory or predictive purposes.*

Partner 14 continued the effort to reconcile vocabularies of ciliary disease phenotypes present in SysWiz database with clinical features/phenotype. The data will be subsequently used to analyze phenotype relevant molecules (genes/proteins) and pathways describing them.

A summary of progress towards each task in WP4:

- ***Task 4.1. Integrating outcome from the consortium***

Deliverables under this Task: D4.2 (month 24) and D4.6 (month 42) both delivered.

Partner 14:

CCNet harmonized and integrated vocabularies of ciliary disease phenotypes present in SysWiz database with clinical features/phenotype data from Human Phenotype Ontology (HPO).

Partner 1c:

Has finalised analysis on the Bayesian integration of SYSCILIA data and produced the Ciliacarta, a compendium of ciliary genes. Partners 1a, 1b, 4, 6, 8, 9, 10, 11, and 16 have finalised the validation of 36 genes and discovered a total of 25 novel ciliary genes (**figure 4.1**). The range of employed experimental approaches (dye uptake response and roaming essays in worm, fluorescence microscopy of eCFP fused constructs, immunofluorescence microscopy in human lung epithelial cells and mouse retina, immunoelectron microscopy in mouse retina, and zebrafish morpholino studies) is extremely broad and adds additional credibility to the validation as multiple facets of properties of ciliary genes and proteins have been tested. The experimentally determined False Discovery Rate (FDR) is 0.69, which is not significantly different from the theoretical FDR of 0.75.

By combining our Bayesian predictions with Gene Ontology annotations as well as our published set of known ciliary genes (**figure 4.2**), we now have a compendium of 801 genes likely to be involved in the cilium (the Ciliacarta). The manuscript is in preparation and will be targeted towards Genome Research (impact factor 14).

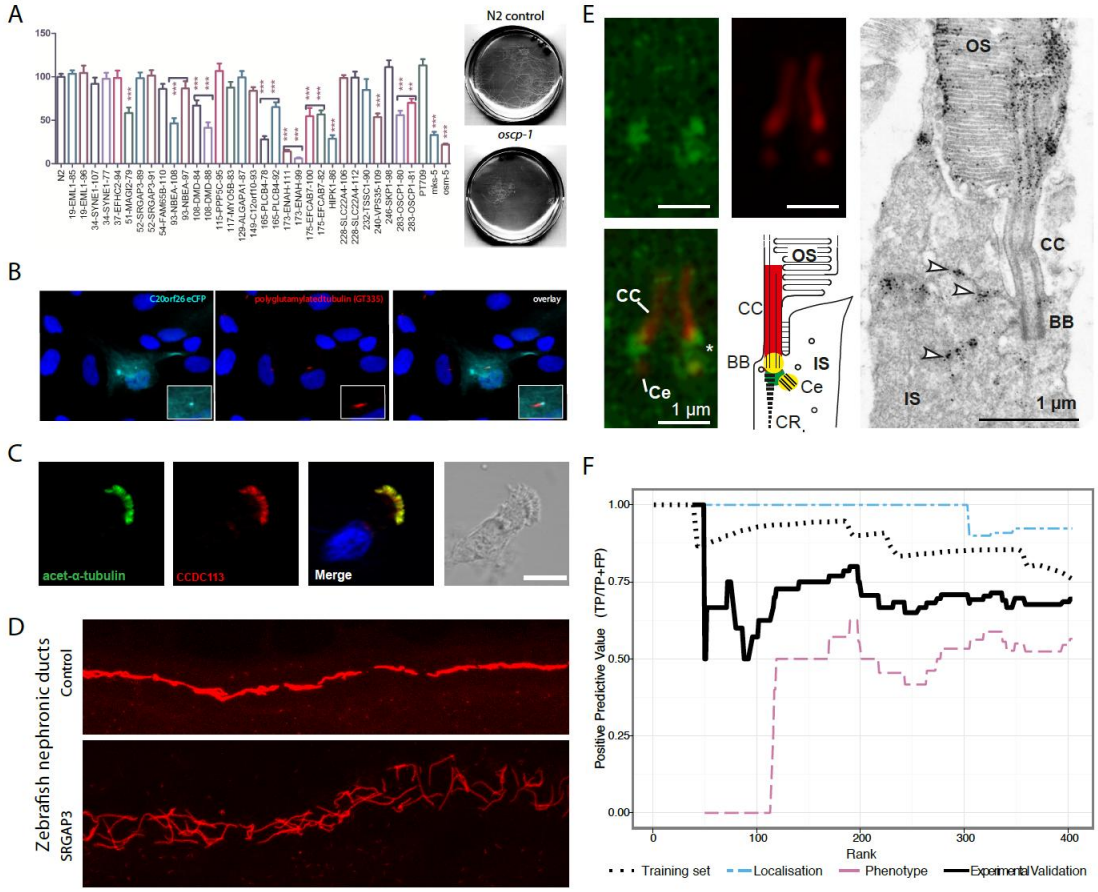

***Figure 4.1*: Selection of results from our validation approach**. **a**) Roaming assay of C. elegans null mutants compared to N2 control to determine changes in cilia related osmotic avoidance, chemoattraction to volatile odorants, and foraging behaviour. **b**) Fluorescence microscopy of eCFP fused to C20orf26. **c**) Co-localisation of CCDC113 and acetylated alpha tubulin in human lung epithelial cells. **d**) Imaging of nephronic ducts in Zebrafish SRGAP3 morphant. **e**) Immunofluorescence microscopy and immunoelectron microscopy of murine retina for C6orf165 suggest localisation to pericentriolar material at base of cone photoreceptors. **f**) Positive predictive value of the Bayesian classifier based on validation as a function of gene rank.

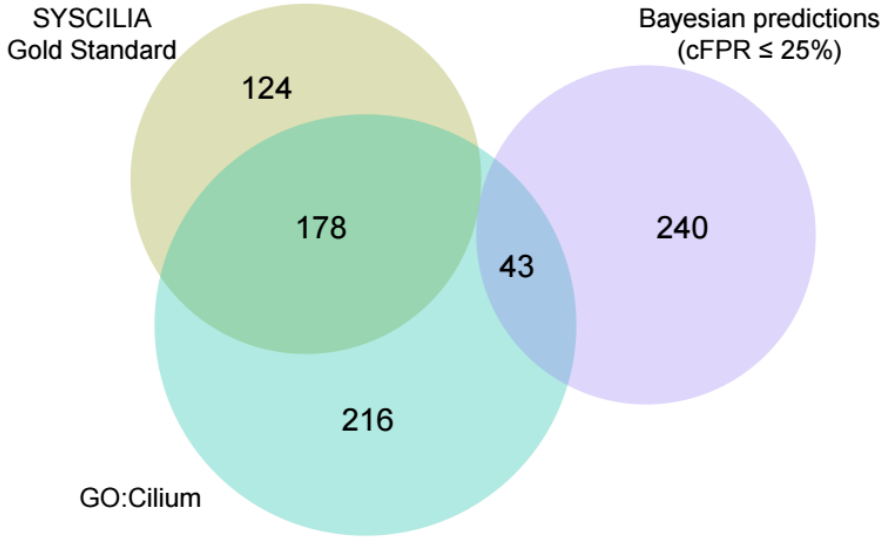

***Figure 4.2*: Proportional Venn diagram showing the contributions of each of the sources to the Ciliacarta compendium.** Our work expands currently known ciliome by almost 30%.

Partner 18:

Worked on the efficient integration of exome-sequencing data provided by partner 4 with protein-protein interaction data. Our aim was to identify candidate ciliopathic genes by filtering out common variants. Towards this end, sequencing data for 1092 controls were downloaded from the "1000 Genomes" project and for each mutation in the SYSCILIA dataset the allele frequency was computed from the controls. Sequencing data were also enriched with SIFT and PolyPHEN scores, that predict the possible impact of an amino acid substitution on the structure and function of a protein. The latter can be used to discriminate between deleterious and benign mutations. For the identification of disease causing genes we computed for each case (patient/control) the mutational load that indicates the accumulation of mutations for a specific gene. By comparing the distribution of the mutational load between controls and patients we can identify genes that exhibit a higher mutational load on patients than controls (termed "causal mutations" hereafter). The above genes were finally mapped to the ciliary interactome to identify network modules associated with specific ciliopathies. For almost all identified protein complexes, except for BBSome, there was no clear association with a specific ciliopathy (**figure 4.3**). This may indicate that often combinations of mutations affecting different parts of the ciliary system are responsible for ciliopathies and not single mutations.

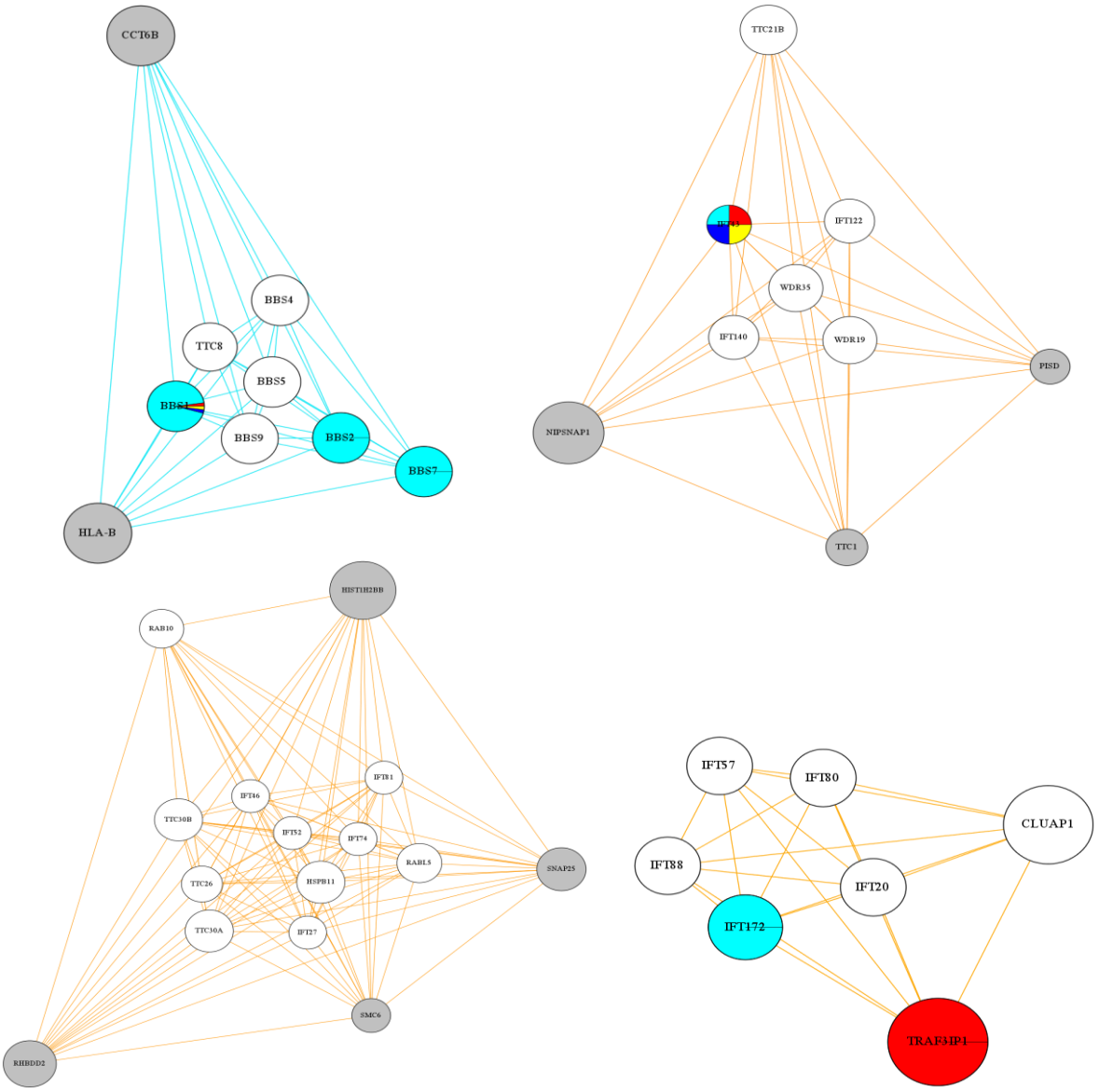

***Figure 4.3*: Gene-disease associations for identified ciliary mechanisms.** Each gene is coloured according to the diseases with which it is associated (cyan: Bardet-Biedl Syndrom, red: Meckel–Gruber syndrome, blue: Usher Syndrome, yellow: other ciliopathies). Gene-diseases associations were extracted from exome-sequencing data provided by partner 4 after filtering out common variants.

- ***Task 4.2. Partitioning of the network of core ciliary processes into functional modules***

Deliverable under this Task: D4.4 (month 36) delivered.

Partner 18 analysed the latest PPI data using the graph-clustering algorithm that had been previously developed (HCI). Given that it is the first time that the specific algorithm is used we also compared its performance to the performance of several existing graph-clustering algorithms. For our analysis we used two large-scale AP-MS datasets from *Saccharomyces cerevisiae*. Although these datasets date back to 2006, they have been extensively used as

benchmark in the literature, and they are ideal for the purposes of our study. *S. cerevisiae* is one of the best-studied organisms for which manually curated complex sets are available. In total 11 methods (including HCI) were tested in PPI networks constructed from the AP-MS data with and without using a score threshold (refered as Thresholded and Unthresholded network hereafter). From the 11 methods 7 introduce several parameters. To properly evaluate their performance we used several parameter sets. The performance of each algorithm was evaluated using a combination of scores that compute how well the predicted clusters match known gold-standard complexes. As is shown in **figure 4.4**, the developed method provides better results in almost all cases.

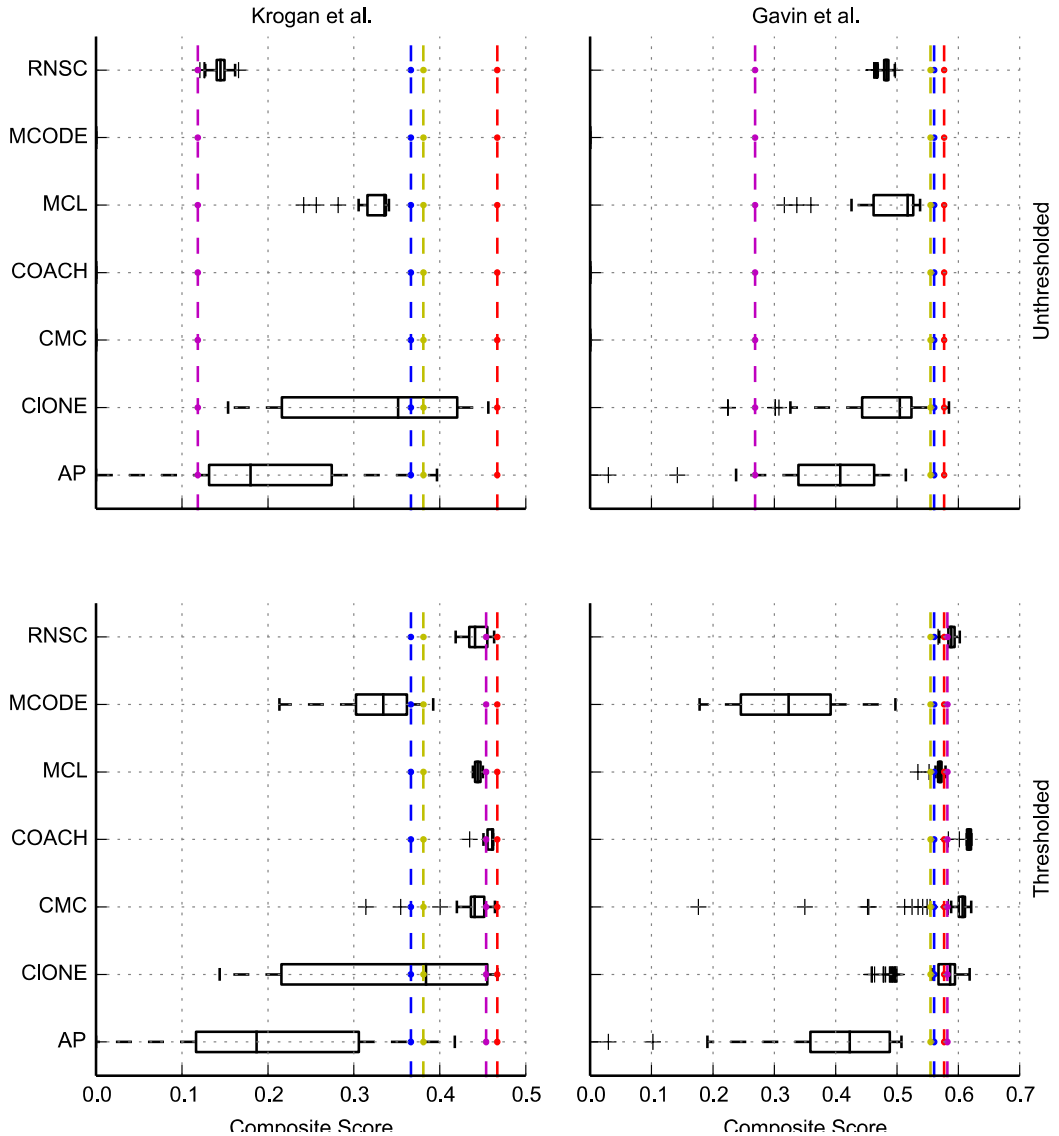

***Figure 4.4*: Evaluation of HCI performance.** The 7 parametric graph-clustering methods (y-axis) were compared to 4 non-parametric methods: HCI (red), CORE (magenta), CODEC (blue) and CACHET (yellow). CODEC and CACHET are not clustering methods specifically developed for the analysis of AP-MS data.

The two yeast datasets have a striking difference with the SYSCILIA data. Both of them are very large-scale studies including more than 2000 baits. We investigated how the performance of the best performing algorithms is affected by incomplete data by applying them to subsets of the

initial yeast datasets. From the graph-clustering algorithms we selected ClusterOne (ClONE) and MCL as these were the ones that performed very well both in thresholded and unthresholded networks. For ClusterOne and MCL the best performing parameter set was used. Again the results (**figure 4.5**) indicate that the performances of the other algorithms are upper-limited by HCI performance.

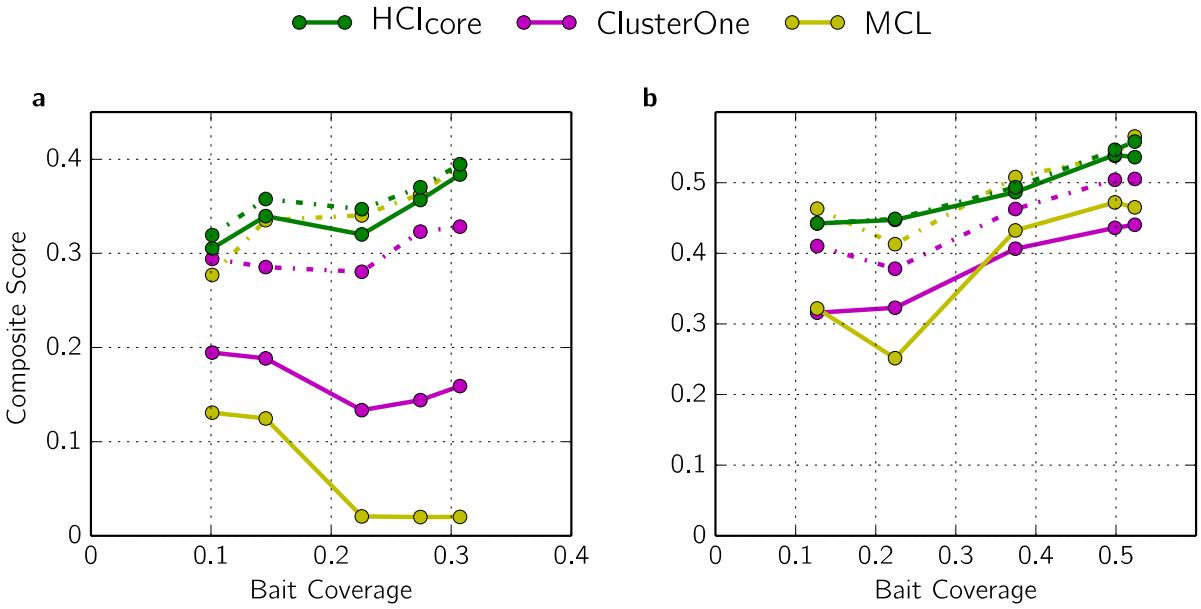

***Figure 4.5*: Evaluation of HCI performance in incomplete data** For each subset the corresponding PPI network was constructed using SA score and the algorithms were applied to both thresholded (dashed lines) and unthresholded networks (solid lines).

While the two yeast datasets have been extensively used as benchmarks in many similar studies, they differ from modern AP-MS experiments, which employ quantitative proteomics to discriminate true interaction partners from contaminants. We investigated how the three graph-clustering algorithms, MCL, ClusterONE, and HCI, perform on such kind of data using a more recent dataset from Drosophila melanogaster (**figure 4.6**). Similarly to the yeast datasets, HCI predictions gave the best matching scores when compared to the predictions of MCL and ClusterONE when the latter are applied on the unthresholded network (**figure 4.6**). The performances of both graph-clustering algorithms improved with the filtering of the data, but they remained slightly worse than HCI performance.

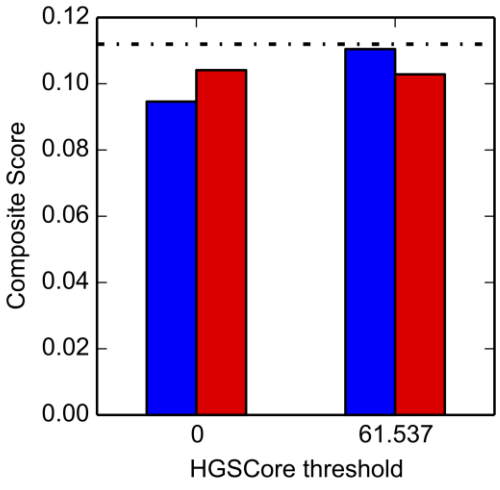

***Figure 4.6:* Performance on quantitative AP-MS data.** Evaluation of the complexes predicted by HCI (black dashed line), ClusterONE (red bars), and MCL (blue bars) for the Drosophila melanogaster dataset. ClusterONE and MCL were applied to the unthresholded, tantamount to a 0 threshold, and the thresholded network.

The above results clearly indicate that the developed method performs considerably better than most existing clustering methods, providing support to the complexes predicted using SYSCILIA data. A manuscript including our analysis is under preparation and will be submitted to a high-impact computational biology journal.

- ***Task 4.3. Dynamic and spatial modelling of regulatory and signalling paths***

Deliverables under this Task: D4.1 (month 12), D4.3 (month 30) and D4.5 (month 39), D4.8 (month 54) and D4.9 (month 60) all delivered.

Partner 14:

CCNet continued the effort to reconcile vocabularies of ciliary disease phenotypes present in SysWiz database with clinical features/phenotype data from Human Phenotype Ontology (HPO) and subsequently to analyze relevant molecules (genes/proteins) and pathways describing them.

- ***Task 4.4. Modelling intra-flagellar transport***

Deliverable under this Task: D4.7 (month 48) delivered.

Having the proteomic data generated inside the SYSCILIA project including interaction data from Y2H and TAP experiments (WP1), phenotype screening results from siRNA experiments (WP7) and mutation data from targeted re-sequencing (WP8) available, we are able to group the genes into functional modules. The resulting set of modules covers the most key functional components of intra-flagellar transport, including IFT-A and B complexes, complexes responsible for the "turnaround" mechanism, BBsome, and molecular motors (see deliverable report D4.7). The most recent interaction network identified an array of membrane-associated IFT interactors, which may intermediate or directly play a roll in the cilia cargo loading, unloading, and transport system (**table 4.1** below).

Table 4.1 Membrane-associated IFT-interactors

Membrane-associated Protein	IFT-interactor	Known interaction?
DTNBP1	IFT20	No
DTNBP1	CLUAP1	Yes
BLOC1S2	TRAF3IP1	Yes
STX18	CLUAP1	No
ASAP2	CLUAP1	No
RHBDD2	IFT27	No
RHBDD2	TTC30B	No
TMEM55B	TTC30B	No
SCAMP3	TTC30B	No
HACD2	TTC30B	No
LPCAT3	TTC30B	No
TIMM17B	TTC30B	No
TMEM55A	TTC30B	No
UBAC2	TTC30B	No
MPC2	TTC30B	No
PXMP2	TTC30B	No
TM95SF2	TTC30B	No

Deviations for the technical work planned in Annex I:
For WP4 there are no deviations for the technical work planned in Annex I.

Deviations between actual and planned person-months effort. (see also WP11)
For WP4 there are no major deviations between the actual and planned person-months effort.

Work package number	WP5	Start date or starting event:		Month 1	
Work package title	**Assay systems to study functional ciliary modules**				
Activity Type	RTD				
Participant number	5	4	6 **(L)**	8	11
Participant short name	UKL FR	Duke	JoGuMz	UMC	UCD
Person-months per participant:	27^{+18}	11^{+8}	34^{+7}	11^{+7}	38
Actual person months per participant* Month 48 - 60	3.8^{+6}	1.23	11.375^{+4}	4.6^{+3}	10.7^{+3}

* This is considered as use of resources.
Deviations are explained in the end of the report for this Work package.

A summary of progress towards objectives of WP5:

Objective 5.1. *Quantifying ciliary transport*

Ciliary transport was assessed in two model systems: in C.elegans and in the mouse retina. In the mouse retina, we monitored the translocation of rhodopsin as ciliary cargo in the photoreceptor inner segments towards the ciliary base of rod photoreceptor cells. For this we assessed fluorescence recovery after photobleaching (FRAP) in GFP-rhodopsin knock-in mouse photoreceptor cells three-dimensionally to adjust for sample shifting over long time recordings. The mobility of GFP-tagged TMEM-107, MKS-2/TMEM216 and MKS-6/CC2D2A at the C. elegans transition zone (TZ) was likewise evaluated by FRAP experiments. The results indicate that those proteins are anchored at the TZ membrane. Stimulated emission depletion (STED) in vivo microscopy revealed that GFP-tagged TMEM-107, MKS-2, and TMEM-231 have a periodic pattern of localisation at the TZ membrane, suggestive of a stack of evenly spaced independent concentric rings or one or more continuous spirals at a necklace-like domain of the TZ membrane.

Objective 5.2. *Assaying ciliary polarization*

During the last reporting period, we explored a crucial step during ciliogenesis in multiciliated cells (MCCs): the association of future basal bodies with the apical plasma membrane, followed by their correct spacing and planar orientation. We found a novel role for ELMO-DOCK1, a bipartite guanine nucleotide exchange factor complex for the small GTPase Rac1, and the membrane-cytoskeletal linker Ezrin in regulating centriole/basal body migration, docking and spacing. Downregulation of each component resulted in impairment of basal body docking and spacing, which is likely to account for ciliopathy-related phenotypes in zebrafish and disrupted ciliogenesis in *Xenopus* epidermal multiciliated cells. Biochemical analyses indicate that the ELMO-DOCK1-Rac1 complex influences Ezrin phosphorylation and thereby probably serves as an important molecular switch, orchestrating ciliary basal body migration, docking and positioning in vivo. Furthermore, the results point towards a possible genetic interaction between Arl4a and ELMO1/Ezrin during ciliogenesis in zebrafish, suggesting that Arl4a regulates ciliogenesis by controlling apical migration and docking of the basal bodies upstream of Ezrin and ELMO1.

Objective 5.3. *Measuring ciliary signaling*

During the reporting period, mTOR, Wnt and Sonic Hedgehog (SHH) signaling was assessed.
We evaluated the contribution of the mTOR signalling cascade to ciliopathy-specific disease manifestations by generating kidney specific CRE KIF3A (fl/fl) mice and crossing them with Raptor (fl/fl) mice, so that they lack mTORC1 activity. The latter died significantly later of kidney failure. Extensive microarray profiling of CRE KIF3A (fl/fl) mice with and without mTORC1 activity revealed that in 2-week old KIF3A-deficient mice cell cycle progression programs were activated, whereas KIF3A/mTORC1-deficient mice showed a substantial inflammatory response, including innate immune responses, Jak-Stat signalling, chemokine production and monocyte activation. The two gene profiles become indistinguishable at four weeks of age. The results implicate that ciliary defects are commonly associated with an up-regulation of the mTORC1 signalling cascade and that inhibition (genetically or pharmacologically) appears to rapidly induce "bypass signalling".
The protein DCDC2 has been shown to negatively regulate Wnt signaling in vitro and in vivo. Huwe1, a candidate protein from the siRNA screen performed in WP7, ubiquitinylates Dishevelled regulating its location and thereby regulating Wnt signalling. This assay is being adapted for testing human mutations and cilia function. Ongoing work suggests that systemic treatment of ciliopathy mice carrying CEP290 mutations with the SHH agonist purmorphamine reduces renal cyst development.

A summary of progress towards each task in WP5:

- ***Task 5.1. Monitoring ciliary transport***

Deliverables under this Task: D5.1 (month 24), D5.3 (month 24), D5.4 (month 24), D5.6 (month 24), D5.7 (month 24), D5.12 (month 54) and D5.13 (month 60) all delivered.

A) Ciliary FRAP
B) Elucidating ciliary transport in vertebrate photoreceptor cells *in vivo*
C) Ciliary transport in C. Elegans

Partner 6:
We continued to elucidate the transport of the ciliary cargo rhodopsin in photoreceptor cells by fluorescence recovery after photobleaching (FRAP) analyses of living photoreceptor cells of rhodopsin-GFP knock-in mice (Chan et al. 2004). We focused on the rhodopsin trafficking through the photoreceptor inner segment towards the connecting cilium, the equivalent of the transition zone of primary cilia and specifically on the role of cytoskeletal elements. We are therefore employing different polymerization inhibitors of the microtubules and actin and measure their effect on rhodopsin trafficking. As we reported earlier (4th periodic report), we are facing difficulties with immobilizing the sample. Our solution to monitor FRAP three-dimensionally and adjust for the shift over time is still resulting in highly variable measurements, so that more experiments need to be undertaken to obtain conclusive results.

Partner 11:

We investigated the transition zone membrane distributions of *C. elegans* MKS module proteins using stimulated emission depletion (STED) *in vivo* super resolution microscopy. Specifically, we investigated the localisations of GFP-tagged TMEM-107, MKS-2, and TMEM-231 in live worms. In all cases, single focal plane imaging revealed a similar periodic pattern of localisation at the TZ membrane, suggestive of a stack of evenly spaced independent concentric rings or one or more continuous spirals extending along the TZ length (**figure 5.1a, b**). For amphid and phasmid cilia, this ring-like or spiral-like domain typically appears as 3-5 full turns, whereas fewer turns are observed for the TZs of shorter labial cilia (**figure 5.1a**). In many images, these turns do not appear perpendicular to the longitudinal axis of the TZ, indicating rings may be tilted. Interestingly, this localisation pattern is reminiscent of the evolutionarily conserved ciliary necklace, a membrane specialisation identified more than 40 years ago by freeze fracture studies as 1-7 rows of intramembrane particles at the ciliary base [Gilula, N.B. & Satir, P . *J Cell Biol* 53, 494-509 (1972)]. Interestingly, in hamster bronchial epithelial cilia, the necklace consists of 5-7 parallel rows at an 8^{o} pitch angle suggestive of a continuous spiral [Heller, R.F. & Gordon, R.E. *Exp Lung Res* 10, 137-152 (1986)] (**figure 5.1b**). It is thought that the necklace is a manifestation of Y-link insertion in to the transition zone membrane. Thus, we have provided evidence that MKS module transmembrane proteins are periodically localised at the transition zone membrane, possibly forming ring like structures reminiscent of the ciliary necklace. Since we know that at least some MKS module proteins are immobile (FRAP experimentation; see D6.16), we propose the Y-links may serve as the anchors (**figure 5.1c**).

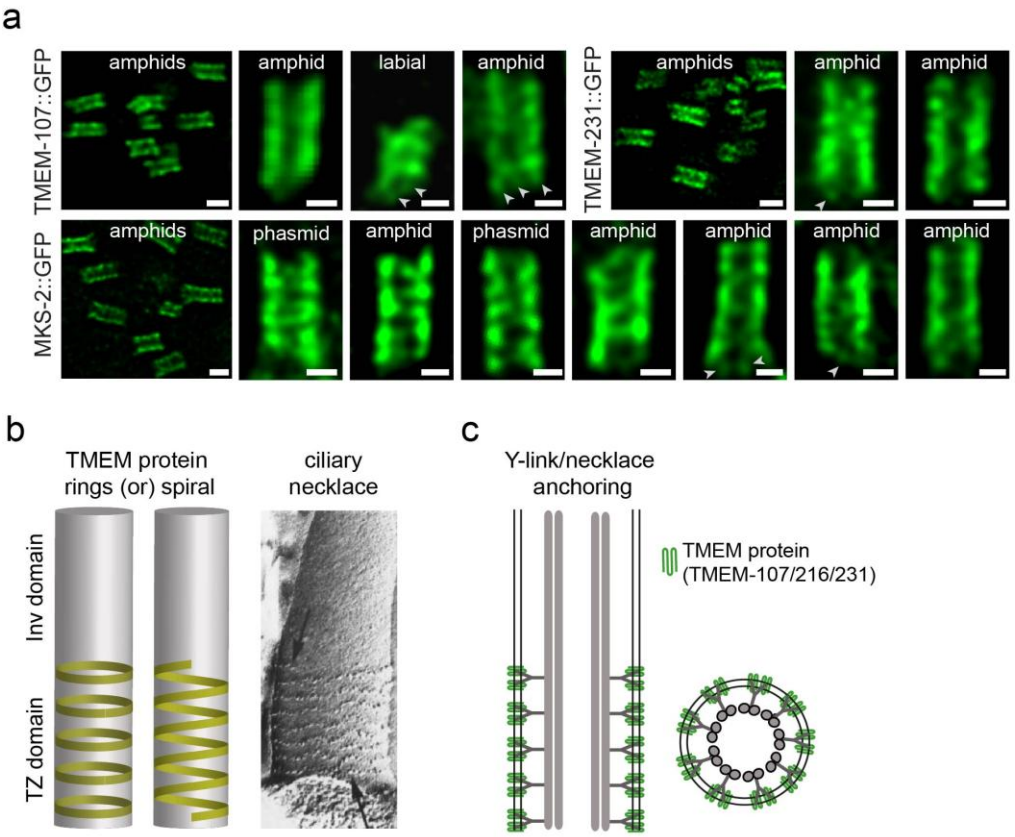

Figure 5.1:

STED imaging of MKS module proteins at the *C. elegans* transition zone. (**a**) Super-resolution STED microscopy images of GFP-tagged MKS module proteins (transmembrane) at the transition zone membrane of live worms. Shown are single plane images of the TZ in longitudinal orientation taken from head (amphid, labial) and tail (phasmid) ciliated neurons. Note the smaller size of the labial cilia TZ. Arrowheads; punctate spots of signal. Bars; 200 nm (high magnification images), 500 nm (low magnification images). **(b, c)** Models. Schematics in (b) suggest a ciliary necklace-type organisation for *C. elegans* transmembrane MKS proteins as anchored ring-like domains (concentric or a continuous spiral). TEM image taken from ref. 7 shows the spiral type ciliary necklace of hamster bronchial epithelial cell cilia, with free ends denoted by arrows. Model schematic in (c) proposes that the anchored ring-like or spiral subdomains of the TZ membrane diffusion barrier results from direct interaction between MKS module proteins and the ends of the Y-link arms, which are inserted into the TZ membrane to create the ciliary necklace.

We also performed STED imaging of endogenous human ciliopathy transition zone proteins (RPGRIP1L, TMEM67) in fixed RPTEC-hTert (renal proximal tubule epithelial) cells. For both proteins we observed a ring of signal, which was not complete and frequently appeared as a set of discrete spots (**figure 5.2**). In some images, the incomplete ring consisted of 7-8 discernible spots. These findings are at least in partial agreement with our nematode observations, showing that mammalian MKS module proteins do not decorate the entire TZ membrane. The mammalian data also supports the hypothesis from our worm work that MKS module proteins may associate with Y-links. Although we did not observe a full ring of 9 discrete spots, correlating with the 9-fold symmetry of Y-links, one could envisage association with 7-8 Y-links in an incomplete ring. The other possibility is that the apparent incomplete ring could be a tilted full ring, which appears as the former due to loss of STED image resolution and signal in the Z-direction.

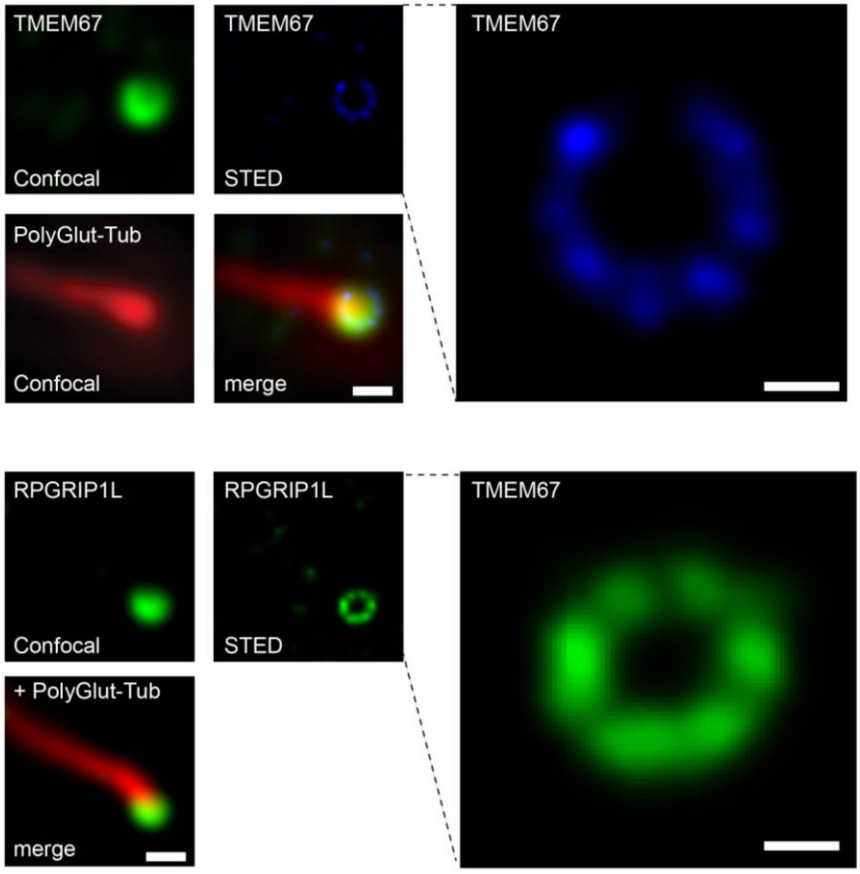

Figure 5.2:

STED imaging of MKS module proteins in human RPTEC-htert cells. Shown are confocal, STED and merged images. STED images enlarged on right hand side. Bars; 300 nm (small panels), 100 nm (large panels). PolyGlu-tubulin (red) staining denotes the ciliary axoneme.

These *C. elegans* and mammalian STED data are presented in full in D5.13.

- ***Task 5.2. Assaying ciliary polarization***

Deliverables under this Task: D5.2 (month 24), D5.5 (month 24), D5.9 (month 48) and D5.14 (month 60) are all delivered.

A) Ciliary polarity
B) Flow direction and speed
C) ciliary angle

Partner 5:
See also Deliverable Report D5.14.

Ezrin is required for normal ciliogenesis in zebrafish and *Xenopus.* Since Ezrin plays a crucial role in apical actin organization of polarized cells and localizes to ciliary basal bodies, we studied its expression and function during zebrafish embryogenesis. In zebrafish two related *ezrin* genes exist, termed *ezrina* and *ezrinb*. Whole mount *in situ* hybridization (WISH) identified a tissue-specific expression pattern only for *ezrinb*, in the following referred to as *ezrin*. At larval stages

ezrin expression was detected in ciliated tissues including the olfactory placode/pit, lining of the brain ventricles, otic vesicle and throughout the pronephric tubule. Immunostaining for Ezrin in 48 hpf *tg(ßact:arl13b-GFP)* zebrafish embryos revealed that Ezrin localized to the base of the cilia, the presumptive basal bodies, in pronephric tubules, and otic vesicles. To investigate the role of Ezrin in ciliary function we used a morpholino oligonucleotide (MO), blocking the translation of *ezrin*. Down-regulation of Ezrin led to prominent hydrocephalus and pronephric cyst formation in zebrafish embryos similar to the phenotypic changes observed in mutant zebrafish lines with defective ciliogenesis, implicating a link between Ezrin and cilia function. Moreover, quantification of cilia length in the pronephric tubule revealed significantly shortened cilia in *ezrin* morphants compared to control at 24 hpf. Co-injection of *ezrin* mRNA and MO partially rescued pronephric cyst formation, confirming the MO specificity of the observed phenotypic changes. Examination of the anterior pronephric tubular segments by transmission electron microscopy (TEM) revealed defective microvillus formation, multiple basal bodies did not attach to the apical membrane and ciliary axoneme formation was impaired in 48 hpf *ezrin* morphants. The significant reduction of microvilli supports MO specificity since it is consistent with the phenotype observed in the intestine of Ezrin$^{(-/-)}$ mice and the reported role of Ezrin during microvillus formation. The population of tubular epithelial cells in zebrafish pronephros consists of mono- and multi-ciliated cells. To confirm the role of Ezrin in MCCs, we took advantage of a second animal model, *Xenopus laevis* since the epidermis of *Xenopus* embryos contains isolated MCCs with motile cilia that are easily accessible for high-resolution imaging. *Ezrin* transcripts were expressed in ciliated epithelial cells, including the otic vesicle, cloaca, pronephros and throughout the epidermis at stage 32 of *Xenopus* development. Downregulation of Ezrin using a translation blocking MO (8 ng), trapped the majority of the ciliary axonemes within the cytoplasm, and prevented their projection to the outside of the epidermal cells. Strikingly, the basal bodies labeled with Centrin-RFP clustered in the cytoplasm close to the cell center in *ezrin* morphants instead of being transported to the membrane and distributed uniformly along the cell surface. Furthermore the apical actin network of the MO-affected epidermal cells appeared to be thinner in comparison to controls with focal points of actin accumulation at the apical membrane directly above the basal body cluster. TEM confirmed that the basal bodies accumulated in some distance to the apical cell membrane in *ezrin* morphants. The ciliary axonemes formed within the cytoplasm revealed an ultrastructure identical to the properly elongated axonemes of the controls. This supports the notion that axonemal formation is controlled by a process independent of basal body docking. Injection of lower doses of *ezrin*-MO (2 and 4 ng) resulted in partial basal body docking, but even distribution, i.e. spacing, of the basal bodies was greatly impaired, causing basal bodies being attached to each other like 'beads on a string' or forming groups. In addition, the rotational polarity of the basal bodies was defective, judged by the orientation of Clamp-GFP. Notably, the gross morphology of MO-injected *Xenopus* embryos appeared normal in both dose ranges of MO injections. These results suggest a unique role for Ezrin in guiding the maturing basal bodies to the cell surface as well as their docking and correct spacing underneath the apical membrane in MCCs.

ELMO1 interacts with Ezrin, and directs ciliary basal bodies to the apical surface in zebrafish and *Xenopus*. Ezrin, similar to other ERMs, physically interacts with members of the ELMO family. ELMO proteins form an unconventional GEF complex with DOCK180, thereby activating Rac1. Several studies showed the essential function of DOCK180/ELMO1 in remodelling the actin

cytoskeleton and controlling cell migration during multiple processes, including engulfment of apoptotic cells, phagocytosis, tumor invasion, myoblast fusion, and angiogenesis. We hypothesized that the DOCK180/ELMO1 complex together with Ezrin controls basal body docking and spacing. In addition to the documented expression pattern of *elmo1* during zebrafish development, sections of *elmo1*/*cadherin17* double-WISH stained 36 hpf zebrafish embryos revealed *elmo1* expression in the pronephric tubule. *Dock180* is ubiquitously expressed throughout early somitogenesis. Immunostaining localized DOCK180 to the base of the cilia in pronephric tubular cells and inner ear cells of 48 hpf embryos. MO-mediated knockdown of *elmo1* or *dock180* led to pronephric cyst formation and left-right asymmetry defects at 48 hpf, and shortened cilia in the pronephric tubule of 24 hpf embryos. Co-injection of *elmo1* mRNA partially rescued the cyst formation of *elmo1* morphants, confirming the specificity of the phenotypic changes observed in the *elmo1* morphants. To uncover a potential genetic interaction between ELMO1 and Ezrin during ciliogenesis in zebrafish, we examined whether the cystic phenotype of *ezrin* or *elmo1* morphants could be rescued by *elmo1* or *ezrin* mRNA, respectively. Indeed, ELMO1 or Ezrin overexpression ameliorated the defects caused by *ezrin* or *elmo1* depletion, respectively, suggesting that both proteins act in the same pathway that coordinates basal body migration in zebrafish. Similar to the *ezrin* morphants, TEM studies revealed defective basal body transport to the apical membrane in *elmo1*- and *dock180* morphants.
In *Xenopus*, two homologs of ELMO, ELMO1 and ELMO2 exist, sharing 70% identity. Both homologs were expressed similarly including ciliated tissues. The *dock180* mRNA expression pattern overlapped with *elmo1* and *elmo2*. Translation-blocking MOs targeting ELMO1/ELMO2 did not have a significant effect when injected separately. However, the combined ELMO1/ELMO2 knockdown in the medium dose range showed defective apical migration and membrane attachment of basal bodies and intracellular cilia formation similar to the phenotype observed after depletion of Ezrin. Injection of lower doses of *elmo1/2*-MOs led to a phenotype where basal body docking and axoneme formation occurred, but spacing and rotational polarity of the basal bodies was impaired. Notably, the gross morphology of MO-injected *Xenopus* embryos appeared normal in both dose ranges of MO injections. In summary, these results show that ELMO proteins genetically interact with Ezrin and are expressed in ciliated organs in zebrafish and *Xenopus*. The loss-of-function studies reveal that the DOCK180/ELMO complex is required for specific aspects of the cilia formation, i.e. basal body docking and spacing across the apical cell membrane.

ELMO1 and DOCK180 localize to the basal body in primary cilia of MDCK cells. The cilia in zebrafish pronephros and olfactory placodes as well as in *Xenopus* epidermis are motile cilia of MCCs. Cilia in zebrafish Kupffer's vesicle and in *Xenopus* gastrocoel roof plate are motile mono-cilia, and are implied in establishing left-right asymmetry in the developing embryo. To determine if ELMO proteins and DOCK180 display a similar localization in non-motile primary cilia, we performed immunostainings for ELMO1 and DOCK180 in polarized Madin-Darby canine kidney cells (MDCKs). A specific staining pattern for ELMO1 as well as for DOCK180 was observed at the base of the cilium. Co-labelling of ELMO1 with γ-Tubulin, a marker for the mother and daughter centriole, revealed expression of ELMO1 in only one of the centrioles. Co-immunostainings with Cep164, a marker for the mother centriole confirmed that ELMO1 localized exclusively to the mother centriole whereas DOCK180 localized to both. The specific localization of ELMO1 to the

mother centriole/basal body of non-motile cilia further supports a role of ELMO1 in the molecular machinery targeting the basal body to the apical membrane.

Depletion of Arl4a resembles the Ezrin and ELMO phenotype. ADP-ribosylation factors (ARFs) are a class of more than 20 small GTPases with essential roles in membrane transport, cilia formation and cytoskeletal rearrangement. Arl4 proteins belong to the ARF-like proteins and represent a subgroup of the ARF family, consisting of three closely related members, Arl4a, Arl4c and Arl4d. Recently, Arl4a was identified as an interactor of ELMO proteins. We examined two related *arl4a* genes, *arl4aa* and *arl4ab*, in zebrafish. WISH detected expression of both forms in the pronephric tubule at 24 hpf. While depletion of *arl4ab* did not result in significant pronephric cyst formation, *arl4aa* morphants displayed prominent hydrocephalus, cyst formation and shortened cilia in the pronephric tubule at 48 hpf. Co-injection of *arl4aa* mRNA partially rescued the pronephric cyst formation of *arl4aa* morphants, confirming the specificity of the phenotypic changes observed in the *arl4aa* morphants. To investigate a possible genetic interaction between Arl4aa and Ezrin/ELMO1 during ciliogenesis, we performed rescue experiments by co-injecting *elmo1* or *ezrin* mRNA together with *arl4aa* MO and vice versa. Overexpression of either ELMO1 or Ezrin significantly reduced pronephric cyst formation in Arl4aa morphants whereas overexpression of Arl4aa in *elmo1* or *ezrin* morphants only led to a mild rescue effect. These results point to a possible genetic interaction between Arl4aa and ELMO1/Ezrin during ciliogenesis in zebrafish, placing Arl4aa upstream of ELMO1/Ezrin. TEM studies of *arl4aa* morphants revealed defects in basal body docking to the apical membrane consistent with a functional relationship between Arl4aa and ELMO1/Ezrin.
In the MCCs of the *Xenopus* epidermis, Arl4a depletion caused a phenotype virtually identical to the knockdown of Ezrin or ELMO1/2: Intracellular localization of ciliary axonemes and intracellular accumulation of basal bodies. These results suggest that Arl4a regulates ciliogenesis by controlling apical migration and docking of the basal bodies upstream of Ezrin and ELMO1.

The DOCK180/ELMO downstream effector Rac1 is important for ciliogenesis. Rac1 is the major downstream effector of DOCK180/ELMO, and involved in remodelling of the actin cytoskeleton in different morphogenetic programs. In ciliogenesis a role for Rac1 for the positioning of the cilium on the posterior cell surface in mouse ventral node cells has been postulated. Moreover, in Lowe syndrome a deficiency of Rac1 activity is associated with abnormal primary cilia formation, but the exact function of Rac1 in this context remains unclear. In zebrafish two related *rac1* genes exist, *rac1* and *rac1l*. While depletion of *rac1* resulted in minor pronephric cyst formation, depletion of *rac1l* caused prominent pronephric cyst formation. Knockdown of both proteins caused shortened cilia in the pronephric tubule at 24 hpf. Co-injection of *rac1l* mRNA partially rescued the pronephric cyst formation of *rac1l* morphants, confirming the specificity of the phenotypic changes observed in the *rac1l* morphants. In addition, depletion of *rac1* and/or *rac1l* led to striking defects of cardiac looping in zebrafish embryos at 48 hpf, suggesting an essential role of these gene products during the establishment of a normal left-right asymmetry. TEM studies of *rac1/rac1l* double-morphants revealed a transport defect and abnormal accumulation of basal bodies in the cytoplasm at 48 hpf. Consistent with the observed abnormalities in zebrafish, depletion of Rac1 during *Xenopus* epidermis development resulted in irregular basal body docking and spacing at the apical membrane.

Rac1 controls ERM activity during ciliogenesis. During T-cell activation Rac1 inactivates ERMs in T-lymphocytes, resulting in relaxation of the cortical actin cytoskeleton from the plasma membrane, leading to the formation of the immunological synapse. To analyze whether Rac1 regulates ERMs during ciliogenesis in vertebrates, we isolated pronephric tubules at 24 hpf of *rac1/rac1l-, elmo1- and dock180*-depleted zebrafish embryos, and determined the phosphorylation level of ERMs by western blot. Increased phospho-ERM levels were observed in all three conditions as well as after *rac1* or *rac1l* single knockdown. To determine Ezrin function in the zebrafish pronephric tubule, wildtype and mutant forms of Ezrin, including the phosphorylation-defective Ezrin^{T567A} mutation and the phospho-mimetic mutant Ezrin^{T567D}, were targeted to the zebrafish pronephros, using a transient transgenesis approach. The Cadherin17 promoter-driven expression of both mutant forms caused cyst formation on the left or right hand side of the pronephric glomerulus dependant on which side the motile cilia bearing MCCs in the mid-portion of the pronephric tubule were most affected. The majority of MCCs is located in this tubular segment, creating the fluid flow within the pronephric tubule that is necessary for normal pronephric development. Taken together, Rac1 plays an essential role during ciliogenesis in vertebrates by acting downstream of DOCK180/ELMO to regulate Ezrin activity by inducing its dephosphorylation.

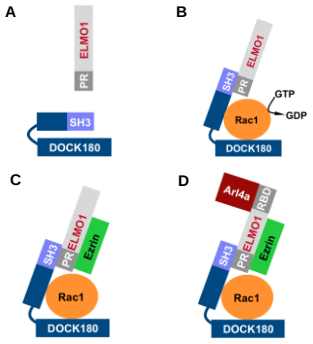

Figure 5.3: **Interaction of Arl4a with the Ezrin/ELMO1/ DOCK180/Rac1 (EEDR) complex.** (**A**) ELMO1 binds to DOCK180 and thereby releases self-inhibition. (**B**) The ELMO1/DOCK180 complex serves as a Guanine nucleotide exchange factor (GEF) for the small GTPase Rac1. Active Rac1 has functions in remodeling of the actin cytoskeleton during phagocytosis and cell migration. (**C**) ELMO1 interacts with the FERM protein Ezrin that is known to localize to ciliary basal bodies. (**D**) Arl4a binds to the Ras-binding domain (RBD), thereby recruiting the EEDR complex to the plasma membrane.

In conclusion, the Arl4a, Ezrin, DOCK180/ELMO1/Rac1 complex is an essential component module that orchestrates ciliary basal body migration, docking, and spacing at the apical cell membrane by modulating the cortical actin web in multi-ciliated cells in both *Xenopus* and zebrafish (**figure 5.4**).

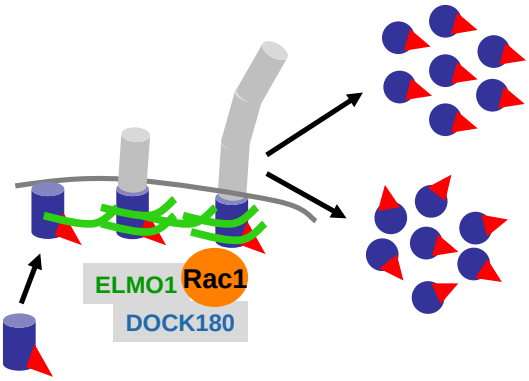

Figure 5.4: **The ELMO1/DOCK180/Rac1 complex controls ciliary polarization.** ELMO1/DOCK180/Rac1 complex mediates docking of the basal body at the cell membrane, and the orienting of the basal body with respect to the rootlet. Furthermore, the ELMO1/DOCK180/Rac1 complex is essential for tethering the basal bodies in the same direction in multiciliated cells via the apical actin network to ensure that all motile cilia beat in the same direction.

➢ *Task 5.3. Measuring ciliary signalling*

Deliverables under this Task: D5.3 (month 24), D5.8 (month 36), D5.10 (month 48), D5.11 (month 48) and D5.15 (month 60) all delivered.

A) Mechanosensory signaling

Completed by month 24.

B) mTOR signaling

Partner 5

To determine the contribution of the mTOR signalling cascade to ciliopathy-specific disease manifestations, we generated KspCRE KIF3A (fl/fl) mice to induce rapid cystic kidney disease in the distal nephron segments. These mice typically die between week 7 and week 10 of kidney failure (**figure 5.5**). We subsequently crossed these mice with Raptor (fl/fl) mice to create mice strains that lack mTORC1 activity in the same nephron segments prone to cyst formation. These mice experienced a dramatically increased survival rate.

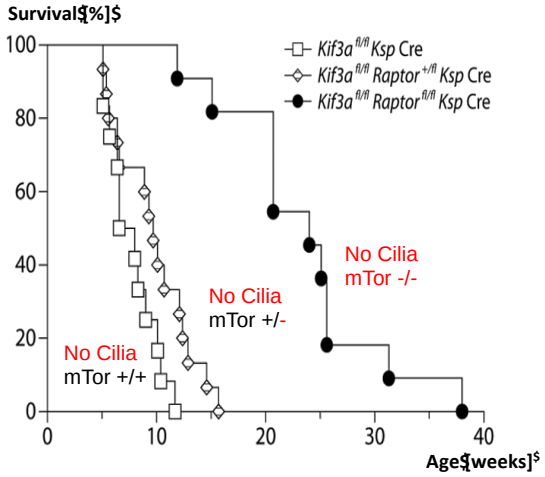

Figure 5.5

However, even the Raptor (i.e. mTORC1)-deficient mice will ultimately succumb to cyst formation and renal failure.

To determine the drivers of cyst formation in KIF3A/mTORC1-deficient mice, we performed extensive microarray profiling in both mice strains at postnatal week 2 and week 4. Unsurprisingly, these analyses revealed that cyst formation in 2-week old KIF3A-deficient mice was characterized by extensive activation of cellular programs related to cell cycle progression. Unexpectedly, the 2-week KIF3A/mTORC1-deficient mice were remarkable for a substantial inflammatory response, entailing several parallel acting pathways, including innate immune responses, Jak-Stat signalling, chemokine production and monocyte activation.

We next compared the gene profiles of 4-week old KIF3A-deficient and KIF3A/mTORC1-deficient mice. Surprisingly, the gene profiles had become indistinguishable despite the lack of functional mTORC1 activity: cell cycle programs were now quite prominent in the KIF3A/mTORC1-deficient mice, while inflammatory responses were now clearly detectable in KIF3A-deficient mice with fully active mTORC1 (**figure 5.6**).

A comparison of the two sub-networks “cell cycle” and “inflammation” revealed that the major transcriptional regulators were almost identical in these two mice strains after a 4-week period.

Our findings have **important therapeutic implications:** 1) ciliary defects are commonly associated with an up-regulation of the mTORC1 signaling cascade. Genetic deletion or pharmacological inhibition of this signalling cascade slows ciliopathy-associated disease manifestations. 2) Inhibition (genetically or pharmacologically) appears to rapidly induce “bypass signalling”, which is a common phenomena in cancer treatment. Thus, therapeutic approaches aimed to ameliorate ciliopathy-associated disease manifestations or progression likely need to utilize sequential or combinatorial treatment protocols, and may consist of induction and maintenance therapies.

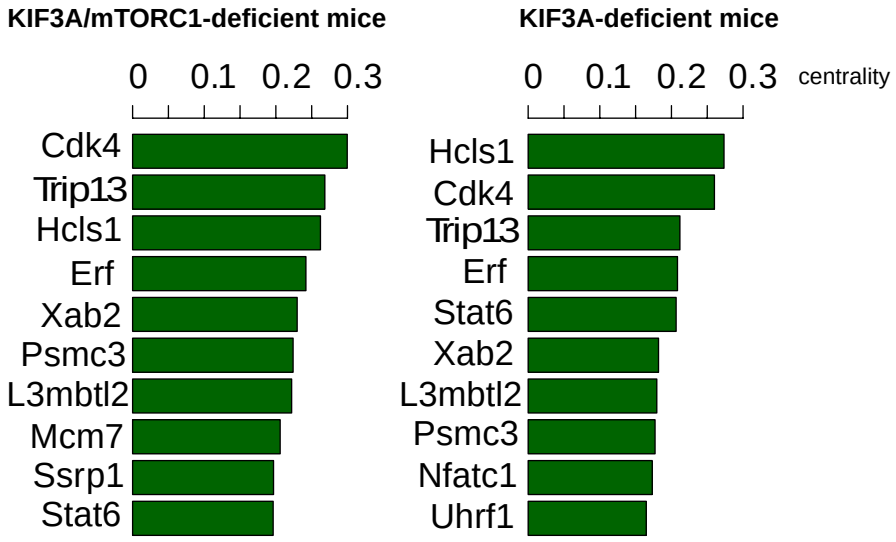

Figure 5.6: **Transcripitional regulators controlling cell cycle progression and inflammation in 4-week old KIF3A- versus KIF3A/mTORC1-deficient mice.** Centrality analysis reveals that the top drivers of these two sub-networks (cell cycle, inflammation) are almost identical in these two mice strains, revealing that alternate pathways and signalling cascades are rapidly activated to drive the same disease-promoting programs in both mice strains, thus circumventing the genetic deletion of mTORC1.

C) Wnt signaling

Partner 8:

We have performed assays on two proteins associated with Wnt signalling as a result of ciliary dysfunction: DCDC2 and HUWE1. The data for DCDC2, which we show is mutated in patients with hepato-renal cystic disease, has been accepted for publication in American Journal of Human Genetics, with SYSCILIA acknowledgement. DCDC2 acts as a negative regulator of Wnt signalling in vitro and in vivo. HUWE1 came out of the SYSCILIA siRNA whole genome screen (partner 10) as a strong candidate, and mutations were found in 9 Bardet-Biedl/MKS or PCD patients (**Table 5.1** below) by partner 9. Our institute (Partner 8) recently published that Huwe1 ubiquitinylates Dishevelled regulating its location and thereby regulating Wnt signalling (de Groot et al, Sci Signal. 2014 Mar 18). We have adapted this assay to test our human mutations and test cilia function.

Patient	Sex	Ciliopathy	AA Change	N change	Var Reads
#1	F	MKS	A-3557-V	G → A (X:53573753)	100%
#3	F	BBS	V-1215-M	C → T (X:53620422)	45%
#4	F	BBS	E-2304-K	C → T (X:53591654)	28%
#9	F	Ciliopathy	A-1955-T	C → T (X:53603881)	28%
#13	F	PCD	R-4220-H	C → T (X: 53561649)	51%
#14	F	PCD	R-1282-Q	C → T (X: 53619485)	50%
#LVO		LVO	R-3219-C	G → A (X:53576300)	

Table 5.1 HUWE1 mutations in Ciliopathy patients.

D) Sonic Hedgehog (SHH) signalling

Partner 8:

Systemic treatment of ciliopathy mice with CEP290 mutations (Hynes et al. 2014) with SHH agonist purmorphamine (500 µM) seems to reduce renal cyst development in 10 pups (**figure 5.7**); however this work needs to be repeated before firm conclusions and statistics can be performed.

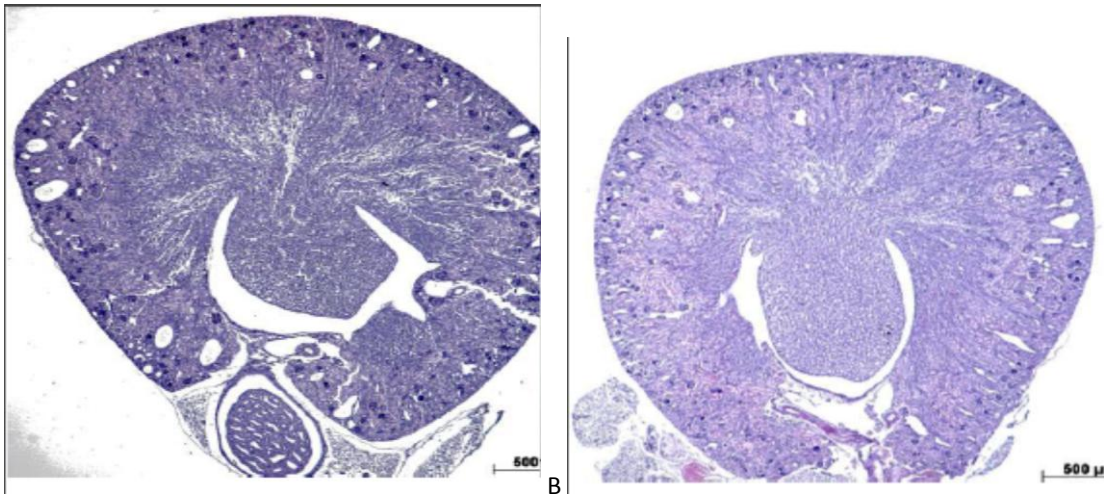

Figure 5.7: **A) Cep290-/- DMSO B) Cep290-/- purmorphamine**

Also, Partner 8 published a protocol in this reporting period in Nature Protocols for 3D spheroid growth *ex vivo* (from urine cells of patients, Giles et al, Nature Protocols, 2014). Partner 8 has also published non-invasive ways of obtaining ciliated cells from patients for ex vivo study (Ajzenberg et al, Cilia, 2015).

E) Cell migration and tubulogenesis

Partner 4:

As reported initially at month 48, we developed an htert RPE mammalian cell culture model to monitor Wnt signaling readout in the context of stable BBS4 suppression. We identified 29 negative hits (suppressors of the aberrant Wnt readout in the context of *BBS4* ablation); 13 genes passed secondary validation (*AXIN2* qPCR as a confirmatory test of Wnt readout); and we have functionally validated ten genes *in vivo* using multiple relevant readouts (convergent extension; cerebellar integrity; and proximal renal tubule convolution). We now have a list of seven genes that ameliorate significantly *bbs4* suppression defects in the developing zebrafish and these represent novel drug targets for ciliopathy treatment. *In vivo* validation of these findings in mouse models will continue in Partner 4's laboratory following the completion of the SYSCILIA funded period.

We also continue to utilize specific assays to evaluate ciliary phenotypes in physiologically relevant tissues of the developing zebrafish. Partner 4 employs three readouts to validate modulators ciliary and basal body defects; these include convergent extension (cell migration); cerebellar atrophy (as indicated by anti-acetylated tubulin staining at 3 days post fertilization; dpf); and anti-Na+/K+ ATPase staining at 4 dpf in fixed whole-mount zebrafish embryos followed by evaluation of proximal tubule convolution; and Alcian blue staining (at 5 dpf) to evaluate integrity of cartilaginous structures in the pharyngeal skeleton of the developing zebrafish. As described also in WP8 and WP6, these assays have been applied to novel CAMs identified by WP8, including centrosomal proteins CEP55 (see figure and details in WP6) and CEP76 (Frangakis et al, manuscript in preparation); intraflagellar transport complex genes (Davis et al, manuscript in preparation); and Bardet-Biedl syndrome genes harboring both single nucleotide variants and copy number variants (Lindstrand et al, in revision at the *American Journal of Human Genetics*).

Deviations for the technical work planned in Annex I:

For WP5 there are no deviations for the technical work planned in Annex I.

Deviations between actual and planned person-months effort. (see also WP11)

Partner 5:

Due to the enhanced technical and experimental work as a consequence of the amendment of Annex 1 to switch from *in vitro* to *in vivo* assays the work load of WP5 and 6 was increased. As mentioned in the previous periodic report 13^{+4} PMs have been reduced in WP9 and shifted to WP 5 and 6. In addition further PMs were necessary to reach the aims of WP 5+6. At month 60 the difference between the actual and indicated person months (including PMs of WP9) amounts to $15{,}4^{+26}$ in total for WP5 and WP6.

Partner 11:

Has reconfigured the personnel costs from the beginning of the project in a cost neutral way and can dedicate more person months effort to the project. No additional human resources are being requested.

Work package number	WP6		Start date or starting event:		month 01				
Work package title	Assays to Distort Ciliopathy-Associated Modules (CAMs)								
Activity Type	RTD								
Participant number	11(L)	1b	4	5	6	7	8	9	10	12
Participant short name	UCD	RUNMC *Kremer*	Duke	UKL FR	JoGuMZ	FTELE.IGM	UMCU	UCL	LIMM	ICP
Person-months per participant:	49	22^{+7}	50^{+14}	14^{+6}	9^{+7}	80^{+50}	32^{+11}	18^{+9}	16^{+11}	44^{+27}
Actual person months per participant* Month 48 – 60	10.5	18.45^{+5}	9.82	3.4^{+6}	0	28	5^{+4}	20.59	0^{+4}	$20.17^{+9.21}$

* This is considered as use of resources.
Deviations are explained in the end of the report for this Work package.

A summary of progress towards objectives of WP1:

Objective 6.1. *Employ a semi high-throughput approach in mammalian cell culture and C. elegans to validate and further interrogate the roles of candidate CAM components (informed from WP1-4, 7 and 8) in cilium formation, maintenance, function, signaling and trafficking.*

Objective 6.2. *Establish and functionally assess animal models (zebrafish, Xenopus, mice) of individual candidate and known CAM components, employing systematic integrated and strategic methodologies (e.g., ciliary transport, polarity, signalling) developed in WP5 and elsewhere.*

Objective 6.3. *Employ animal models (C. elegans, zebrafish, mice) to determine the genetic interrelationships between known/candidate components of individual and different CAMs.*

Objective 6.4. *Integrate all phenotypic profiling data into a public database of CAM constituents, as a component of the central SYSCILIA resource*

Months 49-60 focused primarily on Objectives 6.1, 6.2 and 6.3. Using cell culture (Task 6.1), **partner 8** published a protocol for assaying cells from the urine of patients in tubulogenesis/3D spheroid assays, published a role for NPHP proteins in renal cell migration, and identified that pan-ciliopathy protein CEP290 regulates replication fork stability and that mutations affecting CEP290 results in replications stress and DNA damage. Using *C. elegans* (Task 6.2), **partner 11** firmly established TMEM107 as an MKS module component and collaborative work identified mutations in Joubert/OFD patients. **Partner 11** also continued work towards understanding the role of *C. elegans* KIAA0556 and this work is now submitted together with data from other SysCilia

partners. Using Xenopus (Task 6.3), **partner 5** characterised identified ANKS3, as a potential binding partner of ANKS6 and a candidate for mutations that lead to NPH or NPH-like disease.Using zebrafish (Task 6.4), **partner 1b** described retinal phenotypes in Spag5 and Csn8 (Cop9 signalosome subunit 8) morphants, **partner 8** showed how a DcDc2 morphant recapitulated a renal-hepatic ciliopathy phenotype rescuable by a Wnt inhibitor, and **partner 9** described ciliopathy-associated tissue and ciliary level phenotypes in Cep120, C21orf2 and Txtex1D2 morphants. **Partner 9** also provided evidence for a cilium-associated role for Oscp1, Cep120, C21orf2 and Tctex1D2 and established CRISPR assays for disrupting gene function in zebrafish. Using mice (Task 6.5), **partner 8** published a murine model of *Cep290*, **partner 7** further delineated the phenotype of OFD knockout mice to include cardiac defects and showed that inducible kidney OFD1 knockout mice possess renal tubule dilation and abnormal mTor pathway activation, and **partner 12** identified a candidate mTOR signaling target during renal morphogenesis. In Task 6.6, **partner 12** identified differentially expressed genes between wild-type and *Hnf1b* mutant mouse embryos before the formation of tubules. Work stemming from WP6 has been published in at least 22 papers this reporting period and partners have presented their data at many meetings.

A summary of progress towards each task in WP6:

- ***Task 6.1. Perturbation of CAMs in ciliated mammalian cell culture***

Deliverables under this Task: D6.7 (month 24) delivered;

A: Ciliary transport
B: Cellular morphology and migration
C: Ciliary signaling

Partner 4:
We contributed to WP6 to study tissue developmental phenotypes through the evaluation of a novel ciliopathy gene, *CEP55.* In collaboration with clinical colleague in Canada (Patrick Frosk, University of Manitoba), we recently analyzed a pedigree with a perinatal lethal syndrome hallmarked by hydranencephaly, renal dysplasia, multinucleated neurons, and syndactyly. Subsequent to whole exome sequencing, only two rare variants were left after variant prioritization of the data. First, we identified a synonymous change in *ZDHHC16* that is not predicted to affect splicing (Human Splicing Finder v2.4.1). The other variant was a homozygous nonsense mutation in *CEP55* (c.1274C>A and p.S425X; NM_001127182). The variant resides in the last exon of CEP55 and is predicted to result in a loss of 40 C-terminal amino acids. *CEP55* encodes a centrosomal protein, and centrosomal dysfunction has been associated previously with hydrocephaly and hydranencephaly. We have evaluated multiple phenotypes in zebrafish (**figure 6.1**), including generalized edema (a readout for renal function); HuC/D staining (to assess postmitotic neurons in the brain); Alcian blue staining (to evaluate the pharyngeal skeleton; and Acetylated tubulin staining (to evaluate the axon tracks in the brain). All of these phenotypes can be rescued with a WT human mRNA and the truncation fails to rescue these defects indicating

that it is a loss of function variant, thereby defining a novel causal locus for a complex human genetic syndrome.

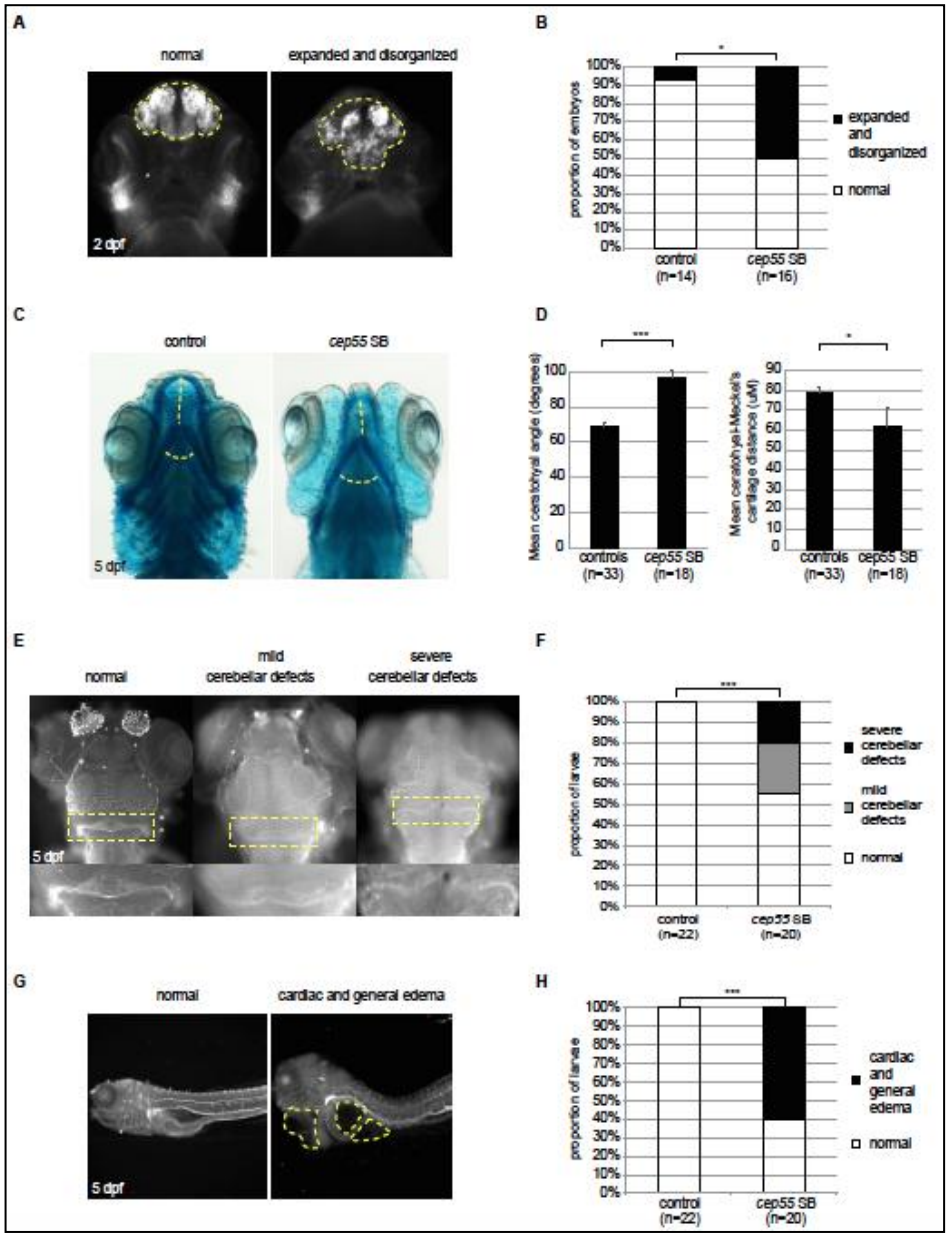

***Figure 6.1. Cep55* suppression recapitulates syndromic phenotypes of humans with a perinatal lethal disorder. A.** Representative images of the head (dorsal view, anterior end pointing up) of 2 days post fertilization (dpf) zebrafish embryos stained with HuC/D antibody, showing expansion and disorganization of the proliferation zone **B.** Proportion of zebrafish embryos with normal or expanded and disorganized proliferation zone in forebrain as shown in **(A)**, Fisher exact test, * indicates $p<0.05$. **C.** Representative images 5 dpf zebrafish larvae stained with Alcian blue, showing increased ceratohyal angle and reduced ceratohyal-Meckel's cartilage distance (yellow dashed lines). **D.** Quantification of ceratohyal angle and reduced ceratohyal-Meckel's cartilage distance as shown in **(C)**. *T*-test, * indicates $p<0.05$, and *** indicates $p<0.001$. **E.** Representative images of 5dpf zebrafish larvae stained with acetylated-tubulin antibody, showing cerebellar defects. **F.** The proportion of larvae with cerebellar defects shown in **(E)**, Fisher exact test, *** indicates $p<0.001$. **G** Representative images of the lateral view of 5dpf zebrafish larvae, showing general edema (marked with yellow dashed lines), suggesting kidney defects. **H.** proportion of larvae with edema shown in **(E)**. Fisher exact test, with *** indicates $p<0.001$.

Partner 8:

Published a protocol for assaying cells from the urine of patients in tubulogenesis/3D spheroid assays (Giles et al, Nature Protocols, 2014). Furthermore, published a role for nephronophthisis proteins in renal cell migration using scratch-wound assays (Slaats et al, PLoS Genetics, 2014).

Partner 8 also looked in detail at a series of fibroblasts taken from various patients diagnosed with Joubert syndrome and with known mutations causing the disease (MKS1 from a MKS patient and from 3 Joubert patients, ARL13B, and INPP5E). We measured ciliary frequency and length under identical culturing conditions.

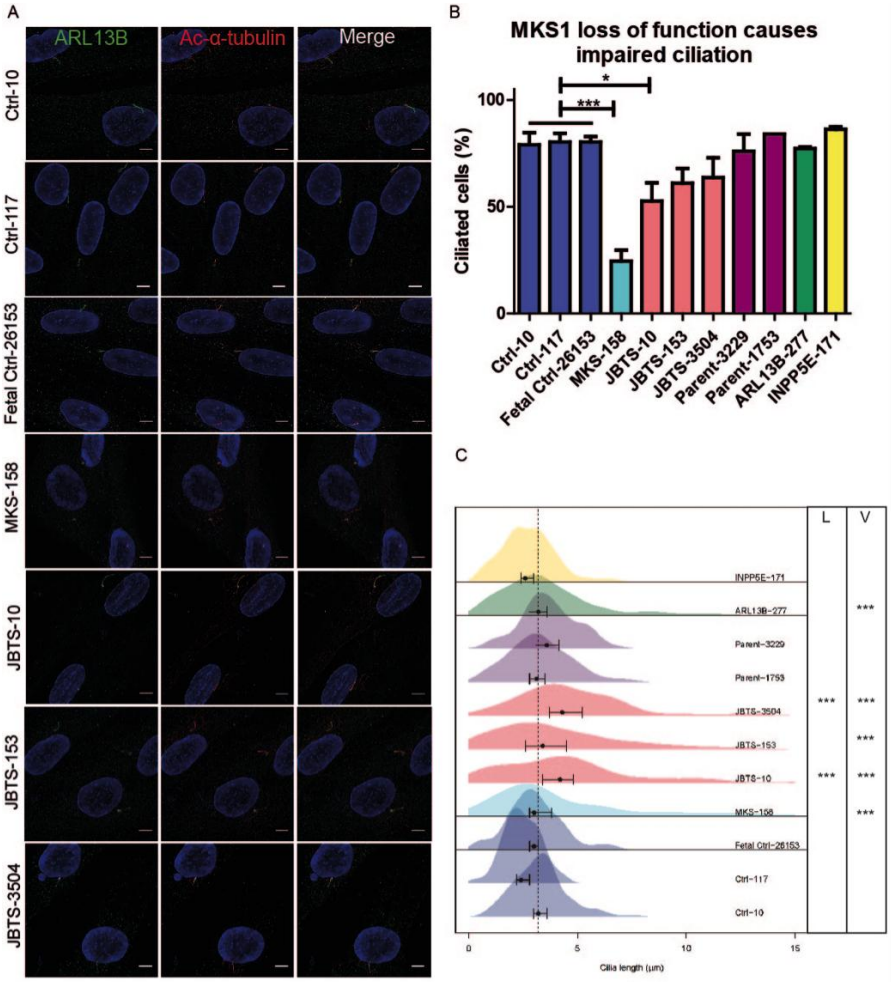

Figure 6.2. **Fibroblasts from individuals with MKS1-related Joubert syndrome display primary cilia defects.** (**A**) Immunostaining of fibroblasts derived from skin biopsies of JBTS-10, JBTS-153, JBTS-3504, MKS-158, and controls. ARL13B (green), gamma tubulin (g-tub; white) and cilia (acetylated tubulin, red; scalebar 5 µm). Brightness and contrast were identically adjusted across photos for visualization purposes. (**B**) Quantification of cilia frequency (mean and SEM) in fibroblasts from controls (Ctrl-10, Ctrl-117, Fetal Ctrl-26153), three individuals with JS (JBTS-10, JBTS-153 and JBTS-3504), the carrier parents of JBTS-3504 (Parent-3229 and Parent-1753), one fetus with MKS1-related MKS (MKS-158), and ARL13B (ARL13B-277) and INPP5E (INPP5E-171) mutants. * indicates $p<0.05$, *** $p<0.001$ (One-way ANOVA). (**C**) Kernel density plots depicting distribution of cilia length (x-axis) in fibroblasts obtained from individuals with different MKS1 mutations and controls (y-axis). Points and error bars represent medians and 99% confidence intervals respectively. JBTS-10 and JBTS-3504 have longer (L) cilia than the controls Ctrl-10 and Ctrl-117. *** indicates $p<0.001$ (Kruskal-Wallis test). Variance ($\sigma 2$) in ciliary length was different between Fetal Ctrl-26153 and MKS-158, and between Ctrl-10 and Ctrl-117 compared to JBTS-10, JBTS-153, JBTS-3504 and ARL13B-277. *** indicates $p<0.001$ (F-test). Number of cells scored 100-300 in 2 batches.

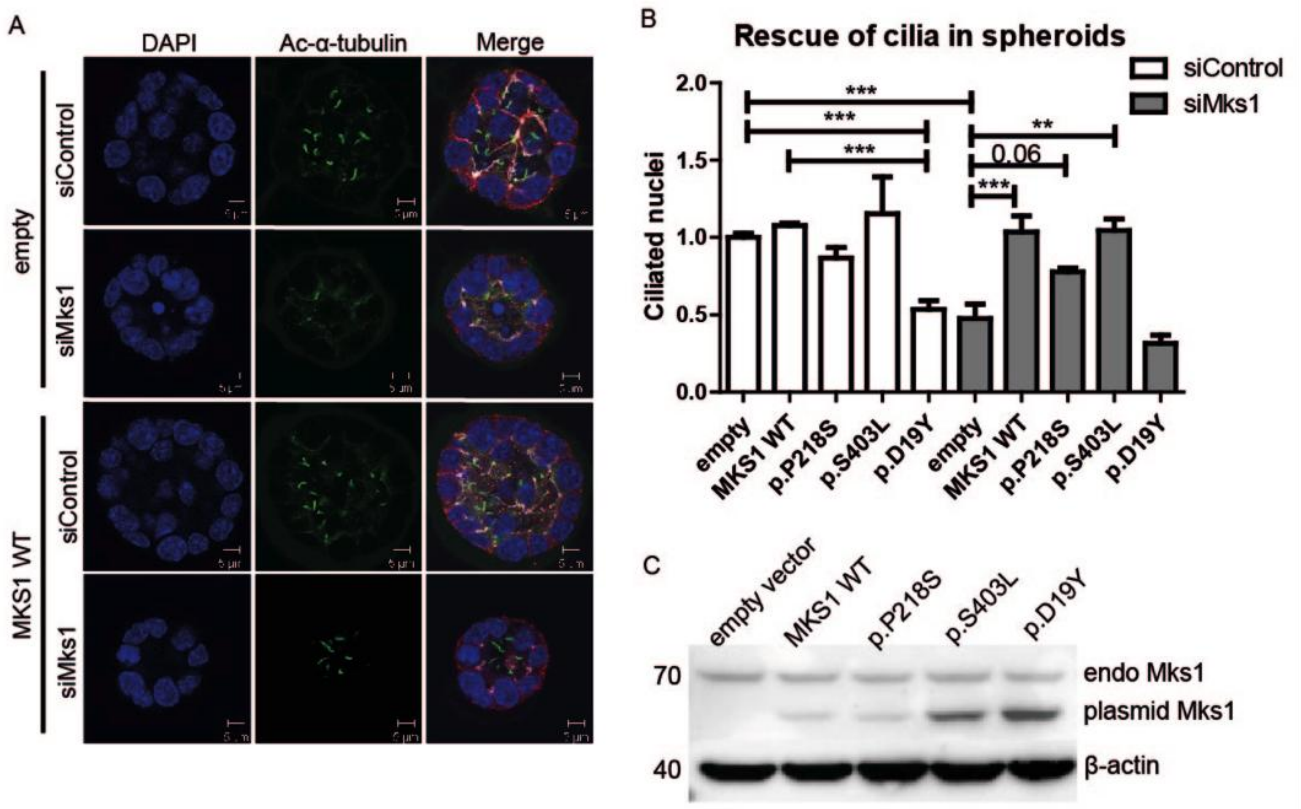

Figure 6.3. **Mks1 knockdown impairs ciliogenesis in 3D spheroid culture of IMCD3 cells.** (**A**) Immunostaining of spheroids for cilia (acetylated tubulin, green), tight junctions (ZO1, white), and adherens junctions (**β**-catenin, red) with DAPI counterstaining (blue) shows loss of cilia after Mks1 siRNA transfection, and rescue by MKS1-WT. (**B**) Quantification of ciliary frequency in spheroids shows significant differences between control spheroids and spheroids depleted for MKS1 (indicates $p<0.0003$), and a potential dominant negative effect of transfection with MKS1-p.D19Y ($p<0.001$). Complete rescue of ciliary frequency was obtained upon transfection with MKS1-WT or MKS1-p.S403L ($p<0.01$), and a partial rescue upon transfection with MKS1-p.P218S ($p<0.06$). 50 spheroids were scored per condition. Error bars represent SEM (n = 3 experiments), (**C**) Immunoblot for MKS1 in IMCD3 lysates (siControl) transfected with different MKS1 alleles. Upper band indicates equal endogenous levels of MKS1 in IMCD3 cells. Lower band indicates different MKS1 alleles (not full-length human MKS1 construct). **β**-actin is used as loading control.

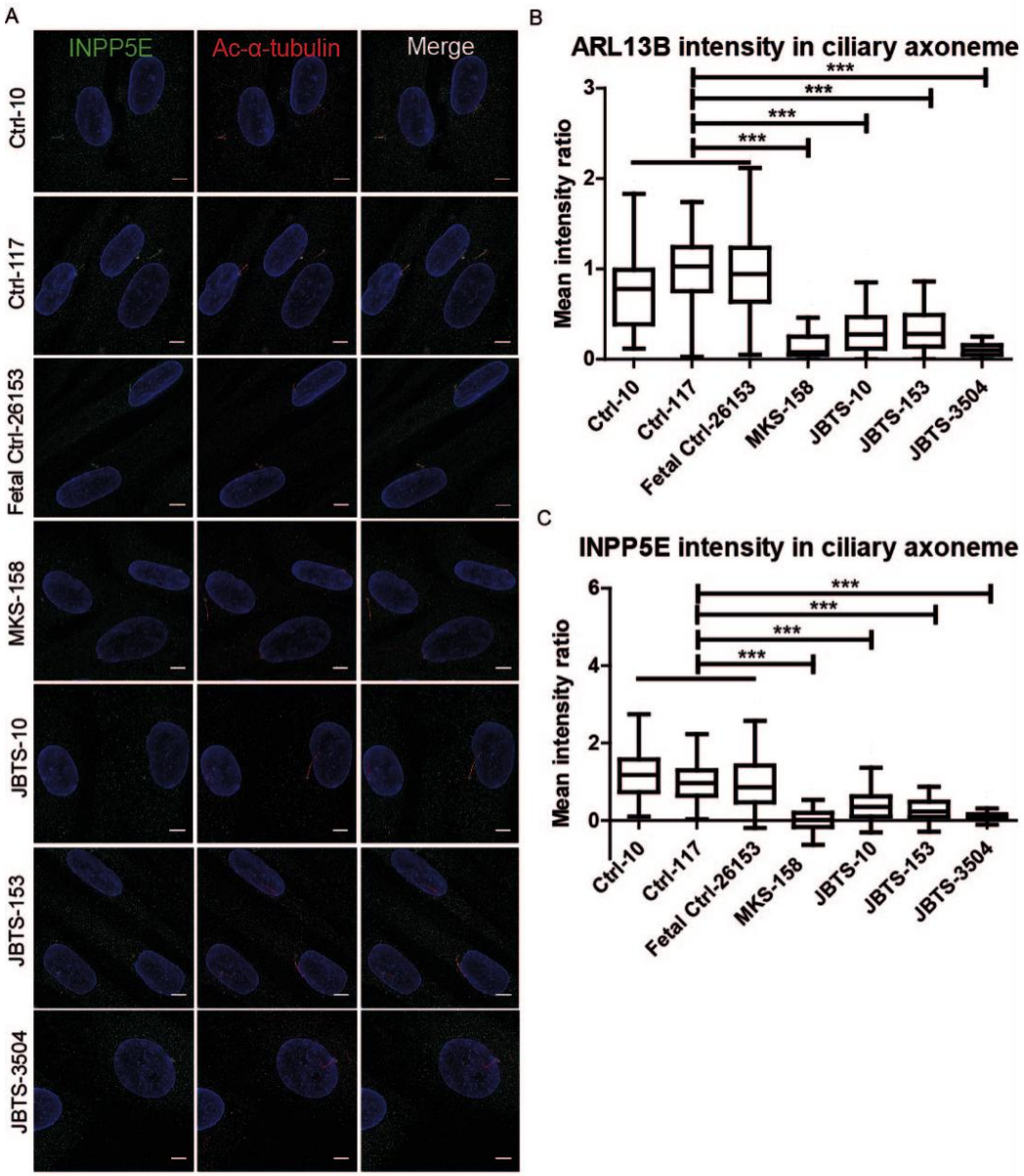

Figure 6.4. **Reduced ciliary ARL13B and INPP5E in fibroblasts from individuals with MKS1-related Joubert syndrome.** (**A**) Immunostaining of fibroblasts derived from skin biopsies of JBTS-10, JBTS-153, JBTS-3504, MKS-158, and controls. INPP5E (green), gamma tubulin (g-tub; white) and cilia (acetylated tubulin, red; scalebar 5 µm). Brightness and contrast were identically adjusted across photos for visualization purposes. (**B**) MKS1-mutant fibroblasts have less ARL13B in the cilium than control cells (Tukey whiskers). *** indicates p<0.001 (Kruskal-Wallis test). (**C**) MKS1-mutant fibroblasts have less INPP5E in the cilium than control cells (Tukey whiskers). *** indicates p<0.001 (Kruskal-Wallis test). Axonemal fluorescence intensity was calculated by subtracting cytoplasmic background from cilium signal and normalizing to Ctrl-117 intensity to be able to combine batches (n = 50-150 cilia in 2 batches).

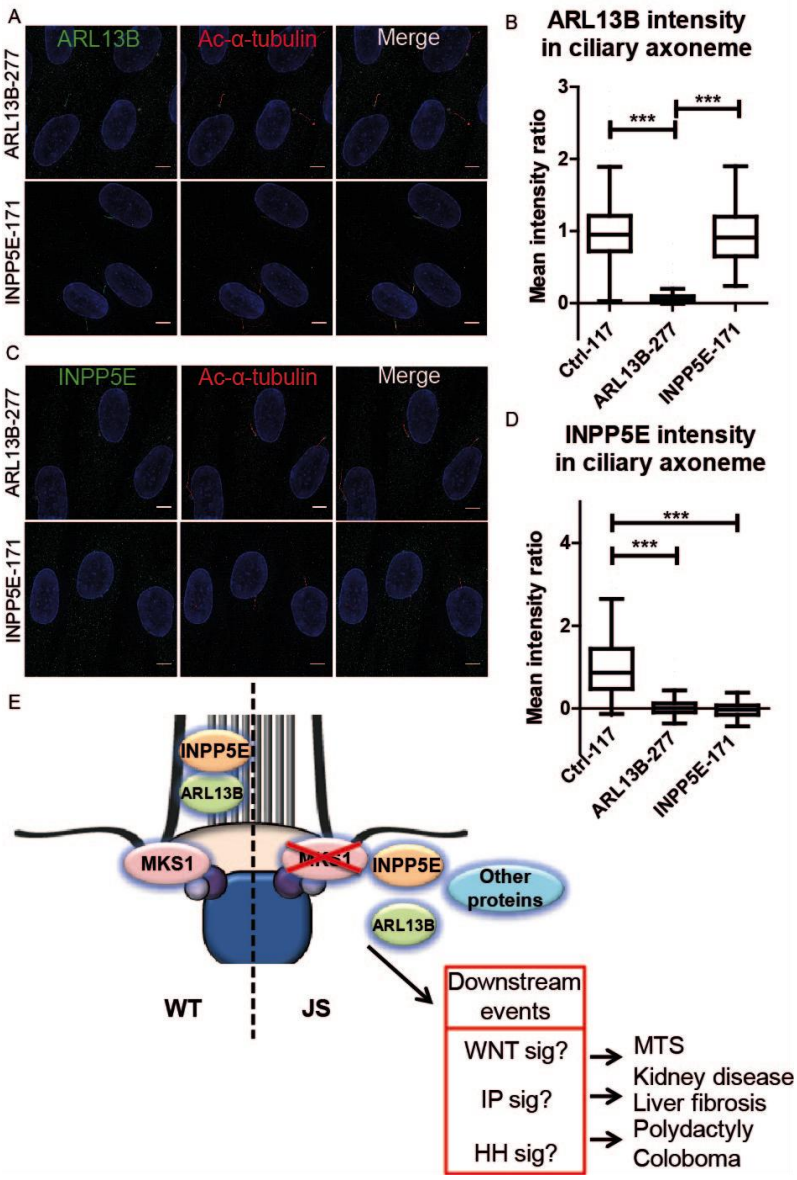

Figure 6.5. **Reduced ciliary ARL13B and INPP5E in fibroblasts from individuals with ARL13B- and INPP5E-related Joubert syndrome.** (**A**) Immunostaining of fibroblasts derived from skin biopsies of ARL13B- 277 and INPP5E-171. ARL13B (green), gamma tubulin (g-tub; white) and cilia (acetylated tubulin, red;scalebar 5 µm). Brightness and contrast were identically adjusted across photos for visualization purposes. (**B**) Only ARL13B-277 fibroblasts have less ARL13B in the cilium than control (Tukey whiskers). *** indicates p<0.001 (Kruskal-Wallis test, n > 100 cilia in 2 batches). (**C**) Immunostaining of fibroblasts derived from skin biopsies of ARL13B-277 and INPP5E-171. INPP5E (green), gamma tubulin (white) and cilia (acetylated tubulin, red; scalebar 5 µm). Brightness and contrast were identically adjusted across photos for visualization purposes. (**D**) Both mutant fibroblasts have less INPP5E in the cilium than control (Tukey whiskers). *** indicates p<0.001 (Kruskal-Wallis test, n > 100 cilia in 2 batches). Axonemal fluorescence intensity was calculated by subtracting cytoplasmic background from cilium signal and normalizing to Ctrl-117 intensity. (**E**) Schematic overview of the roles of MKS1, ARL13B and INPP5E in Joubert syndrome. Loss of function mutations in MKS1 cause transition zone (TZ) dysfunction and disturb ciliary localization of ARL13B and INPP5E. Our data support the hypothesis that loss of ARL13B-dependent localization of INPP5E is a central mechanism underlying JS. The downstream events are hypothetical based on data in the literature.

We concluded that although ciliary frequency and length does seem to differ between patients and controls, the clearest assay that should be checked is the presence of INPP5E in the ciliary

axoneme. The paper has been drafted and under second-round review at J Medical Genetics after positive first-round reviews.

Furthermore, partner 8 investigated the role of ciliopathy protein CEP290 in the DNA damage response, and a manuscript is now accepted for publication at Journal of Clinical Investigation on June 26 2015.

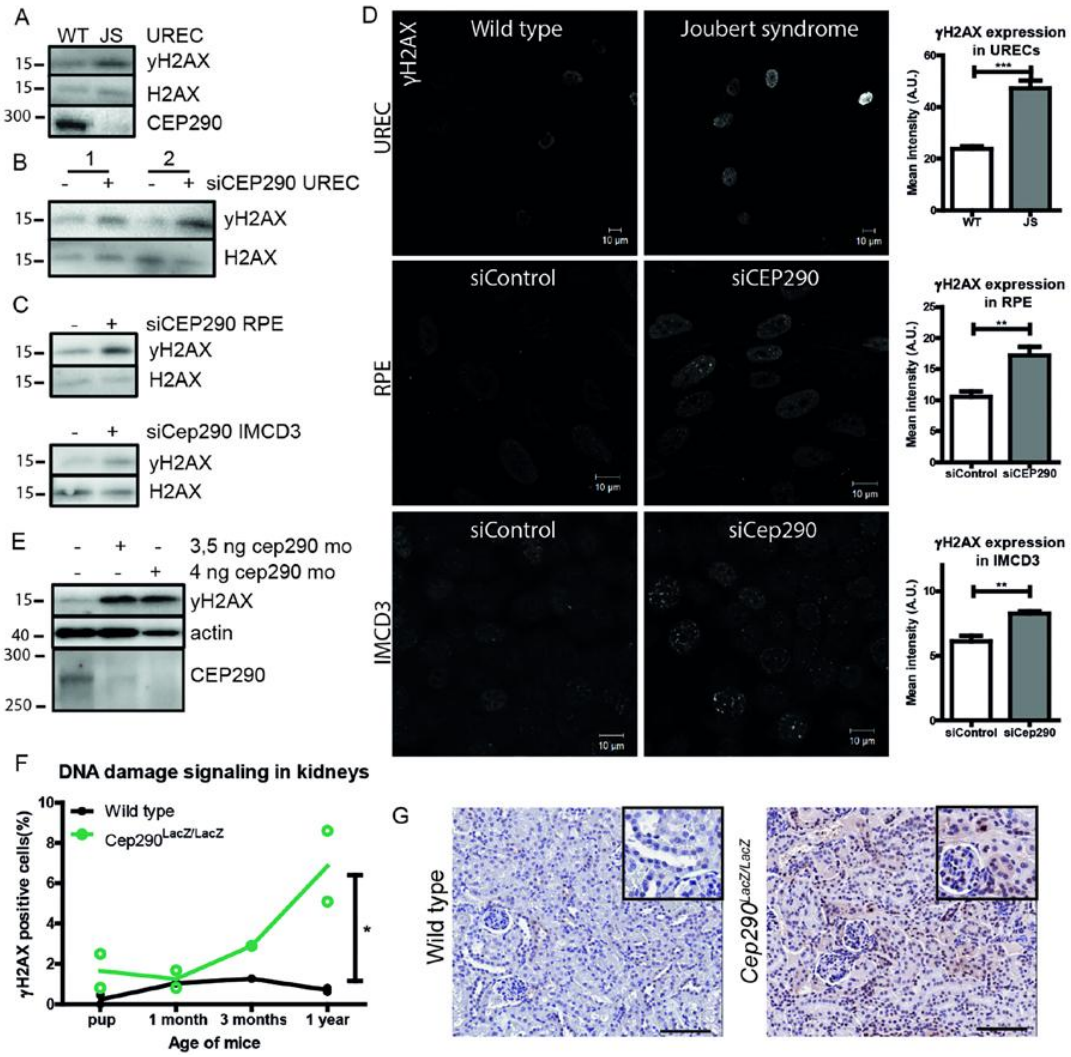

Figure 6.6. **DDR signalling is enhanced ex vivo, in vitro, and in vivo. (A)** Western blot of urine-derived epithelial cells (URECs) lysates of a healthy donor (WT) and Joubert syndrome (JS) patient with compound heterozygous mutations in *CEP290*, p.Q950Pfs*6 het and p.K939N het. Loss of CEP290 protein expression and increased γH2AX levels are detected in the JS protein lysate. H2AX is loading control. **(B)** Increased γH2AX levels are detected in siCEP290 transfected WT-URECs, 48 hours after siCEP290 transfection. H2AX is loading control. **(C)** RPE and mIMCD3 cells depleted for CEP290/Cep290 by siRNA show increased γH2AX levels compared to control siRNA transfection (56 hours). H2AX is loading control (n=3). **(D)** Immunofluorescent staining of γH2AX in WT and JS URECs, and RPE and mIMCD3 cells depleted for CEP290/Cep290 by siRNA, and quantification of intensities/nucleus (10 µm scale bar; n=3; 100 cells scored/condition; T-test **p<0.01, ***p<0.001). **(E)** Western blot of zebrafish injected with 3.5 or 4 ng cep290 ATG-targeting mo. Loss of CEP290 protein expression and increased γH2AX levels are detected in cep290 mo-injected zebrafish lysates 48 hpf. Actin is loading control (n=3). **(F)** More γH2AX (brown) staining in kidneys of homozygote *Cep290*$^{LacZ/LacZ}$ gene trap mice compared to wild type, increasing with age (n=13, between 5,000–7,000 cells scored per animal) (Linear model, goodness of fit R^2=0.86; *p<0.05). **(G)** Example of wild type mouse kidney and *Cep290*$^{LacZ/LacZ}$ gene trap mouse kidney at age 3 months stained for γH2AX (brown). Inserts show magnification. Scale bar represents 100 µm.

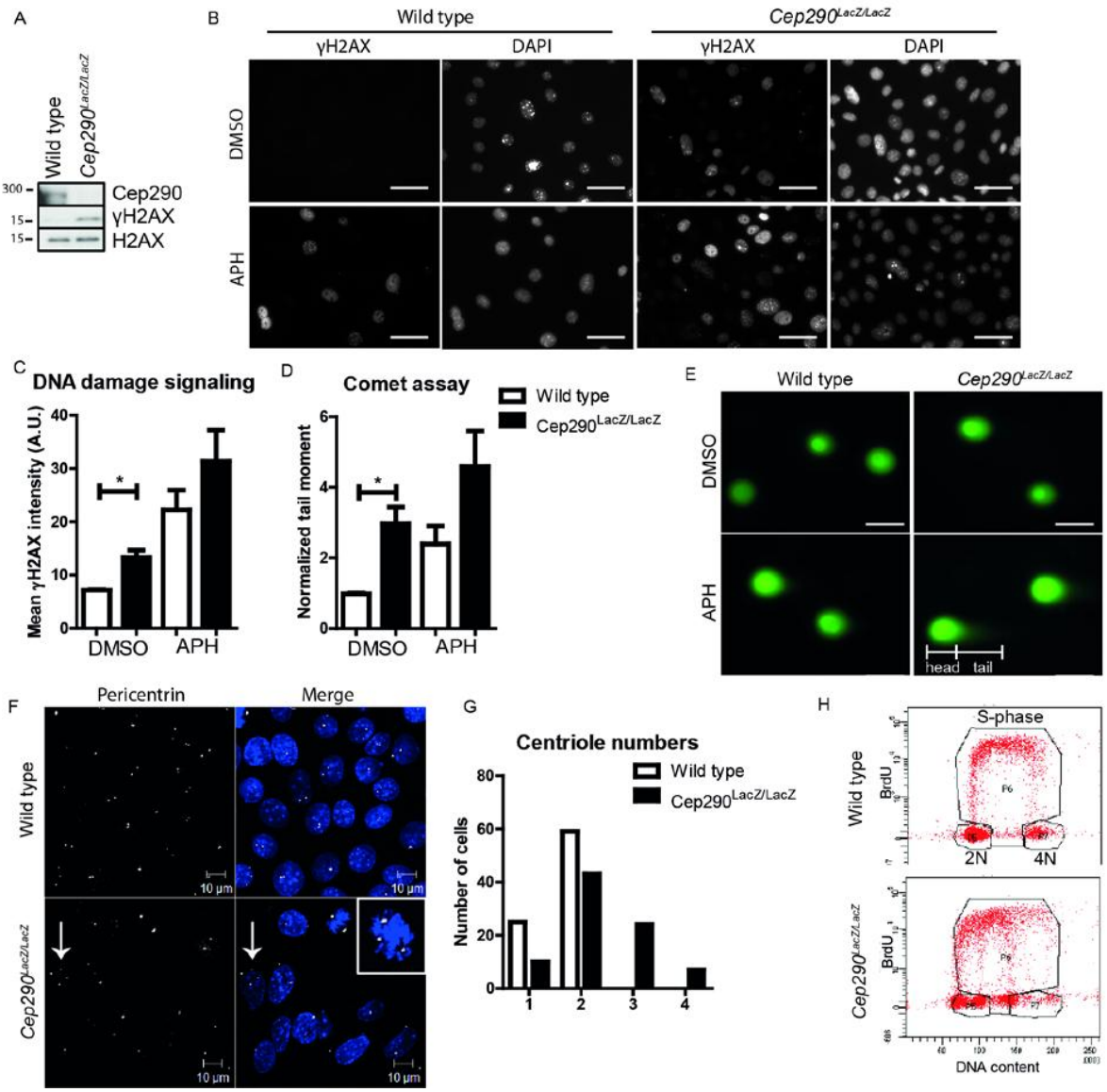

Figure 6.7. **DNA damage is enhanced in Cep290 depleted cells.** (**A**) Western blot of Cep290$^{LacZ/LacZ}$ and wild type primary mouse kidney cell lysates. Increased H2AX phosphorylation is detected in the Cep290 depleted cells, with H2AX as loading control. (**B**) Immunofluorescent staining of γH2AX in control DMSO and 400 nM APH (18 hours) treated cells, scale bar represents 10 µm. (**C**) Quantification of γH2AX intensities per nucleus of control DMSO and 400 nM APH (18 hours) treated cells (n=3; 100 cells scored/condition; Two-way ANOVA, *p<0.05). (**D**) Quantification of comet tail moments of 400 nM APH (18 hours) treated cells normalized to control DMSO treated wild type cells (n=3; 50 cells scored/condition; Two-way ANOVA, *p<0.05). (**E**) Images of SYBR-gold stained DNA in comet tail assays, scale bar represents 10 µm. (**F**) Immunofluorescent staining of wild type and *Cep290*$^{LacZ/LacZ}$ cells for pericentrin (white) reveals supernumerary centrioles (arrow) in *Cep290*$^{LacZ/LacZ}$ cells. Insert is multipolar (>2) spindle, scale bar represents 10 µm. (**G**) Quantification of centriole number in wild type and *Cep290*$^{LacZ/LacZ}$ cells (84 cells scored per cell line; n=3). (**H**) BrdU FACS of wild type and *Cep290*$^{LacZ/LacZ}$ cells shows normal DNA content and cell cycle for wild type cells, however, *Cep290*$^{LacZ/LacZ}$ cells have irregular DNA content (10,000 events measured; n=3).

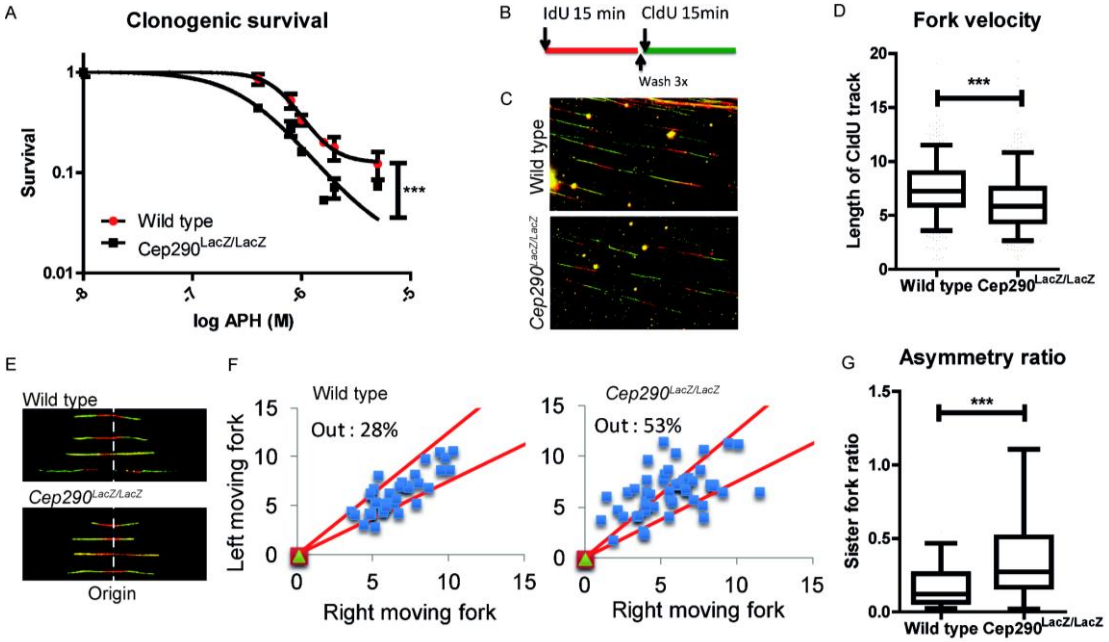

Figure 6.8. **Loss of Cep290 leads to replication stress.** (**A**) Clonogenic survival (on log scale, -6 means $1{\cdot}10^{-6}$ M) of control DMSO and 500 to 5000 nM APH (18 hours) treated cells showing sensitivity to replication stress of Cep290$^{LacZ/LacZ}$ cells. Log IC50 curves are compared (n=3; ***p<0.001) (**B**) Schematic overview of pulse labeling of cells with IdU and CldU for 15 minutes. (**C**) Immunofluorescent staining of DNA fibers after pulse labeling with IdU (red) and CldU (green) respectively. (**D**) Quantification of replication fork velocity by measuring length of the CldU track. Cep290$^{LacZ/LacZ}$ cells demonstrate decreased fork velocity (700 tracks scored/condition; n=4; T-test ***p<0.001). (**E**) Immunofluorescent staining of DNA fibers after pulse labeling with IdU (red) and CldU (green) respectively. Asymmetric replication at origins in Cep290$^{LacZ/LacZ}$ cells is present. (**F**) Quantification of fork asymmetry at origins in Cep290$^{LacZ/LacZ}$ cells. When replication track differs more than 25% between the right and left moving fork, the measurement falls out the cutoff (50 tracks scored/condition). (**G**) Fork asymmetry ratio as calculated by the ratio of the right and left moving forks (50 tracks scored/condition; n=2; 5-95 percentile; T-test ***p<0.001).

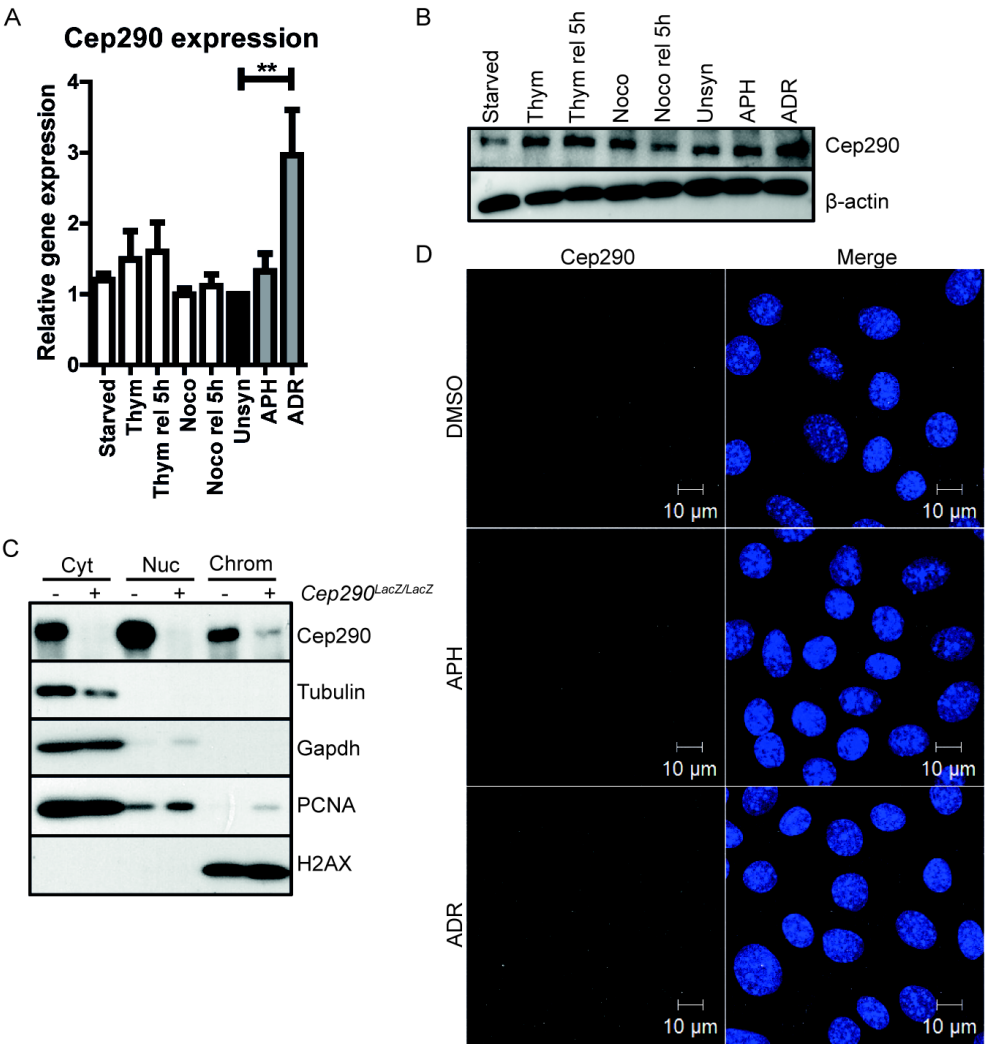

Figure 6.9. **Expression and localization of Cep290.** (**A**) Normalized *Cep290* gene expression levels were measured by RT-qPCR of wild type cells synchronized by serum starvation (G1), thymidine (S), nocodazole (G2) and release for 5 hours of these synchronizations, and unsynchronized, APH (400 nM) and ADR (1 µM) (24 hours) treated cells (n=4; One-way ANOVA **p<0.01). Concomitantly, protein expression was detected by Western blot, using β-actin as loading control (**B**). (**C**) Western blot of chromatin fractionation of wild type (-) and $Cep290^{LacZ/LacZ}$ (+) cells. Cep290 is expressed in the cytosol (GAPDH, tubulin), nucleus (PCNA) and chromatin enriched fraction (H2AX). (**D**) IF staining of Cep290 expression (white) of DMSO, APH (400 nM) and ADR (1µM) (18 hours) treated wild type cells. ADR exposure caused increased Cep290 levels. Scale bar represents 10 µm.

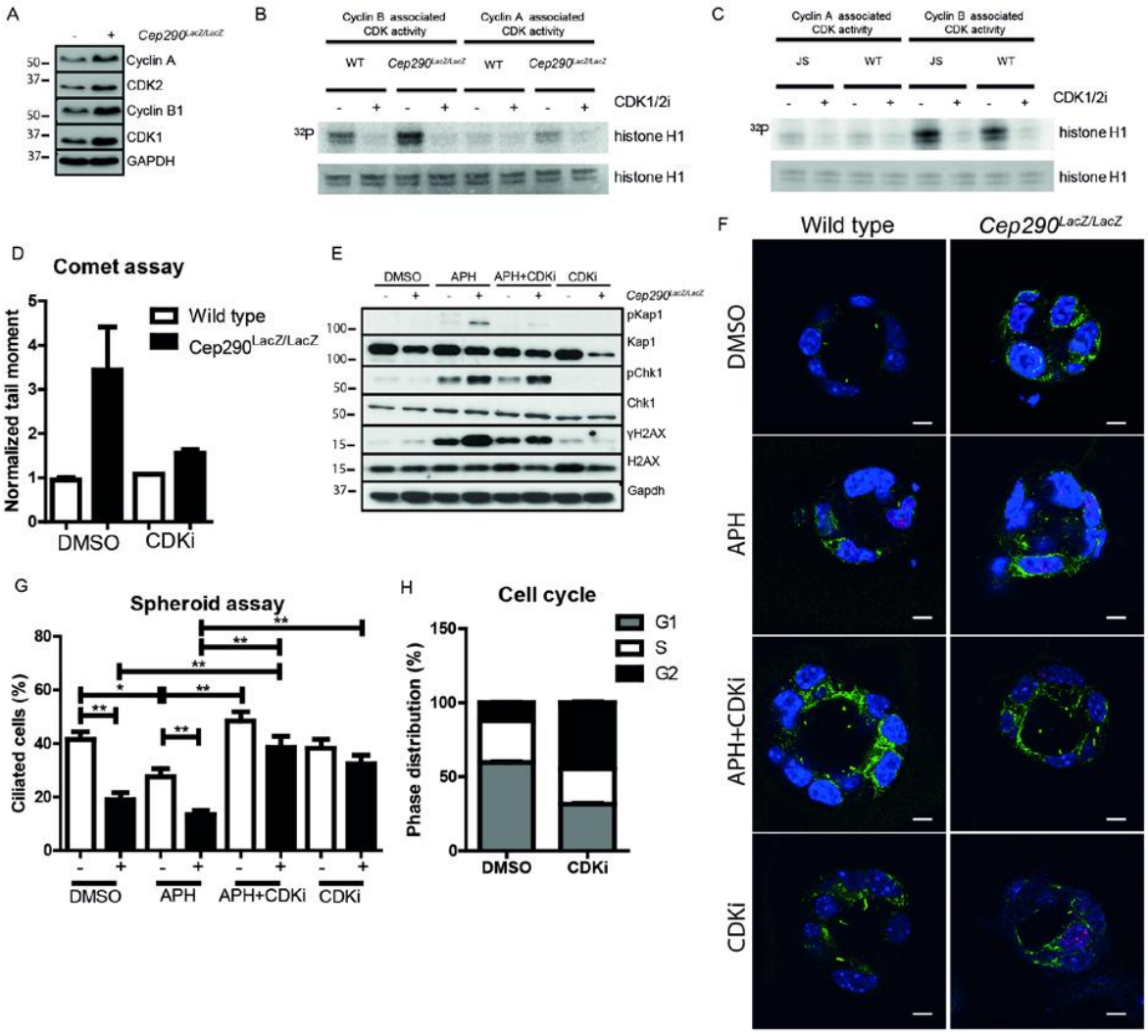

Figure 6.10. **CDK1/2 inhibitor rescues DNA damage and primary cilia.** (**A**) Western blot of *Cep290*$^{LacZ/LacZ}$ (+) and wild type (-) cell lysates show increased levels of CDK1, CKD2, Cyclin A, Cyclin B1 in Cep290-depleted cells. GAPDH is loading control. (**B**) In vitro CDK kinase assay of *Cep290*$^{LacZ/LacZ}$ and wild type (WT) cell lysates after precipitation of Cyclin A-CDK and Cyclin B1-CDK complexes (n=4). **(C)** CDK kinase assay of WT and JS patient URECs (n=1). Histone1 represents the substrate level control. **(D)** DNA breaks are rescued by CDKi in comet tail moments of 200 nM CDK1/2 inhibitor (CDKi) (18 hours) treated cells normalized to control DMSO treated wild type cells (n=3; 50 cells scored/condition). (**E**) Western blot of Cep290$^{LacZ/LacZ}$ (+) and wild type (-) cells treated with 400 nM APH and/or 200 nM CDKi (18 hours). Higher phosphorylation levels of Kap1, H2AX, CHK1 in Cep290$^{LacZ/LacZ}$ cells with/without APH treatment, rescued by CDK1/2i. Unphosphorylated protein and GAPDH are loading controls. (**F**) 3D spheroids of wild type and Cep290$^{LacZ/LacZ}$ cells, stained for γH2AX (red) and ciliation (acetylated tubulin; green), treated with 400 nM APH and/or 200 nM CDKi (18 hours). Scale bars are 5 µm. (**G**) CDKi rescues ciliation in Cep290$^{LacZ/LacZ}$ and APH treated spheroids. (35 spheroids scored/condition) (n=3; data shown for single experiment; Three-way ANOVA *p<0.05, **p<0.01). (**H**) Cell cycle distribution of wild type cells treated with DMSO or 200 nM CDKi (18 hours) reveals increased cell number in G_2 (black), decreased cell number in G_1 (grey) after CDKi treatment (10,000 events measured; n=3).

We conclude from these studies that pan-ciliopathy protein CEP290 regulates replication fork stability and mutations affecting CEP290 results in replications stress and DNA damage.

- ***Task 6.2. Perturbation of CAMs in C. elegans ciliated sensory neurons, an invertebrate model***

Deliverables under this Task: D6.11 (month 30), D6.12 (month 36), D6.16 (month 42), and D6.25 (month 54) all delivered.

A: Cilium structure/integrity and sensory function

B: Intraflagellar transport (IFT)

C: Dissection of the genetic relationship between different CAM components

D: Ciliary membrane biogenesis, morphological signaling and membrane protein targeting to cilia

Partner 11:

We continued our work on the functional investigation of *tmem-107*. First, we completed the localisation interdependency analysis reported in figure 6 of D6.16. We now show that the localisation of TMEM-107 and MKS-1 is interdependent and further refine the position of TMEM-107 within the layered model of the MKS module (**figure 6.11**).

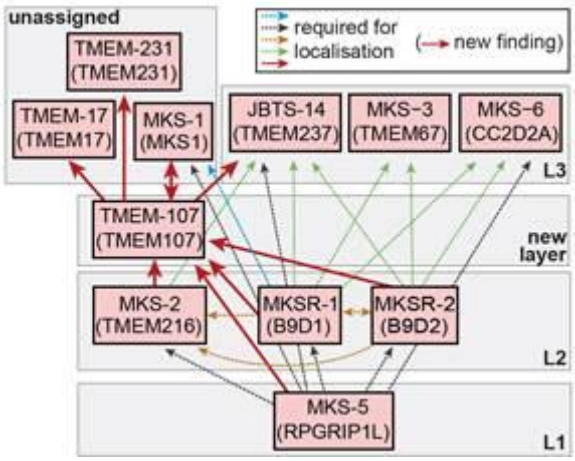

Figure 6.11. **TZ localisation dependencies of nematode MKS module proteins, including TMEM-107.** Assay involves examining the localisation of GFP-tagged TMEM-107 in mutant alleles of the other MKS module components, and the reverse experiment where the localisation of fluorescence tagged MKS module proteins are examined in a *tmem-107(oq100)* allele. Schematic shows a suggested new position (new layer) for TMEM-107 within the hierarchical three layer (L1-3) model of MKS module assembly (drawn based on data in Williams *et al.* 2010, Huang *et al.* 2011). Human protein orthologues denoted in brackets. Proteins in 'unassigned' grouping not yet mapped to a particular layer.

In collaboration with Colin Johnson (partner 10), co-immunoprecipitation (coIP) assays were performed in mammalian cells to determine if TMEM107 biochemically associates with MKS module proteins. GFP-tagged TMEM107 was exogenously co-expressed with FLAG-tagged TMEM216, TMEM231, TMEM17 or TMEM237, or with myc-tagged MKS1, and assessed for associations using binding conditions previously optimized for membrane proteins. We found TMEM107 immunoprecipitates full-length TMEM216/231/237 and MKS1, but not TMEM17 (**figure 6.12**). In the case of TMEM237, TMEM107 did not detectably interact with an N-terminal

cytoplasmic domain of this protein (TMEM237Nt), indicating the TMEM237 association is dependent on its transmembrane domains (**figure 6.12**).

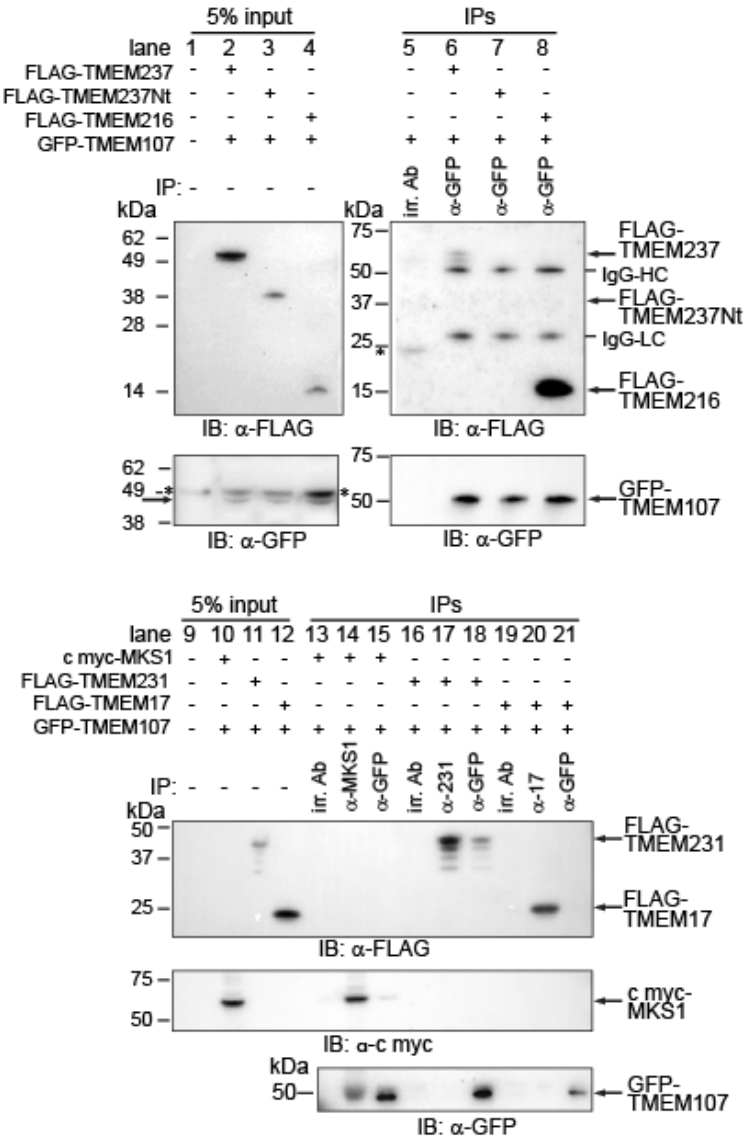

Figure 6.12: **Coimmunoprecipitation (coIP) assays showing biochemical interaction between TMEM107 and mammalian MKS module proteins.** Left panels (lanes 1-4): input material from whole cell extracts (WCEs) transfected with the indicated TMEM constructs and immunoblotted (IB) with either mouse monoclonal anti-denatured GFP or anti-FLAG. Right panels (lanes 5-8): proteins immunoprecipitated by either an irrelevant antibody (irr. Ab; anti-MICU3) or rabbit polyclonal anti-native GFP, and then immunoblotted for either FLAG or GFP. Tagged TMEM proteins are indicated by arrows. IgG heavy chain (HC) and light chain (LC) in coIPs are indicated. Asterisks (*) mark non-specific proteins. Molecular mass standards are shown to the left of all blots.

We also collaborated with Martijn Huynen (partner 1c) who used differential Dollo parsimony to obtain eukaryote-wide co-evolutionary relationships for MKS module proteins including TMEM107. In agreement with the nematode MKS module hierarchy, Layer 2 protein orthologues TMEM216, B9D1 and B9D2 form a strongly co-evolving MKS core. This 'core' co-evolves with Layer 3 protein orthologues TMEM67 and CC2D2A, consistent with localisation dependencies in

mammalian systems, though not in worms. In agreement with nematode localisation data, we also identified a co-evolving TMEM107/17/231 submodule (**figure 6.13**). Unexpectedly, this submodule does not connect to TMEM237 because orthologues are missing in stramenopiles, alveolates and excavates (data not shown), indicating late evolutionary origin and incorporation of TMEM237 into the MKS module. Also surprising was that despite its central role in nematode module organisation, RPGRIP1L only marginally co-evolves with other MKS components (**figure 13**). However, this may be explained by low levels of RPGRIP1L sequence conservation. Indeed, although RPGRIP1L orthologues are reported to be missing in highly diverged species such as *Naegleria gruberi* and *Thalassiosira pseudonana*, we were able to identify orthologues in these species using iterative profile-based sequence analysis. Finally, the interdependent localisation between nematode MKS1 and TMEM107 is not reflected in the co-evolution data. Thus, our evolutionary findings support conserved roles for *C. elegans* TMEM107 in organising an MKS submodule with TMEM231 and TMEM17, but differences in the modular arrangements of TMEM107 with other MKS proteins might exist between species.

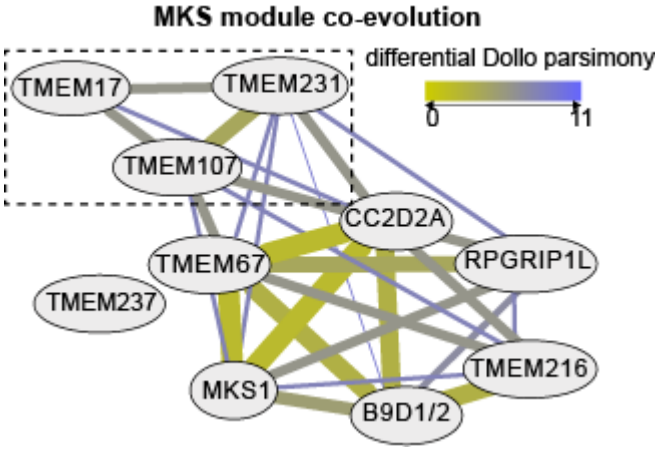

Figure 6.13: **Co-evolution relationships between MKS components** using differential Dollo parsimony that counts along a phylogenetic tree how often two genes are lost independently from each other. Thickness and color gradient indicate strong co-evolution. Edges with a differential Dollo parsimony score of >11 are not shown. Dashed box indicates a co-evolving MKS submodule.

The nematode data for TMEM-107 makes it a strong ciliopathy gene candidate. To investigate further, we collaborated with SYSCILIA partners 8 and 10 (Rachel Giles; Colin Johnson) who performed siRNA knockdown experiments in murine IMCD3 cells and demonstrated that mammalian TMEM107 regulates ciliogenesis and lumen size in 3D spheroids (**figure 6.14a, b**), similar to other ciliopathy genes. Through an additional collaboration with Christel Thauvin-Robinet (University of Lyon), 238 individuals with JBTS or OFD type VI were screened using Sanger and next generation sequencing for mutations in the coding exons of *TMEM107*. Two OFDVI female twins born from consanguineous parents were found with a homozygous *TMEM107* missense variant (NM_183065: g.8079298T>C; p.Glu45Gly) and a JBTS male was found with compound heterozygous *TMEM107* mutations consisting of one frameshift deletion (NM_032354.3: g.8077560delT; p.Leu134Phefs*8) and one in-frame deletion (NM_032354.3: g.8077890_8077893delGAA; p.Phe106del) (**figure 6.14**). All patients presented with similar neurological disturbances (ataxia, oculomotor apraxia, and intellectual disability), retinopathy,

and brain magnetic resonance imaging (MRI) revealed cerebellar hypoplasia with molar tooth sign (**figure 6.14**). Two of the three individuals had OFDVI syndrome because of associated lingual hamartomas and abnormal frenulae. All three mutations were absent from the Exome Variant Server and were predicted to be damaging by Human Splicing Finder or PolyPhen-2. In direct support of mutation pathogenicity, fibroblasts isolated from patient 3 (p.Leu134Phefs*8/p.Phe106del) show reduced ciliation frequency, and cilia that do form are abnormally long (**figure 6.14 m-o**).

Together, these data reveal TMEM107 as a ciliopathy protein required for normal cilium formation and highlight the allelic nature of JBTS and OFD.

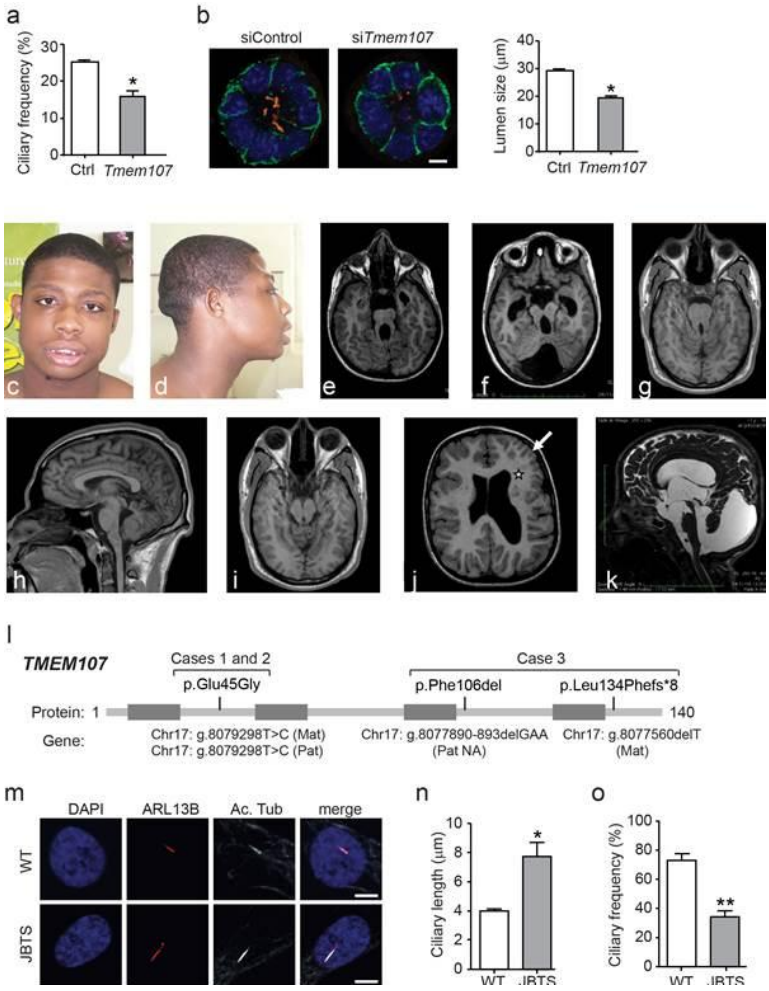

Figure 6.14. **Clinical presentation and molecular data of ODVI and JBTS individuals with causal TMEM107 mutations. (a)** siCtrl or si*Tmem107* transfected IMCD3 cells demonstrate that TMEM107 affects cilia formation. **(b)** 3D IMCD3 cells grown into spheroids display smaller lumen formation. Bar; 5 µm. **(c, d)** Facial picture of Patient 3. **(e-g)** Brain MRI with MTS in cases 1 (e), 2 (f), and 3 (g). **(h-k)** Vermian dysplasia (h, i) in case 3; heterotopias (star), hydrocephalus and polymicrogyria (white arrow) (j) and enlarged posterior fossa with a cystic dilatation of the fourth ventricle with a hypoplasic vermis (star), a severe midbrain dysplasia (white arrow) and a thin corpus callosum with enlarged ventricles in case 2 (k) in case 1. **(l)** Schematic of human TMEM107 protein showing the position of identified patient mutations. Grey boxes correspond to the transmembrane domains. Mat; maternal, Pat; paternal, NA; not available. **(m-o)** Immunostaining of fibroblasts derived from skin biopsies of healthy control and Patient 3. ARL13b (red) and cilia (acetylated tubulin, white) staining shows longer cilia in Patient 3 compared to control fibroblasts (n). Quantification of ciliary frequency in fibroblasts from control and TMEM107 mutant shows reduced ciliary frequency in mutant (o). ** indicates p<0.01, * p<0.05 (T-test), Bars; 5 mm.

These data together with the data in D6.16 and in the WP5 60 month report (super resolution localisation of TMEM-107 to ring like domains of the transition zone membrane) is currently in revision.

Partner 11:

K04F10.2/KIAA0556 functional investigation

Although we previously reported that cilium ultrastructure was grossly normal in K04F10.2 loss of function mutants (*tm1830*), we have found that the distal segments of amphid channel cilia possess a subtle microtubule defect. In wild-type worms, these cilia are segmented into a proximal region (transition zone and middle segment) consisting of nine outer doublet MTs, and a distal segment consisting only of singlet A-tubules due to the termination of each doublet B-tubule at the middle segment tips (**figure 6.15**). In the cilia of *tm1830* mutants, age matched with wild type controls (early day 1 adult), a 40% reduction in A-tubule number was observed in distal segments; also, whilst many *tm1830* cilia retained a bipartite MT arrangement, microtubule doublets were occasionally observed at the ciliary tips (**figure 6.15**). Together, these data show that the K04F10.2(*tm1830*) mutant possesses reduced ciliary microtubule load and organisation, although various aspects of gross cilium length and function remain normal, at least in those cilia examined. Thus, loss of KIAA0556 in *C. elegans* appears to destabilise ciliary microtubules.

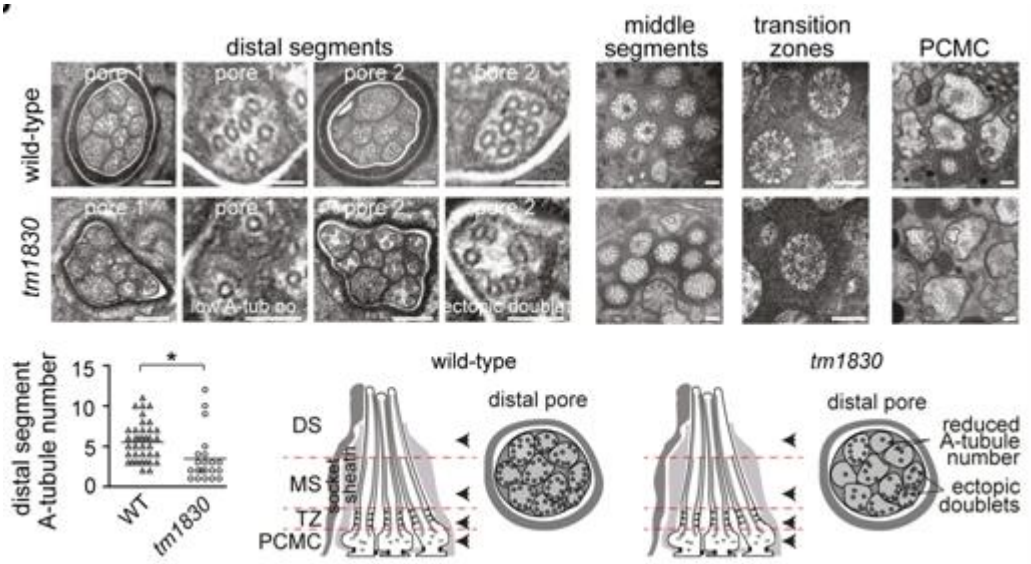

Figure 6.15. **K04F10.2 mutant worms possess defects in ciliary microtubules.** Transmission electron microscopy (TEM) of amphid channel cilia in age-matched (early day 1 adult) wild-type and K04F10.2*(tm1810)* worms. Wild type channels (pores) contain 10 ciliary axonemes, each possessing a distal segment (DS) containing singlet A-tubules, a middle segment (MS) containing doublet A/B tubules, a transition zone (TZ) with Y-link connectors, and a periciliary membrane compartment (PCMC). Images and graph show that *tm1810* mutants possess reduced numbers of distal segment A-tubules; also, ectopic microtubule doublets are sometimes observed in distal segments. Note that wild-type early day 1 adults do not possess a full complement of 9 distal segment A-tubules. Schematics show the ultrastructural phenotypes (only 3 cilia shown for simplicity in longitudinal cartoons) and the arrowheads indicate approximate regions of pore where imaged sections were captured. Distal segment images shown at low (1st and 3rd images) and high (2nd and 4th images) magnifications. Bars; 200 nm (low magnification images), 100 nm (high magnification images). *p<0.05 (t-test vs WT).

These findings are consistent with partner 1b's finding that the human K04F10.2 orthologue (KIAA0556) biochemically interacts with katanin microtubule severing proteins. It is also consistent with our finding (D6.12) that at least one katanin gene (F47G4.5; a KATNBL1 orthologue) is expressed solely in ciliated cells in *C. elegans* and encodes a protein that localises to ciliary structures. To investigate if F47G4.5 serves ciliary functions similar to K04F10.2, we

employed *ok2667*, a 570 bp deletion (spanning exons 2 and 3) that induces a frameshift. *ok2667* is therefore a likely null allele. Like K04F10.2 mutants, *ok2667* worms possess normal dye-filling, osmotic avoidance, benzaldehyde chemoattraction and foraging (figure 2A-E). However, TEM analyses revealed that one axoneme is missing from the distal regions of both *ok2667* amphid pores, and an abnormal number of axonemes possess B-tubule seam breaks (5 vs 2 axonemes in WT controls; [Jauregui 2008]) (**figure 6.16F**). Furthermore, in one *ok2667* axoneme, an A-tubule is associated with two B-tubules.

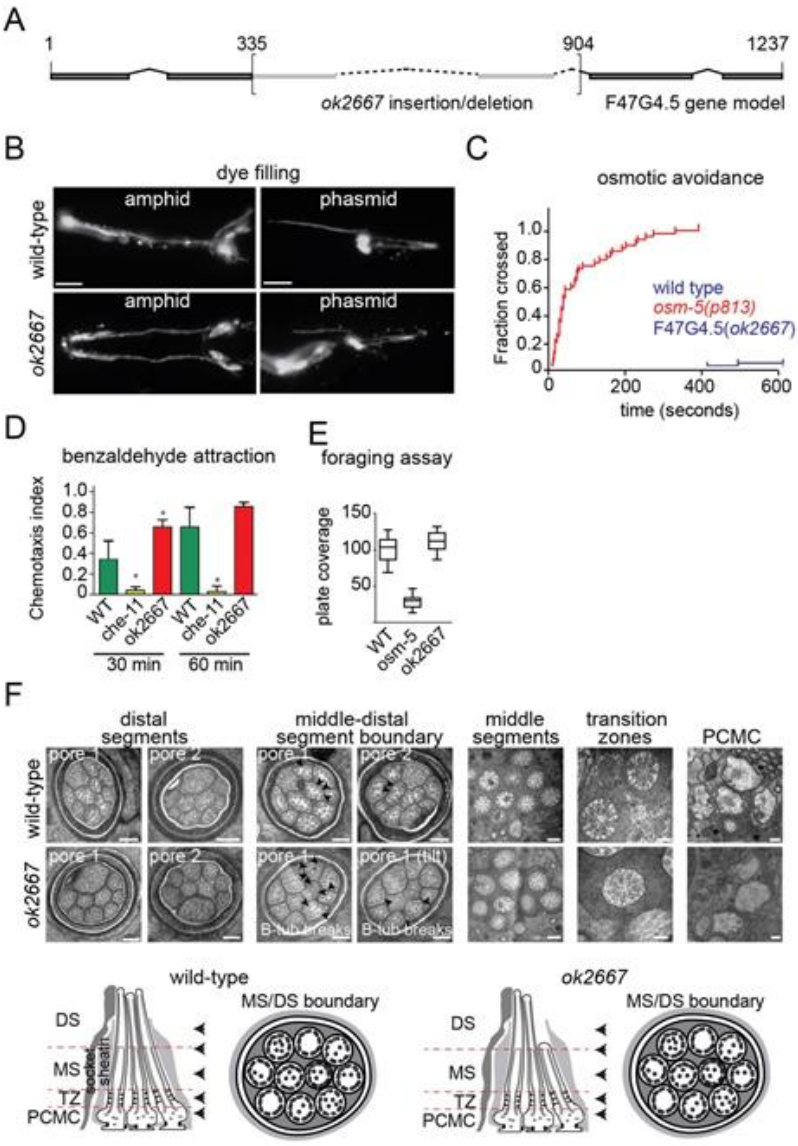

Figure 6.16 **Ciliary phenotypes in F47G4.5 (KATNBL1) mutants. (A)** Schematic of F47G4.5 gene showing the *ok2667* insertion/deletion spanning exon 2 to intron 3. Boxes define exons. Numbers indicate genomic positions relative to start codon. **(B)** F47G4.5(*ok2667*) mutants possess normal fluorescent dye (DiI) filling in amphid (head) and phasmid (tail) neurons. Bars; 15 µm (all images similarly scaled). **(C-E)** F47G4.5 mutants possess normal sensory behaviours. Shown are population-based assays for osmotic avoidance, benzaldehyde chemoattraction, and single worm assays for foraging/roaming. Chemotaxis index assayed at two time points (30 and 60 minutes). *che-11(e1810)* and *osm-5(p813)* are negative controls. **(F)** Transmission electron microscopy (TEM) of amphid channel cilia in age-matched (early day 1 adult) wild-type and *ok2667* worms. In *ok2667* worms, 9 ciliary axonemes are present in the distal pore region, indicating 1 cilium is truncated. All axonemes are present in the middle and proximal regions of *ok2667* pores. An abnormal number of *ok2667* cilia possess incomplete B-tubules (B-tub) and corresponding A-tubule seam breaks (black arrowheads), especially near the middle segment tips where B-tubules normally terminate. Schematics show the ultrastructural phenotypes (only 3 cilia shown for simplicity in longitudinal cartoons) and indicate (arrowheads) approximate regions of pore where imaged sections were taken. Bars; 200 nm. DS; distal segment, MS; middle segment; TZ; transition zone, PCMC; periciliary membrane compartment.

Since B-tubule breaks are also observed in worm and mouse models of ciliopathy genes associated with IFT [Caspary 2007; Cevik 2010; Li 2010; Jauregui 2008], we analysed IFT in *ok2667* worms using GFP reporters. Although the ciliary localisations and distributions of OSM-3/KIF17, OSM-6/IFT52, CHE-11/IFT140, and the IFT regulator ARL-13, were unaffected (**figure 6.17**), IFT rates were disrupted in *ok2667* mutants (**figure 6.17**). Specifically, the anterograde rates for OSM-6 (middle segment), CHE-11 (distal segment) and OSM-3 (distal segment) were reduced, as were the retrograde rates for all three proteins (figure 3). In contrast, the IFT rates for K04F10.2 mutants were mostly normal, although middle segment anterograde rates for OSM-6 were 10% reduced (**figure 6.17**).

These data are presented in full in D6.22. A manuscript containing data is under review with *Genome Biology*.

A

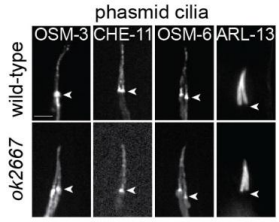

B

IFT protein	Strain	Anterograde (MS) Mean velocity /SD	n/N	t-test	Anterograde (DS) Mean velocity /SD	n/N	t-test	Retrograde Mean velocity /SD	n/N	t-test
OSM-3::GFP	wild-type	0.77/0.18	151/7		1.53/0.23	223/7		1.31/0.24	110/7	
	K04F10.2 *(tm1830)*	0.71/0.09	62/3	0.002	1.44/0.30	96/3	0.006	1.34/0.19	42/3	0.32
	F47G4.5 *(ok2667)*	0.73/0.14	341/9	0.03	1.26/0.25	372/9	<0.001	1.16/0.25	116/9	<0.001
CHE-11::GFP	wild-type	0.73/0.11	176/4		1.45/0.20	177/4		1.49/0.27	102/4	
	K04F10.2 *(tm1830)*	0.73/0.11	159/5	0.95	1.40/0.18	119/4	0.006	1.40/0.27	108/5	0.015
	F47G4.5 *(ok2667)*	0.75/0.10	69/5	0.17	1.16/0.15	59/2	<0.001	1.21/0.25	98/7	<0.001
OSM-6::GFP	wild-type	0.73/0.13	174/6		1.31/0.14	167/5		1.31/0.23	159/5	
	K04F10.2 *(tm1830)*	0.65/0.12	129/8	<0.001	1.30/0.16	151/7	0.56	1.35/0.22	147/9	0.12
	F47G4.5 *(ok2667)*	0.66/0.15	170/11	<0.001	1.26/0.28	250/11	0.023	1.13/0.21	200/11	<0.001

C

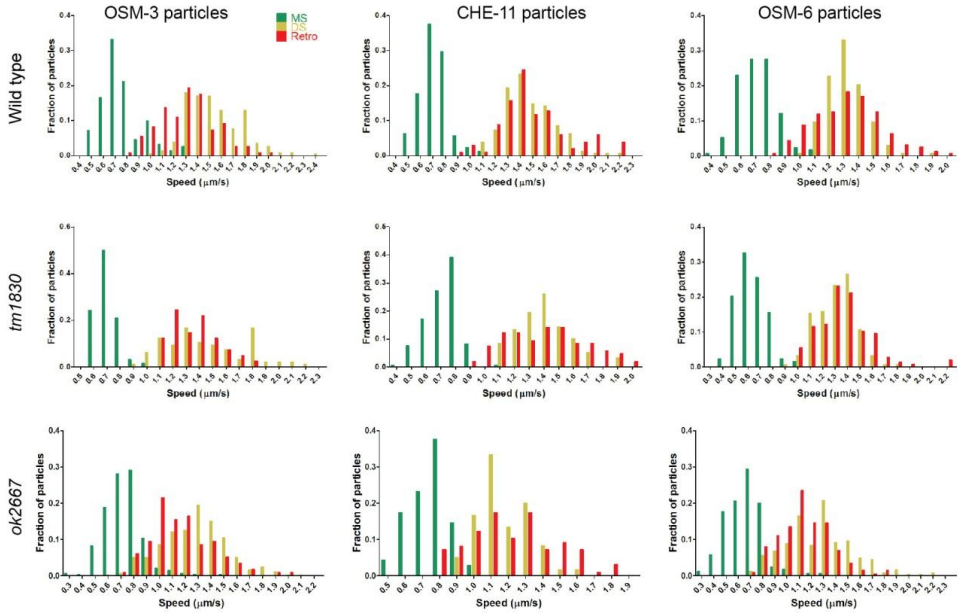

Figure 6.17 **Intraflagellar transport analyses. (A)** Ciliary localisations of GFP-tagged IFT markers OSM-3 (KIF17), CHE-11 (IFT140), OSM-6 (IFT52) and the ARL-13 (ARL13B) IFT regulator are not affected in *ok2667* mutants. Arrowheads denote ciliary base. Bar; 3 µm (all images similarly scaled). **(B)** Intraflagellar transport rates. Shown are velocities µm.s^{-1}/standard deviation (SD) of GFP-tagged IFT proteins along amphid and phasmid channel cilia. t-test; pairwise comparison with wild-type controls. n; number of particles. N; measured number of amphids and phasmids. **(C)** IFT rate profiles in wild type and mutant worms. Retro; retrograde IFT. MS; middle segment anterograde, DS; distal segment anterograde IFT.

Partner 11

Functional investigation of a novel ciliary kinesin:

We have examined a *C. elegans* kinesin-8 orthologue (*klp-13*). We find that the *klp-13* gene is expressed almost exclusively in ciliated neurons and encodes a protein that localises to the ciliary axoneme, with specific enrichment at the tip (**figure 6.18A**). However, this kinesin does not undergo IFT (**figure 6.18B**). Cilium structure is grossly normal in a *klp-13* null mutant, as measured

using dye filling, GFP markers and TEM (**figure 6.18C**; TEM and GFP marker data not shown). Also, cilia-associated sensory behaviours (benzaldehye chemoattraction; foraging/roaming) are normal in a *klp-13* mutant (**figure 6.18D**). However, we found that *klp-13* genetically interacts with *klp-11* (kinesin-2 subunit) to regulate these cilium functions (**figure 6.18D**). Efforts are ongoing to determine the functional relationshiop of klp-13 and kinesin-2.

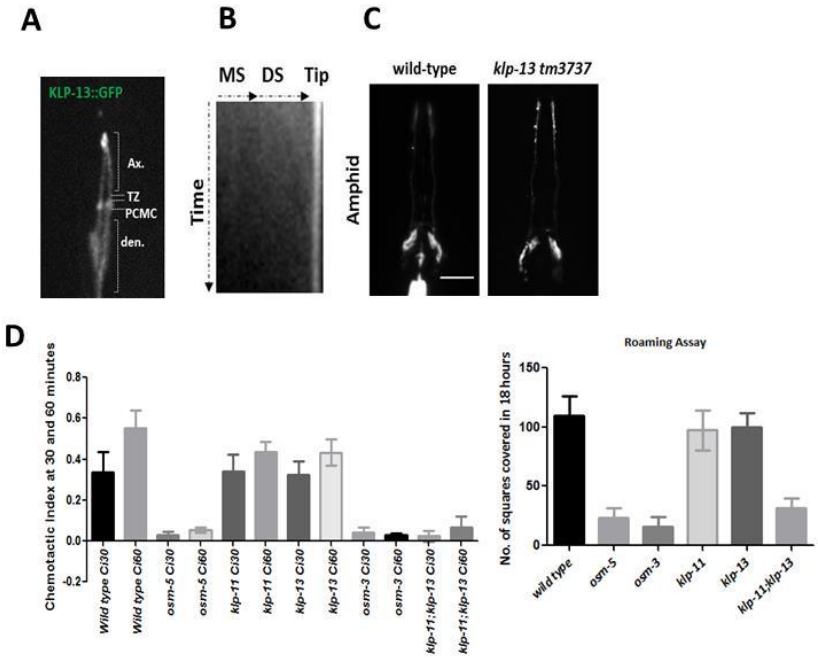

Figure 6.18 (A) GFP-tagged KLP-13 accumulates at the tip of cilia. (B) Kymograph (time vs distance plot) from a time-lapse movie of KLP-13::GFP ciliary signals in live worms. No signals can be seen to move along the ciliary axonemes. (C) Dye-filling assay showing the head region of wild-type and klp-13 mutant worms. (D) Chemotaxis (left) and roaming (right) assays.

- ***Task 6.3. Perturbation of CAMs and assessment of polarity in Xenopus, a vertebrate model***

Deliverables under this Task: D6.5 (month 24) and D6.18 (month 48) both delivered.

Partner 5:

A recent mass spectrometry (MS) analysis, using NPHP1-9, JTBS and MKS proteins as baits identified several distinct NPHP clusters, suggesting that NPHPs exert their tissue-specific function in large protein networks.

We have recently characterized a novel family member ANKS6 (NPHP16, SamCystin) in a MS screen, using NEK8/NPHP9 as bait. ANKS6, an ankyrin-repeat protein with a C-terminal sterile alpha motif (SAM) domain, was found to interact with several NPHPs, including NPHP2, NPHP3 and NPHP9 as well as with BICC1, an RNA-binding protein, which contains a C-terminal SAM domain in addition to three N-terminal K homology RNA-binding (KH) domains. A subsequent MS screen, using ANKS6 as bait, identified an ankyrin-repeat/SAM-containing protein with similar domain architecture, ANKS3, as a potential binding partner of ANKS6 and a candidate for mutations that lead to NPH or NPH-like disease.

Anks3 and Anks6 form heteromeric protein complexes, and interact with Bicc1. We validated the interaction by co-expression and immunoprecipitation analysis in HEK 293T cells. Using differentially tagged proteins (Flag, GFP, V5), we observed that the precipitation of Flag-tagged mouse Anks3 immobilized V5-tagged mouse Bicc1 (V5.Bicc1) as well as GFP-tagged rat Anks6, while precipitation of Flag-tagged Anks6 immobilized V5.Bicc1 as well as GFP-tagged Anks3. These findings confirm the previously mapped interaction between rat Anks6 and Bicc1, and suggest that the ankyrin-repeat/SAM proteins Anks3 and Anks6 engage in heteromeric protein-protein interactions with the SAM domain containing RNA-binding protein Bicc1.

To validate the endogenous interaction between Anks3 and Anks6, we generated a tetracycline-inducible Anks6-knockdown IMCD cell line. Of six different shRNAs tested, two (#1 and #5) reduced the levels of Anks6 mRNA to 10-25%. Exposure to tetracycline resulted in a disappearance of Anks6 protein levels after 3 days. Immuno-precipitation of Anks6 yielded a clearly detectable band in non-induced cells (**figure 6.19**), while little Anks6 precipitated from cells after exposure to tetracycline, and no Anks6 precipitated with a control rabbit IgG antibody. Anks3 co-precipitated with Anks6, but was not detectable in any of the other lanes. These findings demonstrate that endogenous Anks3 and Anks6 proteins form heteromeric complexes in tubular epithelial cells.

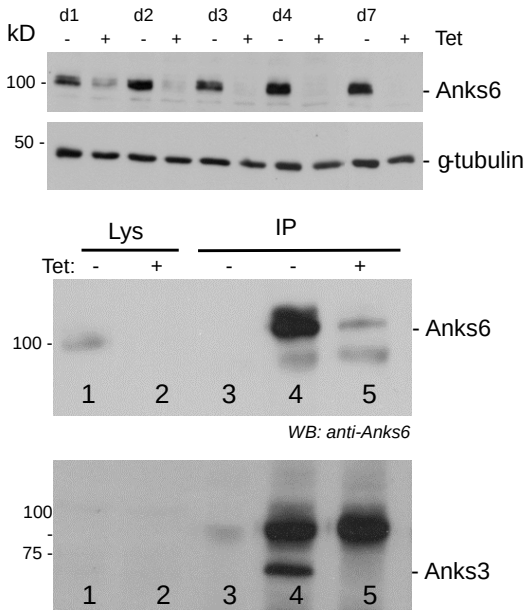

Figure 6.19. **Endogenous interaction between Anks3 and Anks6 in IMCD cells.** (top panel) Western blot analysis demonstrated the rapid depletion of Anks6 protein levels within three days after tetracycline exposure (+ Tet) in comparison to cells without (w/o) tetracycline treatment. Gamma tubulin (γ-tubulin) served as loading control. (middle panel) The mIMCD3 Anks6 shRNA cell line #1 was treated for 3 days with our without tracycline. Endogenous Anks6 was precipitated using an Anks6-specfic rabbit antiserum (lane 4 and 5). No Anks6 protein was detectable in the lysates of tetracycline-treated cells (lane 2), and little Anks6 was detectable in the lysates of untreated cells (lane1) as well as in the precipitates of treated cells (lane 5). No Anks3 was detectable in the lysates of mIMCD cells (bottom panel, lane 1 and 2). However, Anks3 protein was clearly detectable in the Anks6 precipitates (bottom panel, lane 4), but not in the tetracycline-treated, Anks6-depleted precipitates. Rabbit IgG was used a negative control (lane 3). Note that the additional bands are likely non-specific since we ruled out that the Anks6 antiserum cross-reacts with Anks3.

Anks3 interacts with the NPHP1-4-8 module. We previously found that Anks6 interacts with NPHP2, NPHP3, and NPHP9. We tested therefore whether Anks3 displays similar binding properties, co-expressing Flag-tagged Anks3 with V5-tagged NPHPs. Anks3 co-precipitated with NPHP1 and NPHP9/NEK8; weaker interactions were also observed for other NPHPs. Since NPHP1 is a member of the NPHP1-4-8 module, we examined whether Flag-tagged NPHP8 and NPHP9 differentially interact with Anks3- and Anks6-containing protein complexes. V5-tagged NPHP1 and NPHP4 were co-expressed with either V5-tagged Anks3 or Anks6. Immuno-precipitation of NPHP8 immobilized NPHP1, NPHP4, and Anks3, but failed to precipitate ANKS6. In contrast, immuno-precipitation of NPHP9 immobilized both Anks3 and Anks6. These findings suggest that the NPHP1-4-8 module preferentially interacts with Anks3. However, the recently established NPHP2-3-9-containing Anks6 module also associates with Anks3.

Anks3 interacts with HIF1AN. HIF1AN interacts with NPHP2 and ANKS6, and hydroxylates both proteins on conserved asparagine residues located within the ankyrin repeat domains. We tested therefore whether Anks3 can also serve as a substrate for HIF1AN. Anks3 contains two potential HIF1AN asparagine hydroxylation sites. Flag-tagged Anks3 precipitated V5-tagged HIF1AN in a similar fashion as Flag-tagged NPHP2 and Anks6. Furthermore, the prolyl-hydroxylase inhibitor dimethyl-oxalylglycine (DMOG) promoted the interaction between HIF1AN and its substrate Anks3 as was previously observed for ANKS6 and NPHP2. We postulated therefore that Anks3, similar to ANKS6 and NPHP2, is a HIF1AN substrate that can be hydroxylated on asparagine residues in response to changes in oxygen supply, and performed mass spectrometry on Anks3 precipitated from HEK 293T cells in the absence or presence of co-transfected HIF1AN. This experiment demonstrated a striking increase in hydroxylation at N96, while no peptide was identified at position N162. Mutational analysis of N96 (replacement of asparagine with alanine) confirmed that N96 appears to be the major target of HIF1AN in Anks3.

Anks3 depletion is associated with typical NPH-like manifestations. Since Anks3 integrates into the NPHP network and behaved in many ways identical to ANKS6, we analyzed the defects caused by anks3 depletion in zebrafish embryos (**figure 6.20**). Blast searches identified the zebrafish homolog of the human Anks3 (ENSDARG00000038557). This gene has two annotated transcripts, anks3-001 and anks3-002, which share the same set of coding exons and translation start site. We subsequently designed two different antisense morpholino oligonucleotides (MO) to deplete zebrafish anks3. One of the MOs was a splice blocking MO (SBM) and targeted the acceptor splice site of the second exon of the anks3-002 transcript (corresponds to exon 3 in anks3-001), thus depleting both transcripts. Injection of the anks3 SBM in zebrafish embryos resulted in intron inclusion with an in-frame stop codon. The second MO was a translation-blocking MO (TBM) targeting the ATG translation start site. Depletion of anks3 by either TBM or SBM resulted in formation of pronephric cysts with frequencies of 7 to 30%, as well as in body curvature defects and hydrocephalus, commonly observed after knockdown of NPH-associated genes. Concurrent knockdown of zebrafish anks6 resulted in a moderate additive effect at low MO concentrations. Patients with Anks6 mutations present with *situs inversus* and cardiac abnormalities, suggesting a role of Anks6 in motile cilia. Consistent with an involvement in body laterality, depletion of anks3 increased the frequency of *situs inversus* in developing zebrafish embryos. Although cilia were present in the zebrafish pronephros, analysis of the ciliary beating pattern within the zebrafish pronephros by time-lapse video-microscopy revealed that the motility of the cilia was either largely absent or reduced. In some cases, cilia were also beating in the wrong direction,

suggesting a disruption of the normal ciliary polarization. Collectively, these data establish Anks3 as a cilia-associated molecule.

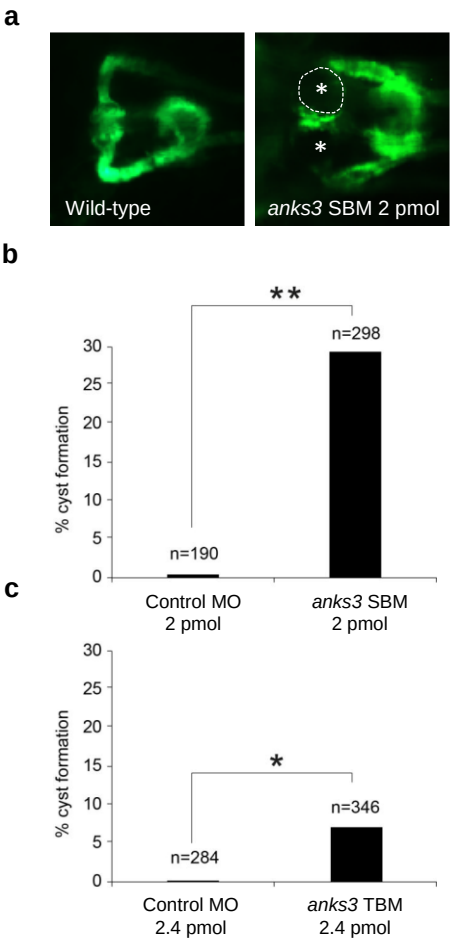

Figure 6.20. **Anks3 depletion in zebrafish by morpholino injection results in cyst formation.** (**a**) An example of pronephric cyst formation in the zebrafish embryo after morpholino oligonucleotide (MO)-induced knockdown of zebrafish anks3 (stars in the right panel) compared to the normal morphology of an embryo injected with control morpholino (left panel). The transgenic zebrafish line Wt1b::GFP, which labels the proximal tubules, was used. The cyst in the upper pronephric tubule is outlined by a dashed white line. Both cysts are marked by asterisks. (**b**) Quantification of the pronephric cyst formation at 48 hours post fertilization caused by the anks3 depletion after injection of a splice-blocking MO (SBM); n is the total number of scored embryos (**, p ≤0.01, two-tailed Student's t-test). (**c**) Quantification of the pronephric cyst formation caused by the anks3 depletion after injection of a translation-blocking MO (TBM) injection; n is the total number of scored embryos (*, p ≤0.05, two-tailed Student's t-test).

NPHP1 prevents Anks3 aggregation. Since the analysis of cilia-associated Anks3 is limited by the availability of antibodies that detect Anks3 by immunohistochemistry in vivo, we resorted to epidermis of *Xenopus* embryos (**figure 6.21**). When we analyzed the localization of GFP-tagged Anks3 in the motile cilia of these multi-ciliated cells, we found that the GFP-Anks3 fusion co-localized with the basal bodies marked by RFP-Centrin. Noticeably, each multi-ciliated epidermal cell contained multiple bright GFP-positive small spots as well as a few large GFP-Anks3 aggregates. Although GFP can engage in homodimeric interactions, we did not observe these fluorescent spots for GFP alone or other GFP-NPHP fusion proteins, suggesting that this finding represents a specific property of the GFP-Anks3 fusion consistent with the previously reported

tendency of Anks3 to form polymers *in vivo*. Hence, we concluded that the bright GFP-Anks3 speckles as well as the large aggregates likely represent Anks3 polymers. Knockdown of NPHP1 resulted in a mild disruption of GFP-Anks3 co-localization with the basal bodies, i.e. not every basal body was decorated with GFP-Anks3. However, more strikingly, the knockdown of *Xenopus* NPHP1 dramatically increased the accumulation of GFP-Anks3 aggregates, while the knockdown of *Xenopus* NPHP2 had no effect. These findings suggest that components of the NPHP1-4-8 module might interact with Anks3 to prevent polymerization of this protein. Supporting this hypothesis, the fusion of a negatively charged GFP (net charge: -30) reduced the formation of Anks3 aggregates. Furthermore, increased concentrations of micro-injected NPHP1 reduced the number of GFP-Anks3 aggregates consistent with our hypothesis. It is conceivable that some degree of Anks3-polymer formation is required for normal basal body function. However, since knockdown of anks3 in the zebrafish embryo disrupted both motility as well as polarity, Anks3 polymerization may provide the structural support required for correct polarization and beating of cilia.

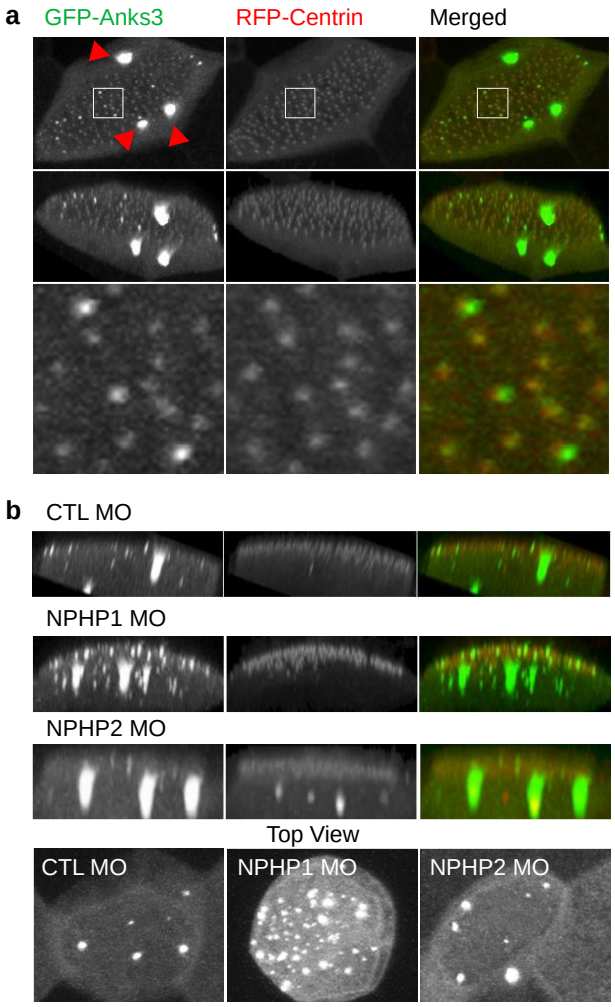

Figure 6.21. **Basal body localization and aggregate formation of GFP-Anks3 in multi-ciliated cells of the Xenopus epidermis.** (a) GFP-tagged Anks3 (green) localized to the RFP-Centrin labeled basal bodies (red). Multiple bright spots were noticeable in the GFP-Anks3-expression multi-ciliated epidermal cells, but for example, not in the neighboring cells. In addition, large GFP-Anks3 aggregates (red arrow heads) occurred in smaller numbers, the depicted cell shows three such aggregates (top panels: maximum intensity projection of confocal images, middle panels: 3D reconstruction, bottom panels: magnified images of the area indicated by white boxes). (b) Depletion of *Xenopus* NPHP1 increased the number of the small and large GFP-Anks3 aggregates, while depletion of *Xenopus* NPHP2 had no significant effect. Shown are serial confocal images, projected in the x-z plane, and a top view.

➢ ***Task 6.4. Perturbation of CAMs in zebrafish, a vertebrate model***

Deliverables under this Task: D6.7 (month 24), D6.11 (month 30), D6.13 (month 36), D6.15 (month 42), D6.23 (month 54), D6.24 (month 54) and D6.25 (month 54) all delivered.

Partner 1b:

We initiated an investigation of SPAG5 in relation to retinal dystrophies. A candidate variant in *SPAG5* was identified by dr. Mohammad Imran Kahn, in the group of prof. F. Cremers (dept Human Genetics, Radboud University Medical Center). We have previously identified SPAG5 as a direct interaction partner of USH2A (causative for Usher syndrome type 2; Kersten et al 2012 PMID23351521). Morpholino knockdown of *spag5* in zebrafish results in smaller eyes (**figure 6.22**) and a curved body axis. Our collaborators from the group of prof. M. Westerfied (University of Oregon, Eugene, USA) demonstrated that the retina of spag5 morphants has decreased immunoreactivity for the cone-marker Zpr1. In addition, we observed an increased number of apoptotic photoreceptors in the morphant retina through anti-active caspase 3 immunohistochemistry.

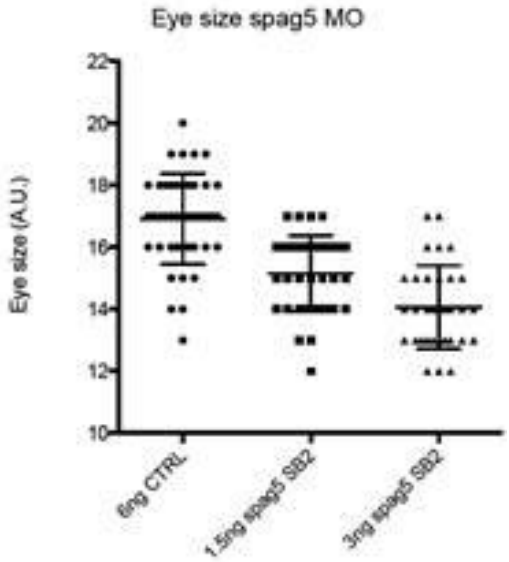

Figure 6.22. Knockdown of *spag5* decreases eye size in zebrafish larvae. Compared to control injected larvae, injection of 1.5 ng or 3 ng splice-blocking morpholino (SB2) markedly decreased the size of the eyes of 4dpf zebrafish larvae.

We assessed the visual acuity of the *spag5* morphants via optokinetic reflex measurements (**figure 6.23**). We are currently working on the validation of the phenotype via mRNA rescue experiments and an additional morpholino.

Figure 6.23: **Optokinetic reflex measurements of 5-day-old spag5 morphants**. The results are expressed as the percentage of stimuli to which the larvae responded with an eye movement. On average, control injected animals followed 60% of stimuli, while most spag5 morphants did not respond at all. For the mRNA rescue group (right panel), two morphologically normal and two morphologically affected morphants were selected. As expected, the morphologically normal larvae display an optokinetic reflex.

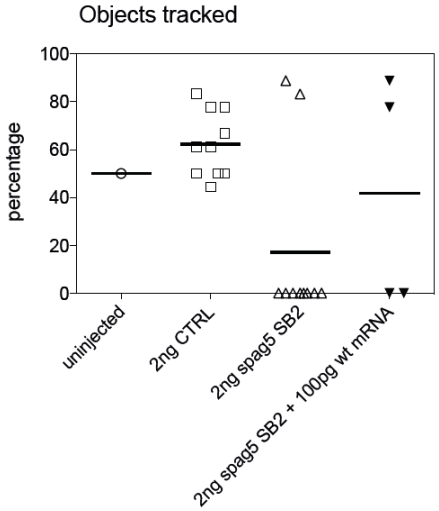

In a study on the Joubert-gene *AHI1*, partner 1b collaborates with partner 1a and Prof. F. Cremers. Candidate variants in *AHI1* were previously identified in patients with non-syndromic inherited retinal degeneration (IRD) by the groups of prof. F. Cremers and dr. A. Webster (University College London, London, UK) and by Huang et al 2014 (PMID: 25356976). Via co-injection of wildtype and variant *AHI1* mRNA in Ahi1 morphants, we planned to assess whether the identified missense variants in *AHI1* indeed are likely to be causative for non-syndromic IRD. To do so, we first tried to establish the phenotype caused by Ahi1 knockdown in zebrafish. It proved difficult to reproduce the results previously published by Simms et al (PMID 21959375). Since we were not able to detect the alternative splicing of the ahi1 gene with the morpholinos used by Simms et al, we dsigned and ordered new morpholinos which we validated for alternative splicing and a Joubert-like phenotype. The new morpholinos were shown to be successful in redirecting ahi1 pre-mRNA splicing and did result in a Joubert like phenotype. Morphants displayed curved body axis, cardiac and brain oedema as well as dilated pronephric ducts. However, specificity of this phenotype could so far not be validated by co-injection of wildtype human mRNA. In the work of Simms et al, rescue studies were done with murine mRNA, but since it is our desire to test human variants associated with inherited retinal diseases, we are limited to human mRNA.

An exciting module that we have under investigation is the Cop9 signalosome. A set of Cop9 subunits were identified in tandem affinity purification studies and yeast two-hybrid screens of several USH proteins. Partner 1b has previously reported this in WP1. Cop9 signalosome subunit 8 (COPS8/CSN8) was identified as a direct interaction partner of USH2A. Preliminary results of Csn8 knockdown are indicative of a specific retinal phenotype. Size of the morphants eyes is reduced, and formation of photoreceptor outer segments is severely impaired (**figure 6.24**). Although these promising results in morphants, we decided to generate a mutant zebrafish because of the trend in zebrafish research towards the use of mutants instead of morpholino-based knockdown of genes of interest.

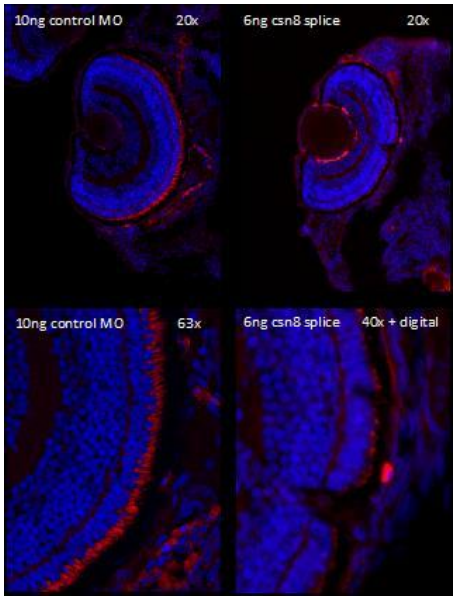

Figure 6.24. Knockdown of Csn8 decreases the length of photoreceptor outer segments.

Cryosections are made of control injected (10ng) or csn8 splice MO injected (6ng) larvae at 4dpf. Outer segments were stained in red with bodipy and nuclei are stained with DAPI (blue). Compared to controls, the eyes of csn8 morphants are smaller (top panels). At higher magnification (bottom panels), it is evident that the length of the outer segments is decreased, while photoreceptor nuclei and retinal lamination remains intact.

For COPS8/CSN8 we decided to generate a knockout zebrafish that we can breed with several of our *ush2a* mutant fish. Via the CRIPSR-Cas9 system, we were able to mutate the 4th exon of *cops8*. We recently identified one fish with a frameshift mutation (resulting in a premature stop-codon) in its germline. We will maintain this line to characterize these mutants in homozygous offspring.

Next to our zebrafish *ush2a* mutants have been crossed to homozygous mutant fish. First analysis of these fish point towards a ERG response to light stimuli and increased presence of (yet uncharacterized) vesicles in the photoreceptor inner segments (shown by tEM). We are currently testing markers for immunohistochemistry on zebrafish retina's in order to identify the nature of these vesicles.

Partner 8:

We disrupted a novel nephronophthisis gene, DCDC2, in zebrafish (**figure 6.25**). Knockdown of dcdc2 in zebrafish recapitulates the nephronophthisis-related ciliopathy phenotype (NPHP-RC) found in patients, including renal cysts and hydrocephalus, which is rescued by aWnt inhibitor and by WT, but not by mutant, DCDC2.We thus demonstrate a central role of Wnt signaling in the pathogenesis of NPHP-RC, suggesting an avenue for potential treatment of NPHP-RC. The paper has been published in the American Journal of Human Genetics.

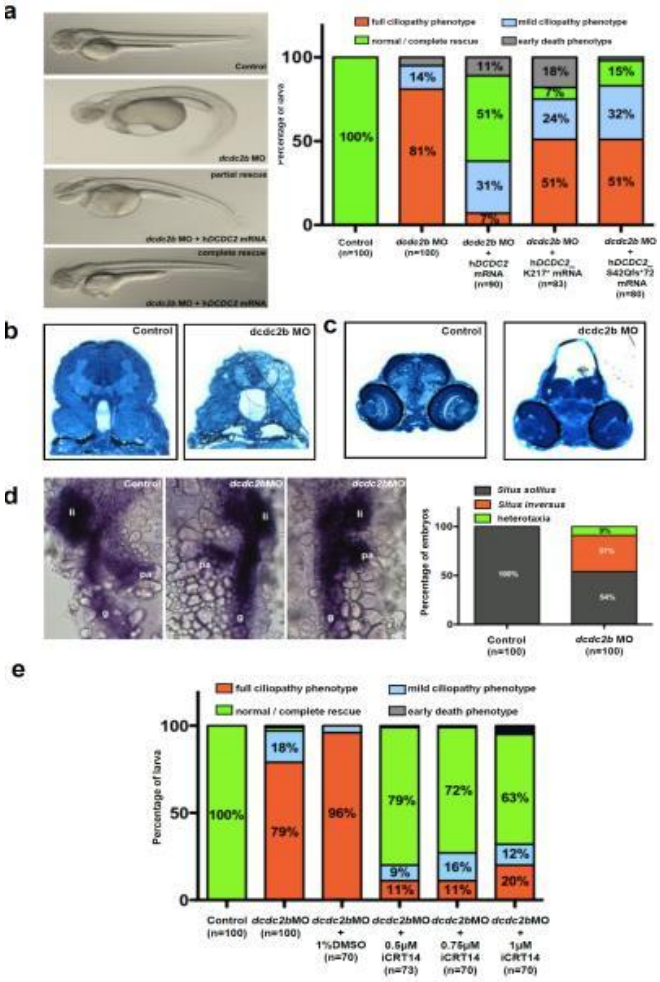

***Figure 6.25*. MO knockdown of *dcdc2b* replicates ciliopathy phenotypes in zebrafish that cannot be rescued by cDNA clones representing human ciliopathy mutants**. (**a**) Zebrafish embryos injected with AUGMO at one-cell stage produced defects characteristic of cilia dysfunction. Lateral view of 2 days old control and morphant embryos. *dcdc2b* morphant developed ventrally bent body axis, hydrocephalus, tail kinks and pericardial edema. Morphologically visible ciliopathy phenotypes in *dcdc2b* morphants were completely or partially rescued by coinjection of 5'capped mRNA of wild-type human *DCDC2*. Coinjection of AUGMO with capped mRNA of either of the two human DCDC2 mutant clones h*DCDC2_K217** or h*DCDC2_S42Qfs*72* did not completely rescue ciliary defects. (**b**) Histological sections of pronephros of control and morphant embryo at 3.5 dpf. *dcdc2b* morphants clearly showed dilation of the pronephric duct as compared with control embryos. (**c**) Transverse brain sections showed hydrocephalus in *dcdc2b* morphants as compared with control brain sections. (**d**) Quantification of left-right asymmetry defects in liver, gut and pancreas as visualized by in situ hydridization for the expression of *foxa3*. (**e**) Treatment with β-catenin inhibitor iCRT14 within the dose range of 500 nM-1 µM rescued *dcdc2b* knockdown cilia phenotypes in the morphants. Abbreviations: li, liver; pa, pancreas; g, gut. Graphs are representation of two or three independent experiments.

Partner 9:

Zebrafish models of JATD

Cep120 (Published in Human Molecular Genetics (2014)).

Inhibition of the *CEP120* ortholog in zebrafish produced phenotypes characteristic of other ciliary morphants including abnormal body curvature, hydrocephalus, otolith defects and abnormal renal, head and craniofacial development. Cilia length was reduced in the neural tube of Cep *CEP120* morphants, and the pronephric cilia appear disorganised. These results are consistent with the finding that CEP120 is a causative gene in the skeletal ciliopathy JATD.

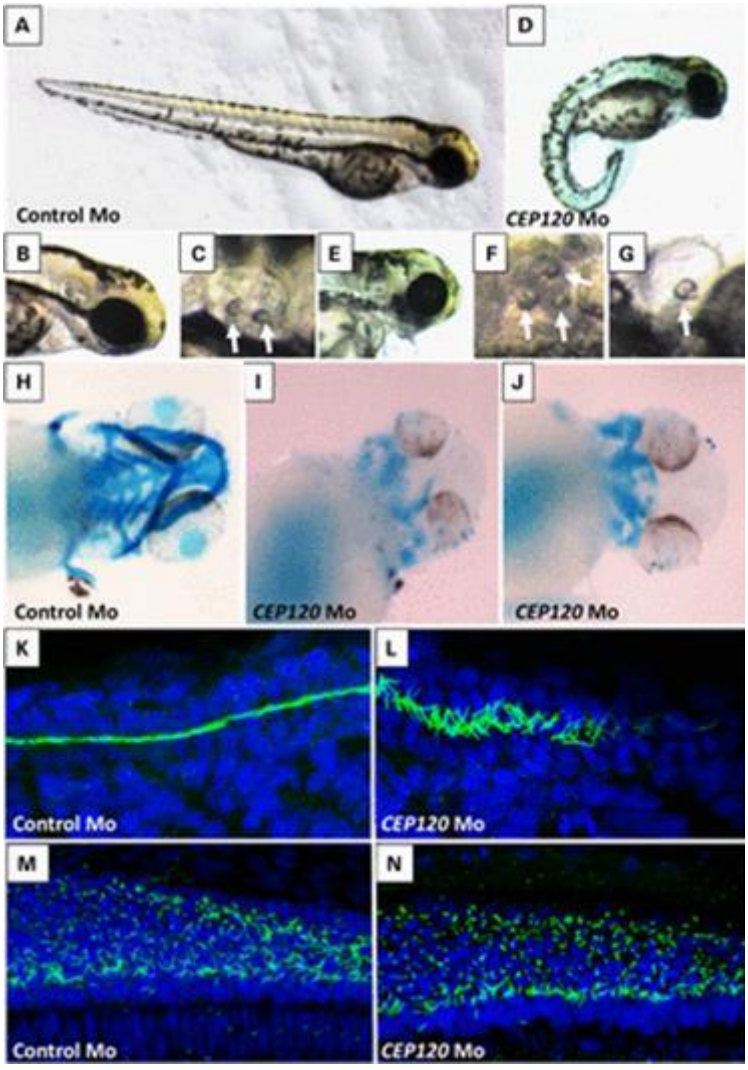

Figure 6.26 **Knockdown CEP120 ortholog in ZF results in typical ciliopathies associated phenotypes in ZF.** Injection of *CEP120* antisense morpholino oligonucleotide resulting in centrally curved tail (**D**), hydrocephalus (**E**), otolith defects (**F** and **G**) and craniofacial defects (**I** and **J**) compared with control morpholino-injected embryos (**A**, **B**, **C** and **H**). Visualization of cilia using anti-acetylated tubulin in *CEP120*-injected embryos showing disorganized cilia in the pronephros (**L**) and shorter cilia in the neural tube (**N**) compared with controls (**K** and **M**).

C21orf2 (Published in Nature Cell Biology, 2015)

C21orf2 is a JATD model that shows classic phenotypes including curved tail, hydrocephalus and abnormal otolith numbers and also shows genetic epistasis with Nek1 which is known to be causative in skeletal ciliopathies (**figure 6.27 A-H**). C21orf2 mutants show craniofacial abnormalities characteristic of skeletal ciliopathy models (**figure 6.27 I-P**).

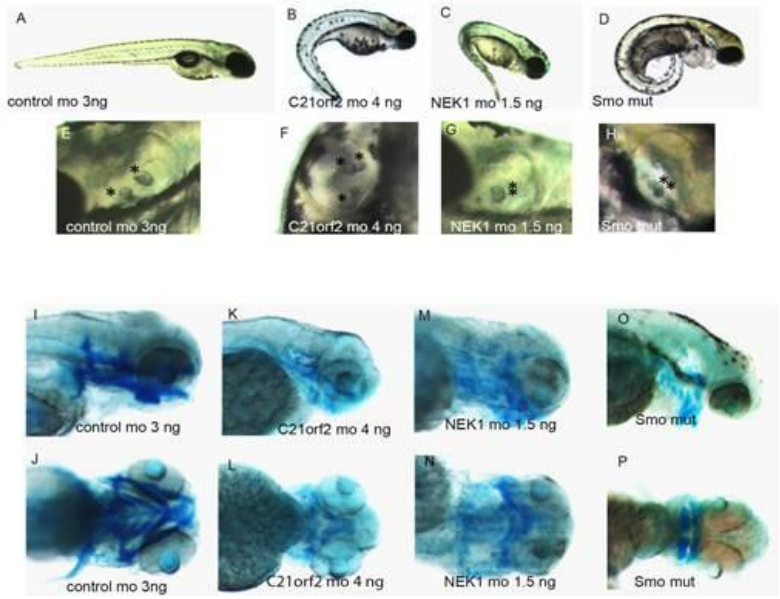

***Figure 6.27* zebrafish phenotypes for C21orf2 mutants.**

These morphants show loss of photoreceptor cell layer and a ciliogenesis defect in the retina (**figure 6.28 A-G**).

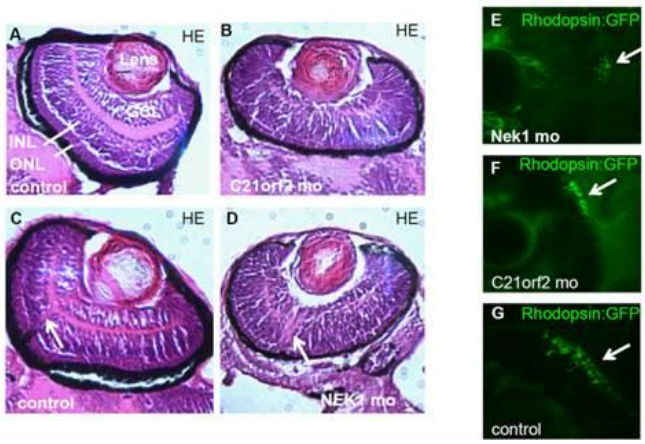

Figure 6.28

Ciliation in the pronephros is disorganised (**figure 6.29 H-K**)

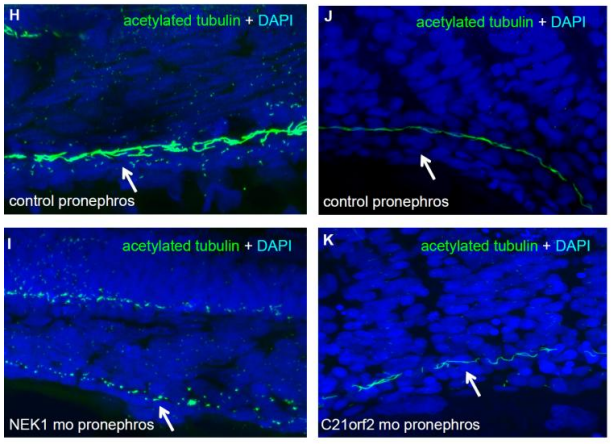

Figure 6.29

TCTEX1D2 (Published in Nature Communications,2015).

Knockdown of TCTEX1D2 leads to classic ciliopathy phenotypes in zebrafish, including curved tail, renal cysts, hydrocephalus, abnormal otolith numbers, craniofacial cartilage abnormalities and shorter pronephric cilia (**figure 6.30**).

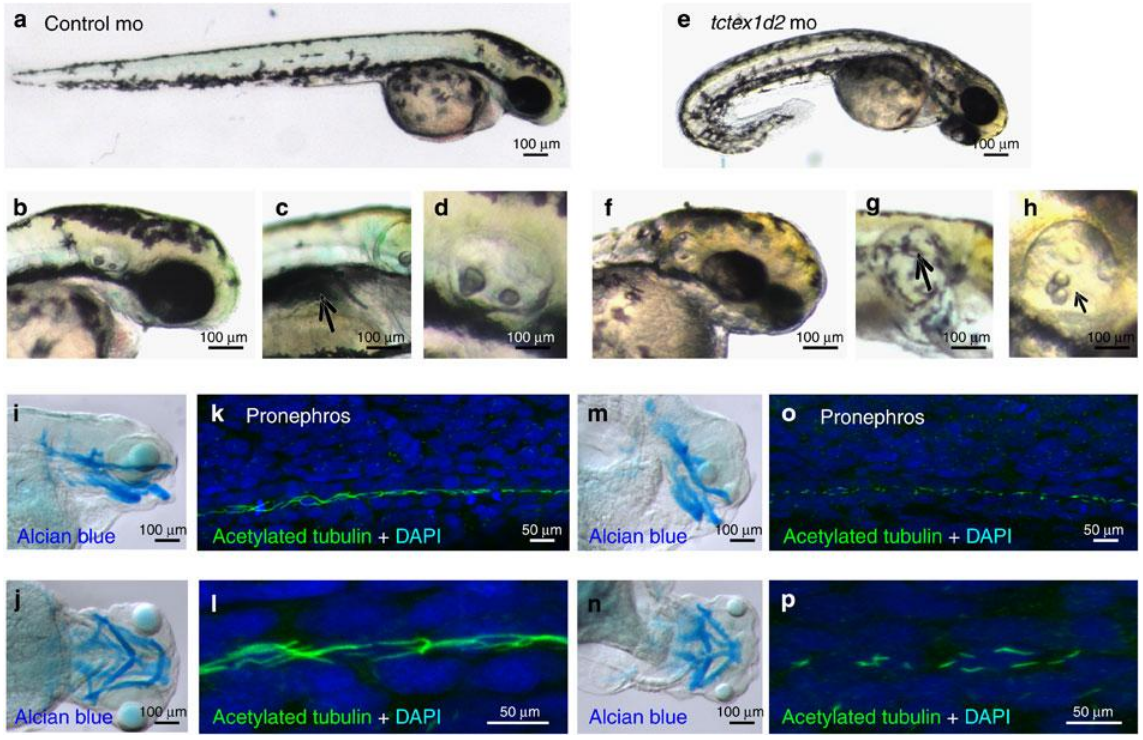

Figure 6.30 Whole-mount light microscopy showing control morpholino (mo)-injected embryos (**a**–**d**) and *tctex1d2* morphants at 4 days post fertilization (**e**–**h**). Compared with controls, knockdown of *tctex1d2* results in ventrally curved body axis (**a**,**e**), small eyes **(b**,**f**), pronephric cysts (**c**,**g**) and otolith defects (**d**,**h**). Alcian blue staining of cartilage identifies craniofacial cartilage defects in *tctexd2* morphants (**m**,**n**) compared with controls (**i**,**j**). Immunofluorescence analysis after staining of cilia at 24 h.p.f. with anti-acetylated tubulin antibody reveals shorter cilia in the pronephric duct of *tctex1d2* morphants (**o**, magnified in **p**) compared with control embryos (**k**, magnified in **l**); however, this difference was no longer evident at 48 h.p.f. (data not shown). Scale bars, 100 µm (**a**–**j**,**m**,**n**) or 50 µm (**k**,**l**,**o**,**p**).

Partner 9:

Functional analysis of Oscp1

Oscp1 Knockdown in zebrafish: An exon 4 splice site morpholino has generated fish showing phenotypes indicative of ciliary involvement, namely small eyes, small head, body curvature, disorganised pronephric duct cilia (**figures 6.31 and 6.32**). Work is ongoing to investigate the phenotypes more fully for publication with the Baysian dataset.

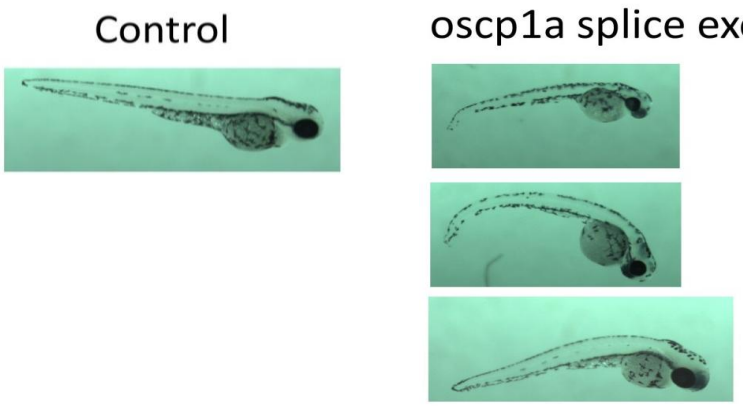

Figure 6.31

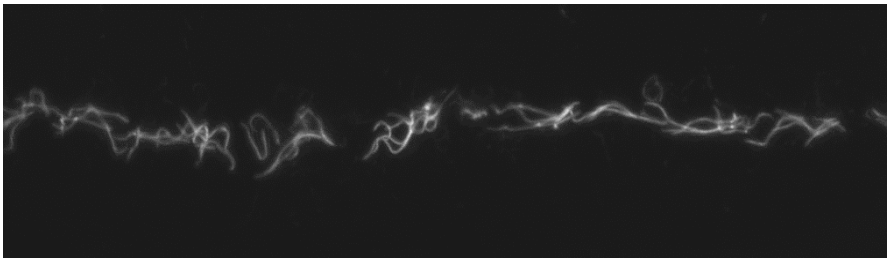

Oscp1 pronephric duct cilia

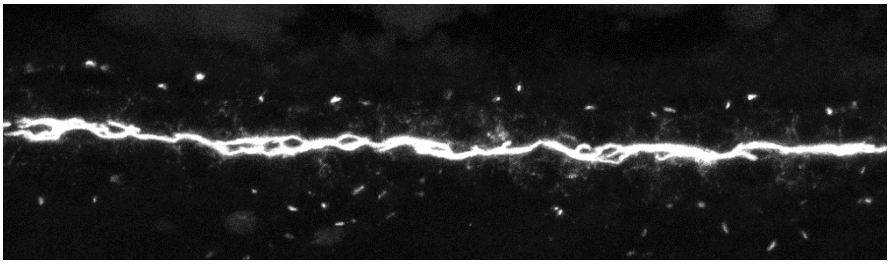

WT pronephric duct cilia

Figure 6.32

Localisation of Oscp1 in mammalian cell lines using commercially available antibodies. To look at possible ciliary localisation of Oscp1 in mammalian cell lines three commercially available antibodies were obtained. These were used to stain serum starved IMDC3 (murine collecting duct) and ATDC5 (murine pre chondrocyte) cell lines available in the lab of partner 9.

The Biorbyt antibody failed to show any ciliary specific localisation in either ATDC5 or IMCD3. Both other antibodies showed similar localisation patterns to each other. In ATDC5 cells (**figure 6.33**) there was ubiquitous punctate cytoplasmic staining but also regions of localisation at or near the basal body probably in the transition zone and in a very weak way as a punctate stain along the axoneme. In IMCD3 (**figure 6.34**) the majority of staining is again ubiquitous punctate

cytoplasmic. However in these cells a ciliary localisation is also observed - the basal body or transition zone stain is less apparent or missing but the axonemal stain is stronger especially using the proteintech antibody.

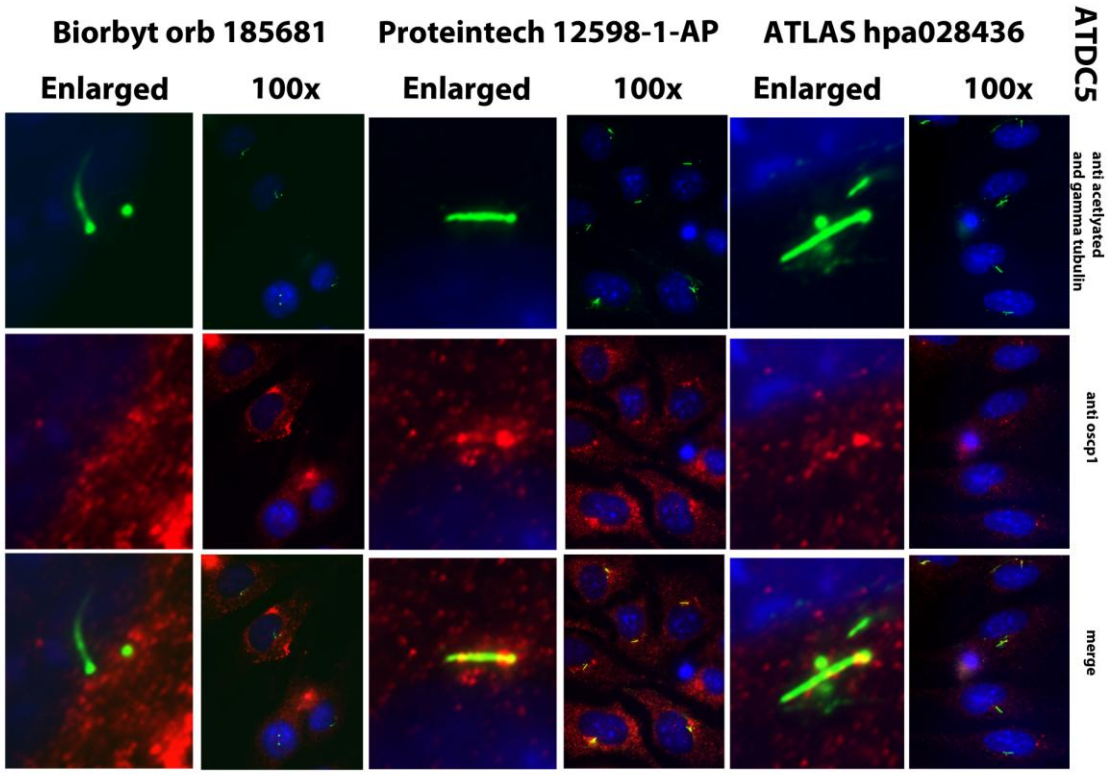

Figure 6.33 **Localisation of Oscp1 in ATDC5 cells using commercially available antibodies.**

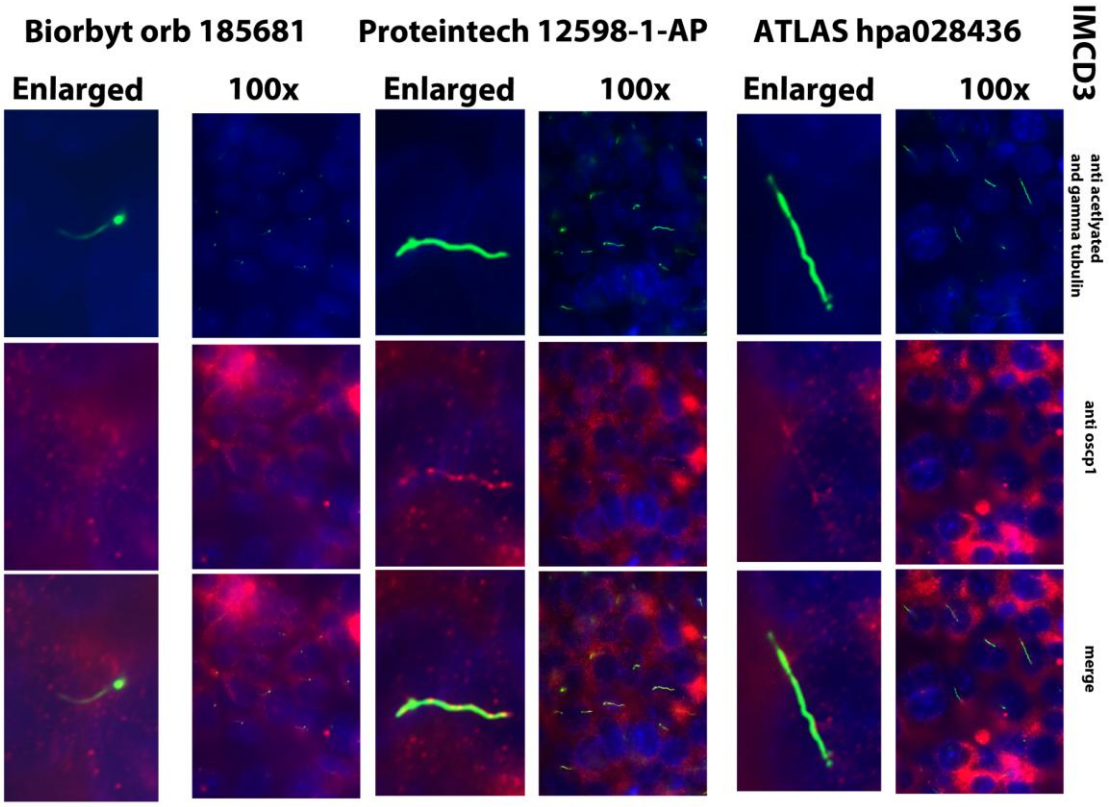

Figure 6.34 **Localisation of Oscp1 in IMCD3 cells using commercially available antibodies.**

Oscp1 knockdown in IMCD3 cells using lentivirally expressed shRNA. To look at the effect of Oscp1 knockdown in mammalian cell lines three different shRNAs targeting murine OSCP1 were obtained (vh1-3) and one scrambled (vh4) and one empty vector (empty) were used as controls. Cells were incubated with the virus and then Puromycin selected to give stable colonies of knockdown cells. Each of the three shRNAs was used separately and in combination to determine which worked with the highest efficacy (**figure 6.35**). VH2 was chosen as it showed a knockdown of around 40% in this initial experiment.

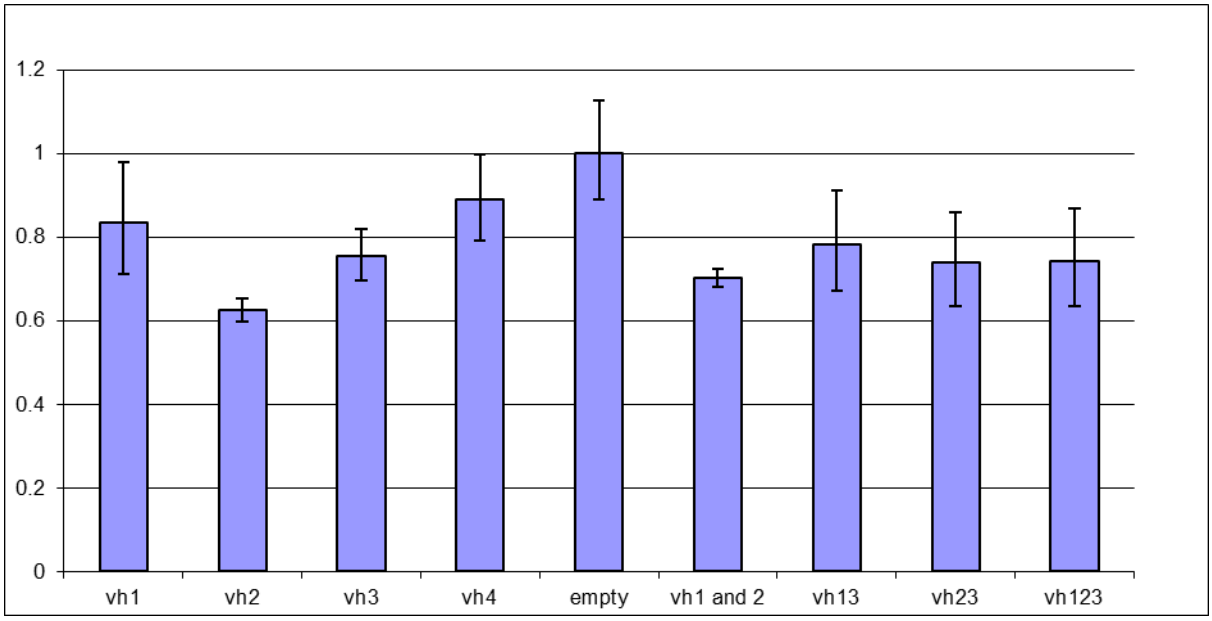

Figure 6.35 **Relative expression of Oscp1 in each shRNA transfected cell line. Values shown are arbitrary units relative to the level of expression in the empty vector control.**

As a quick readout to see the rough level of oscp1 expression relative to other ciliary genes a BBS1 primer set routinely used in the lab was also included in the realtime experiment. Surprisingly the expression of BBS1 seemed to roughly correlate with the expression level of Oscp1 (**figure 6.36**).

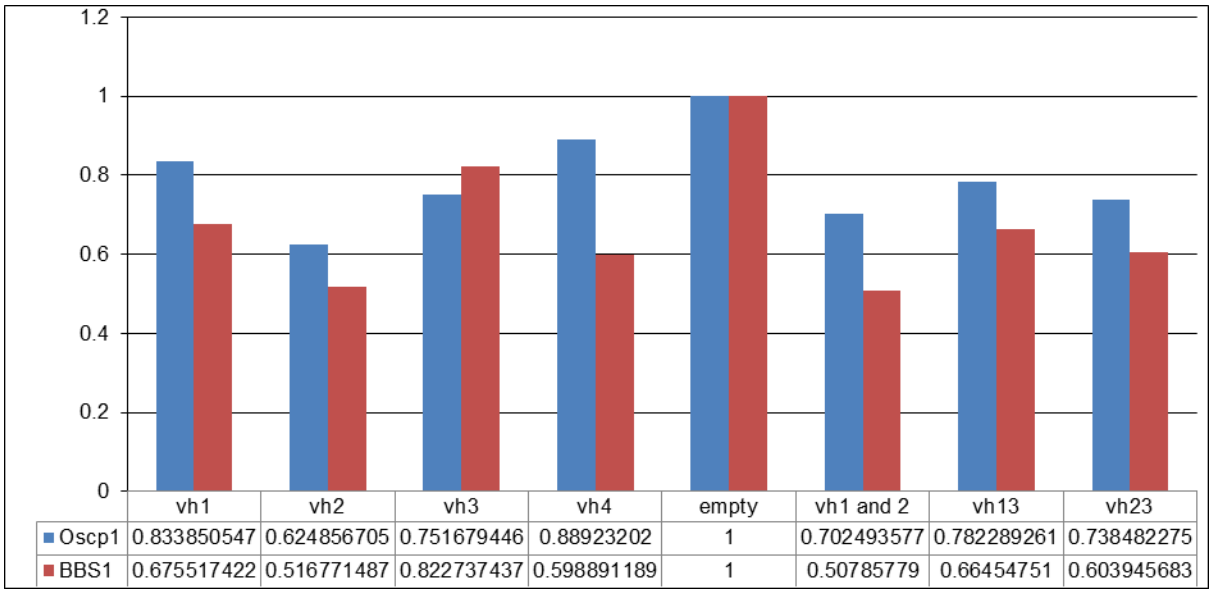

	vh1	vh2	vh3	vh4	empty	vh1 and 2	vh13	vh23
Oscp1	0.833850547	0.624856705	0.751679446	0.88923202	1	0.702493577	0.782289261	0.738482275
BBS1	0.675517422	0.516771487	0.822737437	0.598891189	1	0.50785779	0.66454751	0.603945683

Figure 6.36

Further RNA samples were taken from the VH2 cell line at three different timepoints after Puromycin selection to check if the level of knockdown Oscp1 was consistent. BBS1 and a range of other BBS gene primer sets were used to check if the apparent correlation between Oscp1 and BBS1 expression levels was replicable or if it had been an aberrant result (**figure 6.37**).

In all three replicates the level of Oscp1 is reduced in the VH2 sample but not to such a great extent as in the initial experiment with levels of between 75 and 85% of the level in the empty vector control. This small reduction is unlikely to be biologically relevant. Unfortunately the levels of Oscp1 expression are also affected in the scrambled control suggesting this may not be a specific effect. Interestingly many of the BBS genes not just BBS1 appear to be affected in a similar manner to Oscp1 in these cell lines. This would be interesting to follow up if we could get a better level of knockdown with Oscp1. Due to the lack of replicability of these experiments this section of the project was halted.

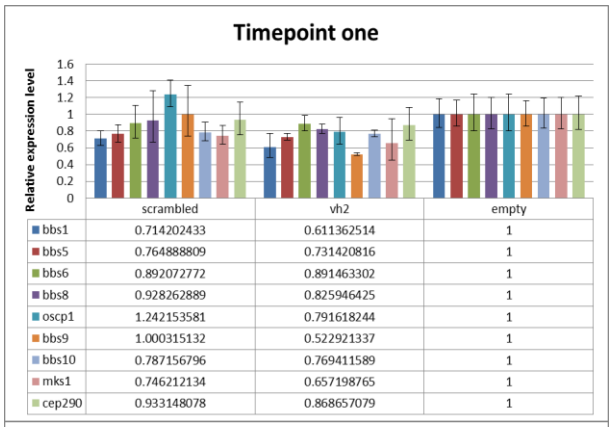

	scrambled	vh2	empty
bbs1	0.714202433	0.611362514	1
bbs5	0.764888809	0.731420816	1
bbs6	0.892072772	0.891463302	1
bbs8	0.928262889	0.825946425	1
oscp1	1.242153581	0.791618244	1
bbs9	1.000315132	0.522921337	1
bbs10	0.787156796	0.769411589	1
mks1	0.746212134	0.657198765	1
cep290	0.933148078	0.868657079	1

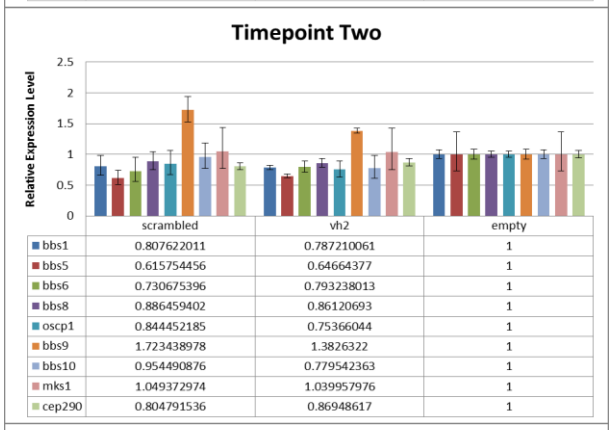

	scrambled	vh2	empty
bbs1	0.807622011	0.787210061	1
bbs5	0.615754456	0.64664377	1
bbs6	0.730675396	0.793238013	1
bbs8	0.886459402	0.86120693	1
oscp1	0.844452185	0.75366044	1
bbs9	1.723438978	1.3826322	1
bbs10	0.954490876	0.779542363	1
mks1	1.049372974	1.039957976	1
cep290	0.804791536	0.86948617	1

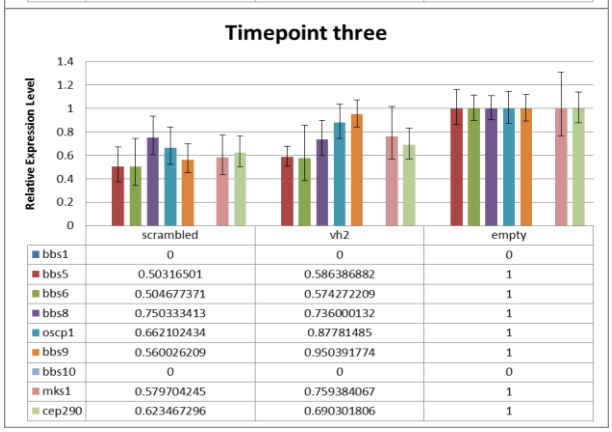

	scrambled	vh2	empty
bbs1	0	0	0
bbs5	0.50316501	0.586386882	1
bbs6	0.504677371	0.574272209	1
bbs8	0.750333413	0.736000132	1
oscp1	0.662102434	0.87781485	1
bbs9	0.560026209	0.950391774	1
bbs10	0	0	0
mks1	0.579704245	0.759384067	1
cep290	0.623467296	0.690301806	1

Figure 6.37

Partner 9:

CRISPR mediated generation of mutant zebrafish

The use of morpholinos has become controversial over the timecourse of the SYSCILIA project. At the current time publications based solely on morpholino models are unlikely to be accepted for publication. As such, a new efficient and reliable method to generate zebrafish models for genes of interest was sought. The recently developed CRISPR/Cas9 system has quickly become a trusted technique in the field and as such was an ideal avenue to pursue. To establish the technique in the lab and test its efficacy two initial candidates were chosen based on their relevance to SYSCILIA and to our current research interests.

Choice of Initial Candidates

As part of the SYSCILIA consortia efforts, protein-protein interactions involving many/most ciliary proteins have been mapped. We were specifically interested in two ciliopathy genes, *IFT80* and *RAB23*, which our group has found to be mutated in Jeune and Carpenter syndromes, respectively. IFT80- and RAB23-TAP has been undertaken, and novel protein interactions identified within SYSCILIA. One protein that we became particularly interested in from this work is NUDC, a novel interactor with IFT80. In this project we undertook genome-editing, using the CRISPR/Cas 9 system, to set the stage for future functional studies on *rab23* and *nudc* in zebrafish. We have generated gene specific mutations to yield both heterozygous and biallelic mutants in a select set of genes.

We defined two main objectives for the present study. (1) To establish and optimize the CRISPR/Cas9 technique in zebrafish for *rab23* and *nudc* genes, and to test different methods for detection of the induced mutations. (2)To analyse the phenotype(s) if any, of the mutants generated and to compare them with previously described phenotypes from morpholino-based experiments.

Design of the sgRNAs

The selection of the sgRNA sequence in the gene of interest is performed essentially according to established criteria. The target sites conform to the sequence 5'-GG (N19) GG-3'. In the 5'>3' orientation we chose Oligo 1 as: TAGG (N1-N18) and Oligo 2 as: AAAC (N18-N1), the latter in the reverse/complement. The list of different sgRNAs for both *rab23* and *nudc* that we have designed are shown in **table 6.1.**

Table 6.1

Target gene	Target site(5'>3' PAM is underlined)	Oligonucleotide 1 (5'>3')	Oligonucleotide 2 (5'>3')
Rab23	GGACATGGAGGTGGCCATCAAGG	**TAGG**ACATGGAGGTGGCCATCA	**AAAC**TGATGGCCACCTCCATGT
2	GGAGGTGGCCATCAAGGTGGTGG	**TAGG**AGGTGGCCATCAAGGTGG	**AAAC**CCACCTTGATGGCCACCT
3	GGTGGCCATCAAGGTGGTGGTGG	**TAGG**TGGCCATCAAGGTGGTGG	**AAAC**CCACCACCTTGATGGCCA
4	GGCCATCAAGGTGGTGGTGGTGG	**TAGG**CCATCAAGGTGGTGGTGG	**AAAC**CCACCACCACCTTGATGG
5	GGTGGTGGGAAACGGAGCGGTGG	**TAGG**TGGTGGGAAACGGAGCGG	**AAAC**CCGCTCCGTTTCCCACCA
6	GGACGTCAGACTGATGTTGTGGG	**TAGG**ACGTCAGACTGATGTTGT	**AAAC**ACAACATCAGTCTGACGT
7	GGAGAAGGTGGAGATGGAGGTGG	**TAGG**AGAAGGTGGAGATGGAGG	**AAAC**CCTCCATCTCCACCTTCT
8	GGCTGAAGTTGAGATTCTACCGG	**TAGG**CTGAAGTTGAGATTCTAC	**AAAC**GTAGAATCTCAACTTCAG
9	GGGCGACATTCCCACTGTCCTGG	**TAGG**GCGACATTCCCACTGTCC	**AAAC**GGACAGTGGGAATGTCGC
10	GGTGGAGAAAACCAGCACACAGG	**TAGG**TGGAGAAAACCAGCACAC	**AAAC**GTGTGCTGGTTTTCTCCA
11	GGCCTCGAATGACTCTCTGTCGG	**TAGG**CCTCGAATGACTCTCTGT	**AAAC**ACAGAGAGTCATTCGAGG
12	GGTCGATTTTGTTCTGCACCAGG	**TAGG**TCGATTTTGTTCTGCACC	**AAAC**GGTGCAGAACAAAATCGA
13	GGAGTCTGCAGCTGCCGAAGGGG	**TAGG**AGTCTGCAGCTGCCGAAG	**AAAC**CTTCGGCAGCTGCAGACT

Target gene	Target site(5'>3' PAM is underlined)	Oligonucleotide 1 (5'>3')	Oligonucleotide 2 (5'>3')
Nudc	GGTCACCCGCCTCTGATCGATGG	**TAGG**TCACCCGCCTCTGATCGA	**AAAC**TCGATCAGAGGCGGGTGA
2	GGAGAGCTCATGGCTCATCGAGG	**TAGG**AGAGCTCATGGCTCATCG	**AAAC**CGATGAGCCATGAGCTCT
3	GGATGGCGAGACGCGCAGTATGG	**TAGG**ATGGCGAGACGCGCAGTA	**AAAC**TACTGCGCGTCTCGCCAT
4	GGTGTTGATTTCAGGGTCTGTGG	**TAGG**TGTTGATTTCAGGGTCTG	**AAAC**CAGACCCTGAAATCAACA

Preparation of Cas 9 nRNA

We have synthesized a Cas9 coding sequence with nuclear localization signals (nls) at both its amino and carboxyl termini and codons optimized for zebrafish expression (pT3TS-nCas9n). Injection of *in vitro* transcribed nls-zCas9-nls mRNA with a gene-specific guide RNA consistently resulted in high mutagenic efficiency in both somatic and germline cells.

T3TSnCas9n Purificate

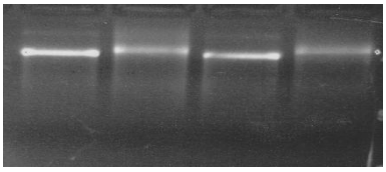

After *in vitro* transcription, we added a poly (A) tail to the 3' termini of our pT3TS-nCas9n RNA. Polyadenylation plays an important role in the stabilization of RNA in eukaryotes and enhances the efficiency of translation initiation. The additional adenine residues confer stability to the mRNA and may increase translational efficiency of *in vitro* synthesized capped RNA in microinjection and transfection experiments.

Microinjection

sgRNA and Cas9 were co-injected into one cell stage zebrafish embryos. Each embryo was injected with approximately 2 µl of solution containing 12.5 ng/ µl of sgRNA and 200 ng/ µl of Cas 9 mRNA. The mutagenesis efficiency is dose-dependent and likely target-dependent. The doses of sgRNA/Cas9 were adjusted accordingly to obtain the desired efficiency. One day following injection, numbers of normal, abnormal and dead embryos were scored. Genomic DNA was extracted from embryos at 2 days after injection for either restriction enzyme experiments or T7 Endonuclease I assay.

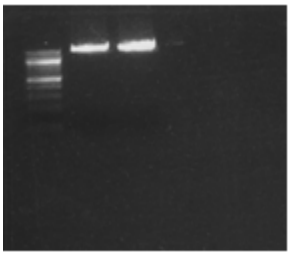

***Figure 6.38: Rab23* sgRNA after in vitro transcription and before adding DNase**

Genotyping DNA

The target site was amplified by PCR using genomic DNA extracted from embryos injected with sgRNA/Cas 9 endonuclease.

Restriction enzyme assay

The mutagenesis efficiency for *rab23* and *nudc* were assessed by restriction enzyme digestion (**figure 6.39**). In both cases we did not see any difference between WT embryos or possible mutants.

***Rab23* target site digested with Msp I**

***Nudc* target site digested with Tsp 45**

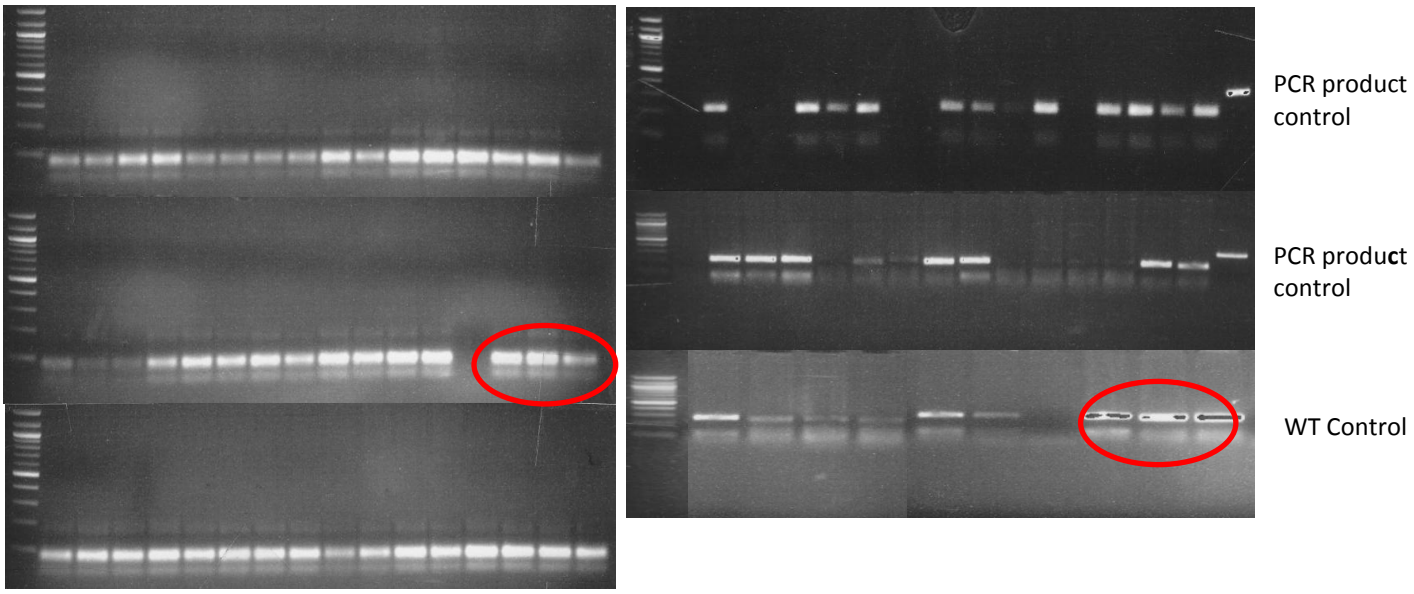

Figure 6.39

However, we show a successful restriction enzyme assay (**figure 6.40**) that we performed in our lab for another gene of interest, for which we optimised the protocol.

Figure 6.40.

We can observe a different band in embryos injected with sgRNA/Cas 9 when we compare with WT control.

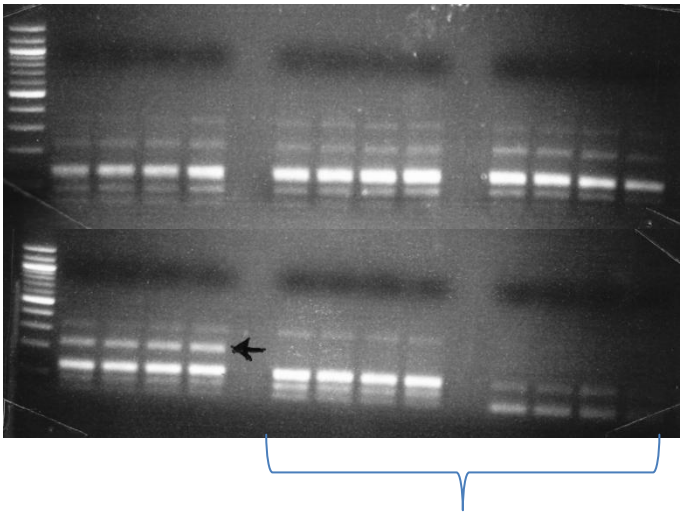

T7 Endonuclease I Assay

Because CRISPR/Cas9 induced double-strand breaks are partially repaired by the non-homologous end joining pathway, and T7 Endonuclease I recognizes and cleaves the non-perfectly matched DNA, we used the T7EI assay to analyse mutations in *rab23* gene.

The results for *rab23* did not show any heteroduplexes according to this technique, as compared to embryos injected with WT control. We show another successful T7 Endonuclease I assay tested in our lab.

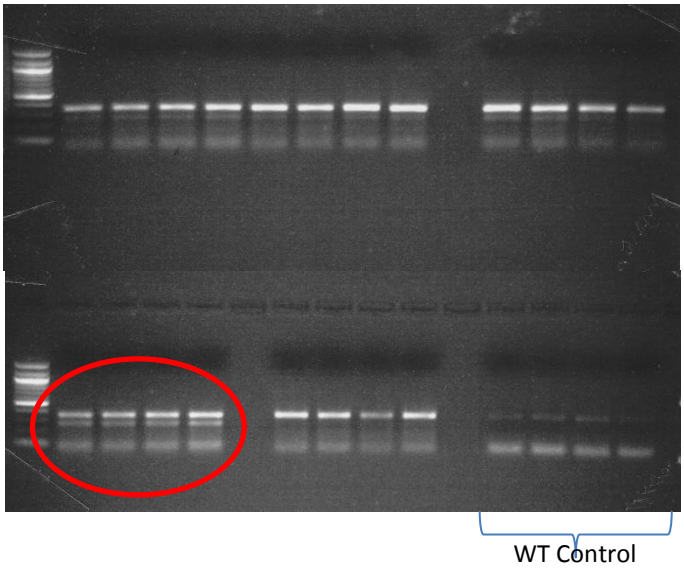

High Resolution Melt Analysis (HRMA)

The melt curve of a PCR product can be revealed using dyes which only bind to double-stranded DNA. Each DNA sequence produces a characteristic melt curve, which can be discerned from one another even when the sequences being compared differ by a single base-pair. This feature of DNA melt curves allows us to quickly identify heterozygous sequences in the progeny of CRISPR founders. This technique utilizes differences in the melting temperature of heteroduplexes containing insertions or deletions to differentiate them from wild-type homoduplexes.

Given that we were unable to detect to detect mutations using the restriction and T7EI assay, we used HRMA for *rab23* (**figure 6.42**) and *Nudc* (**figure 6.41**) genes to detect mutations in the mosaic F_0 zebrafish embryos injected, as it is a more sensitive technique. This was extremely effective in detecting mosaic mutations.

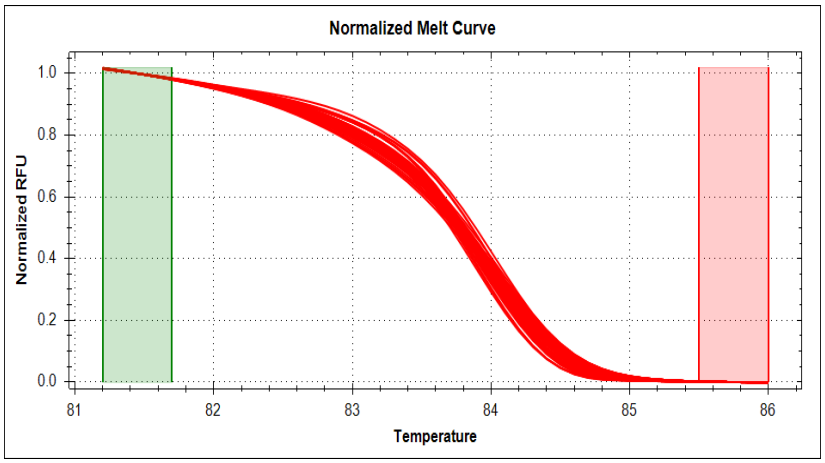

Figure 6.41 nudc **Normalized Melt Curve.**

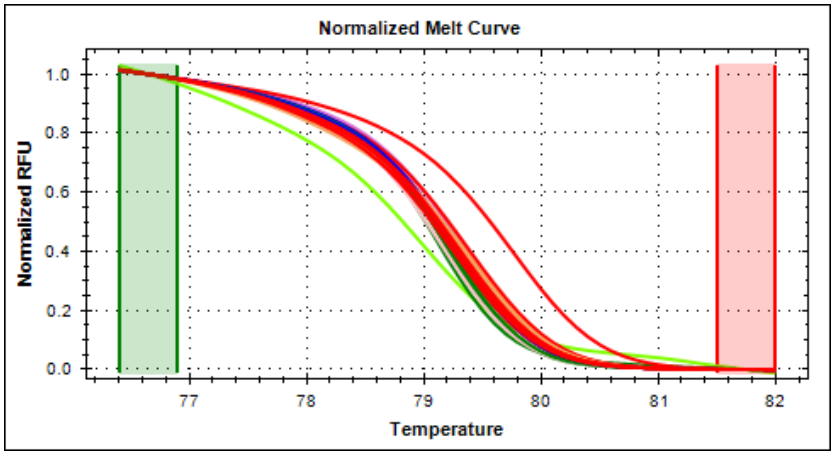

Figure 6.42 rab23 **Normalized Melt Curve.**

The normalized melt curve allows melt profiles to be analysed independent of amplification level. Difference curves highlight small changes in melt temperatures. Note that wild-type samples exhibit a higher melt temperature and so are represented by curves to the top of each graph, whereas successfully mutated alleles have a lower melt temperature owing to the presence of heteroduplexes within the PCR products. These are represented to the bottom of each graph. Note a spectrum of species are detected according to the different levels of mutant alleles produced.

Sanger sequencing

Following HRMA, we have now also confirmed the presence of successfully targeted alleles producing indel mutations induced by engineered sgRNA/Cas 9 in another gene studied in our lab.

Mutations in 7 out of 10 sequenced alleles

```
CTCGAGGGAAGTAGAACTTTGGAATGCTTTCACTTAAGGCTGGTGTAACGGGCTCCTCTTTCTTGGCCT  Wild type

CTCGAGGGAAGTAGAACTTTGGAATGCTTTCACTTAAaaaagcaGGCTGGTGTAACGGGCTCCTCTTTC  +7
CTCGAGGGAAGTAGAACTTTGGAATGCTTTg--TaAcGGCTGGTGTAACGGGCTCCTCTTTCTTGGCCT  -2(-5,+3)
CTCGAGGGAAGTAGAACTTTGGAATGCTTTCACTT--G--TG---TAACGGGCTCCTCTTTCTTGGCCT  -7
CTCGAGGGAAGTAGAACTTTGGAATGCTTTCACTT-A--CTGGTGTAACGGGCTCCTCTTTCTTGGCCT  -3
CTCGAGGGAAGTAGAACTTTGGc----------------TGGTGTAACGGGCTCCTCTTTCTTGGCCT  -17 (-18,+1)
CTCGAGGGAAGTAGAACTTTGGAATGCTT----ggAAtGCTGGTGTAACGGGCTCCTCT            -4 (-7,+3)
CTCGAGGGAAGTAGAACTTTGGAATGCTTTCAC-T-----TGGTGTAACGGGCTCCTCTTTCTTGGCCT  -6
```

The wild-type sequence is shown at the top with the target site highlighted in yellow and the PAM sequence highlighted as underlined text. Deletions residues are indicated by dashes highlighted in blue and insertions as lower case letters highlighted in purple. Some alterations have both insertions and deletions of sequence and in these instances the alterations are enumerated in the parentheses.

For this gene, the sequences of alleles shown were amplified from pooled genomic DNA isolated from four embryos, which were subcloned and subject to Sanger sequencing (**figure 6.43**).

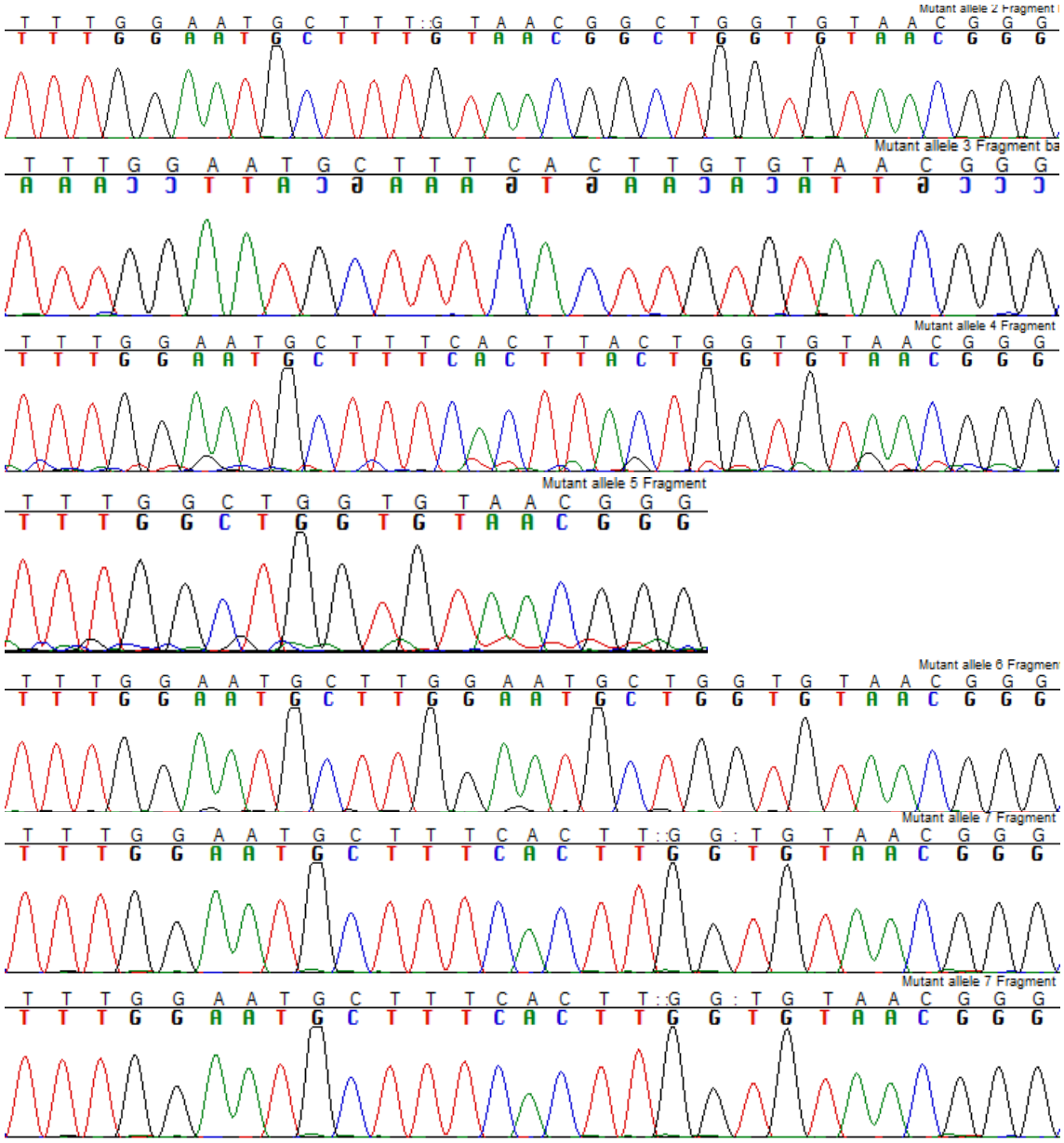

***Figure 6.43*: Chromatograms showing the sequences in differents mutants found in F0 in embryos injected with sgRNA/Cas9, as schematised above.**

Following these sucessful results on our third gene of interest we returned to Nudc and Rab23 and finish generating those mutants to ensure the technique is fully established and functioning efficiently in the lab. These test runs and early mutant generation experiments have given us the knowledge and experience to start using this technique more routinely for mutant generation and

which will totally overcome the issues surrounding the use of morpholinos and allow us to validate work previously carried out in morpholino models.

- ***Task 6.5. Perturbation of CAMs in mice, a mammalian model***

Deliverables under this Task: D6.1 (month 12), D6.2 (month 12), D6.3 (month 12), D6.6 (month 48), D6.10 (month 30), D6.14 (month 36) and D6.17 (month 48) and D6.26 (month 54) all delivered.

A: Phenotypic assessment of cilia and tissue morphologies

Partner 7:

We continued the characterization of the Ofd1 null mice. We analyzed 35 heterozygous mutant *Ofd1*$^{\Delta 4\text{-}5/+}$ females at E9.5 and they were all grossly indistinguishable from *Ofd1*$^{+/+}$ wild-type embryos. Indeed, they showed a normal looped heart without pericardial effusion or other aberrant morphological features (**figure 6.44 A and B**). We observed 55 *Ofd1*$^{\Delta 4\text{-}5/y}$ male embryos at E9.5 and all of them showed pericardial effusion, a generic sign of cardiac failure. Twenty-one embryos (38%) had a normal D-looping (*situs solitus*) but twenty-six embryos (47%) displayed an abnormally L-looped heart (*situs inversus*) and ballooning of the pericardial sac (**figure 6.44 C**). Six embryos were not scorable due to the high degree of degeneration already observed at the time of harvesting (E9.5). We observed an intermediate phenotype similar to that described for other mutants displaying laterality malformations in two *Ofd1*$^{\Delta 4\text{-}5/y}$ embryos (4%). In our studies the abnormal loop seemed to be restricted to the outflow tract (asterisk in **figure 6.44 D**). A summary of the different phenotypes observed in Ofd1 mutants is reported in **Table 6.2.** Hematoxylin eosin staining of mutant male embryos revealed the presence of extremely abnormal cardiac structures with a marked expansion of the cardiac jelly (**figure 6.44 G**, red arrowheads). However the cardiac cushions, although expanded, are normally situated. Injection of ink into the heart of E9.5 *Ofd1*$^{\Delta 4\text{-}5/y}$ embryos showed that the circulation was not obstructed. This analysis revealed an enlarged aortic sac (red arrowhead in **figure 6.44 L**) and occasional, but inconsistent abnormalities of pharyngeal arch arteries in female mutants.

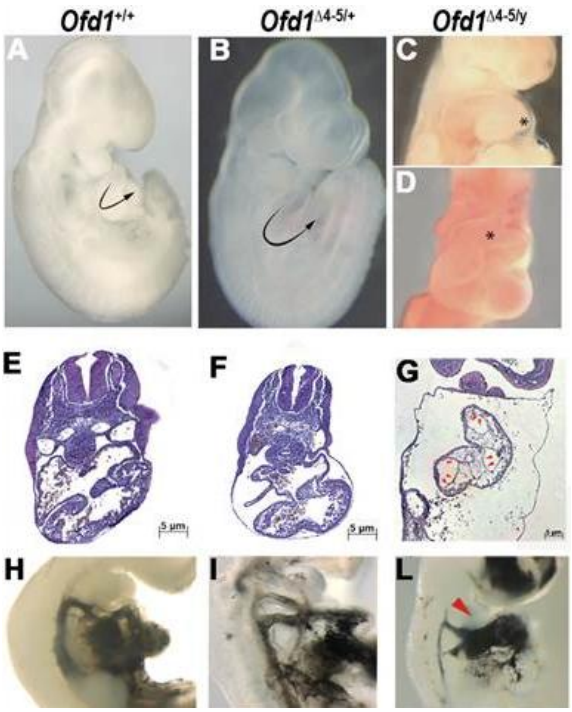

Figure 6.44

We analyzed female embryos at a later stage of development. At E18.5, *Ofd1*$^{\Delta 4\text{-}5/+}$ mutants (6 out of 6 examined) showed a reduced left pulmonary lobe compared to wild-type littermates. Hematoxylin eosin staining revealed a normal tissue structure of the lung.

Table 6.2 Heart Looping in *Ofd1*$^{\Delta 4\text{-}5/y}$ males at E9.5 stage	
Direction of heart looping	Examined Embryos (Percentage)
Normal D-Looped	21 (38%)
Abnormal L-Looped	26 (47%)
Not scorable	6 (11%)
Intermediate	2 (4%)

Partner 8:
Published a Cep290-/- murine model in PNAS (Hynes, Giles et al., Proc Natl Acad Sci U S A. 2014 Jul 8;111(27):9893-8).

Partner 12:
We addressed the possible implication of mTOR signaling in the phenotype of Hnf1b deficient embryos carrying a renal specific inactivation. Very little is known about the activation of the mTOR signaling pathway during renal morphogenesis. Our results indicated that one of the target activated by mTOR, the phosphoS6RP, is specifically phosphorylated in peculiar compartments of the developing nephrons (**figure 6.45**). In particular, specific signals are detected in (1) already differentiated proximal tubules and in (2) the distal part of the developing renal vesicles. In addition, a specific activation is systematically seen in (3) the developing Bowman capsule cells. All these compartments are characterized by the presence of HNF1beta expression. Our results have shown that this activation maintained activated in HNF1beta deficient developing kidneys (**figure 6.46**).

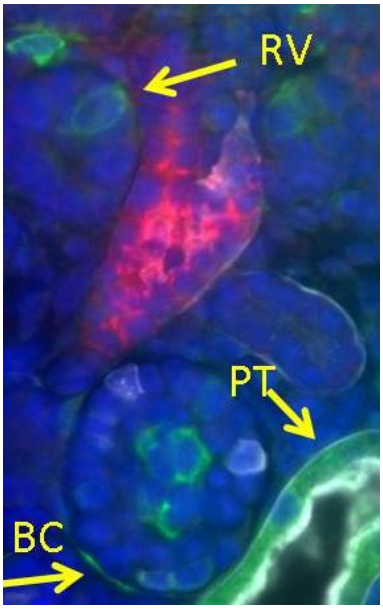

***Figure 6.45* mTOR signalling in developing kidneys of wild-type embryos at E19.** Renal vesicle (RV); Bowman capsule (BC) and in the Proximal tubules (PT)

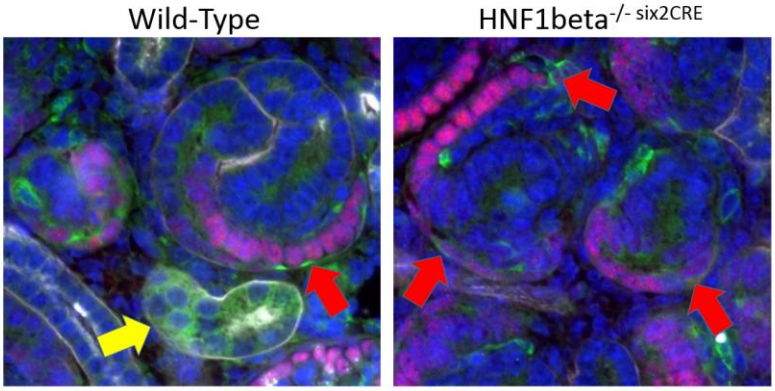

***Figure 6.46* mTOR signaling in epithelia of developing nephrons of wild-type and *Hnf1b-/-* six2CRE embryos.** Yellow arrow indicates a proximal tubule whereas the red arrows indicate parietal Bowman capsular cells.

B: Genetic interrelationschips between CAMs and CAM components

Partner 10:

Cross-breeding experiments with the *Tmem67* knock-out line into different genetic backgrounds have suggested the existence of modifier allele(s) that could 1) reduce the phenotypic variability of the line as it becomes more congenic and 2) explain the occurrence of heterozygous affected animals in non-congenic lines. However, the variant identification pipeline from RNA-seq data needs to be optimized and further biological replicates need to performed in order to confirm the potential pathogenic status of the *Tctn2* c.170G>C, p.S57T variant as a modifier allele in the *Tmem67* line. Please refer to Deliverable report D6.26.

C: Impact of CAM disruption on Planar Cell Polarity signaling

Task completed by month 48.

Partner 12:

We have previously demonstrated (see annual report month 48) that early nephron precursors, in the absence of HNF1beta, give rise to deformed S-shaped bodies, characterized by the absence of the typical bulge of epithelial cells at the bend between mid- and lower segments. The absence of this bulge eventually leads to the complete absence of tubules. This defect is caused by the decreased expression of Dll1, a direct target of HNF1beta and the consequent defective activation of Notch in the prospective tubular compartment of comma and S-shaped bodies. In mutant embryos deformed s-shaped bodies give rise to dilated glomeruli connected directly to the collecting duct via a primitive and short tubule. The malformation that is at the basis of HNF1beta deficient glomeruli could be linked to a spatial distortion/displacement of this patterning/boundary. Interestingly, one of the markers of the boundary of cells inside and outside the glomerulus is represented by the frontier of the expression of HNF1beta itself. HNF1beta is expressed in tubular and capsular precursor cells (outer cells) but absent in podocyte precursors (inner cells) and in their fully differentiated podocyte descendent cells. One possibility is that the expression of HNF1beta at this critical frontier might play a key role in the morphogenetic events that drive glomerulogenesis. To explore this possibility we have taken advantage of a specific knock-in allele where a betagalactosidase cassette is put under the control of the endogenous HNF1beta promoter. Our results have shown that betagal positive cells are finally trapped inside the glomerulus (**figure 6.47**).

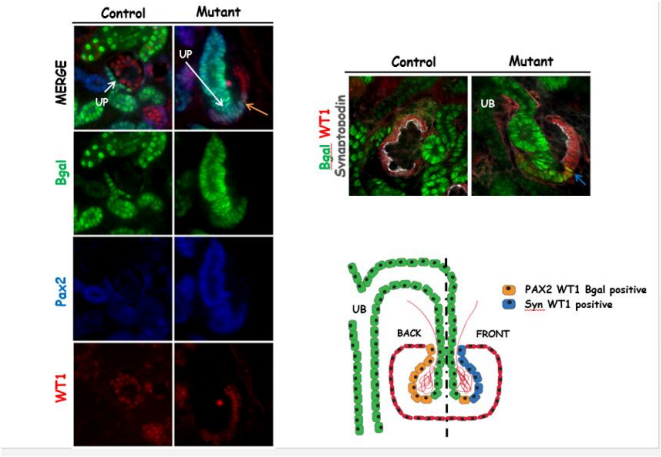

Figure 6.47: **Developmental fate of cells that are programmed to express HNF1beta in the absence of HNF1beta itself**. Detection of a LacZ reporter cassette under the control of HNF1beta promoter.

We then inspected the possible implication of Wnt signaling in the phenotypes of induced by HNF1beta deficiency during renal development. When we inspected the localization of beta catenin in nephron precursors we could not see any significant difference in the membrane intensity nor in the nuclear staining of mutant HNF1b mice (**figure 6.48**) .

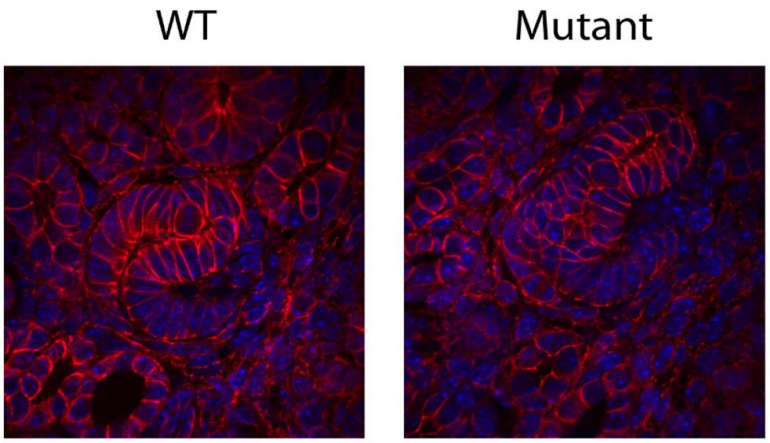

***Figure 6.48*: Expression of beta catenin in nephron precursors from wild-type (left) or Hnf1b^{six2CRE} (right) embryos**

In order to further verify if any implication of Wnt pathway could be involved in the phenotypes of HNF1beta deficiency, we monitored the beta catenin activation in the proliferative cystic epithelia of novel developed system of inactivation of HNF1beta in post natal kidney with an inducible (tamoxifen) inactivation of HNF1beta. The development of cystic lesions starts progressively in a matter of few days to reach a situation where HNF1beta-deficient kidneys acquire a typical polycystic phenotype at 30 days (**figure 6.49**). In these proliferating cystic kidneys we could observe a significantly ($P<0.05$) increased expression of Axin2 mRNA, a typical target of this pathway (**figure 6.50**). However, another target, the cyclin D1 was not significantly altered in its expression. In a similar way, a transcriptomic analysis revealed that many typical targets of the WNT-betacatenin pathway were altered.

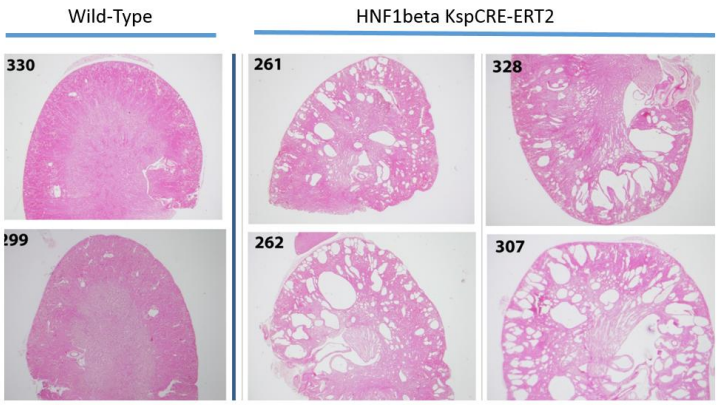

***Figure 6.49* Renal cyst formation with the perinatal deletion of HNF1beta with an inducible CRE recombinase**

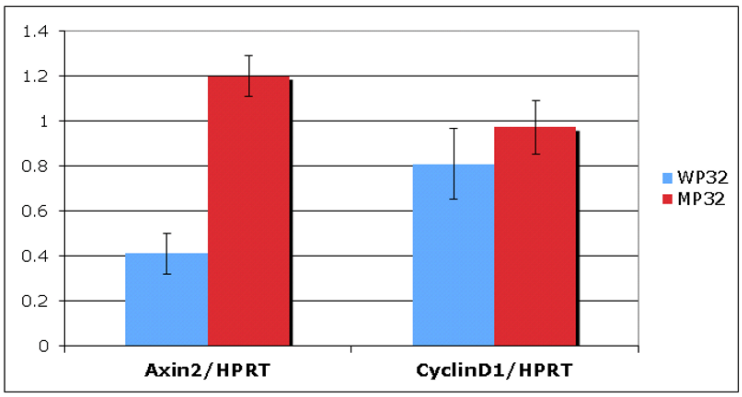

***Figure 6.50:* Expression level of Axin2 and Ccnd1 (Cyclin D1) in kidneys from wild-type (blue bars) or Hnf1bKsp$^{CRE-ERT2}$ (red bars) animals a month after a perinatal deletion of Hnf1b.**

.

In a similar way we monitored the level of activation of Shh pathway in these polycystic animals. Our results showed that the transcription of Gli1 was significantly increased (P <0.001) in polycystic kidneys of HNF1beta deficient animals that had been inactivated perinatally and analyzed 30 days after the deletion (**figure 6.51**). On the other hand, Patched expression was not significantly altered.

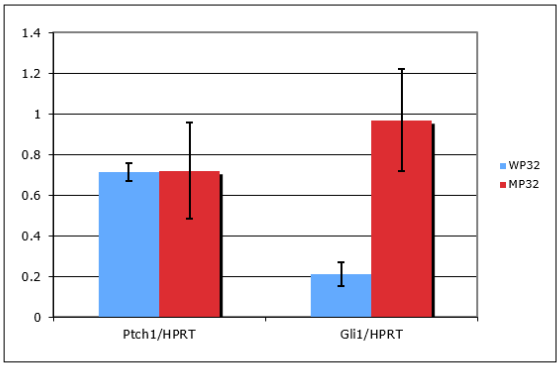

Figure 6.51 **Shh signalling pathway in proliferative cystic epithelium of kidneys of mice 30 days after perinatal inactivation of *Hnf1b*.**

➢ ***Task 6.6 Assessing the renal transcriptome (mRNA and miRNA) of CAM disrupted mice***

Deliverables under this Task: D6.8 (month 24) and D6.21 (month 48) both delivered.

A: Generation of appropriate Cre-floxed CAM mutant mice

Partner 7:

We continued the characterization of the inducible model with time-induced inactivation of the OFD1 gene. The level of *Ofd1* inactivation in the kidney was assessed by Real-Time PCR and confirmed at protein level by Western Blot analysis. Both approaches revealed that the level of gene/protein inactivation is 80% on average (**figure 6.52a**). Hematoxylin-eosin staining showed dilatation of renal tubules by postnatal day (P) 10 (P10). By P18 the majority of the parenchyma is replaced by cysts (**figure 6.52b**). Upregulation of the mTOR pathway was detected by western blot analysis from P10 (**figure 6.52c**). Analysis of Phospho4EBP1 (P4EBP1), another readout of the mTOR pathway activation, shows an evident accumulation in kidneys from *Ofd1*-IND mice at P18 while at P8 the levels of P4EBP1 where comparable between controls and mutants. Enhanced signal for PS6 was also demonstrated by immunofluorescence at P18 in *Ofd1*-IND mutant kidneys (**figure 6.52d**).

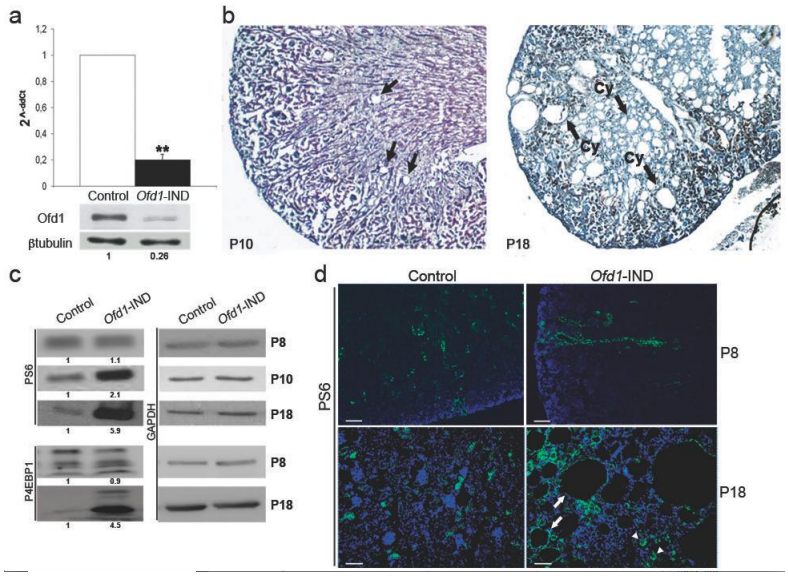

Figure 6.52

We extracted polysomes from HEK293 cells and wild type (wt) murine kidneys and demonstrated the presence of the OFD1 protein. We also validated *in vivo* the interaction between Ofd1 and one of the members of the Preinitiation complex of translation (PIC), namely eIF3B, in polysomes extracted from wt kidneys (**figure 6.53a**). We then analysed the polysomal profile in kidneys from *Ofd1*-IND mice. The RNA content of polysomes was quantified *in vivo* at two different time points, i.e. a precystic (P8) and a cystic (P20) stage. A significant difference was observed at P20, possibly due to the upregulation of the mTOR pathway observed at this stage. At P8, when the mTOR pathway is not upregulated, the polysomal profile was similar between *Ofd1*-IND and controls, indicating that mRNA translation, as a whole, is not altered. We reasoned that OFD1 might regulate the translation of specific targets and thus performed microarray analysis on total and polysomal RNA from control and *Ofd1*-IND mutant kidneys at P8. This stage was selected to eliminate targets associated to upregulation of the mTOR pathway. We identified 141 targets differentially expressed in polysomal RNAs with a p value <0,05 suggesting that OFD1 controls the protein synthesis of specific targets in the kidney.

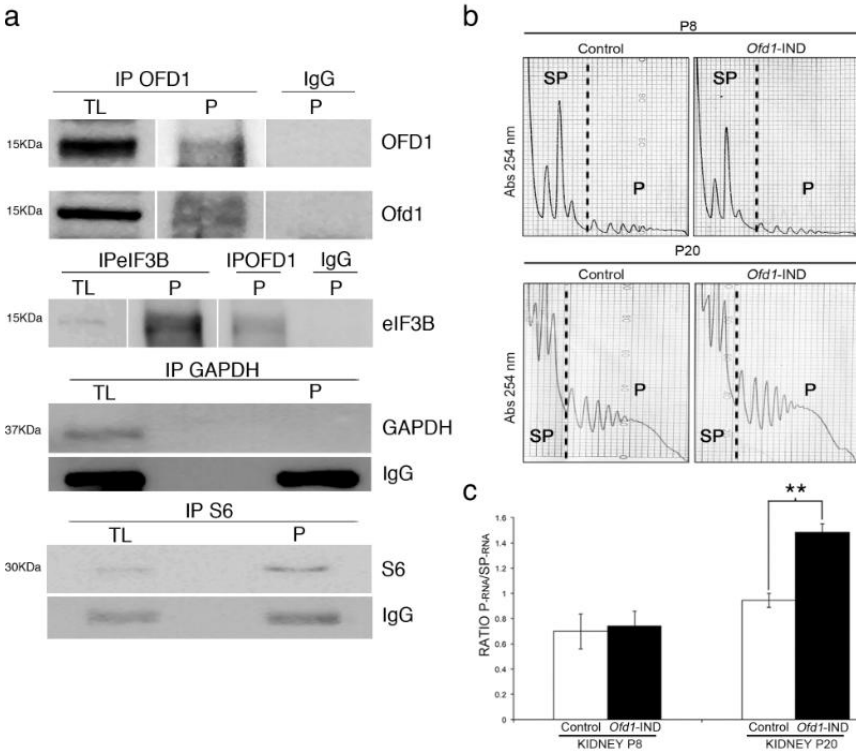

Figure 6.53

B: Transcriptome analysis of kidneys in CAM mutant mice

Partner 12:

To analyze the impact of the inactivation of *Hnf1b* on gene expression in mouse kidneys we took advantage of an Hnf1b floxed allele and a mouse strain carrying a tamoxifen inducible CRE recombinase under the control of the Ksp promoter. This CRE is known to target quite efficiently most nephron tubular segments. We decided to analyze the effect of the deletion of *Hnf1b* in two distinct phases of postnatal kidney maturation (**figure 6.54**). The first is the perinatal period, which is notoriously characterized by massive proliferative tubular elongation whereas the second

step that we considered is the postweaning period, characterized by a much lower proliferation context. Mice were injected for 3 consecutive days either at birth (P0-P3) or just after weaning (P21-P23). At first we verified that already 4-5 days after the injection of tamoxifen, we have a consistent and reproducible prompt decrease of HNF1beta protein. Our results (**figure 6.55**) showed that the vast majority of tubular cells had lost the expression of the protein in mutant mice injected with tamoxifen. In fact only few tubular cell nuclei maintained some expression of HNF1beta protein. We therefore decided to collect kidney samples either shortly after the deletion of Hnf1b (4-5 days), namely at P7 and P28 (**figure 6.54**) or 30 days later to monitor the fate of kidneys deleted for HNF1beta for a longer period of time (30 days) at P32 and P53, respectively (**figure 6.54**). To this end we collected kidneys to carry out histological examination and RNA transcriptome analysis.

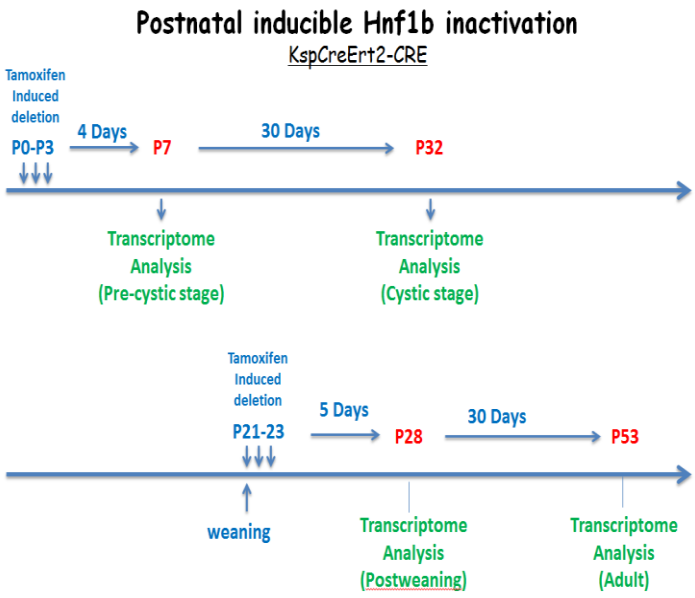

Figure 6.54: **strategy for the analysis of the renal transcriptom of Hnf1b**

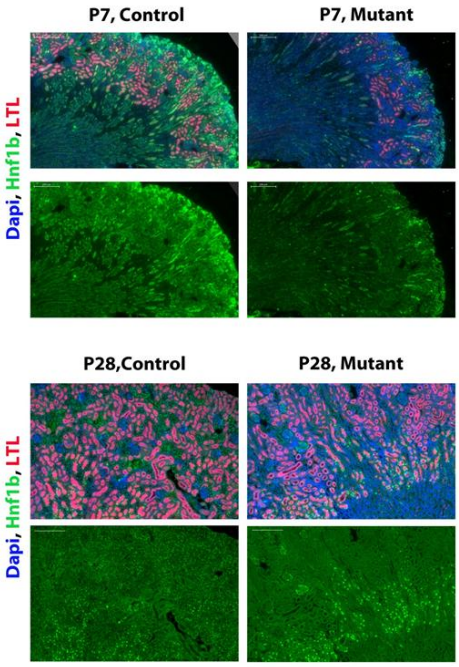

Figure 6.55: **Immunofluorescence on kidney sections showing the efficient depletion of HNF1beta protein 4-5 days after the inactivation.**

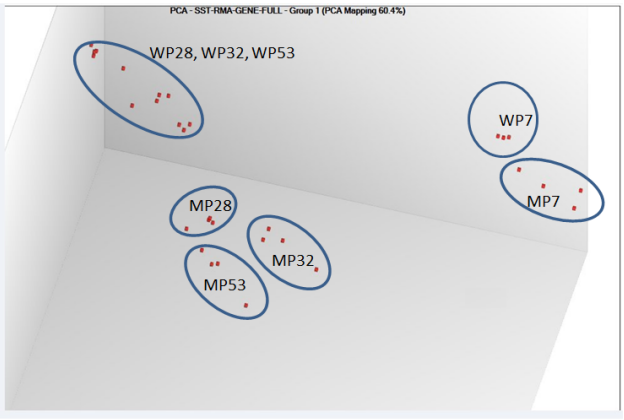

Figure 6.56: **Principal component analysis of the transcriptome of kidney lacking the expression of Hnf1b.** "W" stands for Wild-type whereas "M" stands for Mutant. The number indicate the day of the sacrifice.

The analysis of RNA was carried out on 4 replicas for each condition/time point by affymetrix hybridization (MTA-1). The analysis of the results showed first of all that the principal component analysis of gene expression levels lead to a consistent repartition of samples (**figure 6.56**). As expected the transcriptome of mice at P7 both wild-type and mutants, (WP7 and MP7), were separated from the rest of the other samples since there is a large number of genes that are specifically differentially expressed at this stage.

The comparison of the gene expression at different developmental stages revealed that a considerable number of genes varied in their expression. In particular, it is worth to note that just 5 days after the deletion of Hnf1b the expression level of the majority of genes tends to be decreased in the absence of HNF1beta (103 vs 13 at P7) and (184 vs 36 at P28), indicating that HNF1beta acts predominantly with a positive effect on transcription (**figure 6.57**). Interestingly, a month later, the situation is inverted at P32 with a majority of genes that becomes predominantly overexpressed in the animals that lacked the expression of HNF1beta (440 up vs 144 down). These kidneys underwent the inactivation of HNF1beta 30 days before, in a proliferative context (perinatally). We have previously published that the inactivation of HNF1beta in a proliferative (perinatal) context leads to a severe polycystic kidney disease in a matter of one month. In fact, the histological analysis of these kidneys (Mutant at P32) showed that they were strongly cystic (data not shown). On the other hand, the kidney that were inactivated in a postweaning, non-proliferative context a month later showed a massive change in gene expression with 438 genes upregulated and 449 downregulated in the absence of HNF1beta.

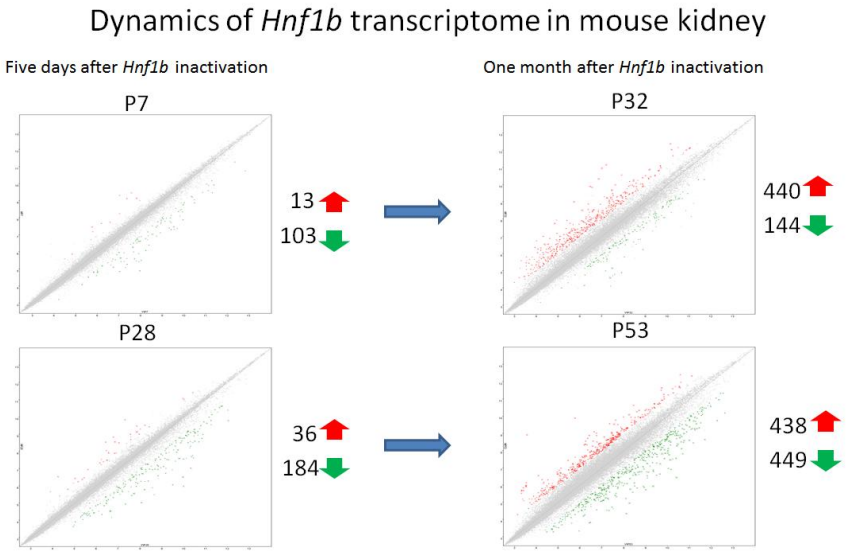

Figure 6.57 **The comparison of transcriptome of kidneys at different stage of development.**

Our results lead us to understand that already at P7, in spite of a normal histology of the kidneys at this stage (**figure 6.55**), there is an already consistent modification of gene expression with more than 100 genes differentially expressed (fold change >2 and a significance of P <0.05). The analysis of the results with the "Ingenuity Pathway" leads us to realize that a considerable and significant ($P< 10^{-17}$) number of genes were in common with the transcriptome of LHX1 kidney specific knockout. One of the characteristics of the expression of these genes is the fact that they are systematically downregulated at any time point that we have analyzed. The embryos lacking the expression of LHX1 (Lim1) were characterized by the defective development and differentiation of nephrons, therefore the transcriptome of these embryos, compared to their controls, lacks the expression of all the genes that are normally expressed in nephrons. The overlap of this list of genes included Umod, Tmigd, Slc5a8, Slc22a19, Pah, Mep1b, Kap, Hsd3b4, Fut4, Cyp2j5, Acsm2 and Aadat. All these genes are characterized by the fact that they are expressed in the nephron tubular structures. This observation indicates an important impact of

the inactivation of Hnf1b on the specific gene expression of nephron tubular cells. Another remarkable correlation at this stage is represented by the overlap of genes known to be modified in Pkd1 inactivation ($P< 10^{-5}$). All these results indicate that even before the appearance of a clear histological phenotype, the differentiation state of renal tubular cells lacking HNF1Beta is already significantly
deteriorated.

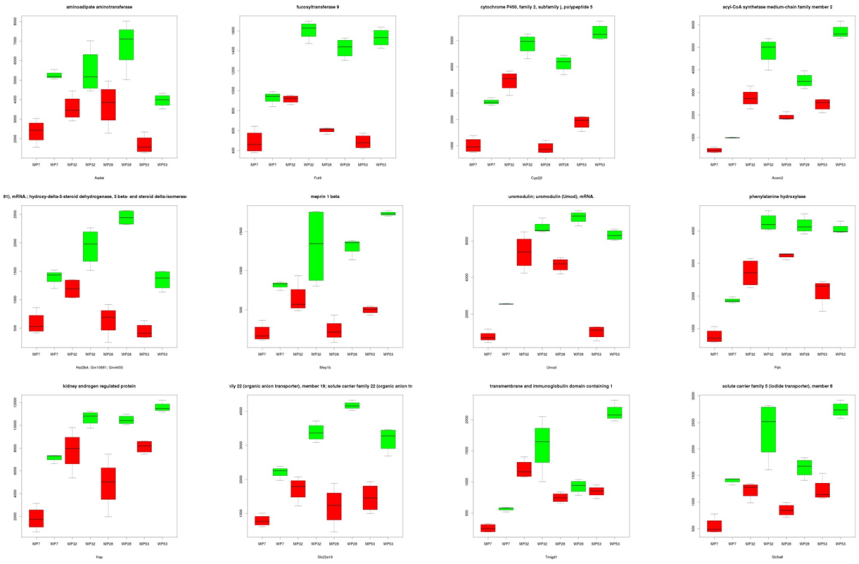

Our results showed that at P32, the cystic epithelium of HNF1beta deficient kidney is characterized by a transcriptome that presents with a drastic increase of TGFB1 activated pathway ($P< 10^{-29}$) and by the activation of pathways linked with several pro-inflammatory cytokines including TNF, IL1B ($P< 10^{-21}$) and IL13 ($P<10^{-17}$).

Another remarkable finding is the considerable differential gene expression in kidneys that were inactivated at weaning and analyzed only 5 days later at P28. Also in this case, there is a significant overlap with the transcriptome previously mentioned (LHX1, $P< 10^{-14}$) and that of HNF1alpha ($P<10^{-12}$), a close homologue of HNF1beta that is predominately expressed in proximal tubules. Therefore, similarly to what happens in kidney at P7, in spite of a normal histology (data not shown), there is already a massive deterioration of gene expression.

One of the surprising results that we observed is that the deletion of HNF1beta after weaning leads, in a matter of 30 days, to an even increased distortion of gene expression with globally almost 900 genes with a distorted gene expression level. The major significant “upstream effects” included LHX1 inhibited ($P < 10^{-20}$), Lipopolysaccharide activated ($P< 10^{-15}$); HNF1A, inhibited ($P<10^{-13}$) and TGFB1 activated ($P<10^{-12}$).

Another remarkable pathway affected 30 days after the deletion of HNF1beta at weaning (P53 animals) is the defective LXR/RXR pathway ($P< 10^{-8}$) with 14 genes out of 114 significantly affected, including Apoh, Apom, CD36, Clu, Cyp51a1, Gc, Il33, IL1R1, Lbp, Lpl, Lyz, Nr1h4, Ptgs2 and Serpinf2.

Finally, the comparison of the canonical pathways affected by the inactivation of Hnf1b at different time points after birth is represented by the **figure 6.58**. One of the most prominent features is the appearance of an Acute Phase Response that becomes evident only 30 days after the inactivation, either in the perinatal or the post weaning inactivation. This inflammatory

response is accompanied by a massive overall activation of TGBeta and fibrosis in the renal interstitium (Data not shown).

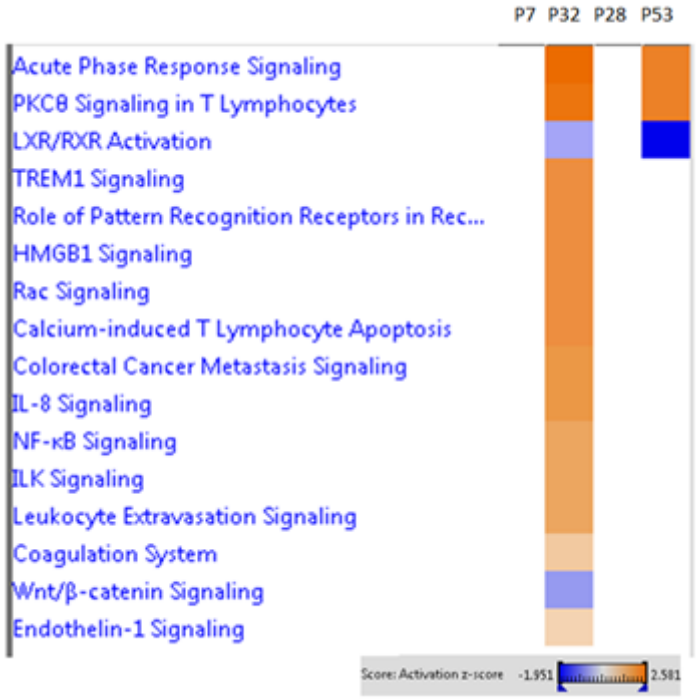

Figure 6.58: **Canonical Pathways significantly affected in the comparison among the 4 time points.**

Deviations for the technical work planned in Annex I:

For WP6 there are no deviations for the technical work planned in Annex I.

Deviations between actual and planned person-months effort. (see also WP11)

Partner 1b has shifted person month from WP8 to WP6 since the work in WP8 has mainly been performed by partner 4. These additional months on WP6 were spent on detailed (immune)histological evaluation of zebrafish after gene knockdown and in functional evaluation of the eye. In addition to a shift of person months between workpackages, we have reallocated €18,000 from materials to personel costs due to the time consuming procedures of histological and functional characterization of CAMs in zebrafish. No additional funds are requested from the EU.

Partner 5:

Due the enhanced technical and experimental work as a consequence of the amendment of Annex 1 to switch from *in vitro* to *in vivo* assays the work load of WP5 and 6 was increased. As mentioned in the previous periodic report 13^{+4} PMs have been reduced in WP9 and shifted to WP 5 and 6. In addition further PMs were necessary to reach the aims of WP 5+6. At month 60 the difference between the actual and indicated person months (including PMs of WP9) amounts to $15{,}4^{+26}$ in total for WP5 and WP6.

Partner 9:
We have exceeded our planned person months for WP6. We were required less in WP8 than expected and thus transferred those resources to this workpackage, in the main part to aid the validation efforts for novel CAMs found in the big datasets. Furthermore given the change in acceptance by the wider scientific community for morpholino derived models over the five year timeframe of SYSCILIA we began in the final 12 months to establish CRISPR models in the lab as described in this report. This need for new models could not have been forseen at the outset of this project and therefore took extra person months to complete than originally allocated. No additional funds are requested from the EU.

Partner 10:
There are deviations between actual and planned person-months as detailed in Annex 1. The total person months dedicated to WP6 exceeds the indicative effort by 4.5pm to be able to achieve the aims of WP6. No additional human resources are being requested.

Partner 11:
Has reconfigured the personnel costs from the beginning of the project in a cost neutral way and can dedicate more person months effort to the project. No additional human resources are being requested.

Work package number	WP7	Start date or starting event:		month 1
Work package title	Systematic RNAi screens to distort and identify ciliopathy-associated modules			
Activity Type	RTD			
Participant number	10 (L)	1a	8	
Participant short name	LIMM	RUNMC *Roepman*	UMCU	
Person-months per participant:	52^{+9}	27^{+18}	21	
Actual person months per participant* Month 48 - 60	2	14	1.6^{+4}	

* This is considered as use of resources.
Deviations are explained in the end of the report for this Work package.

A summary of progress towards objectives of WP7:

Objective 7.1. *To distort the expression of known CAM genes in small- and medium-scale ciliome-wide screens*

We have successfully completed pilot small-scale, medium-scale and secondary high-throughput screens in two different ciliated cell-lines (partners 1a & 10, human hTERT-RPE1 cells; partner 10, mouse mIMCD3 cells). The small-scale kinesome screen (partner 8) has been submitted for publication. Hits from the medium scale ciliome screen (partner 1a) have been cross-referenced with protein-protein interaction data (partner 1a) and will be integrated in a manuscript under preparation. The screen for UPS hits is now published (partners 1a & 10), with selected hits (USP39 and RBX1) now being taken forward for further biochemical validation. New medium-scale secondary screens have been completed that identify additional ciliopathy and ciliary-related hits.

Objective 7.2. *To confirm known and to identify novel CAM genes using large-scale genome-wide screens*

We have successfully completed the primary large-scale genome-wide screen in mIMCD3 cells (partner 10) of 19,860 genes in duplicate. A very high confidence list has been generated from a series of secondary and tertiary screens that include components of the spliceosome and proteasome, G-protein-coupled receptors (GPCRs), the non-motile primary cilium and the photoreceptor outer segment. Further screening has validated genes encoding GPCRs, pre-mRNA processing factors (PRPFs) and predicted centrosomal proteins. An additional secondary screen has validated ubiquitin-proteasome system (UPS) hits that were identified from the original primary screen.

Objective 7.3. *Integrate a high confidence list of validated known and novel CAM genes with other WPs to prioritize targets of interest*

The list of validated hits from the genome-wide screen continues to be analyzed and integrated with data from protein-protein interaction experiments and sequence variants identified in ciliopathy patients. This analysis has identified two novel ciliopathy genes that are mutated as a cause of human genetic disease. New data-sets from this screen include: increase in cilia number (separate data-sets for >1 cilium per cell, and >2 cilia per cell); increase/decrease in cilia intensity (a measure of cilia length); increase/decrease in cell number (a measure of proliferation); and increase/decrease in apoptotic nucleus. These highlight links between ciliogenesis and cell cycle progression, enhancing the interpretation of the proteomics datasets.

Objective 7.4. *Integrate RNAi screening data with outputs from other WPs and the central SYSCILIA resource to create a public database of validated CAM genes.*

This process of integration of data-sets is being finalized towards publication. It relies on validated hits that have been confirmed from the secondary screens, other tertiary confirmatory screens, and other validation experiments.

A summary of progress towards each task in WP7:

- ***Task 7.1: Small-and medium-scale RNAi screens***

Deliverables under this Task: D7.3 (month 18), D7.4 (month 30) and D7.9 (month 48) all delivered in time.

A: Kinesome-wide RNAi screens

Task completed by month 48.

B: Ciliome-wide RNAi screens

Partner 1a*:*
The medium-scale ciliome screen targeting known human regulators of cilium assembly/maintenance, gene-products that are known to localize in or in a close proximity of the cilium, Retnet gene-products and gene-products that have not been linked so far to cilium function has been completed (see *Deliverable D7.2 "Description of standardized methodologies for small (50 to 200 targets), medium- and pilot screens (1500 to 2000 targets)"* and *Deliverable D7.9 "Results of further novel putative CAM genes identified from new rounds of medium-scale screens (at least 500 targets)"*). In addition, we have performed new secondary siRNA screens in ciliated hTERT-RPE1 cells. Partner 1a has investigated all enriched human ubiquitin-proteasome system (UPS) components from the primary whole-genome siRNA screen (n=57/1829) by individual siRNA duplexes (3 per gene) on cell number, cilium number and cilium length in hTERT-

RPE1 cells. A ciliary phenotype was scored when at least 2 out of 3 duplexes showed a significant effect on cilium presence and/or length (**Table 7.1;** see *Deliverable Report D7.10 "Report on further validated, very high confidence novel CAM genes identified from medium-scale screens (at least 200 targets)*"). This has validated a total of n=44/57 genes that had a significant effect on cilia number and/or cilia length ciliogenesis (using cut-offs of z<-2 or z>+2) for n>=2 out of 3 individual duplexes. These hits have been confirmed in secondary and validation screens with a different ciliary marker (ARL13B) and siRNA duplex design (partner 10). The hits (USP39 and RBX1) are now being taken forward for further biochemical validation (Partner 10).

Gene Symbol	Gene ID	Robust z-score cilium length ($z_{\text{cilia length}}$)			Robust z-score % cells ciliated (z_{cilia})		
ANAPC4	29945	3.60	3.11	2.43	-2.33	-2.18	-1.98
CUL4A	8451	-0.28	-2.04	-1.39	-2.61	1.13	-1.21
POMP	51371	-5.09	-5.07	-5.07	-7.37	8.73	-2.89
PSMA6	5687	-3.29	-4.37	-1.71	-1.46	14.34	1.22
PSMB7	5695	-5.42	7.06	-0.86	6.63	2.54	-6.84
PSMC6	5706	2.16	-0.64	-5.05	-9.88	-7.24	0.23
PSMD7	5713	-6.23	13.19	-5.88	18.59	12.10	63.70
UBA1	7317	-3.90	0.74	-1.13	-8.43	0.47	-3.17
UBE4A	9354	0.14	-0.98	5.84	-1.45	-6.65	0.74
ANAPC5	51433	6.58	-7.70	-2.17	-10.92	4.18	-0.11
DDB1	1642	4.60	-8.84	3.39	3.67	-9.86	-1.08
PSMA7	5688	-6.12	-2.77	5.52	29.92	4.28	2.09
PSMC1	5700	na	12.34	13.13	na	-0.27	2.51
PSMD11	5717	-2.28	-7.22	0.14	-3.43	66.46	3.79
PSMD8	5714	1.94	-7.78	-4.11	18.97	69.16	4.50
UBA7	7318	-2.15	-5.51	-3.56	-6.04	-5.29	-4.20
UBR5	51366	-0.31	-3.58	-0.34	-5.11	-4.61	0.14
CDC16	8881	-1.26	5.10	-2.26	-2.15	2.35	-4.66
FBXW7	55294	0.58	-1.28	0.62	-0.43	1.93	-0.29
PSMA1	5682	-5.72	-5.12	3.31	15.07	2.74	-6.04
PSMB1	5689	0.61	-4.61	0.42	1.99	17.62	23.54
PSMC2	5701	8.41	9.42	9.73	-2.04	-4.55	0.94
PSMD12	5718	1.96	-0.34	-3.14	9.64	23.96	22.36
RBX1	9978	-1.93	-1.09	-1.84	-9.32	-2.18	-5.34
UBE2E2	7325	-1.08	-1.54	-0.14	3.98	0.91	-0.54
CDC20	991	-4.64	na	-0.15	-11.01	na	-0.06
HERC3	8916	-5.82	0.82	0.85	0.62	-2.73	-2.63
PSMA2	5683	-0.49	-4.55	-0.68	5.69	13.12	5.44
PSMB2	5690	3.25	0.35	3.74	4.11	22.07	2.59
PSMC3	5702	2.39	10.18	-4.75	7.47	-3.60	17.71
PSMD14	10213	-2.74	-5.89	-2.22	16.27	26.01	-5.05
SYVN1	84447	-2.09	-7.06	4.91	-1.24	-7.80	-2.00
UBE2E3	10477	-1.57	-2.89	0.41	-0.66	-9.04	-0.56
CDC23	8697	12.10	-0.36	1.39	-3.10	-1.72	-0.64
HUWE1	10075	0.34	-0.68	-2.04	0.62	-0.94	0.41
PSMA3	5684	-1.64	-2.81	-1.48	10.05	14.68	-0.39
PSMB4	5692	-6.54	-5.04	-1.98	-8.55	38.15	-1.39
PSMC4	5704	-4.72	-0.63	-5.02	15.54	16.73	17.96
PSMD2	5708	13.39	8.07	-7.02	0.08	1.97	34.85
TCEB2	6923	-9.10	-4.40	-4.38	-0.59	1.53	-2.02
UBE2I	7329	-3.86	4.22	-2.05	-3.09	-1.49	-3.66
CDC27	996	-3.74	-6.09	-2.73	-2.97	4.24	0.08
PIAS1	8554	-4.17	-0.54	-2.38	-1.87	-1.86	-1.80
PSMA4	5685	-5.44	-0.16	-1.09	-3.64	21.67	0.69
PSMB6	5694	6.74	-3.72	4.91	15.94	16.77	1.70
PSMC5	5705	6.60	-7.97	-7.42	9.19	52.81	-2.68
PSMD6	9861	-9.03	3.86	-4.08	124.68	-1.52	29.68
TRIM32	22954	2.09	-0.70	-0.75	3.95	-4.14	-1.18
UBE2R2	54926	4.20	-2.74	-1.70	0.95	-10.81	-2.40
USP12	219333	-2.07	1.12	-2.73	-0.92	-4.57	-0.88
USP5	8078	1.07	-0.35	7.95	-0.36	-0.66	-2.19
USP15	9958	-0.22	-0.92	-10.39	0.15	0.45	-3.77
USPL1	10208	1.16	5.33	-3.45	-6.62	-2.00	-9.74
USP18	11274	0.73	0.17	0.40	0.13	-1.86	2.12
USP29	57663	-0.76	-0.75	-0.13	-2.07	-0.77	-2.20
USP39	10713	-1.56	1.81	-3.39	-5.15	-3.73	-4.01
USP4	7375	0.20	2.59	2.62	-2.27	-0.56	-3.79

Table 7.1. Complete dataset for the secondary screen of all ubiquitin-proteasome system (UPS) hits. All primary screen hits for UPS components (n=57) are listed with NCBI Entrez Gene ID and Gene Symbol. Knockdown of a total of n=44/57 genes had a significant effect on cilia number and/or cilia length, for n>=2 out of 3 individual siRNA duplexes using human hTERT-RPE1 cells. Transfection and image analysis methods were the same as for the tertiary screen in hTERT-RPE1 cells, listing robust *z*-scores for cilia length ($z_{\text{cilia length}}$) and for % cells with a single cilium (z_{cilia}), using cut-offs of *z*<-2 (red) or *z*>+2 (green).

➢ ***Task 7.2: Large-scale primary siRNA screen***

Deliverables under this Task: D7.1 (month 9), D7.2 (month 12), D7.5 (month 30) and D7.6 (month 30) have all been delivered on time.

Task completed by month 29.

Partner 10:
Datasets have been formatted and are published in a manuscript at ***Nature Cell Biology***.

➢ ***Task 7.3: Secondary validation of RNAi screens***

Deliverables under this Task: D7.7 (month 36), D7.8 (month 42) and D7.10 (month 54) have all been delivered on time.

Partner 8:
Very high confidence hits from the large scale whole-genome screen have been taken forward in further validation experiments, and include work on the ion channels KCNQ1 and KCNJ10, and the E3 ubiquitin-protein ligase HUWE1.

1. *KCNQ1*: partner 8 has validated knockdown and rescue of ciliogenesis in mIMCD3 cells following expression of wild-type cDNA.Expression of cDNAs with mutations from long QT syndrome patients does not rescue the ciliary phenotype observed. Partner 8 will perform patch-clamping in order to assess any correlation of mutations with the rescue data; e.g. to test if non-functional channels are the ones that do not rescue ciliogenesis. KCNQ1 localizes to renal but not cardiomyocyte cilia in cell lines and murine immunohistochemical staining, but knockdown in cardiomyocytes has not been successful at the present time. A manuscript has been drafted and submitted.
2. *KCNJ10*: partner 8 has fully validated this hit with rescue data from the wild-type cDNA and knockdown in mIMCD3 2D monolayer and 3D spheroid culture. KCNJ10 strongly localizes to renal cilia in mouse IHC sections. EAST syndrome patient-specific mutations have been tested for rescue of ciliogenesis in mIMCD3 cells; all patient alleles tested rescued the phenotype indicating that although KCNJ10 does regulate renal cilia, the mutations found in EAST patients do not disturb that function. EAST syndrome is therefore not a ciliopathy.
3. *HUWE1*: Huwe 1 is not localized to the cilium, but gives a punctate-like distribution throughout the cell (**figure 7.1**). siRNA knockdown was validated by qPCR (**figure 7.1**), with reductions in cilia numbers in both mIMCD3 2D monolayer and 3D spheroid cultures (**figure 7.2**). Rescue experiments are being performed for Bardet-Biedl syndrome patient-specific mutations. A knock-out *C. elegans* mutant huwe1 line shows no dye filling phenotype. Several TALEN mutant knock-out fish have also been generated. Heterozygotes are already established and we are phenotyping homozygote embryos. Preliminary evidence suggests a heart-looping defect, with cardiac edema, and early renal failure, which is consistent with ciliary dysfunction (not shown, work ongoing).

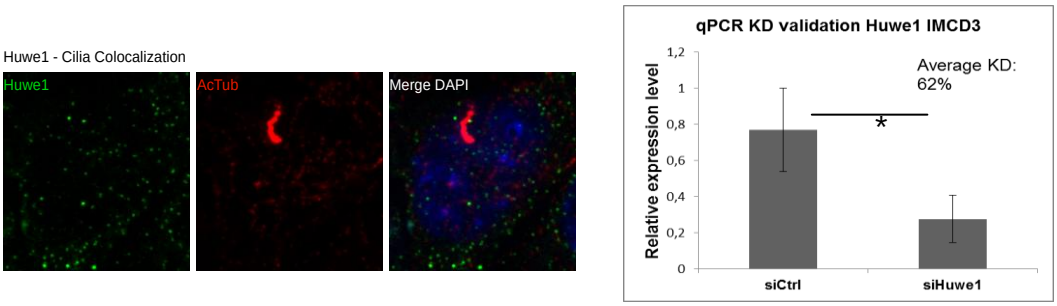

Figure 7.1

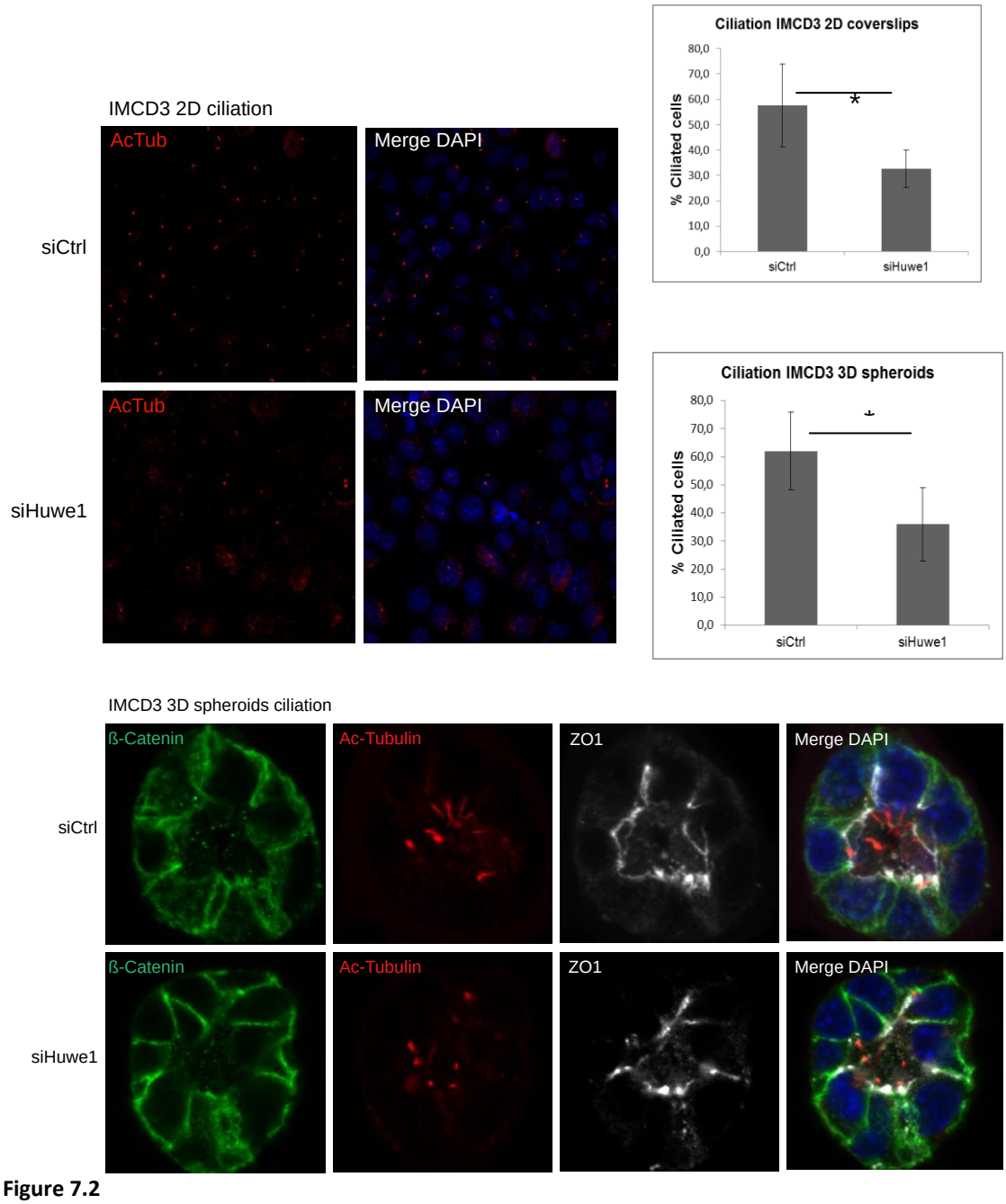

Figure 7.2

Partner 10:

In total, 194 functional candidates with human orthologs have been taken forward for validation in a secondary screen. Secondary screening in mIMCD3 cells validated a total of n=68/194 mouse genes that had a significant effect on cilia number ($z_{cilia}<z_{cilia\ cutoff}$) for n>=1 out of 4 individual siRNAs in duplicate, and n=29/192 for n>=2 out of 4 individual siRNAs in duplicate. A new re-analysis of validation screening data of all validated hits from the whole-genome siRNA screen using SMARTPools in hTERT-RPE1 cells (partner 1a) has confirmed a very high confidence list of hits; see *Deliverable Report D7.10 "Report on further validated, very high confidence novel CAM genes identified from medium-scale screens (at least 200 targets)*"). From the hits that were identified by the secondary screen, n=37/68 human genes had defects in cilia number and/or length (using conventional cut-offs of z<-2 or z>+2) including: *C21orf2*, *CCDC41*, *OFD1*, *PIBF1* and *PLK4*, and several *PRPF*s (*PRPF31*, *PRPF6* and *PRPF8*).

A secondary screen (partner 10) has now been completed and identifies additional ciliopathy and ciliary-related hits. This dataset comprises n=780 hits from the original primary screen with an effect on cilia number that is significantly greater (z>+2) than any effect on cell number. In a tertiary screen, n=100/780 hits have been validated using individual siRNA duplexes (3 per gene) with robust z scores calculated for cell number and cilium number (**Table 7.2**). Functional annotation of validated hits by DAVID, identified significant enrichment for proteasome subunits (q=2.34x10^{-24}, Benjamini-Hochberg correction for multiple testing with FDR<0.01), the spliceosome and mRNA processing (q=1.73x10^{-11}) and the nuclear pore complex (q=6.81x10^{-4}).

Re-analysis of the primary screen has also identified n=88 hits that increase cilia number >2 per cell (**Table 7.3**). This identifies significant enrichment for components of the cell cycle (q=3.1x10^{-3}). In particular, strong hits include CCNB1 (cyclin B1) which complexes with p34 (CDC2A) to form maturation-promoting factor (MPF) that is implicated in G1/S and G2/M phase transitions of the cell cycle. CDC27 is a component of the anaphase-promoting complex (APC), which mediates ubiquitin-mediated proteolysis of B-type cyclins and regulates the timing of mitosis. Furthermore, FOXM1 transcriptional activator involved in cell proliferation that is phosphorylated in M phase, and regulates both cyclin B1 and cyclin D1. These hits will be taken forward in a secondary screen in order to identify new mechanistic links between ciliogenesis and cell cycle progression.

Other data-sets for further validation include:

- increase in cilia number (separate data-sets for >1 cilium per cell, and >2 cilia per cell)
- increase/decrease in cilia intensity (a measure of cilia length)
- increase/decrease in cell number (a measure of proliferation)
- increase/decrease in apoptotic nucleus
- RNA-seq expression data for the cell-line used for this screen (intended as a filter for false positives hits)

A manuscript describing the major findings of, and resulting from this workpackage is currently *in press* with Nature Cell Biology (Wheway et al., doi: 10.1038/ncb3201; PMID: 26167768).

mouse gene	GENEID	human gene	z cilia number	z cell number	summary of protein function
0610009D07Rik	66055	SF3B14	-7.30	-7.04	14 kDa protein subunit of the splicing factor 3b complex
Cactin	70312	CACTIN	-3.85	-3.01	cactin, spliceosome C complex subunit
Acat2	110460	ACAT2	-4.82	-1.22	cytosolic acetoacetyl-CoA thiolase; lipid metabolism
Arcn1	213827	ARCN1	-7.28	-6.75	similarities to heat shock proteins and clathrin-associated proteins, may be involved in vesicle structure or trafficking
Cltc	67300	CLTC	-5.37	-1.55	subunit of the clathrin coat in coated vesicles and coated pits; intracellular trafficking of receptors and endocytosis
Copb2	50797	COPB2	-7.39	-8.12	subunit of Golgi coatomer complex in nonclathrin-coated vesicles; Golgi budding and vesicular trafficking
Crnkl1	66877	CRNKL1	-6.41	-5.84	homologue of Drosphila crooked neck (crn); required for cell cycle progression and pre-mRNA splicing
Cse1l	110750	CSE1L	-6.76	-3.60	regulation of the importin-alpha/beta heterodimer and nuclear localization; nucleocytoplasmic transport
Ctnna1	12385	CTNNA1	-4.89	-1.88	catenin (cadherin-associated protein), alpha 1
Ecd	70601	ECD	-5.71	-2.44	ecdysoneless homolog
Hmgcr	15357	HMGCR	-7.14	-7.15	HMG-CoA reductase; cholesterol synthesis
Hmgcs1	208715	HMGCS1	-5.36	-5.30	3-hydroxy-3-methylglutaryl-CoA synthase 1 (soluble)
Hnf1b	21410	HNF1B	-4.72	-0.29	hepatocyte nuclear factor 1-beta, a homeodomain-containing transcription factors; embryonic development
Hpn	15451	HPN	-5.37	-5.44	type II transmembrane serine protease
Hspa1a	193740	HSPA1A	-4.92	-2.66	70kDa heat shock protein; mediates folding and stabilization of proteins against aggregation
Htatsf1	72459	HTATSF1	-4.71	-2.17	cofactor for transcriptional elongation by HIV-1 Tat
Ighmbp2	20589	IGHMBP2	-5.44	-5.80	helicase superfamily member, binding to immunoglobulin mu chain switch region
Ik	24010	IK	-7.48	-6.67	contains RED repeat, localizes to discrete dots within the nucleus, excluding the nucleolus; function unknown
Ildr1	106347	ILDR1	-5.73	-4.32	contains an immunoglobulin-like domain; multimeric receptor
Inha	16322	INHA	-4.62	-2.11	alpha subunit of inhibins A and B protein complexes
Irf6	54139	IRF6	-3.67	-3.11	member of the interferon regulatory transcription factor (IRF) family
Isg20l2	229504	ISG20L2	-5.46	-4.84	interferon stimulated exonuclease gene 20kDa-like 2; 3'-5' exoribonuclease for processing 12S pre-rRNA
Kctd21	622320	KCTD21	-6.09	-5.59	potassium channel tetramerization domain containing 21
Klc2	16594	KLC2	-6.00	-7.55	kinesin light chain; generates ATP-dependent movement of vesicles and organelles along microtubules
Klf10	21847	KLF10	-5.43	-6.13	Kruppel-like factor 10; a transcriptional repressor implicated in TGF-beta signaling
Klk7	23993	KLK7	-5.84	-6.00	member of the kallikrein subfamily of serine proteases
Kpnb1	16211	KPNB1	-7.71	-7.24	member of the importin beta family; nucleocytoplasmic transport
Lgals1	16852	LGALS1	-5.41	-5.91	member of galectins family of beta-galactoside-binding proteins; cell-cell and cell-matrix interactions
Lgmn	19141	LGMN	-5.86	-4.46	cysteine protease; hydrolysis of asparaginyl bonds
Magoh	17149	MAGOH	-6.04	-6.18	mago nashi homolog
Mr1	15064	MR1	-4.15	-1.64	major histocompatibility complex, class I-related
Mybl2	17865	MYBL2	-4.05	-5.70	member of the MYB family of transcription factors; cell cycle progression
Mycl	16918	MYCL	-4.01	-2.60	v-myc avian myelocytomatosis viral oncogene lung carcinoma derived homolog
Myd88	17874	MYD88	-4.81	-3.51	cytosolic adapter protein; innate and adaptive immune response
Mylk3	213435	MYLK3	-5.27	-4.06	kinase that phosphorylates cardiac myosin heavy and light chains
Naa25	231713	NAA25	-3.36	-2.35	subunit of the heteromeric N-terminal acetyltransferase B complex
Naca	17938	NACA	-6.88	-6.31	associates with basic transcription factor 3 (BTF3) forming nascent polypeptide-associated complex (NAC)
Nanos1	332397	NANOS1	-5.47	-4.95	nanos homolog 1
Nap1l3	54561	NAP1L3	-6.11	-4.86	member of the nucleosome assembly protein (NAP) family
Ndufb2	68198	NDUFB2	-5.33	-4.37	subunit of the multisubunit NADH:ubiquinone oxidoreductase (complex I)
Nhp2l1	20826	NHP2L1	-7.07	-5.46	component of the [U4/U6.U5] tri-snRNP
Nipbl	71175	NIPBL	-4.91	-3.01	homolog of Nipped-B; sister chromatid cohesion, chromosome condensation, and DNA repair
Nln	75805	NLN	-5.71	-4.30	member of the metallopeptidase M3 protein family
Nlrx1	270151	NLRX1	-5.42	-3.54	member of the NLR family
Nob1	67619	NOB1	-5.07	-4.97	required for pre-rRNA processing to produce the mature 18S rRNA during ribosome assembly
Nrd1	230598	NRD1	-4.71	-3.88	zinc-dependent endopeptidase; cell migration and proliferation
Nsl1	381318	NSL1	-4.31	-3.46	component of kinetochores, bridging centromeric heterochromatin and outer kinetochore structure
Nup54	269113	NUP54	-5.80	-5.64	member of FG repeat-containing nucleoporin family; nucleocytoplasmic transport
Nup62	18226	NUP62	-7.58	-7.41	member of FG repeat-containing nucleoporin family; nucleocytoplasmic transport
Nup98	269966	NUP98	-6.57	-6.60	nucleoporin; nucleocytoplasmic transport
Osgep	66246	OSGEP	-3.92	-1.88	O-sialoglycoprotein endopeptidase
Pabpc1	18458	PABPC1	-5.80	-4.44	poly(A) binding protein binding to 3' poly(A) tail of mRNA; mediates ribosome recruitment and translation initiation
Pcf11	74737	PCF11	-6.79	-5.52	PCF11 cleavage and polyadenylation factor subunit
Polr2a	20020	POLR2A	-5.90	-7.89	largest subunit of RNA polymerase II
Ppp1r12a	17931	PPP1R12A	-5.66	-4.68	protein phosphatase 1, regulatory subunit 12A, subunit of myosin phosphatase
Psma1	26440	PSMA1	-6.58	-9.06	member of the peptidase T1A family, 20S core alpha subunit of proteasome
Psma2	19166	PSMA2	-6.46	-9.57	member of the peptidase T1A family, 20S core alpha subunit of proteasome
Psma3	19167	PSMA3	-5.91	-6.89	member of the peptidase T1A family, 20S core alpha subunit of proteasome
Psma6	26443	PSMA6	-6.67	-9.20	member of the peptidase T1A family, 20S core alpha subunit of proteasome
Psma7	26444	PSMA7	-6.01	-7.75	member of the peptidase T1A family, 20S core alpha subunit of proteasome
Psmb1	19170	PSMB1	-6.61	-7.37	member of the proteasome B-(T1B) type family, 20S core alpha subunit of proteasome
Psmb3	26446	PSMB3	-5.35	-7.33	member of the proteasome B-(T1B) type family, 20S core alpha subunit of proteasome
Psmb4	19172	PSMB4	-6.07	-8.35	member of the proteasome B-(T1B) type family, 20S core alpha subunit of proteasome
Psmb6	19175	PSMB6	-6.24	-8.34	member of the proteasome B-(T1B) type family, 20S core alpha subunit of proteasome
Psmb7	19177	PSMB7	-5.59	-7.88	member of the proteasome B-(T1B) type family, 20S core alpha subunit of proteasome
Psmc1	19179	PSMC1	-5.78	-6.52	member of the triple-A family of ATPase subunit of 26S proteasome
Psmc2	19181	PSMC2	-6.56	-7.38	member of the triple-A family of ATPase subunit of 26S proteasome
Psmc3	19182	PSMC3	-7.47	-8.24	member of the triple-A family of ATPase subunit of 26S proteasome
Psmc4	23996	PSMC4	-6.95	-8.32	member of the triple-A family of ATPase subunit of 26S proteasome
Psmc6	67089	PSMC6	-7.45	-9.18	member of the triple-A family of ATPase subunit of 26S proteasome
Psmd14	59029	PSMD14	-7.34	-7.73	component of the 26S proteasome
Psmd6	66413	PSMD6	-6.24	-7.84	component of the 26S proteasome
Psmd7	17463	PSMD7	-6.57	-7.25	non-ATPase subunit of the proteasome 19S regulator
Ranbp2	19386	RANBP2	-3.91	-2.64	giant scaffold and mosaic cyclophilin-related nucleoporin; nucleocytoplasmic transport
Rpp30	54364	RPP30	-5.43	-4.71	ribonuclease P/MRP 30kDa subunit
S100a10	20194	S100A10	-6.61	-4.52	member of the S100 family of proteins containing 2 EF-hand calcium-binding motifs
Sart1	20227	SART1	-6.61	-4.95	SART1(259) isoform recruits the tri-snRNP to the pre-spliceosome during spliceosome assembly
Scap	235623	SCAP	-5.77	-5.18	contains a sterol sensing domain (SSD) and seven WD domains
Scarf2	224024	SCARF2	-3.74	-3.05	SREBF chaperone, scavenger receptor protein; binding and degradation of acetylated low density lipoprotein
Sf3b1	81898	SF3B1	-7.43	-7.74	subunit 1 of the splicing factor 3b protein complex
Sf3b4	107701	SF3B4	-7.16	-5.88	subunit 4 of splicing factor 3B
Sf3b5	66125	SF3B5	-7.88	-8.42	subunit 5 of splicing factor 3b,
Sfpq	71514	SFPQ	-5.79	-4.39	splicing factor proline/glutamine-rich
Slc25a1	13358	SLC25A1	-4.75	-3.13	mitochondrial tricarboxylate transporter (citrate transport protein, CTP)
Slu7	193116	SLU7	-6.75	-6.17	splicing factor for pre-mRNA splicing
Smu1	74255	SMU1	-7.01	-5.91	smu-1 suppressor of mec-8 and unc-52 homolog
Snrnp200	320632	SNRNP200	-6.99	-5.63	DEXH-box putative RNA helicases; component of U4/U6-U5 snRNPs required for pre-mRNA splicing
Snrpa1	68981	SNRPA1	-6.23	-5.30	small nuclear ribonucleoprotein polypeptide A
Sptlc2	20773	SPTLC2	-5.06	-3.13	long chain base subunit of serine palmitoyltransferase; sphingolipid biosynthesis
Srebf2	20788	SREBF2	-6.79	-6.08	transcription factor of sterol-regulated genes
Supt6	20926	POLR2A	-5.78	-4.80	polymerase (RNA) II (DNA directed) polypeptide A, 220kDa
Tgif1	21815	TGIF1	-6.12	-3.91	TALE homeobox protein
Tnfrsf12a	27279	TNFRSF12A	-4.77	-0.40	tumor necrosis factor receptor superfamily, member 12A
Traf3	22031	TRAF3	-4.90	-6.43	member of the TNF receptor associated factor (TRAF) protein family
Trim8	93679	TRIM8	-4.89	-2.99	member of the tripartite motif (TRIM) family; localizes to nuclear bodies
Ttbk2	140810	TTBK2	-4.91	-0.79	serine-threonine kinase that phosphorylates tau and tubulin proteins
U2af2	22185	U2AF2	-6.45	-5.03	large subunit of U2 auxiliary factor; non-snRNP protein required for binding of U2 snRNP during spliceosome assembly
Ubl5	66177	UBL5	-7.53	-4.31	ubiquitin-like protein
Wbp11	60321	WBP11	-5.80	-4.18	colocalizes with mRNA splicing factors and intermediate filament-containing perinuclear networks
Xab2	67439	XAB2	-7.61	-6.88	XPA binding protein 2

Table 7.2. Tertiary screen in mIMCD3 cells. The table lists robust z scores for cilia number ($z_{\text{cilia number}}$) and % cells with a single cilium ($z_{\text{cilia number}}$) following re-screening with pooled siRNAs in mIMCD3 cells for n=780 hits from the original primary screen with an effect on cilia number that is significantly greater (z>+2) than any effect on cell number. Results are given for pooled siRNA duplexes for each gene, listing gene ID and mouse gene symbol and gene symbol of the human ortholog. This screen validated n=100/780 hits.

mouse gene	GENEID	human gene	z cilia number	z cell number	summary of protein function
TSHR	22095	TSHR	3.49	-6.80	receptor for thyrothropin and thyrostimulin; thyroid cell metabolism
HECTD2	226098	HECTD2	3.55	0.03	HECT domain containing E3 ubiquitin protein ligase 2
LMX1B	16917	LMX1B	4.16	-1.59	member of LIM-homeodomain family; embryonic development
Espl1	105988	ESPL1	3.94	-7.39	ESPL1 (separase) initiates the final separation of sister chromatids during anaphase
PSMA7	26444	PSMA7	4.07	-7.95	member of the peptidase T1A family, 20S core alpha subunit of proteasome
Cela2a	13706	CELA2A	3.17	-4.44	chymotrypsin-like elastase family, member 2A
CDC2A	12534	CDK1	5.88	-8.62	cyclin-dependent kinase 1, catalytic subunit of M-phase promoting factor; G1/S and G2/M phase transition
STK10	20868	STK10	3.33	-4.93	Ste20 serine/threonine protein kinase, phosphorylates polo-like kinase 1; cell cycle progression
RASGRP1	19419	RASGRP1	2.64	-2.30	member of Ras superfamily with guanine nucleotide exchange factor (GEF) domain
MKL1	223701	MKL1	3.48	-0.87	interacts with the transcription factor myocardin; smooth muscle cell differentiation
SSRP1	20833	SSRP1	3.41	-7.06	subunit of chromatin transcriptional elongation factor FACT
Dcps	69305	DCPS	2.50	-0.68	decapping enzyme, scavenger
PHOX2A	11859	PHOX2A	3.64	-0.58	contains paired-like homeodomain; development of autonomic nervous system
Scg5	20394	SCG5	4.89	-2.24	secretogranin V
SOX2	20674	SOX2	2.79	-1.12	member of the SRY-related HMG-box (SOX) family of transcription factors; embryonic development
DTR	15200	HBEGF	2.18	-6.60	heparin-binding EGF-like growth factor
CCNB1	268697	CCNB1	5.45	-13.01	cyclin B1 complexes with p34(cdc2) to form maturation-promoting factor (MPF); G1/S and G2/M phase transition
POLE3	59001	POLE3	2.99	-1.93	histone-fold protein that interacts with other histone-fold proteins
VPREB3	22364	VPREB3	4.09	0.99	required for B-cell differentiation, possibly for mu chain transport in pre-B cells
AXUD1	215418	CSRNP1	2.65	-3.47	cysteine-serine-rich nuclear protein 1, possible role in Wnt signalling pathway
TTF1	22130	TTF1	4.36	-15.51	transcription termination factor required for ribosomal gene transcription
POMT2	217734	POMT2	4.37	-4.99	O-mannosyltransferase that interacts with POMT1; endoplasmic reticulum function
E2F4	104394	E2F4	4.96	-4.60	member of the E2F family of transcription factors
FGF21	56636	FGF21	3.41	-7.85	member of the fibroblast growth factor (FGF) family
Sord	20322	SORD	3.00	-1.98	sorbitol dehydrogenase, catalyzes interconversion of polyols and their corresponding ketoses; sorbitol pathway
FOXM1	14235	FOXM1	4.39	-4.43	transcriptional activator involved in cell proliferation, phosphorylated in M phase, regulates cyclin B1 and cyclin D1
HTATIP2	53415	HTATIP2	4.49	-2.87	HIV-1 Tat interactive protein 2, 30kDa
RANBP9	56705	RANBP9	2.46	-0.94	small GTP binding protein of RAS superfamily at nuclear pore complex; nucleocytoplasmic transport
Narf	67608	NARF	4.08	-4.91	may be a component of a prelamin A endoprotease complex
TPMT	22017	TPMT	2.52	-1.06	thiopurine S-methyltransferase; enzyme that metabolizes thiopurine
Oca2	18431	OCA2	5.11	-4.75	encodes the human homologue of the mouse p (pink-eyed dilution) gene
2410195B05RI	67956	SETD8	3.11	-11.50	SET domain containing (lysine methyltransferase) 8
TFDP1	21781	TFDP1	7.24	-5.81	transcription factor that heterodimerizes with E2F proteins
STAT5A	20850	STAT5A	2.42	-2.81	member of the STAT family of transcription factors
PRIM2	19076	PRIM2	2.30	-4.37	large 58 kDa primase subunit; synthesizes small RNA primers for Okazaki fragments
MCM7	17220	MCM7	5.24	-4.73	a mini-chromosome maintenance protein (MCM) essential for initiation of eukaryotic genome replication
TAF6	21343	TAF6	3.04	-3.15	TATA-binding protein (TBP)-associated factor (TAF) of transcription factor IID (TFIID)
RACGAP1	26934	RACGAP1	3.78	-8.46	member of GTPase-activating protein (GAP) family
YPEL1	106369	YPEL1	2.83	-6.40	potential zinc-binding protein
Cdc27	217232	CDC27	3.38	-6.51	component of anaphase-promoting complex (APC); ubiquitin-mediated proteolysis of B-type cyclins; timing of mitosis
BC031181	407819	C18orf32	2.93	-6.02	chromosome 18 open reading frame 32
Zfp804a	241514	ZNF804A	2.45	-1.27	zinc finger protein 804A
LHB	16866	LHB	3.13	-2.60	beta subunit of luteinizing hormone
Olfr723	259147	OR4L1	8.29	-1.76	olfactory receptor
OLFR43	258706	OR1A1	6.71	-1.35	olfactory receptor
4933426K21Ril	108653	RIMKLB	4.10	-1.86	ribosomal modification protein rimK-like family member B
OLFR713	259036	OR10A5	3.83	1.02	olfactory receptor
Tagap1	380608	TAGAP	2.86	-1.92	T-cell activation RhoGTPase activating protein; member of the Rho GTPase-activator protein superfamily
Slitrk1	76965	SLITRK1	3.37	-1.97	member of the SLITRK protein family
Supt7l	72195	SUPT7L	2.68	-0.54	subunit of the STAGA acetyltransferase complex; chromatin modification
Spopl	76857	SPOPL	4.11	-3.64	speckle-type POZ protein-like
BC018242	235044	LPPR2	2.86	-3.71	lipid phosphate phosphatase-related protein type 2
Ccdc85a	216613	CCDC85A	2.29	-2.36	coiled-coil domain containing 85A
DPT	56429	DPT	3.26	-2.42	dermatopontin, extracellular matrix protein with possible functions in cell-matrix interactions and matrix assembly
1110055N21RI	109077	INTS5	3.09	-3.82	Integrator complex subunit 5, mediates 3' processing of small nuclear RNAs U1 and U2
Arpp21	74100	ARPP21	2.90	-2.63	21-kD cAMP-regulated phosphoprotein, regulator of calmodulin
9030617O03RI	217830	C14orf159	3.13	-5.60	chromosome 14 open reading frame 159
Lrrc58	320184	LRRC58	3.10	-2.21	leucine rich repeat containing 58
RNPS1	19826	RNPS1	5.72	-5.53	part of a post-splicing complex mediating mRNA nuclear export and surveillance; nucleocytoplasmic transport
BC089491	280621	SELV	3.84	-7.79	selenoprotein, contains selenocysteine (Sec) residue at active site
C130090K23RI	231293	CWH43	2.19	-1.84	cell wall biogenesis 43 C-terminal homolog
NELF	56876	NELF	4.09	-2.13	guidance of olfactory axon projections and migration of luteinizing hormone-releasing hormone neurons
MAPK8IP3	30957	MAPK8IP3	2.46	0.31	homolog of Drosophila syd gene, required for interaction of kinesin I with axonal cargo; regulation of synaptic vesicle transport
Tmem144	70652	TMEM144	3.65	-1.29	transmembrane protein 144
EBF3	13593	EBF3	2.28	-1.89	member of the early B-cell factor (EBF) family of transcription factors; B-cell differentiation, bone development and neurogenesis
Sec22c	215474	SEC22C	3.31	-3.99	member of the SEC22 family of vesicle trafficking proteins; ER-Golgi protein trafficking
ZFP622	52521	ZNF622	3.84	-4.12	zinc finger protein 622
Vps53	68299	VPS53	2.91	-1.28	possible retrograde vesicle trafficking in late Golgi
Kif27	75050	KIF27	2.53	-1.17	member of the KIF27 (kinesin 4) sub-family of the mammalian kinesin family
KRTAP15	26560	KRTAP15-1	2.37	-1.90	keratin associated protein 15-1
RPS20	67427	RPS20	3.65	-14.75	member of the S10P family of ribosomal proteins, component of the 40S ribosome subunit
DNAJC9	108671	DNAJC9	3.33	-0.07	DnaJ (Hsp40) homolog, subfamily C, member 9
Pomp	66537	POMP	8.78	-15.90	molecular chaperone that binds 20S preproteasome components, essential for 20S proteasome formation
Prtg	235472	PRTG	3.98	-15.74	protogenin, member of the immunoglobulin superfamily
Arglu1	234023	ARGLU1	2.33	-3.26	arginine and glutamate rich 1
Chmp2a	68953	CHMP2A	3.88	-16.45	component of ESCRT-III (endosomal sorting complex required for transport III)
Spc24	67629	SPC24	3.36	-14.63	NDC80 kinetochore complex component
RPS7	20115	RPS7	4.66	-15.64	member of the S7E family of ribosomal proteins, component of the 40S ribosome subunit
1700029I15RIK	75641	C11orf94	4.05	-8.71	chromosome 11 open reading frame 94
Nsl1	381318	NSL1	10.28	-15.54	localizes to kinetochores, bridges centromeric heterochromatin with the outer kinetochore structure
Rplp0	11837	RPLP0	5.46	-15.27	member of the L10P family of ribosomal proteins, component of the 60S ribosome subunit
AI413631	381045	CCDC58	3.10	0.46	coiled-coil domain containing 58
RAET1E	379043	RAET1E	2.59	-3.14	member of RAET1 family; innate and adaptive immune responses
MRPS10	64657	MRPS10	4.01	-4.86	member of the S10P family of ribosomal proteins, component of the 28S mitochondrial ribosome subunit
D130059P03RI	320538	UBN2	3.24	0.09	ubinuclein 2
Cnih3	72978	CNIH3	2.97	0.80	cornichon family AMPA receptor auxiliary protein 3
Clec4b1	69810	CLEC4C	6.31	-2.20	member of the C-type lectin/C-type lectin-like domain (CTL/CTLD) superfamily
Tmed6	66269	TMED6	2.74	-1.32	transmembrane emp24 protein transport domain containing 6
1110008J03RIK	100764	RITA1	6.60	-19.93	RBPJ interacting and tubulin associated 1

Table 7.3. Primary screen re-analyzed for increases of cilia number >2 per cell. This data-set identifies n=88 candidate hits that will be taken forward for validation in a secondary screen.

Deviations for the technical work planned in Annex I:
For WP7 there are no deviations for the technical work planned in Annex I.

Deviations between actual and planned person-months effort. (see also WP11)
Partners 1a and 10 have devoted more person months effort to WP7 to be able to complete and publish the siRNA screens. No additional human resources are requested. Partner 1a reallocates budget under RTD/INNVATION from Other direct costs to Personnel costs.

Work package number	WP8	Start date or starting event:			Month 1
Work package title	**Assessment of the involvement of the predicted ciliary molecular machines in the pathogenesis of ciliopathies**				
Activity Type	RTD				
Participant number	**4 (L)**	1b	7	9	10	16
Participant short name	Duke	RUNMC Kremer	FTELE.IMG	UCL	LIMM	WWU
Person-months per participant:	95^{+81}	10^{+4}	28^{+18}	8^{+9}	16^{+18}	11^{+7}
Actual person months per participant* Month 48 - 60	9.37	0	13.5	0	0.56	2.32

* This is considered as use of resources.
Deviations are explained in the end of the report for this Work package.

A summary of progress towards objectives of WP8:

The objectives of this WP fully match the tasks, therefore progress is reported below.

Objective 8.1. *To establish a cohort of 500 well-characterized patients with diverse types of ciliopathies ranging from mild to severe and create a database with relevant clinical and genetic information*

Objective 8.2. *To perform next generation sequencing of this cohort on a large set (~913) of genes and determine total mutational load, followed by validations and development of a ciliary mutational database*

Objective 8.3. *To functionally validate sequence variants to discern pathogenic from benign variants in a robust and physiologically relevant (in vivo) zebrafish system*

Objective 8.4. *To integrate data on functional sequence variants and clinical information with information on CAMs to come to a system model for explaining and predicting phenotypes and their variability*

A summary of progress towards each task in WP8:

- ***Task 8.1. Establishment of a patient cohort***

Deliverable under this Task: D8.1 (month 12) delivered.

Task and Deliverable under this task achieved by month 12.

- ***Task 8.2. Sequencing***

Deliverables under this Task: D8.2 (month 24) and D8.3 (month 36) are delivered.

Task and Deliverables under this task achieved ahead of time by month 24.

- ***Task 8.3. Allele validation***

Deliverable under this Task: D8.4 (month 42) is delivered..

Task and Deliverable under this task achieved by month 42.

- ***Task 8.4. Functional validations***

Deliverables under this Task: D8.5 (month 48) and D8.6 (month 60) both delivered.

Partner 4 has completed the funding period with a focus on validation and functional annotation of variants identified in the ciliary resequencing study. Specific advances from partners 4, 7, and 16 are listed below:

Orofacialdigital (OFD) syndrome: Partner 7 has contributed to the identification of mutation in a cohort of OFD cases in the evolutionarily conserved *C2CD3* gene. C2CD3 colocalizes with OFD1 at the distal end of centrioles, and C2CD3 physically associates with OFD1. However, whereas OFD1 deletion leads to centriole hyperelongation, loss of C2CD3 results in short centrioles without subdistal and distal appendages. Because C2CD3 overexpression triggers centriole hyperelongation and OFD1 antagonizes this activity, we propose that C2CD3 directly promotes centriole elongation and that OFD1 acts as a negative regulator of C2CD3. Our results identify regulation of centriole length as an emerging pathogenic mechanism in ciliopathies (Thauvin-Robinet, 2014).

Primary ciliary dyskinesia (PCD): Partner 16 is validating variants identified by partner 4 in the targeted re-sequencing of the ciliopathy cohort. A potential compound heterozygous missense mutation of *DNAH11* in PCD patient OP-63 is being investigated (p.Arg2842Gln het; p.Gln2878* het). Partner 16 has confirmed that DNAH11 protein expression in respiratory cilia of OP-63 is negative, as determined by immunofluorescensce microscopy, supporting DNAH11 loss of function. Partner 16 is currently performing segregation analysis to confirm DNAH11 mutations. The relevant fragment of DNAH11 was cloned into the pGADT7 vector for yeast two-hybrid analysis and forwarded to Partner 1a for ciliary interactome studies; Partners 16 and 1a are currently working together to re-configure constructs to make smaller fragments of this large (~13kb) gene and will have to omit a potential microtubule binding motif from further test constructs. This work will continue beyond the SYSCILIA funded period to accompany the immunostaining data from partner 16 suggesting that this variant is pathogenic.

Bardet-Biedl syndrome: Through the ciliary resequencing project (Task 8.2 and 8.3), partner 4 queried the BBS cohort (n=100 individuals) and found that 75% harbored recessive pathogenic variants in known BBS genes (*BBS1-20*). Evaluation of the remaining 25 samples yielded one plausible candidate gene in a BBS pedigree harboring two frameshifting mutations in *CEP76* that segregate with disease. CEP76 is known to restrain centriole duplication (Tsang et al, 2009) and

contains a transglutamase-like domain that is shared among many members of the NPHP and MKS complexes, and a C2 domain which targets proteins to cell membranes (Zhang and Aravind, 2012). However its role in cilia structure or function is unknown. To evaluate the effect of these mutations on cell migration, retinal phenotypes, and tubulogenesis, we employed an *in vivo* zebrafish assay.

Knockdown of endogenous *cep76* with a splice-blocking morpholino results in significant CE defects, which are rescuable with co-injection of wild-type human *CEP76* mRNA (not shown). *CEP76* mRNA containing either of the frameshift mutations found in the patient is unable to rescue the morphant CE phenotype. Although useful, the CE assay is a distant proxy to the BBS pathology. As such, we sought to evaluate the candidacy of *CEP76* by *in vivo* complementation of phenotypes directly relevant to the patient. Upon review of the clinical data, we noted that the patient had many of the hallmarks of BBS, including retinopathy and kidney disease. Defects in rhodopsin transport to the outer segment cause rod cell apoptosis and subsequent vision loss; we asked whether *cep76* morphant embryos also had retinal defects.

Cryosectioning of 5 dpf control and MO injected embryos showed a reduction of rhodopsin staining in the outer segment of rod cells, with a concomitant increase in rhodopsin staining in the inner segment and cell body (**figure 8.1**). This aberrant rhodopsin localization could be rescued by co-injection with wild-type mRNA, but not with mutant S507fs RNA (**figure 8.1**). To test whether this deficiency in rhodopsin trafficking was associated with a defect in ciliary function or structure, we evaluated cilia structure in photoreceptor cells by co-staining 5 day post fertilization (dpf) retina sections with acetylated tubulin and centrin (labeling the cilia axoneme and basal body, respectively), as well as DAPI staining (labeling the nuclei, allowing for localization of the cell body). We found that treatment of zebrafish embryos with *cep76* MO resulted in significant defects in ciliary structure in photoreceptors as evidenced by a reduction in both the length and overall number of cilia, and that these defects could be rescued by coinjection of wild-type mRNA, but not mutant S507fs mRNA (**figure 8.1**). Next, we evaluated photoreceptors in control or MO-injected embryos for cell death. TUNEL staining of the retina of control and MO-injected embryos showed an increase in TUNEL-positive nuclei in the inner nuclear layer (INL) and outer nuclear layer (ONL), though to a lesser extent (not shown). In 5 dpf control embryos the retina contains an average of 0.2% apoptotic cells, compared with an average of 2.6% in morphant embryos (not shown). This increased cell death in morphants can be rescued with co-injection of wt *CEP76* mRNA (0.2% apoptotic cells), but not with mutant S507fs mRNA (2.8% apoptotic cells).

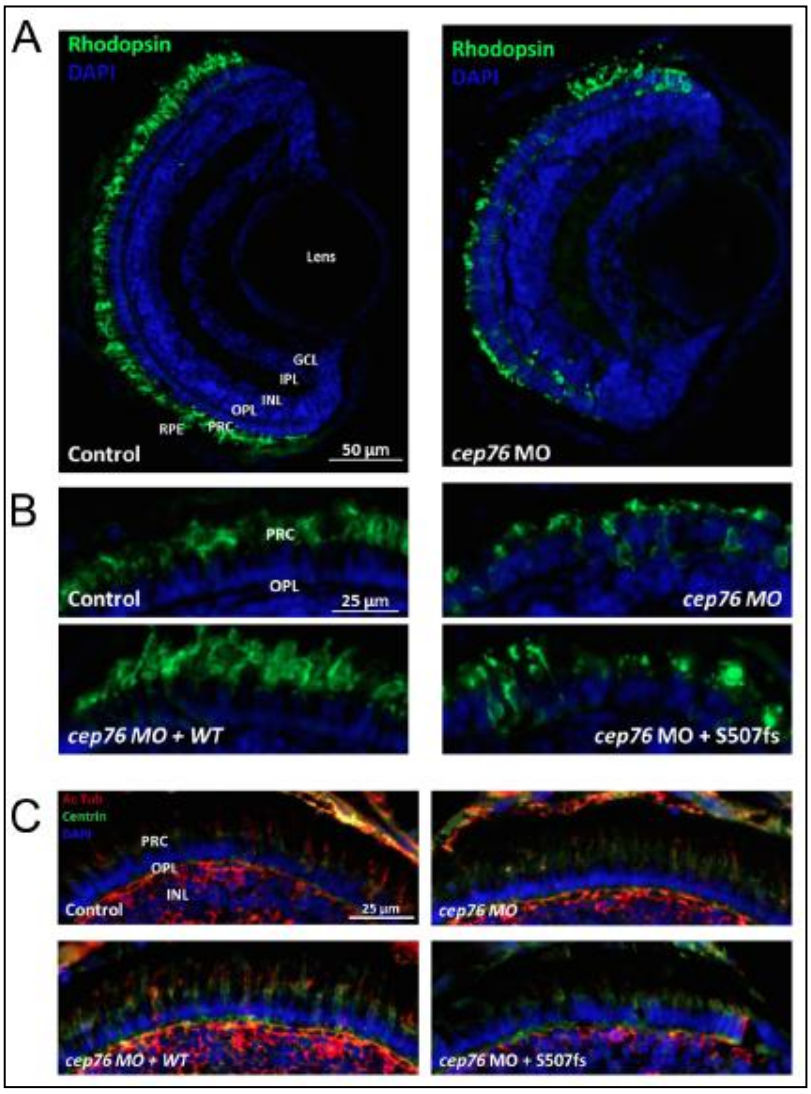

***Figure 8.1*. Immunostaining of Retinal Cryosections for Rhodopsin and Cilia of *cep76* Morphant and Rescue embryos**

A) In 5dpf control embryos, rhodopsin staining is localized to the outermost section of the photoreceptor cell (PRC) layer. B) *cep76* morphant embryos show reduced rhodopsin staining in the outer segment of the rod cell, with increased staining in the inner segment and cell body. This aberrant rhodopsin localization can be rescued with coinjection of wild-type mRNA, but not with mutant S507fs RNA.

C) Staining for cilia in the PRC of 5dpf control and morphant embryos shows a decrease in cilia number and length in morphants, which can be rescued with co-injection of wild-type mRNA, but not with mRNA containing the S507fs mutation. GCL, ganglion cell layer; IPL, inner plexiform layer; INL, inner nuclear layer; OPL, outer plexiform layer; PRC, photoreceptor cells; RPE, retinal pigment epithelium.

Additionally, structure of the nephron was evaluated *in vivo*. Knockdown of endogenous *cep76* resulted in an abnormal tubular structure, likely the result of abnormal cell migration/polarity during development. This phenotype is rescuable with co-injection of wild-type human *CEP76* mRNA (**figure 8.2**). *CEP76* mRNA containing either of the frameshift mutations found in the patient is unable to rescue the morphant kidney phenotype.

These data, combined with the genetic support and renal modeling data (**figure 8.3**), provide compelling evidence for *CEP76* as a novel BBS locus.

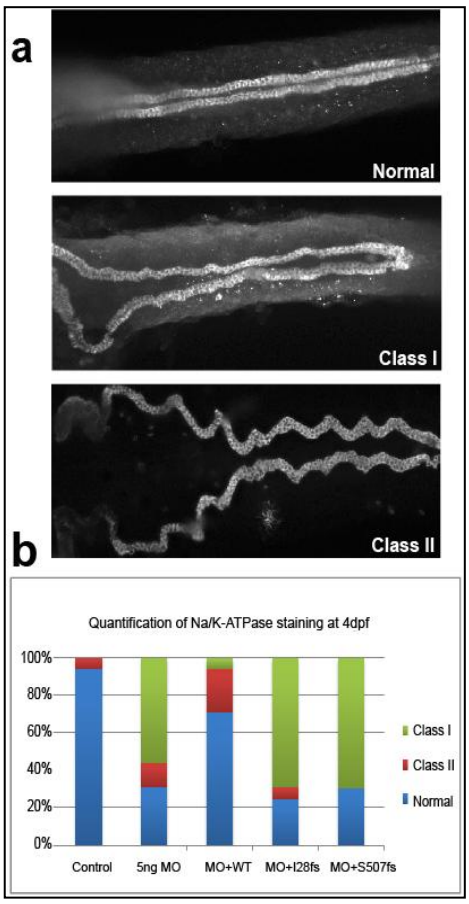

Figure 8.2. **Tubulogenesis defects in cep76 morphants. a.** Representative dorsal images of 4 days post fertilization (dpf) fixed *cep76* morphants immunostained with anti-Na/K-ATPase antibody to demarcate renal tubules. Normal, Class I (mild) and Class II (severe) are shown. **b.** Quantification of larval batches scored according to phenotypic criteria defined in panel (a). 5ng *cep55* MO results in a significantly worse renal phenotype than Controls ($p<0.0001$); co-injection with WT human *CEP55* mRNA rescues this effect ($p<0.0001$); mRNAs harboring truncating mutations found in the patient are unable to rescue the tubulogenesis defect.

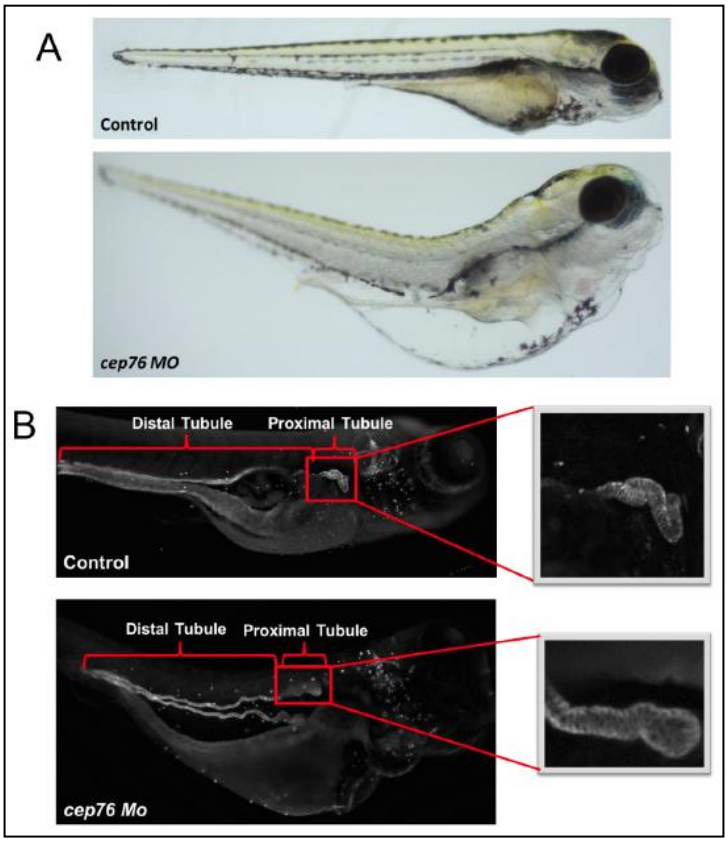

Figure 8.3: **Na+/K+ ATPase Staining of 5 dpf *cep76* Morphant Embryos**
A) At 5dpf, *cep76* morphant embryos have marked edema around gut, heart, and eyes.
B) Na/K ATPase staining shows straight distal tubules and convoluted proximal tubules in control embryos. *cep76* morphant embryos have tortuous distal tubules, with dilated and less convoluted proximal tubules.

Deviations for the technical work planned in Annex I:

For WP8 there are no deviations for the technical work planned in Annex I.

Deviations between actual and planned person-months effort. (see also WP11)

For work package 8 it turns out that the work achieving the project tasks and deliverables was mainly done by partner 4, so other partners devote their person months to other workpackages to achieve these tasks. Partner 1b shifted effort more to WP1 and WP6, partner 9 devoted the effort mainly to WP9 and partner 10 devoted substantial more effort to WP7.

Work package number	WP9		Start date or starting event:				month 0
Work package title	Translational systems biology: ciliotherapeutics						
Activity Type	RTD						
Participant number	8 (L)	5	6	9	13	14	16	18
Participant short name	UMCU	UKL FR	JoGuMz	UCL	CNRS	CCNet	WWU	UEVE
Person-months per participant:	54^{+11}	13^{+6}	16^{+6}	28^{+14}	0	4	13^{+9}	5^{+5}
Actual person months per participant* Month 48 - 60	17^{+5}	0	3.25^{+16}	3.63	-	1	2.43	2^{+2}

* This is considered as use of resources.
Deviations are explained in the end of the report for this Work package.

A summary of progress towards objectives of WP9:

Objective 9.1: *Assaying functional ciliary reconstitution: knowledge-based approach*

This objective has been achieved at month 48.
We have assayed HH, Wnt, and CDK pharmaceutical modulators *in vitro* and *ex vivo* with some success. Several groups are still pursuing pharmaceutical intervention with PTC124.

Objective 9.2: *Assaying functional ciliary reconstitution: compound screens*

This objective has been achieved at month 48.

Objective 9.3: *Lead compound characterization*

This reporting period focused on compound screens performed in zebrafish. Drugs that show promising rescue of the ift172 morpholino induced phenotypes will go on to be studied in more depth, optimizing drug concentrations. We have assessed the viability of potential strategies for translating the *in vivo* and *ex vivo* experiments performed within SYSCILIA to human clinical studies. Since many ciliopathy phenotypes are inborn errors of development (e.g. brain patterning) that are not tractable to therapeutic intervention, we focused on the phenotypes that progress during the lifetime of the patient, such as retinal and renal degeneration.

A summary of progress towards each task in WP9:

➢ *Task 9.1. Correcting nonsense mutations in vivo*

Deliverables under this Task: D9.1 (month 6), D9.3 (month 18), D9.8 (month 42) and D9.9 (month 48) are all delivered in time.

A: Read-through efficiency and toxicity in cell lines

Partner 6:

In the reporting period, we continued our efforts to evaluate read-through capacities of translational read-through inducing drugs (TRIDs) on nonsense mutations of different ciliopathies in cultured cells.

We carried out experiments to evaluate the read-through effect on the p.S243X mutation of the *USH1G* gene *(SANS)* quantitatively. HEK293T cells were transiently transfected with constructs encoding for c-terminally FLAG-tagged USH1G protein SANS-WT or the *USH1G/SANS_p.S243X* (p.S243X) mutation. Treatment with 5 µg/µl and 10 µg/µl PTC124 resulted in a 1.3-fold and 2-fold increase of read-through, respectively, treatment with gentamicin resulted in a 7.9-fold increase as determined by Western blot analyses (**figure 9.1**).

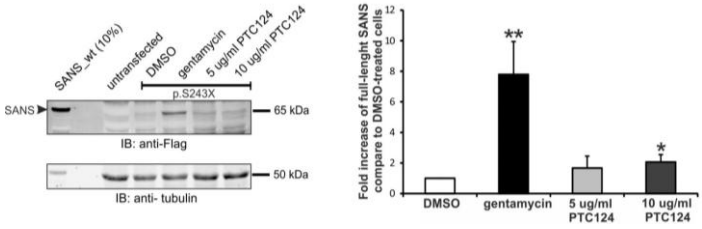

***Figure 9.1*: Read-through of SANS_p.S243X mutation in transiently transfected HEK293T cells analyzed by Western blot with anti-FLAG antibodies**. Treatment with gentamycin and different concentrations of PCT124 restored full-length SF-N-SANS (~65 kDa) expression in *SANS_p.S243X*-transfected cells. Anti-alpha tubulin staining (~50 kDa) was used as loading control. Graph represents quantification of immunoblots of read-through of the *SANS_p.S243X* mutation. The error bars represent SD (n=3). $* p < 0.05$; $** p < 0.01$.

To test the protein function of the recovered SANS protein after TRIDs treatments we utilized interaction assays. Truncated p.S243X SANS lacks the protein-protein interaction domain necessary for the binding interaction of Ush2a, and thereby prohibits the interaction of both USH proteins (Sorusch et al., in prep). We tested the recovered scaffolding function of restored SANS after read-through by the means of interaction assays with USH2a. RFP-Trap experiments using the USH2a intracellular domain (Ush2a icd) as bait, recovered strong SANS bands from the gentamycin and 10 µg/ml PTC124-treated cells indicating functionally active SANS protein, while no band was present in the DMSO-treated control (**figure 9.2**).

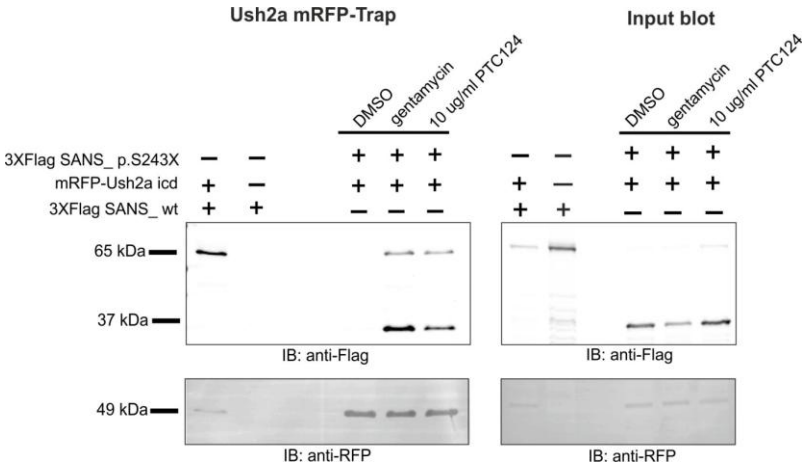

Figure 9.2: **Translational read-through induced restoration of SANS-Ush2a interaction.** Trapped mRFP-Ush2a precipitates full-length 3x FLAG-SANS of SANS_p.S243X transfected cells after gentamycin and PTC124, but not after DMSO treatment.

TRIDs-mediated read-through of the *Clarin1* (*CLRN1*/ USH3A) mutations p.Y63X and p.Y176X was shown by immunofluorescence microscopy (**figure 9.3**). The constructs were cloned into a bi-directional vector for internal transfection control with dsRed. Treatment with PTC124 restored expression of full-length Clarin1 up to 2.5-fold compared to the DMSO-control.

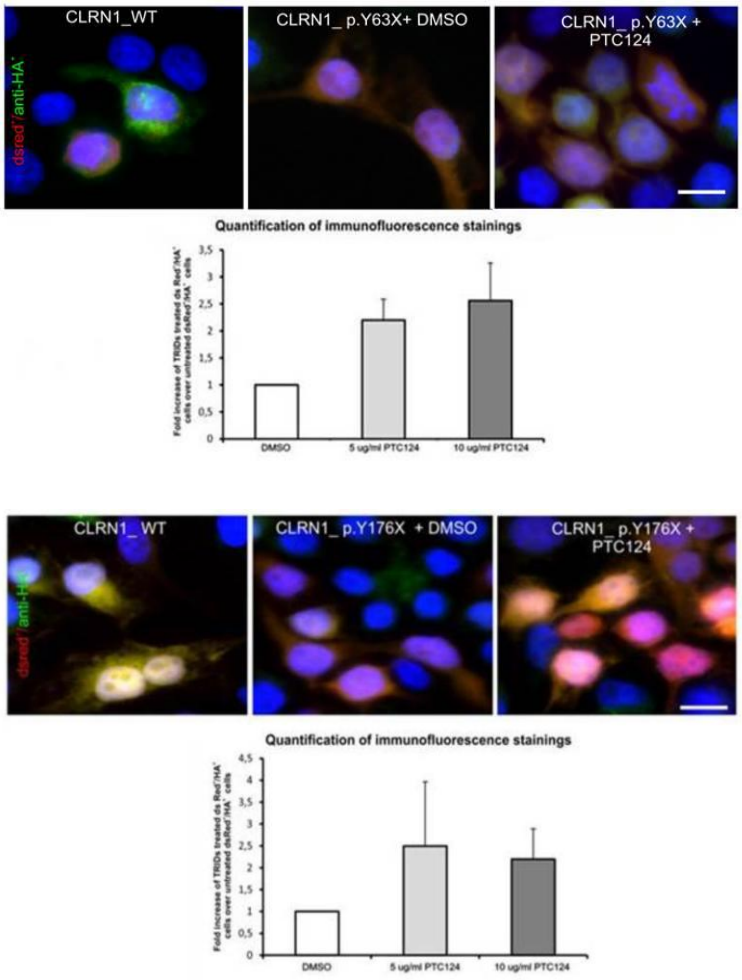

Figure 9.3: **Read-through of CLRN1/USH3A p.Y63X and p.Y176X mutation in transiently transfected HEK293T cells analyzed by indirect immunofluorescence.** HEK293T cells were transiently transfected with constructs encoding for c-terminally HA-tagged CLRN1-WT, CRLN1_p.Y63X, or CRLN1-p.Y176X. Transfected cells are visible by dsRed expression (red). After treatment with 5 or 10 µg/µl PTC124, read-through was analyzed by anti-HA indirect immunofluorescence (green). DMSO treated cells served as controls. CRLN1 staining was detected in CRLN1-WT transfected cells, whereas the staining in untransfected cells or in DMSO-treated controls was only weak. PTC124-treatment restored CRLN1 (green) in cells transfected with the p.Y63X (n=3) or the p.Y176X (n=2) mutation. Nuclear DNA was stained by DAPI (blue). Scale bar 10 µm. Graphs show the according quantifications of the fold increase of CRLN1 positive cells after the treatment with different amounts of PTC124. The error bars represent SD.

In addition, we analyzed the read-through efficiency of PTC124 for the p.R155X nonsense mutation in the harmonin a4 isoform of in *USH1C* in cell culture. In order to confirm the recovery of the scaffold function of restored harmonin after TRID treatment, we tested for the known interaction of the first PDZ domain of harmonin with the C-terminal PDZ-binding motif of Ush2a (Reiners et al., 2005). Our GST pull-down experiments using the C-terminus of Ush2a as bait, recovered an intense harmonin a4 band after gentamycin and 10 µg/ml PTC124-treatment, but only a fade harmonin band in 5 µg/ml PTC124-treated cells (**figure 9.4**). However no band was present when using extracts of harm-a4_p.R155X-transfected, untreated cells.

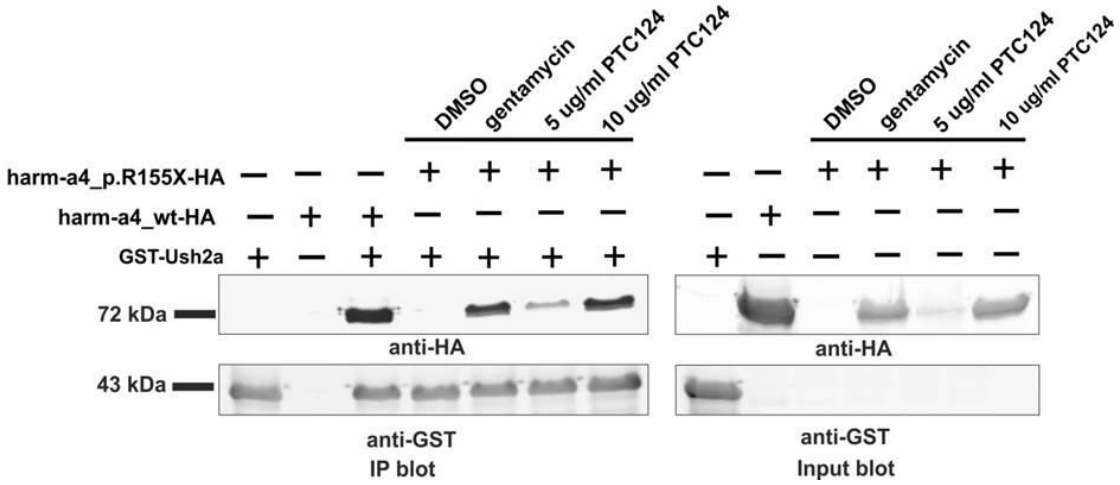

***Figure. 9.4*. Restoration of harmonin a4 scaffold function following TRID treatment assayed by GST pull-down.** HEK293T cell lysates of harm-a4-p.R155X transfected cells treated with gentamycin, 5 µg/ml and 10 µg/ml PTC124 were incubated with the immobilized GST-Ush2a (cytoplasmic tail). Pulled-down proteins were subjected to Western blot analyses using anti-HA antibodies (IP blot).

For testing protein function of recovered harmonin b isoforms, we took advantage of the actin filament-bundling capacity of the harmonin b isoform (Boëda et al., 2002). The translational read-through of the p.R155X nonsense mutation in the harmonin b3 isoform of *USH1C* by PTC124 not only recovered the expression of full-length harmonin, it also restored the characteristic actin filament-bundling capacity of harmonin b (**figure 9.5**).

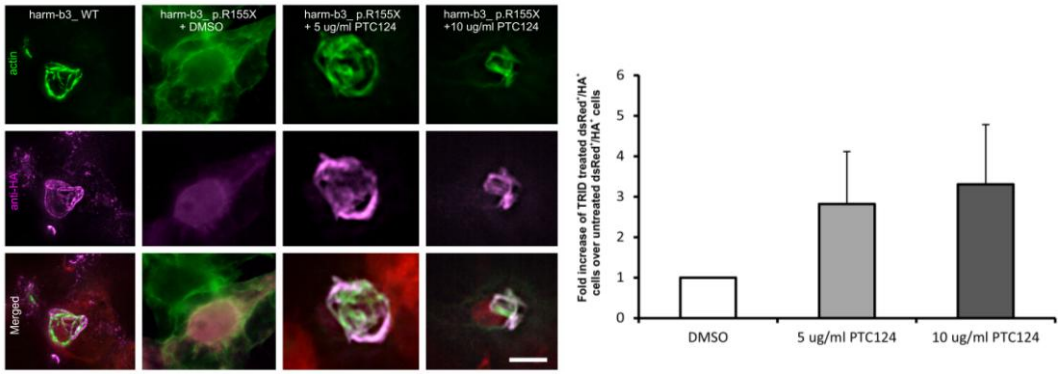

***Figure 9.5*. Functional analyses of restored harmonin proteins.** Representative immunofluorescence analyses of HEK293T cells transiently transfected either with HA-tagged wild type harmonin b3 (harm-b3_WT) or harmonin b3 with the p.R155X mutation (harm-b3_p.R155X) and cultured in the absence or presence of PTC124. Co-staining with anti-HA (violet) and fluorescent phalloidin for actin filament (actin, green) revealed harmonin b3 expression and bundling of actin filaments in wild type and in read-through positive cells but not in DMSO treated harm-b3_p.R155X controls. Graph represents the fold increase of read-through positive cells showing actin bundling activity over DMSO treated cells. Scale bar, 10 µm. The error bars represent SD (n=3).

Further, we continued analyzing the read-through efficacy of PTC124 for the NPHP4 Mutation p.L104X in HEK293T cells. Immunofluorescence analysis revealed a substantial restoration of protein expression after application of PTC124. In seven independent experiments 10 ug/ml PTC124 induced a significant 2-fold increase of read-through efficacy over DMSO treated control cells. These experiments are the basis for *in vivo* studies (task 9.2) in the Nphp4$^{nmfl192/nmfl192}$ mouse model (Won et al., 2011).

In collaboration with partners 8 and 9, we are evaluating read-through efficiency of PTC124 for the p.G73X and the p.Q291X mutation in *BBS1* in cell culture (**figure 9.6**). We have found that PTC124 induces translational read-through of the pathogenic mutation p.G73X in *BBS1*, whereas it does not show a read-through effect on the p.Q291X mutation in the *BBS1* gene. The fact that the read-through efficiency differs shows the importance to test each mutation individually before applying TRIDs to patients with the specific pathogenic mutations. In addition, our data point out that alternative TRIDs to the existing are needed for therapeutic approaches. These experiments are the basis for a clinical pilot study for translational read-through therapy in Bardet-Biedl patients (task 9.6. Lead compound characterization in man).

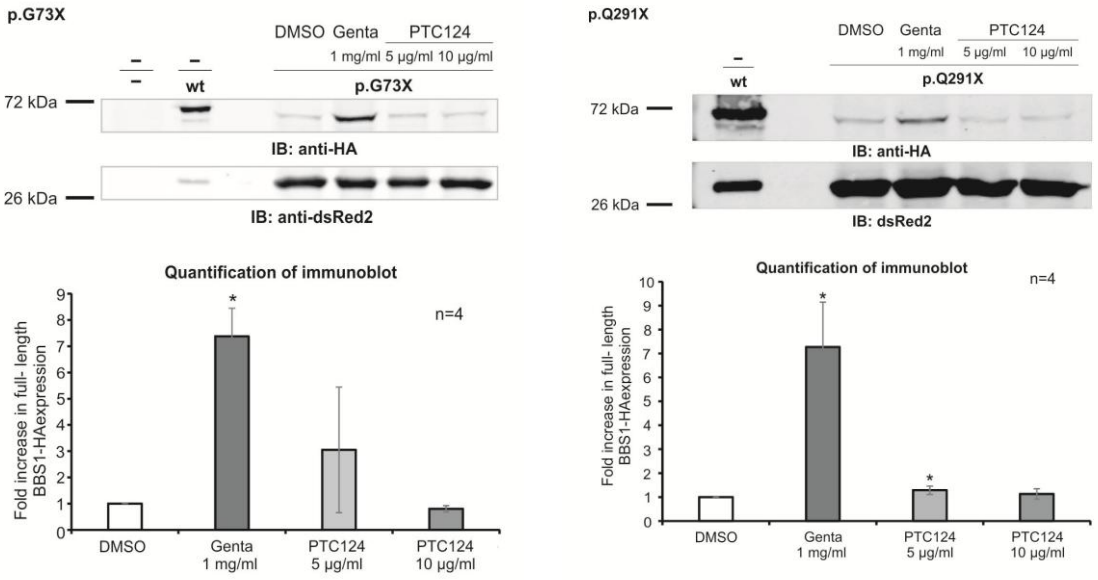

***Figure 9.6*. Western Blot analysis of TRIDs-mediated read-through of the p.G73X and p.Q291X nonsense mutation of *BBS1* in HEK293T cells.** HEK293T cells were transiently transfected with constructs coding for BBS1-WT, BBS1-p.G73X or BBS1-p.Q291X, each C-terminally HA-tagged. Transfected cells were treated with 1 mg/ml gentamycin, 5µg/µl or 10 µg/ml PTC124 or DMSO as control. Read-through was analyzed by Western blot with anti-HA antibodies. dsRed staining was used as loading control. The error bars represent SD.

B: Effect of aminoglycosides/PTC124 on in vitro ciliogenesis of primary human respiratory cells of PCD patients with DNAH5 nonsense mutations

Partner 16:

Has screened additional candidates for PTC read-through studies. Partner 16 has recently published papers describing mutations in *CCNO* (*Wallmeier et al, Nat Genet. 2014*) and *MCIDAS* (*Boon et al, Nat Commun. 2014*), which cause a severe form of respiratory disease resulting from reduced generation of multiple motile cilia (RGMC). Constructs encoding wild-type and nonsense-causing mutations for *CCNO* (c.961C>T hom.) and *MCIDAS* (c.441C>A, p.C147* hom.) have been made. Studies in HEK293 cells showed that myc or FLAG-tagged CCNO is not robustly expressed, thus precluding its further analysis for PTC read-through in this cell line. MCIDAS expression in HEK293 cells was tested and found to be robust. This prompted us, in collaboration with partner 17, to screen NTAP-MCIDAS to identify interaction partners, which reproducibly identified several candidate interacting proteins.

C: Retinal explants

Task completed at month 48.

➢ ***Task 9.2: Molecular pathway intervention***

Deliverables under this Task: D9.2 (month 24), D9.4 (month 18), D9.5 (month 24) and D9.7 (month 30) are all delivered on time.

Task 9.2 was completed according schedule at month 36.

A: Inhibition of Wnt signalling.

Partner 8:

In this last reporting period we have identified a novel regulator of Wnt signalling, DCDC2 to be mutated in ciliopathy patients with a renal and liver phenotype. We could demonstrate that DCDC2 interacts with dishevelled (DVL), and DCDC2 overexpression inhibits β-catenin-dependent Wnt signaling in an effect additive to Wnt inhibitors. Mutations in the affected ciliopathy patients disrupt these effects. This work was published in the *American Journal of Human Genetics*.

B: Antogonize Hedgehog signalling pathway.

Partner 8:

Published a paper in PNAS in this period demonstrating that treating renal cells from ciliopathy mice with purmorphamine rescues their cilia defects: Murine Joubert syndrome reveals Hedgehog signaling defects as a potential therapeutic target for nephronophthisis. All the data is published. We are now treating the mice systemically, work done in collaboration with John Sayer in Newcastle (UK).

➢ ***Task 9.3: Compound screen in zebrafish***

Deliverables under this Task: D9.6 (month 24) and D9.12 (month 60) both delivered on time.

Partner 9:

We have four compounds shown to be effective in our earlier screens: Rapamycin, Geldanamycin, Primaquine and Chloraquine. As this number is not high we decided to try and investigate more candidates using a more targeted approach. We used a drug list provided by partner 14, CCNet, which contained drugs which are either known in the literature or predicted by SysWiz to hit key pathways (mTOR, HSP90, CDK, HDAC, Aurora A kinase, WNT). 10 were chosen (**table 9.1**) for initial zebrafish experiments according to the following criteria:

- Approved for use in humans.
- Not present in the two large drug libraries that we have already screened.
- No consistent literature reports of nephrotoxicity.
- Availability and cost were also taken into account.

A mixture were chosen between those known to affect multiple pathways and those only known to affect one (however SysWiz predicts multiple pathway hits for all these drugs).

Initial screening has begun using the established ift172 morpholino based assays used in our lab. Initial results were inconclusive and drug concentrations are currently being optimised. Drugs that

show promising rescue of the ift172 morpholino induced phenotypes will go on to be studied in more depth.

Table 9.1

Drug	Approved for use in Humans	Comments
Azacitidine	y - cancer	Prevents nephrotoxicity
Decitabine	y-cancer	Non nephrotoxic
paclitaxel	y-cancer	Retards pkd
Sorafenib	y-cancer	Blocks cyst growth in pkd
Lenalidomide	y-cancer	Helps reduce nephrotoxicity from other drugs
nicotinamide	y	Delayed cyst growth in pkd1
Everolimus	y-cancer	Prevents cyst growth in mouse pkd model
Sunitinib	y-cancer	Ameliorates cisplatin nephrotoxicity
tacrolimus	y-transplant infection	Non nephrotoxic
nilotinib	y-cancer	Protective in chronic renal failure

We also trialled two drugs suggested as candidates by partner 8. Initial results were inconclusive so drug doses are in the process of being optimised. These have also been added to the list of candidates used in the report for deliverable D9.12.

- ***Task 9.4. Lead compound characterisation in mice***

Deliverable D9.10 (month 48) and D9.13 (month 60) have been delivered on time.

Task completed by month 48.

Partner 8 is testing two compounds, a HH modulator purmorphamine and a CDK inhibitor in murine models of ciliopathies (Cep290-/- and Sddcag8-/- mice). Results will not be concluded until end of 2015, after the end of SYSCILIA.

- ***Task 9.5. Lead compound characterisation in human cells***

Deliverables under this Task: D9.11 (month 48) has been delivered.

Partner 14, CCNet, continued the identification of alternative drugs for screening if adverse effects of a prospect drug arouse, as well as to characterize a tissue-specific (e.g. kidney, eye) drug effect on Wnt, mTOR, Aurora kinase, Hsp90, HDAC and Cdk signaling pathways, with focus on two compounds, Menaquinone and Aminocarpoic acid, that showed improved ciliopathy phenotype during experimental testing seen by partners 8 and 9.

➢ ***Task 9.6. Lead compound characterisation in man***

Please refer to the report for deliverable D9.13, delivered at month 60. It contains a detailed analysis of the current status of testing in man.

Partner 8 participates in the DIPAK1 trial, an open-label randomized phase 3 trial of lanreotide in renal ciliopathy/ PKD patients:
https://clinicaltrials.gov/ct2/show/NCT01616927?term=renal&cntry1=EU%3ANL&rank=9
Primary Outcome Measure is change in renal function. Time Frame: serial eGFR measurements from month 3 until end of treatment visit (month 30). Change in renal function in Lanreotide versus not treated patients, as assessed as slope through all eGFR measurements taken at study visits during the treatment phase of the trial (n=10), with the value obtained at month 3 as first eGFR value for slope analysis. Results are pending.

Deviations for the technical work planned in Annex I:
For WP9 there are no deviations for the technical work planned in Annex I.

Deviations between actual and planned person-months effort. (see also WP11)
There are small deviations which were made to benefit the project as well as individual partners. For example the excess man-month invested by Partner 9 are tradeoff with Partner 5, who ended up investing more time in other workpackages. Partner 8 also invested more manpower than anticipated, diverting resources to personnel to get the work done in a timely manner. The investment has paid off with exceptionally high number of excellent publications, including J Clinical Investigation, PNAS, Nature Communications, etc. We are satisfied that we have met the milestones and deliverables of WP9 and feel that the participation and communication between all groups has been good.

Work package number	WP10	Start date or starting event:				Month 1
Work package title	**Training, dissemination and translation of knowledge**					
Activity Type	Dissemination and/or exploitation of project results					
Participant number	**14(L)**	1a	3	13	15	17	18
Participant short name	CCNet	RUNMC *Roepman*	EMBL	CNRS	UHEI	UTUB	UEVE
Person-months per participant:	18^{+9}	5	2^{+4}	$0^{+0.75}$	2^{+4}	5^{+2}	3
Actual person months per participant* Month 48 - 60	2	0	0	-	0	1	0

* This is considered as use of resources.
Deviations are explained in the end of the report for this Work package.

To ensure efficient collaborations and transfer of skills among consortium partners the following activities have been employed.

- ***Task 10.1.Internal training and mobility***

Internal training & workshop activities

Internal workshop on April 22, 2015 entitled "Career planning in academia and industry". It has been organized in conjunction with the 5th annual meeting at TIGEM, Pozzuoli, with ~25 people attending the workshop. See deliverable report D10.15 for details, reporting and participants list.

Partner 14 has done preparation for the mentoring and career planning of junior scientists for the workshop. The preparations have taken place over a six month period interviewing individually a number of junior scientists for their interest and assessing talents. The workshop on career planning was prepared with this feedback in mind. The feedback was a success as the junior people said it made a real difference to them to have such a tailored approach, and that they had a much clearer picture about realistic options that were not known to them before.

Webinars (D10.4)

In this period CCNet (partner 14) organized and moderated twelve (12) **Publication Project Shop webinars**, where partners 1a, 3, 15, 17 and 18 discussed about publishable results, ideas for follow-up experiments and tasks, and progress of developing manuscripts. The trajectories toward publication of the final project's results have been set out. Most of these publications are close to the point of submission, while some have already entered the review process or are currently in press.

➢ ***Task 10.2: Outreach***

Contact in reference to SYSCILIA results:

The coordinator was invited to give the Key Lecture at the **7th Santorini Conference Biologie Prospective 'Systems Medicien: Personalized Health & Therapy'.** The lecture, entitled "SYSCILIA: From systems biology to systems medicine of cilia dysfunction in human genetic disease", acknowledged EU FP7 funding for SYSCILIA.

The coordinator has been informed by the CORDIS Editorial Team on behalf of the Research and Innovation Directorates-General and Agencies of the European Commission that the research project's publishable summary has been approved by the European Commission and that it is the basis for the "**Result in Brief**" written by CORDIS science editors.
Results in Brief are published in six languages to support the dissemination and exploitation of EU research results. They are part of the free services provided by the European Commission though CORDIS, the primary repository and website for EU-funded projects and results.
Results in Brief are updated for each publishable summary received by CORDIS and they may also be included in the printed monthly *research*eu results magazine*, also available as e-books and PDF at: http://cordis.europa.eu/research-eu

The SYSCILIA consortium has been contacted by the Project Officer, on behalf of the unit E5 – Novel medical developments, Health Directorate, Directorate General for Research & Innovation, to ask our opinion as an FP7 consortium member and/or as an leading expert, firstly on the progress and potential impact of the systems bio-medicine collaborative/translational efforts in which we are a member, and secondly on the needs for infrastructure facilities/services for the implementation of systems bio-medicine across Europe in a larger scale.
Our input has been communicated to the EC/CASYM workshop organized on the 1st July in Brussels entitled: "*Identification of European infrastructures needs for implementing systems medicine in Europe".* We included a nice slide that we use in SYSCILIA presentations to indicate the systems biology/systems medicine approach:

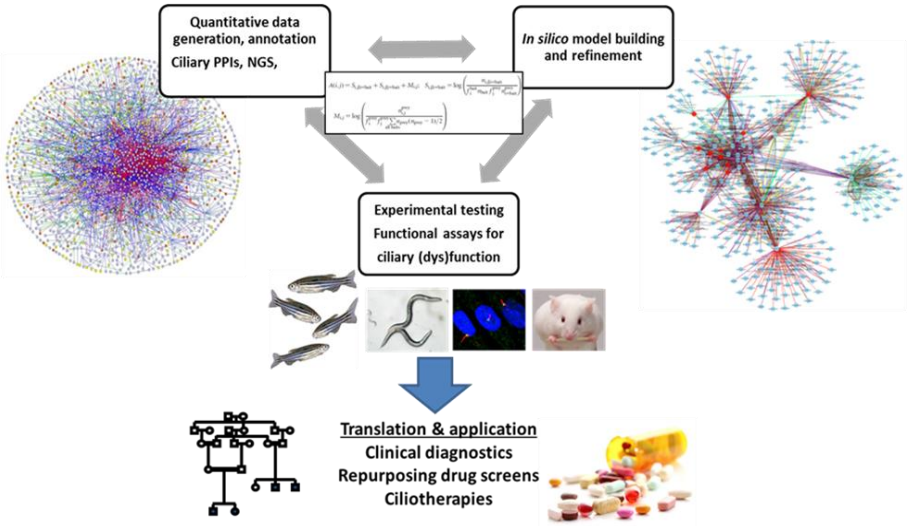

Website

To achieve public participation and awareness about the project, we use our public website http://syscilia.org. Communication of project achievements for the public occurs via the website and internal exchange of information via wiki pages. The ownership of the domain name has been extended for 5 years and the website for SYSCILIA will be kept up to date via regular correspondence between the SYSCILIA management and partner 15.

Webinars aimed at industry, academics and clinicians (D10.7)

The sixth and seventh semi-annual webinar aimed at industry, academics and clinicians "Discovery of potential novel diagnostic options for ciliopathies in the SYSCILIA project" was held on on 16th October 2014 and 7th May 2015. The aim was to facilitate active translation of project results and findings and to introduce academics and industrial partners to ciliopathy arena. In total 900 experts from the academia, industry and clinics were invited. The webinar presentations had the following participants:
Pedersen Gitte, Genomic Expression, Denmark
Bolondi, Giuliano, Instituto C.S.S. Mendel, Italy
Hannah Mitchison, University College London, UK
Liudmila Polonchuk, Roche, Switzerland

Contact with other (EU) projects or researchers

Cilia2014 (http://www.cilia2014.org/overview) was held in Paris from the 18th to the 21st November 2014. It was being organized by 4 European cilia networks: the GDR3581 Cil (France), the British Ciliopathy Alliance, the Nordic Cilia Centrosome Network and the EU-FP7 Programme SYSCILIA.
The meeting, the second international conference in Europe for the cilia scientific and clinical community, was very successful with over 400 registrants, excellent presentations and enthusiastic discussions. It was focused on recent developments in cilia structure and function including trafficking, cilia and development, cilia in human genetic diseases and cilia in infectious microorganisms. An attractive hallmark of the Cilia conferences is the exchange of knowledge of high quality, mainly unpublished work in a friendly and open atmosphere. The conference highlights both scientific and clinical progress, uniquely integrate patient perspective , and brings together scientist from different disciplines.
SYSCILIA was well represented with partners having oral as well as poster presentations, where they outlined the progress and achievements of the project.

SYSCILIA support of the conference - Organising and scientific Committee:
Phil Beales, partner 9; Simone Dusseljee, partner 1a; Matthias Gerberding, partner 17; Rachel Giles, partner 8; Ronald Roepman, partner 1a; Marius Ueffing, partner 17.

A meeting report summarising the main highlights of the meeting has been published in the open access journal *Cilia* and is available at: http://www.ciliajournal.com/content/4/1/5

The next Cilia2016 meeting will be organized in Amsterdam with Ronald Roepman to chair the organizing committee.

Outreach to patients

Cilia 2014 (Institut Pasteur, Paris; November 18 – 21, 2014) gave individuals and families affected by ciliopathies the opportunity to meet and engage with clinicians and scientists. Especially at the gala dinner where all the delegates were mixed at tables, enabling informal and lively interactions. Among the registrants for the meeting were several patient organizations, e.g. EURORDIS, AIRG-France, Laurence-Moon-Bardet-Biedl Society, PKD International, Association Joubert Syndrome NL, Ciliopathy Alliance, The PCD Family Support Group UK, and The Jeune Syndrome Foundation.

Dissemination activities (see Annex I)

All dissemination activities like public presentations, posters and conferences with SYSCILIA and EU funding acknowledgement can be found in Annex I and are submitted via the on-line reporting tool.

Cilia2014 was a perfect opportunity to indulge in almost a full week of ciliary research, meet with patients, clinicians and industry, and explore new collaborative avenues that will further boost our success.

Poster

Several posters reflecting the main results of the SYSCILIA project have been presented at Cilia2014 in Paris, with SYSCILIA and EU FP7 logos displayed.

Deviations for the technical work planned in Annex I:

For WP10 there are no deviations for the technical work planned in Annex I.

Deviations between actual and planned person-months effort. (see also WP11)

The project manager is also acting as a Training Manager. The person months effort is included in the management activities, reported under WP11.

2.3 Project management during the period.

Work package number	WP11	Start date or starting event:	Month 1
Work package title	**Overall Management of the Project**		
Activity Type	Management		
Participant number	**1a (L)**	17	
Participant short name	RUNMC *Roepman*	UTUB	
Person-months per participant:	21	4.5^{+4}	
Actual person months per participant* Month 48 - 60	8.4	0.65	

* This is considered as use of resources.
Deviations are explained in the end of the report for this Work package.

Consortium management tasks and achievements per scientific component:

Communication between beneficiaries

- Regular SYS-IT skype meetings (partners 1a, 1c, 3, 15, 18) and several face-to-face meetings
- Weekly telephone conversations between partner 10 and Partner 1a (Ronald Roepman & Dorus Mans) about plans for data publication and cross-comparison of datasets, following on from three-month secondment of Dr. Mans in the lab of Partner 10. Discussion with partner 1 (Ronald Roepman) about plans for cross-comparison of screen data with protein-protein interaction data and publication.
- Teleconferencesof partner 10 with members of partner 9 group (Miriam Schmidts, Hannah Mitchison) about cross-comparison of screen data with genetic variation data (in, for example, the UK10k ciliopathy panel) and plans for publication.
- Collaborative work of partner 10 with Partner 6 (Uwe Wolfrum), including high resolution confocal microscopy and immunoelecton microscopy localization of candidate hits from the secondary screen in retinal sections.
- Regular email contact between partner 10 and members of group of partner 1a, including discussion of data-sharing and methods of automated analysis of .tiff image files using existing “Columbus” algorithms, sharing of draft figures on DropBox and sharing a draft manuscript on Google Docs.
- Regular email and telephone contact of partner 10 with partner 11 (Oliver Blacque), for further validation of candidate hits from the secondary screen in worm mutants.
- Collaborative work of partner 10 with partner 1c, partner 8 and partner 11 on the function of the novel tetraspan protein TMEM107, a candidate hit from the genome-wide ciliogenesis screen
- Continuing collaborative work of partner 10 with other groups in Leeds, sharing of image data from whole-genome screen for other analysis purposes, including premature

chromosome condensation analysis and cell proliferation (Sandra Bell and Darren Tomlinson).

- Weekly project management meetings with Partner 10 researchers, and members of the Bioscreening Technology Group (BSTG), LIMM, for continuing troubleshooting of minor quality control and scheduling issues and timely delivery of the whole genome screen
- Regular email and telephone contact partner 10 with Dr. Dan Doherty, University of Washington, about cross-comparison of screen data with genetic variation data (in Joubert syndrome patients) and plans for publication.
- Regular email and personal contact partner 10 with Dr. Jarema Malicki, University of Sheffield, to develop TALEN or CRISPR mutagenesis zebrafish models of ciliopathies, ciliary related conditions and eye disorders. Establishment of the "Northern Cilia Club" as an informal venue for poster and spoken presentations for early-career researchers in the cilia biology field.
- Regular emails between Partners 8 and 9, telephone conversations every 2 months.
- A PhD student from Partner 9's lab (Beales) visited Partner 8's lab (Giles) for a period of 6 months. January – June 2015.
- A technician from Partner 1's lab (Roepman) spent 3 months in Partner 8's lab (Giles) to support the final touches in WP9. January –March 2015.

Consortium management issues

None to report.

Networking and Dissemination of the Results

List of project meetings, dates and venues.

As Annex III is provided the participants lists and agenda in which, if applicable, short comments or decisions taken are given.
(See Annex III_Details for the list of SYSCILIA project meetings_month 48-60.pdf)

Annual Meeting April 22-24, 2015; TIGEM Pozzuoli, Italy (**D11.13**)

The **SYSCILIA Steering Committee Meetings** (minutes are published on the private part of the website).

Conference calls:
October 31, 2014 and February 23, 2015.
In person:
November 18, 2014 at Cilia2014 and April 22, 2015 at the annual meeting.

Publications

The publications have been submitted on-line, as required by the FP7 on-line reporting guidelines. The list of publications is also available on the SYSCILIA website: http://syscilia.org, under the tab 'Results'. An overview of publications for period 4 can be found in Annex II.

From June 1, 2014 an impressive total of **45 papers** have been published in peer-reviewed journals acknowledging the EU funding for the SYSCILIA project. **16 articles** appeared in journals having an **Impact Factor above 8 - 7 publications** in the high impact Nature journals like Nature Cell Biology, Nature Genetics, Nature Communications and Nature Protocols.

Since the start of the project **a total of 171 publications** have been published in scientific journals (~45% with IF>8; almost 10% with IF>30). 34 publications featured with more than 1 SYSCILIA partner (almost 20%).

Besides publications in journals, partner 11 has published a chapter in the book Methods in Cellular Biology.

The European Commission was informed about the recent publication, with 10 consortium members as author, in Nature Cell Biology of the whole genome siRNA screen revealing a comprehensive list of genes implicated in ciliopathies.

Overall Management of the Project

Scientific Advisory Board

The Scientific Advisory Board (SAB) gave critical input to our very interdisciplinary team of 18 partners from seven different countries. The important role of self-assessment of the network was pursued by yearly meetings of a SAB with the Steering Committee and General Assembly during the retreat of the consortium. Here the SAB evaluated whether additional expertise and partners were needed for optimal conductance of the project.

The Scientific Advisory Board consists of four independent external scientists. Prof. **Veronica van Heyningen,** DPhil FRS FRSE FMedSci was unfortunately not able to attend the 5th annual meeting. Prof. **M.H. Breuning** M.D.,Ph.D., Prof. Dr. **Erich E. Wanker** and AG Prof. Dr. **Alfred Wittinghofer** were present at the 5th annual meeting at TIGEM in Pozzuoli, April 22-24 2015, and actively participated in the discussions. They generated a report with their concluding remarks for the consortium at the end of the meeting.

April 23, 2015, Pozzuoli, Italy
Scientific Advisory Board (SAB) on the 2015 meeting of the SYSCILIA consortium

SAB members present: Alfred Wittinghofer, Martijn H. Breuning and Erich E. Wanker

The fifth annual meeting of the SYSCILIA consortium was held from 22-24 April at the TIGEM in Pozzuoli, Italy. It was the fourth meeting at which SAB members were present.

Once again we were impressed with the constructive atmosphere, the enormous enthusiasm of all participants, the readiness to share ideas, data and tools, and the willingness to collaborate closely in order to realise project goals. After having experienced several EU-funded projects, the SAB members find SYSCILIA exceptional. The consortium is highly integrated and clearly follows a common research goal.

In previous meetings, research plans and future experiments were presented. Now, in this final meeting many researchers reported very interesting results at a very mature stage. This includes the mapping of the ciliome, the sequencing of patient DNAs, and the knockdown of genes in *Zebrafish Danio rerio, C. elegans, Xenopus*, retina explants form mice, and cell lines. The exome sequencing results strongly supported the notion that more than one gene is modified in ciliopathies and that the spectrum of mutations may eventually explain the variety of phenotypes of the disease. In a collaborative manner, both genome wide and focussed RNAi screens have been successfully completed. Furthermore, a large number of new genes that potentially play an important functional role in cilia formation were functionally validated in cell and *in vivo* model systems.

The consortium has continued the effort started earlier to generate a comprehensive set of protein-protein interactions in ciliogenesis using affinity chromatography-based MS methods and systematic yeast-two-hybrid screens. In total, ~58,000 interactions connecting 4,500 human proteins were collected. A significant fraction of interactions was validated in independent assays and functional studies. Using the available data, various approaches to predict functionally relevant protein clusters were presented. Furthermore, the effects of disease-causing mutations on protein-protein interactions were successfully examined. Quantitative measurements of gene expression were performed at protein as well as RNA level and data were integrated with the protein-protein interaction data sets generated. To avoid working with false positive interactions that are inevitable in systematic operations, the computational biologists developed various strategies to define high-confidence interactions for meaningful further experimental validation. Similarly, computational strategies to predict potentially disease-relevant ciliary genes as well as new functional protein complexes were successfully developed and applied.

In the work package on ciliotherapeutics, high-throughput testing of known drugs for their effects on cilia formation identified several promising compounds. These molecules were subsequently tested in various cell model systems. In addition, good progress was reported on the use of drugs that can initiate the read-through of early stop mutations causing the Usher Syndrome. This approach is innovative and in the medium term may open up novel therapeutic avenues.

The bioinformatics groups have been very active in collecting, storing and organizing the huge datasets, implementing good practice data integration. Furthermore, SYSCILIA researchers have been highly active in exchanging materials and data, as well as organising meetings and webinars. In recent years, a large number of peer-reviewed papers has appeared in the highest-ranking journals. Furthermore, the collaborating groups are in the process of publishing additional “landmark papers” in order to make their data available to the public and to demonstrate the success of their systems biology

approach. It is expected that the release of the available data sets will stimulate additional basic and applied research in the Cilia community.

Overall, it is important to note that this collaborative project has been highly productive. The SAB appreciated the disclosure of part of the exome sequencing results from patients, but urges the quick release of the full data set which will be a great value both to diagnostic as well as to research laboratories. The same holds true for all the other data that the cilia community is eagerly awaiting to be released into the public domain. Evidently the functional role of most proteins, and protein-protein interactions have as yet not been completely elucidated, indicating focal areas of future research.

The large majority of the deliverables and milestones stated in the initial application have been reached; in several aspects the consortium over-fulfilled the original plan. It will be interesting to see how the gained knowledge will be used in future studies to answer mechanistic questions about ciliary development, maintenance and transport. In our view, it seems very likely that the generated knowledge will lead to the development of novel disease-modifying therapies that in the long run will create benefit for patients, their families and health systems.

A systems biology approach was very successfully applied in this collaborative project. The generated data will clearly promote basic and translational research in the field, which is in line with the mission of the Horizon 2020 program.

Alfred Wittinghofer
Martijn Breuning
Erich Wanker

The coordinators are very gratefull for the SAB's thorough feedback and evaluation of SYSCILIA.
"It was an enormous pleasure and benefit to all SYSCILIAns to have you as our advisors, both personally and scientifically. As members of the Scientific Advisory Board you have provided us with critical input and guidance. We think many of our results both in published as in upcoming papers were fuelled by important discussions with our SAB during our annual meetings and beyond. Many thanks for your time, engagement and effort. We hope we will have the chance to interact again in the future, and also wish you all the best."

Quality Assurance

The goal of Quality Assurance is to verify that all products and documentation to be delivered meet all technical requirements. Therefore a Quality Assurance Plan has been drafted, which has led to a document describing the Quality Assurance organization, tasks and responsibilities, activities and reporting (see Deliverable report D11.3), which had been updated in the previous reporting period after the SYSCILIA Gold Standard was established.

Consortium Agreement

The Consortium Agreement has been negotiated, concluded and signed by all projects participants at the beginning of the project (see Deliverable Report D11.1). The purpose of the Consortium Agreement (CA) is to specify with respect to the project the relationship amongst the parties, in particular concerning the organization of the work between the parties, the management of the project and the rights and obligations of the parties concerning inter alia

liability, Access Rights and dispute resolution. The Consortium Agreement has been accessed by partner 18, UEVE after approval of Amendment No3 to the Grant Agreement.

Ethical issues

All research performed by members of the consortium complies with the ethical standards in the countries in which the research is performed and with the rules as set by the European Union. There were no ethical issues associated with the research in SYSCILIA that the Steering Committee needed to evaluate.

Financial management

The 4th Interim Payment

This was transferred to the coordinator after the Commission's approval of the 4th annual report and deliverables. The Interim Payment has been transferred to the partners who were not paid the maximum 85% of the assigned EC contribution yet.

CFS

For period 5 beneficiary 1, RUNMC; beneficiary 4, Duke University; beneficiary 12, INSERM; beneficiary 16, WWU Muenster and beneficiary 17, UTUB have exceeded the threshold of €375,000 requested EC contribution and therefore included a Certificate of Financial Statement with Form C for period 5.

Form C

Adjustment Form C:

Beneficiary 3 has submitted an adjustment Form C for period 4 to correct for hospitality costs at the annual meeting (April 14-16, 2014 Heidelberg)

Beneficiary 6 has submitted an adjustment Form C for period 4 to correct indirect costs (simplified method).

Beneficiary 7 has submitted an adjustment Form C for period 4 to correct for unclaimed subcontracting costs (animal maintenance) and other direct costs (consumables) under RTD.

Beneficiary 11 has submitted an adjustment Form C for period 3 and period 4 to correct for incorrectly claimed costs.

Beneficiary 16 has submitted an adjustment Form C for period 2 and period 3 to correct for incorrectly claimed costs as found by the auditor.

Beneficiary 17 has submitted an adjustment Form C for period 4 to correct incorrectly claimed costs as found by the auditor.

Management costs declared for partner 1a and 17 are eligible according to the FP7 guidelines.
OTHER costs under WP10 claimed for partner 1a, 14 and 17 are eligible according to the FP7 guidelines.

Information letter No.1.
In P4 SYSCILIA received an information letter No1 in which a change in Indirect Cost Method for beneficiary 4, Duke University, was mentioned. The beneficiary indicated to the coordinator that they wish to continue the financial reporting for SYSCILIA with a 20% flat rate for indirect costs. The beneficiary has applied this for the reporting for period 4 and 5.

Shift in budgets

These requests have **no implications for the work** carried out as laid down in the **Technical Annex**, but comes down to differences in expected budget need for consumables and personnel at the time of negotiation of the grant and the real costs spent on personnel and consumables.

Beneficiaries 3, 4, 7, 10, 11 and 16:
Don't request the total assigned EC contribution per beneficairy, which we would like to redistribute to beneficiaries who explained the overspending of the assigned EC contribution as necessary for the project (partners 1a, 17, 5 and 6).

Beneficiary 1:
Beneficiary 1 proposes a shift in budget from Other Direct Costs to Personnel under RTD.
If budget allows, partner 1a would like to be reimbursed for the personnel costs under Mangement made by the dedicated project manager who has spent considerable more time and effort on the project than anticipated at the time of negotiations.

Beneficiary 4:
Proposed a shift in budget from Other direct costs to personnel under RTD (see periodic report 4), but does not request the total Duke assigned EC contribution.

Beneficiary 5:
Besides proposing a shift in budget from Other direct costs to personnel under RTD (see periodic report 4), partner 5 claims €15,731.91 more than the UKL FR assigned budget. These costs have been made for extra person months technical assistance necessary to reach the aims of WP 5+6 after the shift from *in vitro* to *in vivo* assays.

Beneficiary 6:
The total requested EU contribution for Mainz for SYSCILIA over all reporting periods is now quite a bit higher than the originally planned Mainz budget for the project. This is more of a formality to reflect the full costing method at Mainz. At the very beginning, the overhead rate used in Mainz for budget calculation was not correct. So while we have to report according to the simplified

method and full costs, we will of course accept a total reimbursement as originally planned in the GPFs. However, if due to underspending by other partners it is at all possible to increase the reimbursement sum, this will be very welcome.

Beneficiaries 8, 9, 14 and 15:

Reallocate the budget under RTD/INNVATION from Other direct costs to Personnel costs, but do not request more EU contribution.

Beneficiary 12:

Confirms the total budget requested: €523,720.18 and knows that the maximum request for Inserm is €411,800.00.

Beneficiary 17:

The table below shows the budget and its redistribution among the cost categories and the costs stated in periods 1 – 5 on a preliminary basis. Only direct costs are shown.

SYSCILIA COST ITEM RTD WP 1, 2, 3, 4, 10	category	**original budget direct costs**	**budget redistribution direct costs**	**Costs stated Period 1 - 5**	**Remains (+) Overdraft (-)**
1) Personnel	personnel	**520.000,00**	**560.000,00**	**559.213,70**	**786,30**
2) Durable Equipment RTD	equipment	**325.000,00**	**270.200,00**	**316.801,36**	**-46.601,36**
3) Consumables RTD	other	**100.000,00**	**110.000,00**	**97.458,95**	**12.541,05**
4) Other Direct Costs, Travel and Publication etc.	other	**20.000,00**	**24.800,00**	**35.132,46**	**-10.332,46**
Totals:		**965.000,00**	**965.000,00**	**1.008.606,47**	**-43.606,47**
SYSCILIA COST ITEM Other & Management WP 10 & 11	category	**direct costs**	**direct costs**	**Costs stated Period 1 - 5**	**Remains (+) Overdraft (-)**
1) Personnel MGT WP 11 (4,5 PMs)	personnel	**33.500,00**	**33.500,00**	**34.274,22**	**-774,22**
2) Audit MGT	subcon	**3.000,00**	**3.000,00**	**720,75**	**2.279,25**
3) Other Costs MGT per Amendment transferred to Heidelberg (6000 EUR gross: 3750 direct+ 2.250 indirect) Rest transferred to Personnel Other Activities = WP 10)	other	**6.000,00**	**2.250,00**		**2.250,00**
4) Personnel Other Activities	personnel	**4.000,00**	**4.000,00**	**6.250,00**	**-2.250,00**
Totals:		**46.500,00**	**42.750,00**	**41.244,97**	**1.505,03**
Total SYSCILIA Project P17 UTUB direct costs		**1.011.500,00**	**1.007.750,00**	**1.049.851,44**	**-42.101,44**

The budget has been decreased by 6000 EUR (= 3.750 direct costs and 2.250 indirect costs), amount of which has been transferred to Partner 15 – UHEI. (organized several Cross Component meetings/workshops) This amount has been deducted from Pos. 3 MGT. The remaining direct costs of 2.250 were merged with Pos. 4- Other Activities and spent for personnel costs referring to work for WP10.

A budget redistribution has been proposed by Partner 17 UTUB at the beginning of period 4. Although Partner 17 UTUB has not received an explicit permission from the European Officers for this budget redistribution, all further planning and calculation has been made on the basis of the redistributed budget. Furthermore, the personnel cost rates that have been set up during contract negotiations have been too low, so it was crucial to have more funds for personnel to ensure completion of the work plan.

On the other hand, Partner 17 UTUB has decided to state the actual project costs as a whole and this includes the actual workload of the VELOS mass spectrometer for the SYSCILIA project. Over the whole project duration the average workload was 56,38%, but in the last period the workload had to be increased to 73% (= 87.837,95 € depreciation costs in P5 on the basis of the total acquisition costs of the VELOS of 601.150 EUR). Beneficiary 17 UTUB is aware that he is therefore

exceeding the budget by ca. 40.000 EUR, which cannot be claimed unless there would be a redistribution of spare funds among the partners. If a cut of the claim has to be executed and be closer defined, Partner 17 UTUB is requesting to cut from the category durable equipment, rather than from category personnel.

Beneficiary 18:
Has claimed costs for software engineer (scholarship) and master internship as Other Direct Costs under RTD as they cannot be considered, in France, as personnel costs.

Efforts:
Please see overview below for the actual efforts per beneficiary per WP.
For month 0 – 48 it becomes apparent that the actual efforts deviate from the indicative efforts as stated in the Technical Annex for some partners and work packages.

Partner 6 validated putative ciliary proteins for the Ciliocarta-project (workpackage 4) by localization studies in workpackage 1, and because our first approach to generate transgenic SF-TAP mice failed, we had to put a lot of work into solving the problem, we shifted most of our personmonths from other workpackages to *work package 1.* Additional personmonths than indicated in Annex I were necessary to reach those aims. If there is no remaining project budget to cover the additional costs concerning workload and consumables, the expenses will be covered by Johannes Gutenberg University Mainz as part of their commitment towards the success of the project.

Both partner 14 and 15 have devoted more person months effort to *work package 2* than indicated in Annex I, to be able to complete the work needed in the final stages of data analysis and integration. They do not request more EU contribution.

Partners 1a and 10 have devoted more person months effort to *work package 7* to be able to complete and publish the siRNA screens. No additional human resources are requested. Partner 1a reallocates budget under RTD/INNVATION from Other direct costs to Personnel costs.

For *work package 8* it turns out that the work achieving the project tasks and deliverables is mainly done by partner 4, so other partners devoted their person months to other workpackages to achieve these tasks.
Partner 1b has shifted person month from WP8 to WP6. These additional months on *work package 6* were spent on detailed (immune)histological evaluation of zebrafish after gene knockdown and in functional evaluation of the eye. In addition to a shift of person months between workpackages, we have reallocated €18,000 from materials to personel costs due to the time consuming procedures of histological and functional characterization of CAMs in zebrafish. No additional funds are requested from the EU.
Partner 9 has exceeded our planned person months for *work package 6*. We were required less in WP8 than expected and thus transferred those resources to this workpackage, in the main part to aid the validation efforts for novel CAMs found in the big datasets. Furthermore given the change

in acceptance by the wider scientific community for morpholino derived models over the five year timeframe of SYSCILIA we began in the final 12 months to establish CRISPR models in the lab as described in this report. This need for new models could not have been forseen at the outset of this project and therefore took extra person months to complete than originally allocated. No additional funds are requested from the EU.

Partner 10 moved person months from WP8 to WP6 and WP7. The total person months dedicated to these WPs exceeds the indicative effort by 22.2pm to be able to achieve the aims of WP6 and publish the results of WP7. No additional human resources are being requested.

For *work package 9* there are small deviations which were made to benefit the project as well as individual partners. For example the excess man-month invested by Partner 9 are tradeoff with Partner 5, who ended up investing more time in other workpackages. Partner 8 also invested more manpower than anticipated, diverting resources to personnel to get the work done in a timely manner. The investment has paid off with exceptionally high number of excellent publications, including J Clinical Investigation, PNAS, Nature Communications, etc. We are satisfied that we have met the milestones and deliverables of WP9 and feel that the participation and communication between all groups has been good.

Partner 5:
Due to the enhanced technical and experimental work as a consequence of the amendment of Annex 1 to switch from *in vitro* to *in vivo* assays the work load of WP5 and 6 was increased. As mentioned in the previous periodic report 13^{+4} PMs have been reduced in WP9 and shifted to WP 5 and 6. In addition further PMs were necessary to reach the aims of WP 5+6. At month 60 the difference between the actual and indicated person months (including PMs of WP9) amounts to $15{,}4^{+26}$ in total for WP5 and WP6.

Partner 11:
Has reconfigured the personnel costs from the beginning of the project in a cost neutral way and can dedicate more person months effort to the project. No Additional human resources are being requested.

The project manager, partner 1a, is also acting as a Training Manager. The person months effort indicated for *work package 10* is included in the management activities, reported under WP11.

Partner 16:
Although the actual total PM contribution is less than the indicative PM contribution described in Annex I, Partner 16 has performed all the assigned tasks and achieved all assigned deliverables for SYSCILIA. For additional work contributions including technical (D. Ernst, M. Herting, B. Lechtape) and intellectual (N.T. Loges, P. Pennekamp, H. Omran) support no EC contribution was requested and which was financed by other resources provided by Partner 16.

Efforts for month 48 - 60 of the project.

		Actual efforts per beneficiary per WP month 48 - month 60										
Beneficiary nr.	**WP1**	**WP2**	**WP3**	**WP4**	**WP5**	**WP6**	**WP7**	**WP8**	**WP9**	**WP10**	**WP11**	**Total**
1a	6.5	0^{+2}	0^{+2}				14			0	8.4	28.9^{+4}
1b	0.95					18.45^{+5}		0				19.4^{+5}
1c			9	3^{+3}								12^{+3}
3		0^{+2}	11	$0^{+0.5}$						0		$11^{+2.5}$
4		2.39			1.23	9.82		9.37				22.81
5					3.8^{+6}	3.4^{+6}			0			7.2^{+12}
6	17.4^{+11}				11.375^{+4}	0^{+0}			3.25^{+16}			32.025^{+31}
7						28		13.5				41.5
8					4.6^{+3}	5^{+4}	1.6^{+4}		17^{+5}			28.2^{+16}
9						20.59		0	3.63			24.22
10						0^{+4}	2	0.56				2.56^{+4}
11					10.7^{+3}	10.5						21.2^{+3}
12						$20.17^{+9.21}$						$20.17^{+9.21}$
13												
14		18	0	2					1	2		23
15		12^{+3}	0^{+2}	2								14^{+5}
16	3.46		0					2.32	2.43			8.21
17	22^{+8}	2^{+2}	0	0						1	0.65	25.65^{+10}
18		1^{+1}	5^{+3}	8^{+6}					2^{+2}			16^{+12}
Total	50.31^{+19}	35.39^{+10}	25^{+7}	$15^{+9.5}$	31.705^{+16}	$115.93^{+28.21}$	17.6^{+4}	25.75	29.31^{+23}	3	9.05	**$358.045^{+116.71}$**
		Note: the numbers in superscript are the person months from the own resources.										

Cumulative efforts for month 0 - 60 of the project.

		Actual efforts per beneficiary per WP month 0 - 60										
Beneficiary nr.	**WP1**	**WP2**	**WP3**	**WP4**	**WP5**	**WP6**	**WP7**	**WP8**	**WP9**	**WP10**	**WP11**	**Total**
1a	50^{+33}	8^{+2}	$10.5^{+4.5}$				41^{+18}			$0^{+0.7}$	42.7	$152.2^{+58.2}$
1b	25.65^{+15}					36.15^{+21}		$1.79^{+0.5}$				$63.59^{+36.5}$
1c			46^{+10}	11^{+3}								57^{+13}
3		5^{+2}	$38.5^{+2.5}$	$10.5^{+1.5}$						$0^{+0.5}$		$54^{+6.5}$
4		8.57^{+6}			8.51^{+4}	36.41^{+6}		99.37^{+28}				152.86^{+44}
5					36.8^{+28}	32.6^{+26}			0^{+2}			69.4^{+56}
6	42.65^{+43}				35.625^{+13}	6^{+15}			15.25^{+40}			99.525^{+111}
7						98.5^{+14}		$28^{+2.7}$				$126.5^{+16.7}$
8					13.6^{+13}	$35.1^{+29.5}$	16.1^{+23}		57.1^{+19}			$121.9^{+84.5}$
9						27.10^{+9}		4^{+6}	40.12^{+20}			71.22^{+35}
10						20.5^{+18}	69.7^{+21}	3.13^{+11}				93.33^{+50}
11					61.39^{+3}	87.31						148.7^{+3}
12						$50.64^{+30.21}$						$50.64^{+30.21}$
13		3^{+2}	3^{+1}	22^{+11}					0	$0^{+0.75}$		$28^{+14.75}$
14		41^{+1}	21^{+3}	9					4	20^{+6}		95^{+10}
15		32^{+8}	14^{+5}	9						0^{+1}		55^{+14}
16	$21.76^{+3.5}$		1.94					8.27^{+1}	10.93^{+0}			$42.9^{+4.5}$
17	99.25^{+50}	10^{+6}	2^{+2}	2^{+1}						1.925	4.275	119.45^{+59}
18		2^{+3}	6^{+4}	10^{+9}					5^{+5}	0		23^{+21}
Total	$239.31^{+144.5}$	109.57^{+30}	142.94^{+32}	$73.5^{+25.5}$	155.925^{+61}	$430.31^{+168.71}$	126.8^{+62}	$144.56^{+49.2}$	132.4^{+86}	$21.925^{+8.95}$	46.975	**$1624.215^{+667.86}$**
		Note: the numbers in superscript are the person months from the own resources.										